Ultracold Strontium in State-Dependent Optical Lattices
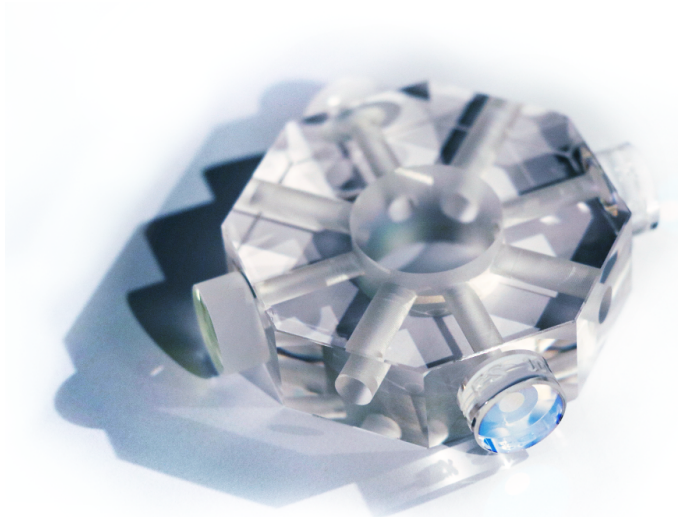
André Heinz

Ultracold Strontium in
State-Dependent Optical Lattices

Dissertation an der Fakultät für Physik
Ludwig-Maximilians-Universität München

vorgelegt von

André Heinz

aus Nürnberg

München, 18.02.2020

Zusammenfassung

Innerhalb der letzten zwanzig Jahre haben sich *ultrakalte Quantengase* mit Alkalimetall-atomen in optischen Gittern als effektives Werkzeug zur Simulation von Quantenviel-teilchenmodellen erwiesen. Eine der wichtigsten technischen Errungenschaften in diesen Quantensimulationsexperimenten war die Entwicklung des Quantengasmikroskops, wel-ches mit der Auflösung und Ansteuerung einzelner Atome in optischen Gittern einen wichtigen Schritt in Richtung absoluter Kontrolle aller internen und externen Freiheits-grade einzelner neutraler Atome ermöglichte.

Im Gegensatz zu Alkalimetallen haben Erdalkalimetallatome eine energetische Struk-tur, welche einen Reichtum an Wellenlängen für *zustandsabhängige optische Fallen* bietet. Ein Beispiel dafür sind "Tune-out Wellenlängen", bei denen die Polarisierbarkeit und somit das Fallenpotential eines Zustands verschwindet. Diese Wellenlängen ermöglichen neuartige Quantensimulationen.

Um Quantensimulationen mit zustandsabhängigen Fallen zu ermöglichen, bauen wir das erste *Strontium Quantengasmikroskop* der Welt. In dieser Arbeit zeigen wir dessen Design und Bauprozess von Grund auf und beschreiben technische Errungenschaften und Erweiterungen. Momentan sind wir in der Lage Temperaturen von $\sim 1~\mu$K mit ^{88}Sr und ^{87}Sr Atomen mittels Laserkühlung zu erreichen. Desweiteren, entwickelten wir eine neue Methode zur Messung von Tune-out Wellenlängen. Unsere *Messung der Tune-out Wellenlänge des $^1S_0$ Grundzustands* ist unserem Wissen nach die genaueste bisher, wenn wir die geringe Sensitivität der Polarisierbarkeit mit der optischen Frequenz mit ein-beziehen. Wir erreichen eine Unterdrückung des Grundzustandsgitters von fast fünf Größenordnungen gegenüber dem Gitter des angeregten Zustands. Mit spektroskopi-schen Messmethoden konnten wir die Polarisierbarkeit des $^3P_0$ Zustands extrahieren und aus unseren Messungen die $^1P_1$ und $^3S_1$ Lebensdauern neu bestimmen. In einem weiteren Experiment demonstrierten wir $^3P_0$ Atome, gefangen in einem optischen Gitter bei der Tune-out Wellenlänge.

Optische Gitterpotentiale unterliegen durch Laserleistung limitierten, harmonisch-ge-formten Potentialhüllen, welche die Systemgröße in Quantensimulationsexperimenten bestimmen. Diese "harmonische Einschränkung" beeinflusst sämtliche Tunnel- und Wech-selwirkungsparameter im gesamten Gitter und führt zu anderen ungewollten, durch die Systemgröße bedingten, Effekten. Viele Quantensimulationsexperimente würden daher von größeren Systemen profitieren, weil entsprechende theoretische Modelle typischer-weise unendlich große, flache Systeme voraussetzen. Um die optische Leistung zur Erzeu-gung von optischen Gittern zu erhöhen, entwickelten wir einen vakuumkompatiblen, monolithischen *Überhöhungsresonator mit gekreuzten Resonatormoden* mit $1/e^2$ Strahlra-dien von $\sim 400~\mu$m, welche Systemgrößen von $\sim 200 \times 200$ Gitterplätzen erwarten lassen. Wir berichten über dessen Design, Bauprozess, Charakterisierung und Implementierung. Der Resonator kann die optische Leistung bei sechs verschiedenen Wellenlängen, inner-halb des sichtbaren bis infraroten Bereich des Spektrums, bis zu einem Faktor ~ 1000 überhöhen und ermöglicht so tiefe und stabile Gitter bei Wellenlängen, bei denen keine hohen Laserleistungen verfügbar sind.

Abstract

Within the last two decades, *ultracold quantum gases* of alkali metal atoms in optical lattices have proven to be a rich toolbox to simulate quantum many-body physics models. One of the crucial technical advances of these quantum simulation experiments was the development of quantum gas microscopes, which initiated a large step towards full control over the internal and external degrees of freedom of single neutral atoms in optical lattices.

In contrast to alkali metal atoms, alkaline-earth metal atoms offer a richer energy level structure, which feature a variety of wavelengths for *state-dependent optical traps*. One example are the so-called "tune-out wavelengths", at which the polarizability and thus the trap potential of one state vanishes. Novel quantum simulation and quantum computation schemes with strontium are based on the implementation of these tune-out wavelengths.

To realize quantum simulations with state-dependent lattices, we are building the world's first *strontium quantum gas microscope*. In this thesis we show its design and assembly from the ground up and describe technical advances we made. At this point, we are able to lasercool ^{88}Sr and ^{87}Sr atoms to a temperature of $\sim 1~\mu$K. Furthermore, we developed a novel technique to measure tune-out wavelengths. To our knowledge, our measurement of the *$^1S_0$ ground state tune-out wavelength* is the most precise measurement to date, if we take into account the small sensitivity to a change in optical frequency. We reach a suppression of the ground state lattice potential with respect to the excited state by almost five orders of magnitude. Moreover, we performed spectroscopic measurements at this tune-out wavelength to extract the polarizability of the $^3P_0$ state. Both results gave rise to a reevaluation of the atomic lifetimes of the $^1P_1$ and $^3S_1$ states. Besides, proof-of-principle trapping of $^3P_0$ atoms in a tune-out wavelength lattice has been demonstrated.

Optical lattice potentials to trap ultracold quantum gases underlie laser-power-limited harmonically-shaped envelopes which set the system size in quantum simulation experiments. This so-called "harmonic confinement" influences tunneling and interaction parameters, leads to inhomogeneities across the system, and to unwanted finite system size effects. Most quantum simulation experiments would greatly benefit from more homogeneous and larger systems, as the corresponding models typically assume flat and infinitely large systems. To enhance the optical power used to generate optical lattices, we have built an in-vacuum monolithic *buildup cavity with crossed, large cavity modes* with $1/e^2$ beam radii of $\sim 400~\mu$m giving rise to expected system sizes of $\sim 200 \times 200$ lattice sites. We show the design, assembly, characterization, and implementation of this buildup cavity. With it, we can enhance the optical power at six different wavelengths in the visible to infrared spectrum by factors up to ~ 1000 to enable working at wavelength at which no suitable high-power lasers are available.

Contents

List of Tables

List of Figures

Chapter 1

Introduction

"CAN [quantum] physics be simulated by a universal [classical] computer?", is *the* question Richard Feynman asked in 1981 [1]. Feynman stated that scaling the system size in numerical simulations of a many-body quantum system would require exponentially "large" classical computers. The validity of this statement can be visualized at the Hilbert space dimension of a chain of n quantum-mechanical two-level systems, so-called "qubits", which already scales exponentially and is given by 2^n. This challenge calls for new theoretical and experimental approaches to gain a better understanding of quantum many-body physics.

To overcome the limitations of classical computation [2], Feynman came up with an idea to simulate many-body quantum systems by directly mapping the quantum mechanical properties of an experimental system to the quantum model of interest [1, 3, 4]. In such an experiment, a quantum state is prepared to undergo a time-evolution of the simulated model in the presence of specifically-chosen parameters, after which a measurement is taken. Various platforms during the last two decades have emerged to perform such tasks, such as photonic waveguides [5], superconducting circuits [6], trapped ions [7], *ultracold neutral atoms* [8, 9, 2] and molecules [10]. All of these platforms have different strengths and limitations.

The field of ultracold neutral atoms achieves large arrangements of particles. To generate a full quantum-mechanical behavior, light-matter interactions are used to trap and cool large ensembles of neutral atoms to almost zero temperature. By investigating ultracold atomic systems in *optical lattices*, which are conservative periodic potentials created by standing-waves of light, this approach is especially suitable for the study of solid-state physics models [2]. A basic example is the *Hubbard model*, which considers tunneling of individual particles to neighboring lattices sites and an on-site interaction for particles occupying the same lattice site [11].

The first ultracold neutral atom quantum simulations were performed with alkali metal atoms such as rubidium, which led to the experimental demonstration of a Mott-insulator phase [12], in which atoms arrange themselves such that a single atom occupies each lattice site. A milestone in extracting information from such quantum gases was achieved by upgrading the experiments to *quantum gas microscopes*, which enable single-site resolved detection, addressing, and state preparation of individual atoms in optical lattices via a microscope objective [13–15]. In addition, the integration of spin-resolved detection in fermionic lattice gases [16–21] offers fascinating perspectives for the understanding of doped antiferromagnets [22–25], a problem relevant to understand the physics of high-

temperature superconductors.

During the time of these developments, the branch of quantum metrology made significant progress on their precision. Nowadays, the most precise atomic clocks, *optical lattice clocks*, reach a fractional precision of 6×10^{-19} using cold atoms in optical lattices [26, 27]. These optical clocks use alkaline-earth(-like) atoms, such as strontium and ytterbium. Thanks to their two valence electrons, these species support extremely narrow (forbidden) optical transitions with linewidths on the millihertz level and are therefore suitable for quantum metrology. The two *clock states* involved in this so-called *clock transition* are well decoupled from environmental influences and motional degrees of freedom [28].

To enable this decoupling in optical clocks, alkaline-earth metal atoms are trapped in optical lattices at so-called "magic wavelengths", which match light-induced energy shifts of the clock states and hence preserve the clock transition frequency to make it a suitable frequency-stable reference for optical clocks [29]. These magic wavelengths also exist in alkali metal atoms at the expense of high scattering rates and low coherence times, as their frequency is traditionally located between adjacent hyperfine energy levels [28]. In alkaline-earth metal atoms, more trap wavelengths with different interesting properties, specific to two (clock) states, exist [30], which is why we call optical lattices generated with these wavelengths "state-dependent lattices".

Additionally, these two-valence-electron systems provide conserved nuclear spin storage and readout during operations on electronic states and an extremely low sensitivity to environmental magnetic field fluctuations. Most of these promising properties have been verified quickly, which triggered a boom of proposals to employ alkaline-earth metal elements in quantum simulation experiments [28].

For these reasons, many quantum gas microscopes started to build to employ elements like strontium and ytterbium in the past few years. A ^{174}Yb quantum gas microscope has been finished [31] and others are being built with strontium [32–34]. In addition, a bottom-up approach by creating optical tweezer arrays of alkaline-earth metal atoms has been launched recently and offers novel perspectives to increase the coherence times of such quantum simulation platforms with respect to alkali metal atoms [35–37]. Other ultracold atom machines have been built to realize phase transitions with several spin-states with ytterbium [38] and to probe spin-orbit coupling in fermionic strontium atoms [39].

The challenge we are trying to take up in this thesis is the symbiosis of quantum gas microscopy with the beneficial properties of the well-known alkaline-earth metal element strontium. We plan to conduct quantum simulations based on state-specific site-resolved particle control which can be achieved with a quantum gas microscope, state-dependent trap wavelengths, and strontium. This setup allows us to further study light-matter interfaces, where our system would mimic atoms closely trapped to photonic materials [40–44]. One of our aims is the local observation of particle bound states to quantum emitters and the resolution of the energy band structure of those systems, as we will see in section 1.5.

On top of that, we tackle a long-term challenge to increase the system size of quantum gas microscopes [45]. Optical lattice envelopes underlie laser-power-limited harmonic-

potential envelopes which set the system sizes of state-of-the-art quantum gas micro-scopes, i.e. $\sim 30 \times 30$ [16, 46]. This so-called "harmonic confinement" also influences tunneling and interaction parameters across the whole system and therefore creates un-wanted inhomogeneities in quantum simulation experiments [47]. By enhancing the laser power used in optical lattices, we expect larger systems with an increased num-ber of particles, an improved homogeneity, and thus a better approximation to quantum many-body models which assume infinitely large systems. The increased particle number in the system will directly improve the statistics obtained from measurements, which are a current limitation of quantum gas microscopes. To gain about two orders of magni-tude in the number of constituents and at the same time employ state-dependent lattices at wavelengths where only low-power lasers are available, we invent an optical buildup cavity. This buildup cavity features large, homogeneous cavity modes at six different wavelengths to generate two-dimensional lattices in our experiment and enables us to conduct light-matter interface quantum simulation schemes [40–44].

In the following sections, we take the opportunity to elaborate more on strontium, quantum simulation with quantum gas microscopes, state-dependent lattices, and system size limitations to provide a good basis to the reader to understand the presented results in this work.

1.1 Why strontium?

Let us take a closer look at the strontium atom. As an alkaline-earth metal atom, it has a rich energy level structure consisting of singlet and triplet states due to its two valence electrons [Fig. 1.1]. The energy level scheme offers a variety of strong allowed transitions with linewidths in the megahertz regime, and narrow forbidden and doubly-forbidden intercombination lines connecting singlet and triplet states with linewidths on the millihertz to kilohertz level.

The $^1S_0$ state in strontium is the electronic ground state. Here, three main transitions are important: first, the broad blue $^1S_0$– $^1P_1$ transition which offers a large decay rate of $\Gamma_{^1P_1} = 2\pi \times 30.41(9)$ MHz useful for scattering process with large momentum transfer. Secondly, the ~ 4000 times narrower, red, forbidden $^1S_0$– $^3P_1$ transition has a scattering rate of $\Gamma_{^3P_1} = 2\pi \times 7.423(7)$ kHz [48], which is slightly allowed due to mixing with the $^1P_1$ state [51]. In addition, the fermionic ^{87}Sr has a 1 mHz narrow, doubly-forbidden $^1S_0$–$^3P_0$ clock transition, which offers a lifetime of ~150 s, and became a frequency standard in optical lattice clocks, especially due to its long coherence times [52]. This transition arises due to the nuclear spin of the fermion of $I = 9/2$, which is responsible for hyperfine interactions leading to mixing of the pure $^3P_0$ state with the $^3P_1$, $^3P_2$, and $^1P_1$ states [51]. In both, the $^1S_0$ and the $^3P_0$ state, the nuclear spin states are decoupled from the electronic states and motional degrees of freedom. This makes the nuclear spin insensitive to atomic collisions, which happen at the electronic shell [53, 28].

The decoupling of the nuclear spin states from the electronic shell with zero net angu-lar momentum ($J = 0$) leads to symmetrically distributed Clebsch-Gordan coefficients between the magnetic sublevels, which is called "SU(N) symmetry". Consequently, the
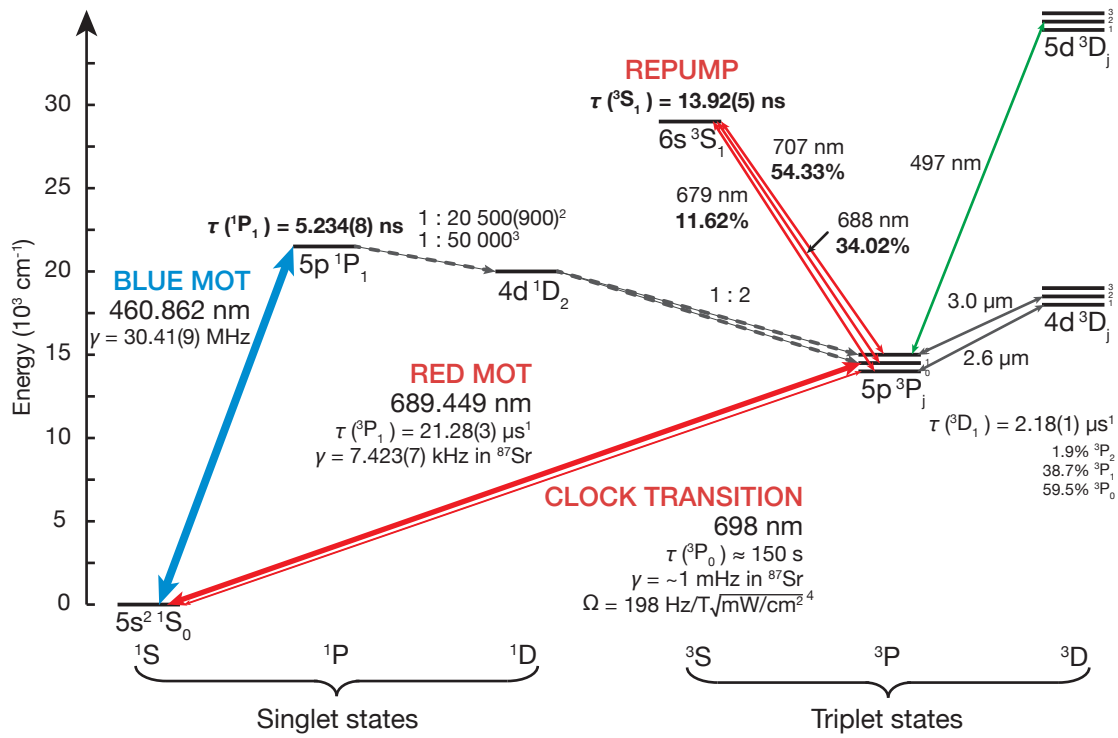
Fig. 1.1 An energy level diagram showing the most important states and transitions including lifetimes and important branching ratios in strontium. The quantities marked in bold are determined in this thesis. Spectroscopic data is taken from Refs. [1] [48] [2] [35] [3] [49] [4] [50].

spin in fermionic strontium can be used as an information storage, which is hardly affected even when transferring atoms from the $^1S_0$ to the $^3P_0$ state and vice versa. With 10 different spin states, the fermionic isotope ^{87}Sr is a great candidate for simulations of exotic quantum phases [54].

All strontium isotopes have a metastable $^3P_2$ state, which has a large electronic spin of $J = 2$. In ^{87}Sr this state has a lifetime of $\sim$21 s [55] and in ^{88}Sr a lifetime of several minutes [56, 57]. The $^3P_2$ is connected to the $^1P_1$ state via the $^1D_2$ decay channel. The $^3S_1$ state with an Einstein coefficient of $\Gamma_{3S_1} = 2\pi \times 11.34(5)$ MHz can decay to all ^3P_J states. The microwave $^3P_0$– $^3D_1$ transition with a transition wavelength of 2.6 μm is close to the blackbody radiation wavelength at room temperature and is responsible for the currently largest uncertainty in atomic lattice clocks, the blackbody radiation (BBR) shift [48].

In the following we give an overview over the technical advantages, which can be employed with strontium. The strong $^1S_0$– $^1P_1$ transition is the cornerstone for quick slowing and cooling mechanisms by radiation pressure, in a Zeeman slower or a magneto-optical trap (MOT), which employ laser light and magnetic fields to slow and cool atoms by radiation pressure [58]. Especially for MOTs, this strong transition allows large atomic velocities of 30 m/s for the atoms to be captured and trapped by the MOT [59], at the expense of a high Doppler-limited temperature of $T_D = \frac{\hbar \Gamma_{1P_1}}{2k_B} = 0.7$ mK [58]. Here, $\hbar$ is the reduced Planck constant and k_B Boltzmann's constant. This makes initial capturing of large atom numbers relatively easy. The recent advent of 461 nm single-mode laser diodes enables the much simpler implementation of diode lasers with wavelengths at this transition, instead of working with frequency-doubled infrared lasers. When operating on the $^1S_0$– $^1P_1$ transition, the internal atomic state can decay to the metastable $^3P_2$ state via the $^1D_2$ decay channel, which is ideal for trapping atoms in this state with a quadrupole magnetic trap.

The narrower, red $^1S_0$– $^3P_1$ transition is beneficial for final cooling procedures and allows to apply MOT schemes to achieve temperatures close to the recoil limit of $T_{\rm rec} = \frac{\hbar^2 k^2}{2mk_B} = 230$ nK [58], as $T_D = \frac{\hbar \Gamma_{3P_1}}{2k_B} = 180$ nK is even lower. Here, m is the mass of the atom and $k = \frac{2\pi}{\lambda}$ is the wavevector of the light with wavelength λ. When loading the atoms in a dipole trap and adiabatically lowering the trap depth, hot atoms from the velocity spectrum can be released, a process called "evaporative cooling". With initial temperatures on the 1 μK level, temperatures below critical temperatures of Bose-Einstein condensates or degenerate Fermi gases are achieved without large atom loss. Due to the narrow linewidth of the $^1S_0$– $^3P_1$ transition, motional sidebands in optical lattices can be resolved and allow direct sideband cooling.

Very important to this thesis is the existence of far-detuned low-scattering trap wavelengths with state-specific properties in strontium, or alkaline-earth atoms in general, which we will introduce in the next section.

1.2 State-dependent lattices for strontium

The electronic energy level structure in alkaline-earth metal atoms allows us to find several state-dependent trap wavelengths with specific properties [28, 30]. In contrast to alkali metal atoms, these wavelengths are often far detuned from atomic transitions and do not lead to large induced scattering rates. In this section, we introduce the concept of state-dependent and state-independent trap wavelength for optical lattices. Therefore, we need to introduce the concept of the polarizability first and explain what optical lattices are. By combining these two, we go through different types of state-dependent and state-independent lattices.

1.2.1 Polarizability

We describe an optical electric field by $\boldsymbol{E}(\boldsymbol{r}, t) = \frac{1}{2}(E(\boldsymbol{r})\exp(-i\omega t)\hat{e}+c.c.)$ with an optical angular frequency $\omega = kc$, where c is the speed of light. Here, $\hat{e}$ is the polarization unit vector and t is time. When an atom experiences an electric field $\boldsymbol{E}$, a dipole moment $\boldsymbol{d}(\boldsymbol{r}, t) = \frac{1}{2}(d(\boldsymbol{r})\exp(-i\omega t)\hat{e} + c.c.)$ is induced, which underlies

$$d(\boldsymbol{r}) = \alpha(\omega)E(\boldsymbol{r}) , \tag{1.1}$$

where $\alpha(\omega)$ is the complex scalar dynamic polarizability [60]. The time-averaged potential this induced dipole moment $\boldsymbol{d}$ experiences in the electric field is given by

$$V_{\mathrm{dip}}(\boldsymbol{r}) = -\frac{1}{2}\langle \boldsymbol{d}(\boldsymbol{r}, t)\boldsymbol{E}(\boldsymbol{r}, t)\rangle = -\frac{1}{2\epsilon_0 c}\mathrm{Re}\left[\alpha(\omega)\right]I(\boldsymbol{r}) , \tag{1.2}$$

where the factor $\frac{1}{2}$ takes into account that the dipole moment is induced and not permanent. In the last step we used the intensity of a plane wave in vacuum $I(\boldsymbol{r}) = \frac{1}{2}c\epsilon_0|E(\boldsymbol{r})|^2$, with the vacuum permittivity ϵ_0, while we neglect rapidly oscillating terms with 2ω by evaluating the time average. This expression leads to a negative energy shift of a state for a positive $\mathrm{Re}\left[\alpha(\omega)\right]$. Hence, a maximum in the intensity $I(\boldsymbol{r})$ leads to a conservative attractive potential which can be used as an atomic trap. We call the frequency shift V_{dip}/h, the AC Stark shift, where h is the Planck constant.

In a Lorentz-oscillator model the polarizability of a state in a two-level system with transition frequency ω_0 can be described in a classical approach via [60]

$$\alpha(\omega) = 6\pi\epsilon_0 c^3 \frac{\Gamma}{\omega_0{}^2(\omega_0{}^2 - \omega^2 - i\Gamma\frac{\omega^3}{\omega_0{}^2})} , \tag{1.3}$$

with the decay rate Γ, which is related to the linewidth γ of the transition via $\Gamma = 2\pi\gamma$ [1]. The derived expression for $\alpha(\omega)$ in combination with Eq. (1.2) describes the energy shift of a state. When dealing with atoms as multi-level systems, we have to sum up the polarizability contributions shown in Eq. (1.3). For an atom in state k, we have to

---

[1]Note that Γ is given in units of $1/\mathrm{s}$ or $2\pi \times \mathrm{Hz}$ and γ is given in units of Hz.
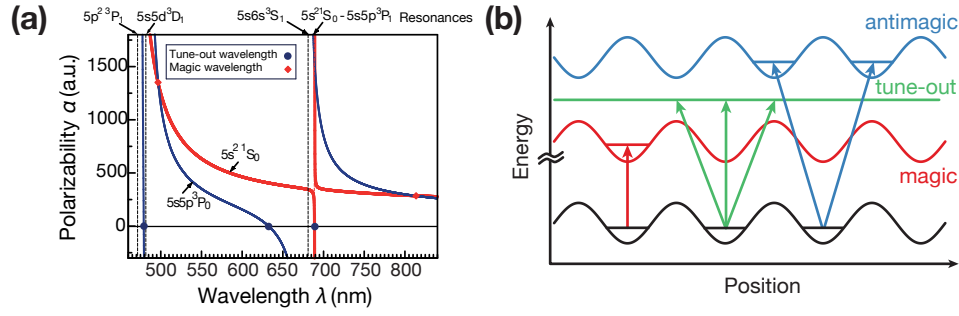
Fig. 1.2 (a) Taken from Ref. [30]. Example for the polarizability of strontium of the $^1S_0$ and $^3P_0$ state. (b) Examples of optical lattice types generated with magic, tune-out, and antimagic wavelengths.

consider all a accessible atomic transitions to higher energy levels j and find

$$\alpha_k(\omega) = 6\pi\epsilon_0 c^3 \sum_j \frac{\Gamma_{jk}}{\omega_j{}^2(\omega_j{}^2 - \omega^2 - iA_j\frac{\omega^3}{\omega_j{}^2})} \,, \tag{1.4}$$

where we have introduced the Einstein coefficient $A_j = 1/\tau_j$ of each state j with the corresponding lifetime τ_j. Note that each state j can decay into several states l with a probability which is distributed via a branching ratio Γ_{jl}/A_j. Multiplying the branching ratio of the decay to such a state with A_j leads then to the corresponding decay rate Γ_{jl} of this transition. The real part of α_k can be positive, negative or even zero for some wavelengths due to the presence of many optical transitions. We show an example of a more precisely calculated polarizability of strontium in Fig. 1.2 (a) in the visible to near-infra-red range. We can harness the complexity of α_k by finding trapping wavelengths with interesting properties.

Note that the imaginary part of the polarizability can be used to calculate the scattering rate of lattice photons at the trapped atom in a state k via $\Gamma_{\rm sc} = \frac{1}{\hbar\epsilon_0 c}{\rm Im}(\alpha_k)I$ [60]. The knowledge of the scattering rate is important to estimate heating effects and coherence times of quantum mechanical states in optical traps.

1.2.2 Optical lattices

In the last subsection, we discussed how the intensity of light can be used to form trap potentials for atoms. With the polarizability α_k of the atom in state k as an atomic property for its interaction with the light intensity, we can introduce the concept of optical lattice potentials. For simplicity we assume a complex plane wave in the form of an optical electric field $E_0 \exp(ikx - i\omega t)$ propagating along the X axis, with frequency ω and wavevector k. By considering a counter-propagating plane wave $E_0 \exp(-ikx - i\omega t)$, we can add the electric fields and calculate the resulting intensity

$$I(x) = \frac{1}{2}cn\epsilon_0|E_0\exp(ikx - i\omega t) + E_0\exp(-ikx - i\omega t)|^2 = 4I_0\cos^2(kx)\,, \tag{1.5}$$

where we replaced the input intensity $I_0 = \frac{1}{2}cn\epsilon_0|E_0|^2$ of a single propagating plane wave in the last step. The resulting expression is a $\cos^2$ function with a periodicity of $\lambda/2$, which already resembles a lattice [Fig. 1.2 (b)]. We use the AC Stark effect from Eq. (1.2) to describe the one-dimensional (1D) potential acting on an atom

$$V(x) = -\frac{1}{2\epsilon_0 c}\mathrm{Re}\left[\alpha(\omega)\right]I(x) = -V_x\cos^2(kx)\,. \tag{1.6}$$

Here, we introduced the optical lattice amplitude $V_x = \frac{2I_0}{\epsilon_0 c}\mathrm{Re}\left[\alpha(\omega)\right]$ in the last step. The potential $V(x)$ is a conservative (time-averaged) standing wave potential, which we can extend to a three-dimensional (3D) case, by adding these 1D expressions along all three axes in space. We find

$$\begin{aligned}V_{3\mathrm{D}}(\boldsymbol{r}) &= V(x) + V(y) + V(z)\\ &= -V_x\cos^2(kx) - V_y\cos^2(ky) - V_z\cos^2(kz)\,,\end{aligned} \tag{1.7}$$

which serves as a good approximation for atoms in optical lattices when the envelope of the lattice beam is not significantly changing along the position of the atoms. We will see that solving the Hamiltonian of a single particle in an optical lattice potential leads to a number of bound states in each lattice well, which are similar to the states in a harmonic oscillator.

We take this opportunity to introduce the harmonic oscillator approximation and the notion of trap frequencies in that regard. In a 1D lattice we refer to this quantity as the "longitudinal trap frequency". This helps us to understand lattice wells as "lattice sites", which will be important when discussing quantum simulation models. To approximate optical lattice wells with harmonic trap potentials, we expand Eq. (1.6) to second order around small deviations $\Delta x = x - x_j$ of the well center x_j and find

$$-V_x\cos^2(kx) \approx V_x(k^2\Delta x^2 - 1)\,. \tag{1.8}$$

As we can neglect the constant part of this expression, the first term already has the quadratic form of a harmonic potential $\frac{1}{2}m\omega_{\mathrm{trap}}{}^2\Delta x^2$. Here, m is the mass of the atom and the longitudinal angular trap frequency reads

$$\omega_{trap} = 2\pi\nu_{\mathrm{trap}} = \sqrt{\frac{2k^2}{m}V_x} = \omega_{\mathrm{rec}}\sqrt{\frac{4V_x}{E_{\mathrm{rec}}}}\,. \tag{1.9}$$

In very deep lattices, where V_x is large compared to the recoil energy $E_{\mathrm{rec}} = \hbar\omega_{\mathrm{rec}} = \frac{\hbar^2 k^2}{2m}$, which is the kinetic energy of an atom at rest after absorbing or emitting a photon with momentum $\hbar k$, we find this approximation by a harmonic oscillator potential to be very accurate. Many different energy levels which are equidistantly spaced by $\hbar\omega_{\mathrm{trap}}$ are present in the lattice well potential.

An analogous approach can be made for the transverse envelope of the lattice beam and is equivalent to dipole trap beams to determine the transverse, or "radial trap frequency". We model the envelope as $V_x\exp(-2r^2/w^2)$, where r is the distance from the optical axis

of the beam and w is the $1/e^2$ beam radius. The resulting radial angular trap frequency reads

$$\omega_{\text{radial}} = 2\pi\nu_{\text{radial}} = \sqrt{\frac{4V_x}{w^2 m}} \, .$$ (1.10)

The lattice wells described by the periodic potentials in Eqs. (1.6) and (1.7) are all equally deep and lead to the same energy level and trap frequency in the lattice well, as the potential barriers separating them are all equally high. This is due to the approximation we made for the lattice envelope, which is the basis of most many-body physics models and is called "local-density approximation". However, we will see in which instances this approximation fails and show that the system sizes obtained are limited by the envelope of the lattice beams.

1.2.3 Different types of state-dependent lattices

So far, we introduced the notion of polarizability and used its real part to describe optical lattice potentials. For clarity, we will call the real part of α the "polarizability" and drop Re. As the polarizability of an atomic state can acquire any value, interesting trap wavelengths with special properties exist. More specifically, we will investigate different cases of $\alpha_g(\omega)$ and $\alpha_e(\omega)$, where g denotes the ground and e the excited state. The states g and e refer mostly, but not only, to the $^1\mathrm{S}_0$ ground state and the $^3\mathrm{P}_0$ excited state in this thesis. In Fig. 1.2 (a), we show the polarizability for both states.

Magic wavelength

When $\alpha_g(\omega)$ and $\alpha_e(\omega)$ acquire the same value the potential for both states is the same [Fig. 1.2 (b)], which makes this a state-independent lattice. Consequently, the quantized energy levels in these potentials are the same, which leads to unchanged transition frequencies between the corresponding energy levels. These wavelengths are well-known for many atoms, which we call "magic wavelengths" and are used in frequency measurements of atomic clocks to cancel out unwanted Stark shifts which would shift the clock transition frequency otherwise. A well-known example in strontium is the $813.4280(5)$ nm wavelength [29], which is far detuned from adjacent transition wavelengths and has a low scattering rate of lattice photons. In addition to that, other magic wavelengths exist due to the large variety of transitions when approaching larger energy scales. For wavelengths shorter than the 461 nm $^1\mathrm{S}_0$– $^1\mathrm{P}_1$ transition, the polarizability of the $^1\mathrm{S}_0$ state is mostly negative, which leads to repulsive potentials. For strontium, we refer to wavelengths shorter than the 461 nm wavelengths as "blue-detuned" and "red-detuned" for longer wavelengths. In a 3D optical lattice, an atom would still be trapped by occupying the nodes of the lattice instead of the antinodes. Trapping strontium with a blue-detuned magic-wavelength lattice at $389.889(9)$ nm has already been demonstrated [61].

Antimagic wavelength

For frequencies where $\alpha_g(\omega) = -\alpha_e(\omega)$, the potentials for both states acquire the same trap depth, while the amplitude of one of them is flipped [Fig. 1.2 (b)]. For an optical lattice, this leads to the same lattice potential with the same energy levels, but shifted by a quarter of the wavelength [62, 28]. As the optical lattice has a periodicity of one half of a wavelength, exciting an atom from the ground to the excited state leads to a superposition of occupying the next neighboring left and right lattice site in the excited state lattice assuming no net momentum transfer along the lattice could lead to a preferred direction of occupation. We call the wavelength corresponding to ω_a "antimagic wavelength".

Tune-out wavelength

In some cases, we find one of the polarizabilities to be zero, i.e. $\alpha_g(\omega) = 0$ or $\alpha_e(\omega) = 0$ [Fig. 1.2 (b)]. In other words, one of the states does not experience any potential while the other state is trapped, which can be used for differential control of both states. We call wavelengths with these properties "tune-out wavelengths". In such an optical lattice, slight detuning from these wavelengths leads to situations where atoms in one state are tightly trapped while atoms in the other state maintain mobility and high tunneling rates. The most favorable ${}^1S_0$ state tune-out wavelength is at 689.2 nm [30], which is slightly blue-detuned from the weak ${}^1S_0$–${}^3P_1$ transition and thereby mostly canceling the ${}^1S_0$–${}^1P_1$ contribution [Fig. 1.2 (a)]. Furthermore, a tune-out wavelengths at 632.8 nm exists for the ${}^3P_0$ state, which has a lower scattering rate for atoms in the ${}^1S_0$ state [30].

1.3 Quantum simulation with quantum gas microscopes

In the previous chapters we introduced the advantages of strontium and the existence of specific trapping wavelengths in optical lattice potentials. Before we proceed by discussing system sizes and specific quantum simulation schemes, we need a basic understanding of quantum simulation of interacting ultracold neutral atoms in optical lattices. Furthermore, we will give an overview of a basic theoretical model used for atoms in optical lattices, the Hubbard model, and derive important parameters by taking a look at the energy band structure of a single particle in an optical lattice potential. With this knowledge we will discuss the formation Mott-insulator and describe the concept of quantum gas microscopes as an experimental apparatus to do measurements on quantum simulated systems.

1.3.1 The Hubbard model

The Hubbard model is one of the most important models in condensed matter physics and describes on-site interacting particles in a periodic lattice potentials [8, 11]. It forms the basis to understand physics in periodic optical lattice potentials, which we have introduced before.

(a)

(b)
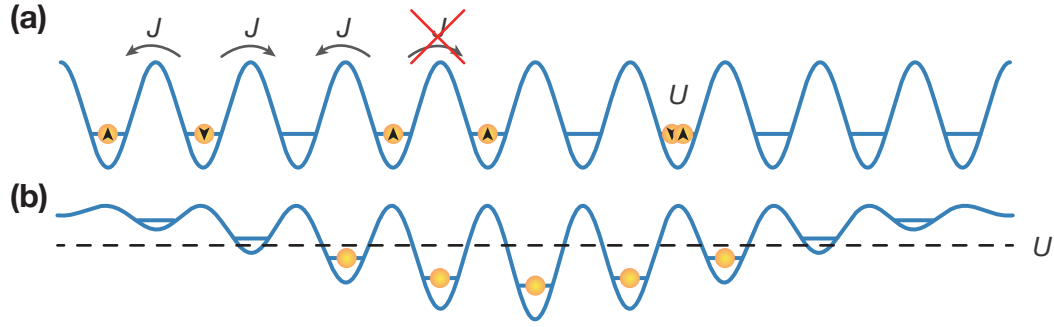
Fig. 1.3 (a) Dynamics of the Fermi-Hubbard model. Fermionic particles can tunnel with a matrix element J to neighboring lattice sites, which are not occupied by a particle with the same spin. Two particles can only occupy the same lattice site having different spins, but at the expense of an on-site interaction energy U. (b) Visualization of the harmonic confinement. Particles can occupy lattice sites with binding energies lower than an interaction energy U. Instead of occupying higher lying energy states, double occupation in the lower lattice sites would be energetically more favorable.

In a 1D optical lattice we enumerate each lattice site with an index j. Particles are trapped in the motional ground state of the lattice and can tunnel, or "hop", from site to site with a matrix element J, which describes the frequency of this process by a tunneling rate $J/\hbar$ [Fig. 1.3 (a)]. Particles, which share the same site, experience an on-site interaction energy U between each other, which can be repulsive or attractive.

In quantum physics, we distinguish between bosonic and fermionic particles to account for the symmetric or anti-symmetric nature of their wavefunction, which differs because of the Pauli exclusion principle. This has far-reaching consequences for the kinetic energy term, or hopping term, and the on-site interaction in the Hubbard model. In this thesis we want to put the focus on fermionic systems and therefore briefly introduce the Fermi-Hubbard model to motivate many-particle physics in optical lattices.

The Fermi-Hubbard model describes fermions in a periodic potential via

$$\hat{H}_{\mathrm{FHM}} = -J \sum_{j,j',\sigma} \hat{c}^{\dagger}_{j,\sigma} \hat{c}_{j',\sigma} + U \sum_{j} \hat{n}_{j,\uparrow} \hat{n}_{j,\downarrow} + \sum_{j,\sigma} \epsilon_j \hat{n}_{j,\sigma} , \qquad (1.11)$$

with the fermionic creation and annihilation operators $\hat{c}^{\dagger}_j$ and $\hat{c}_j$, respectively [11]. Here, $\hat{n}_{j,\sigma}$ is the fermionic number operator acting on lattice site j on particles with spin σ and a site-specific energy shift ϵ_j.

The first term is the hopping term, which sums over neighboring lattice sites j and j', and both possible spin-1/2 states. The so-called "tight-binding approximation" allows hopping only to neighboring lattice sites but only when the other lattice site is not occupied by a fermion with the same spin. The on-site interaction term sums over all lattice sites, which adds an energy U to the total energy in the system when it is occupied by two particles with opposite spins.

The third term adds a site-specific energy shift, which accounts for the lattice beam envelope as shown in Fig. 1.3 (b). The lattice envelopes typically has a Gaussian shape, which can be approximated by a harmonic oscillator potential in the center. At the point, where the potential increased by an interaction energy U due to the envelope, double occupation of the lowest lattice sites becomes more favorable and therefore the system size is limited here. We call this size-limiting effect "harmonic confinement".

Although this energy term allows one to better model the finite system size, it does not take into account that every lattice site is shaped differently leading to site-specific tunneling and interaction energies. This is in contrast to the local-density approximation we made in subsection 1.2.2. This motivates our aim to improve real experimental systems instead of the theoretical description and thereby minimize the harmonic confinement. Ideally, we want large and flat systems as depicted in Fig. 1.3 (a).

This effect is visible in interference experiments with bosons in optical lattice double-wells [47], which were analogous to optical Hong-Ou-Mandel interferometric experiments [63]. In the optical variant, timely-correlated photons incident from two different paths onto a beam splitter showed perfect constructive and destructive interferences, such that both photons took the same out of two paths after the beam splitter. In optical lattice double-wells, identical behavior was observed with two bosons being separated by a potential wall from the optical lattice through which they could tunnel with equal probabilities. However, the results showed that the beam splitter fidelity decreased significantly from lattice site to lattice site. This can be explained by slightly off-resonant energy levels of the lattice-well bound states, which calls for implementing larger systems to improve the quantum simulation fidelity.

Keeping this in mind, we will determine the parameters J and U by assuming an infinitely large lattice without harmonic confinement and calculate the single-particle energy band structure, which is presented in the next subsection.

1.3.2 Band structure in optical lattices

With the simplified 3D optical lattice potential derived in subsection 1.2.2, we can deduce the single-particle energy band structure in optical lattices, which provides the basis to understand the tunneling and interaction parameters of the Hubbard model. Furthermore, we use this mathematical framework to take a look at phase transitions and numerically calculate the corresponding lattice parameters. Here, we only show most important steps while a more explicit and well explained derivation can be found in Refs. [64, 65].

To obtain the energy band structure of the optical lattice potential, we have to solve the eigenvalue problem of a single particle in this potential with the Hamiltonian [66]

$$\hat{H}_{3D} = \frac{\hat{p}_x^2 + \hat{p}_y^2 + \hat{p}_z^2}{2m} + V_{3D}(\boldsymbol{r}). \tag{1.12}$$

Here, $\hat{p}_i$ is the momentum operator acting on the x, y, and z coordinate, respectively, m the mass of the particle, and $\boldsymbol{r}$ the position vector. Note that $\hat{H}$ describes a system of a single particle in an optical lattice potential, which will not be an accurate description

when we add several interacting particles to the system. In section 1.2.2, we showed that V_{3D} can be expressed by a sum of 1D potentials, which is why we use a separation ansatz for the wavefunction $\Psi(\boldsymbol{r}) = \phi(x)\phi(y)\phi(z)$. The 1D Hamiltonian $\hat{H}$, which is left to solve reads

$$\hat{H} = \frac{\hat{p}_x^2}{2m} + V(x) = \frac{\hat{p}_x^2}{2m} + V_x \cos^2(kx) \,, \tag{1.13}$$

with the eigenvalue problem

$$\hat{H}\phi_q^{(n)}(x) = E_q^{(n)}\phi_q^{(n)}(x) \,. \tag{1.14}$$

We find eigenstates $\phi_q^{(n)}$ and eigenenergies $E_q^{(n)}$ for particles with quasi-momentum q in the n-th energy band, as derived later. The potential is periodic with the periodicity $2\pi/k$, which is why we apply Bloch's theorem [66] to the eigenfunctions

$$\phi_q^{(n)}(x) = \exp\left(\frac{iqx}{\hbar}\right) u_q^{(n)}(x) \tag{1.15}$$

and receive the wavefunction $u_q^{(n)}(x)$ with the same periodicity. Keeping this in mind, $V(x)$ and $u_q^{(n)}(x)$ can be expanded in the basis of plane waves with a Fourier series, which yields

$$u_q^{(n)}(x) = \sum_s c_s^{(n,q)} \exp(2iksx) \,, \tag{1.16}$$

and

$$V(x) = \sum_s V_s \exp(2iksx) = \frac{V_x}{4}\left(\exp(2ikx) + \exp(-2ikx) + 2\right) \,. \tag{1.17}$$

Here, all sums run over a parameter $s \in \mathbb{Z}$. From this expression, we directly read off the Fourier coefficients of V and find that it adds a coupling $V_x/4$ to the off-diagonal, and $V_x/2$ to the diagonal entries of the Hamiltonian in the Fourier basis. Taking all these transformations into account, we express Eq. (1.13) in terms of Fourier coefficients

$$\sum_{s'} H_{ss'} c_{s'}^{(n,q)} = E_q^{(n)} c_s^{(n,q)} \,, \tag{1.18}$$

where we find the Hamiltonian in the new basis

$$H_{ss'} = \begin{cases} (2s + \frac{q}{\hbar k})^2 E_{\text{rec}} + V_x/2 & \text{if } |s - s'| = 0 \,, \\ V_x/4 & \text{if } |s - s'| = 1 \,, \\ 0 & \text{else} \,. \end{cases} \tag{1.19}$$

Within this framework, we worked on a numerical solution to this problem. To implement this Hamiltonian in a numerical calculation, we have to limit the dimensionality of the Hilbert space here with a maximum value s_{max} for the index s. We found all calculated numbers to be sufficiently converging for $2s_{\text{max}} + 1 \geq 7$. The parameter s_{max} has to be

(a)

(b)
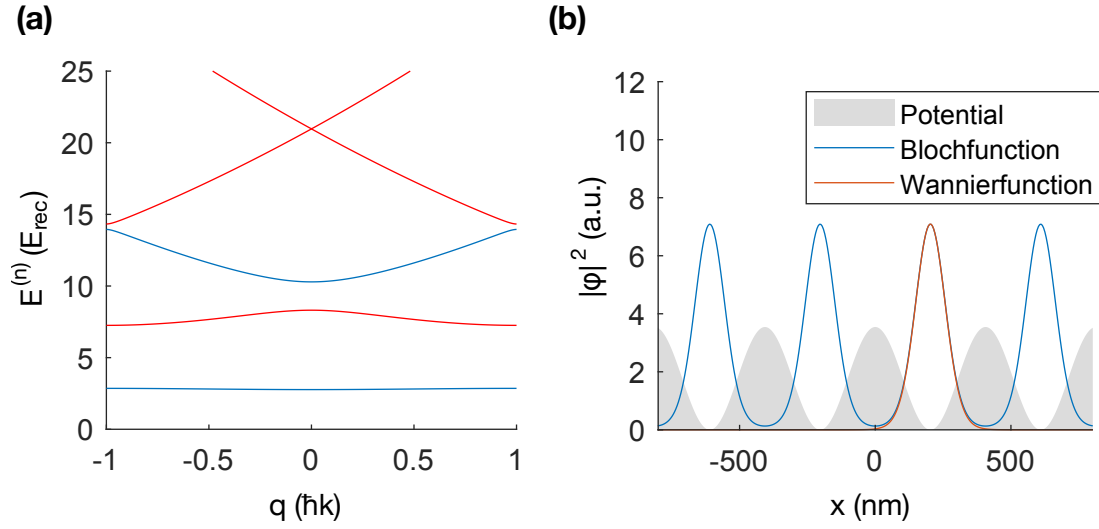
Fig. 1.4 (a) Dispersion relation of a single-particle in an $813\,\mathrm{nm}$ optical lattice with a trap depth of $9.6\,\mathrm{E_{rec}}$. From the lowest band upwards, we observe a transition of a flat energy band to the energy bands of a massive particle in free-space. (b) The probability density $|\phi_0^{(0)}|^2(x)$ is spread out equally over an infinite optical lattice potential. The Wannier function describes the position of a localized particle in the lattice at a specific lattice site.

large enough to consider energy states of at least more than the trap depth V_x, as all other states resemble a dispersion relation of a massive particle in free space. By diagonalizing Eq. (1.18), we find the eigenenergies $E_q^{(n)}$ of the n-th energy band to the corresponding momenta $q \in [-\hbar k, \hbar k)$. A depiction of the energy bands is shown in Fig. 1.4 (a). With the Fourier coefficients as a solution, we use Eqs. (1.16) and (1.15) to reconstruct the Bloch-wavefunction $\phi_q^{(n)}(x)$. In Fig. 1.4 (b) we show the ground state Bloch-wavefunction for $q = 0$, $|\phi_0^{(0)}|^2(x)$, in the optical lattice potential.

So far, the Bloch-wavefunction is spread out over the infinitely large potential (and also cannot be normalized in this form). To find an expression of the interaction energy between two particles, we have to consider, or define, a localized wavefunction of one particle first. For this reason, we introduce the Wannier function [66]

$$w_n(x - x_j) = \frac{1}{\sqrt{N}} \sum_q \exp\left(-iqx_j\right) \phi_q^{(n)}(x), \tag{1.20}$$

which describes a localized particle on a lattice site with coordinate x_j in the n-th energy band. Here, we have to restrict the number of lattice sites to a finite value N to ensure an inverse transformation from the Wannier functions to the Bloch-wavefunctions.

With the Wannier function, we can now calculate the interaction energy in 3D space between two fermionic atoms with opposite spins in the same lattice site (and in the

lowest energy band) via [11]

$$U_{00} = \frac{4\pi\hbar^2 a}{m} \int \mathrm{d}^3 x |w_0(x)w_0(y)w_0(z)|^4 \,, \tag{1.21}$$

where a is the scattering length of the particle, which is a measure for the interaction strength between two particles. The density integral evaluates the product of the probability densities of the ground band Wannier function, which we understand as the probability density that one particle shares the same location with the other particle. The bandwidth of the lowest energy band allows us to calculate the 1D tunneling matrix element [11]

$$J = \frac{1}{4d} \left(\max(E_q^{(0)}) - \min(E_q^{(0)}) \right) \,, \tag{1.22}$$

where d is the dimensionality of the system. We set $d = 1$ when running our numerical solution, as we assumed a 1D lattice here. With higher dimensions, the opportunities to tunnel are doubled and tripled and so is the expression $\max(E_q^{(0)}) - \min(E_q^{(0)})$. The factor $1/d$ compensates for this such that the tunneling rate $J/\hbar$ from one to another lattice site stays unchanged. Note that we can tune the ratio of U_{00} and J by simply changing the trap depth V_x, which we denote as V_{trap} from now on. With these parameters, we are now ready to discuss the formation of a Mott-insulator phase in the next subsection.

1.3.3 Metal-to-Mott-insulator crossover

In shallow lattices ($U_{00} \ll J$), fermions are very mobile while they cannot share the same lattice site when having the same spin state due to Pauli's exclusion principle. This dynamic is analogous to electrons in a metal, such that we call this a "metal". In contrast to fermions, bosons do not underly Pauli's exclusion principle and move independently of other bosons such that this state is called a "superfluid phase".

By comparing the bandwidth $W = 4dJ$ directly to the interaction energy U_{00}, we can obtain a limit at which the inter-particle interaction is comparable to the mobility of the particles. This gives us a criterion for a crossover from a metal to a Mott-insulator in a d-dimensional lattice, which reads [11]

$$U_{00} = 4dJ \,. \tag{1.23}$$

In the parameter regime of a Mott insulator, it is most favorable for the system with each lattice site occupied by a single particle, as the interaction energy for double occupation of lattice sites is too large. This transition has been observed for bosons and fermions [12, 67].

With this expression we can now determine the lattice depth V_{trap}, at which a MI forms. In Table 1.1 we show a selection of state-dependent and magic trap wavelengths for strontium, most of which we introduced in section 1.2.3, with the corresponding trap depth V_{trap}. For shorter wavelengths we find lower values for V_{trap} which we attribute to the rapidly growing interaction energies U_{00}. This growth is caused by the result of the den-

	λ (nm)	V_{trap} (E_{rec})	U_{00} (kHz)	J (Hz)
blue magic $^1S_0$- $^3P_0$, $^3P_1$	389	7.4	6.4	534
tune-out $^3P_0$	633	-8.8	1.7	150
tune-out $^1S_0$	689.22	-9.1	1.4	120
red magic $^1S_0$- $^3P_0$	813	-9.6	0.89	74
red magic $^1S_0$- $^3P_1$	914	-9.9	0.65	54
high power	1064	-10.4	0.43	36

Tab. 1.1 A table of different trap wavelengths for ^{87}Sr. We show the trap depth V_{trap} which is optimal for a MI phase in a 3D lattice with the resulting interaction and tunneling parameters, U_{00} and J, respectively. For shorter wavelength, we find a trend towards higher interaction energies and lower trap depths. The $^1S_0$ tune-out is meant for $^3P_0$ atoms, since the atoms would not experience a potential from this trapping wavelength in the $^1S_0$ state.

sity integral in Eq. (1.21), which is the multiplication of the two probability densities and can be interpreted as the fact that two particles are closer to each on average when they are enclosed in tighter spaces. At the same time, a lower V_{trap} leads to lower barriers for particles to tunnel through and, therefore, to higher tunneling energies J.

Taking all this into account, we conclude that the higher energy scales in short wavelength lattices lead to faster dynamics in the lattice. The sign change in V_{trap} happens at the $^1S_0$- $^1P_1$ transition, which is the strongest transition in strontium. Here, the strong polarizability contribution of the $^1S_0$- $^1P_1$ transition changes the sign of the overall polarizability background and we trap $^1S_0$ atoms in the anti-node (node) when our trapping wavelength is red detuned (blue detuned).

1.3.4 Quantum gas microscopes

Before we move on and talk about system sizes, we will introduce the reader to the concept of the quantum gas microscope, which we want to use for our experiment. A simplified setup is depicted in Fig. 1.5 (a). A high-resolution microscope objective is at a close distance to a two-dimensional (2D) plane of atoms in which lattice sites are typically separated by $\sim$500 nm. In every experimental cycle atoms in a single plane are prepared, while other planes are typically emptied out or removed. This preparation is followed by a time evolution of the system in the framework of the simulated model with a certain parameter set. During that time, the atoms are not imaged as it would lead to an unwanted collapse of the wavefunction.

After the time evolution, an imaging lattice, which can be the same lattice as before, is turned on and made as deep as possible to trap atoms as tightly as possible. Typical imaging lattice trap depths are ranging from a several hundred to a few thousand E_{rec} [68, 69]. This is typically combined with a cooling technique, such that the atoms occupy the ground state of the lattice during imaging. A fluorescence beam is shined onto the atoms, which scatter photons isotropically, while they get heated by the photon recoil. Afterwards, a sufficient number of photons is collected by the microscope objective, such that the signal-to-noise ratio is large enough to resolve a single site. This also requires a suf-
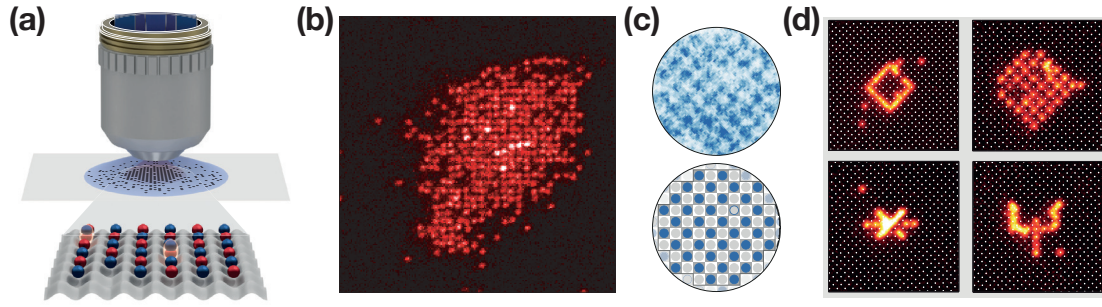
Fig. 1.5 (a) Image taken from Ref. [21]. Working principle of a quantum gas microscope. A micro-
scope objective can image atoms in a plane via fluorescence light with single-site resolu-
tion. (b) Unpublished image provided by our lithium team showing a single-site resolved,
fermionic, lithium Mott-insulator. The few bright spots indicate double occupation of lattice
sites. (c) Image taken from Ref. [21]. Single-site resolved image of one spin component of
an antiferromagnetic phase. The experimental image is on the top and the analyzed image
on the bottom. (d) Image taken from Ref. [15]. Examples for preparation of arbitrary atomic
distributions on a single atoms level.

ficiently high resolution, smaller than the distance a between two atoms. The resolution
can be determined from the diffraction limit [70]

$$a = 1.22 \frac{\lambda}{2\mathrm{NA}} \; . \tag{1.24}$$

Here, λ is the wavelength of the imaging light and NA is the numerical aperture of the
microscope, which is a measure for the solid angle of the collected scattered light at
the atom. It can be determined by $\mathrm{NA} = n \sin(\arctan(\frac{D}{2f}))$, where D is the diameter
of the microscope aperture, f is the focal length, and n is the index of refraction of the
medium [71]. A high NA means a large fraction of the scattered light is collected and
absolutely necessary to maximize the optical resolution.

An exemplary image of a fermionic MI taken with a quantum gas microscope, is shown
in Fig. 1.5 (b). Single atoms are clearly visible as red spots against a black background.
Very bright spots indicate double occupation of two atoms on a single site [16]. Software
algorithms use these indications to evaluate the atomic positions and therefore make
statistics out of ten thousands of such shots. Typical cycle times to obtain such a shot are
~ 20 s.

Furthermore, other detection schemes can be implemented, where for instance shots
of specific atomic state are taken by state-selectively removing the other spin [21]. In Fig.
1.5 (c) a cutout of the atomic plane with of spin-$1/2$ fermions is shown on the top. In the
presence of a bath (not shown in the image) these fermions reach the anti-ferromagnetic
ground state by spin-exchanging collisions with adjacent particles. Removing particles
with one spin component, a checkerboard pattern of particles with the other spin com-
ponent becomes visible.

In addition to that, microscope objectives can also be used to address individual parti-

cles in the lattice. In these addressing schemes, a single or several beams can be focused through the microscope and moved in the atomic plane. In Fig. 1.5 (d), we see how such a beam can be used to select atoms, bring them to a different state, which then can be removed by photon scattering. With this method, arbitrary atom distributions can be created as initial states before the time evolution.

1.4 Enhancing the system size

In subsection 1.3.1 we have seen how the Gaussian envelope of lattice beams leads to a breakdown of the local-density approximation, which we introduced in subsection 1.2.2. We learned that the system size is limited by harmonic confinement given by the lattice beam envelope. In the next subsection we will take a look at state-of-the-art system sizes and the approaches which are used to achieve them.

1.4.1 Fermionic system sizes

State-of-the-art fermionic quantum gas microscopes can produce almost defect-free occupied lattices with $\sim 30 \times 30$ atoms [16, 46]. These sizes are limited by the transverse extent of the laser beams with $1/e^2$ beam waists of ~ 100 μm, which generate optical lattice potentials by creating a standing wave with a retro-reflected laser beam. In compliance with the required specifications on the amplitude and phase noise of lasers, very often 1064 nm lasers with a power of ~ 50 W are used, which are on the high end of the realm of possibility. In that sense, enhancing the system size cannot just rely on stronger lasers, but requires other techniques to enhance the power.

Optical lattice clocks use very similar setups to quantum gas microscopes [52]. Probing the clock transition frequency of atoms in an optical lattice relies on measuring the atomic population in spectroscopic sequences. Therefore, these machines are using similar imaging techniques and would also highly profit from larger systems as more atoms could participate in the readout process to improve the precision or lower interrogation times to achieve the same precision.

1.4.2 Cavities as a tool for intensity enhancement

In the field of cavity-quantum-electro dynamics, extremely high intensities are required to observe dressed-state effects with very few atoms. As light can circulate inside high-finesse cavities many ten thousand times, such cavities with tight-waist cavity modes are employed for a large intensity enhancement.

A similar approach to enhance the intensity in quantum simulation experiments would call for cavities with large modes, to provide homogeneous and large systems. An approach to create optical lattices in a glass cell with cavity mirrors on the outside was created [72]. Nevertheless, this approach was limited by losses at the glass cell walls yielding an intensity enhancement of ~ 100, such that larger enhancements call for building an in-vacuum buildup cavity. Furthermore, an in-vacuum cavity with crossed modes

was built [73]. This setup was prone to temperature changes, vacuum chamber bakeouts in particular, which changed the alignment of the kinematically-mounted mirrors, and thus induced unwanted overlap changes of the two modes for many times.

Taking all this into account, our approach is a monolithic in-vacuum buildup cavity as the solution to overcome these challenges. It should provide large beam waists, to create large and homogeneous lattices. A crossed cavity with optically contacted mirrors to long-term fix their position would preserve the mode overlap without being prone to temperature changes or acceleration. In addition to that, larger intensity enhancement factors of more than 100 would be possible and thus enable the generation optical lattices at interesting wavelengths (introduced in subsection 1.2.3), where no suitable lasers with sufficiently high power are available.

1.5 Prospective experimental directions

After presenting the basics of optical state-dependent lattices, quantum gas microscopes, and strontium, we present a possible initial directions of the experiment.

1.5.1 Collisional phase gates

This following technique could be applied to realize collisional phase gates which are associated with the quantum computation schemes presented in Refs. [74, 75, 62]. A simple sketch of a possible experimental realization is shown in Fig. 1.6. In the following we denote the $^1S_0$ ground state as g state and the $^3P_0$ excited state as e state. A fully-occupied layer with one atom per site, in other words a Mott-insulator, is prepared in a 2D e state tune-out lattice at 633 nm. In this lattice g state atoms are trapped, while e atoms would not experience any potential. At this point we employ a tweezer which combines a 689.2 nm g state tune-out lattice with 698 nm clock laser light. This tweezer, for instance, could be generated by light focused through a microscope. With a numerical aperture of $NA = 0.7$, we achieve a diffraction-limited resolution of $\sim 1.22 \frac{\lambda}{2NA} = 600$ nm with $\lambda = 689$ nm, which cannot fully address a single atom of the 316.5 nm-spaced lattice sites. With the help of magnetic field gradients, single-site addressing can be improved further and a single atom in the e state can be prepared. The tweezer, together with the trapped e state atom, can then be moved through the layer of g state atoms.

1.5.2 Quantum simulation of light-matter interfaces

An alternative experimental scenario can be used to realize quantum simulations of light-matter interfaces. Therefore, the horizontal e state tune-out lattice can be replaced in the previous experimental scheme by a slightly detuned g state tune-out lattice. Therefore, we achieve a shallow potential for atoms in the g state, where atoms can tunnel with a high tunneling rate $J/\hbar$. At the same time we achieve a comparably deep e state potential, where atoms are trapped and tunneling is prevented. One or several tweezers with clock
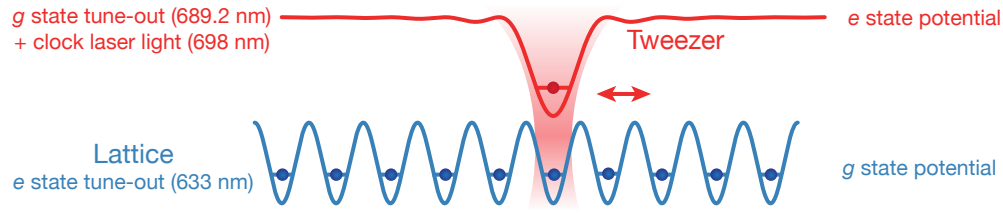
Fig. 1.6 A simple experimental scheme to realize phase gates using state-dependent lattices with strontium. Atoms in the g state are trapped in a lattice while a tweezer is used to excite an atom to the e state and move it across the ground state atoms.

laser light can be used to mediate continuous coupling between the g and e state with Rabi frequency Ω.

It can be shown that the Hamiltonian of these systems is equivalent to matter-wave emitters, which can emit particles, atoms, into a bath, the shallow lattice [40–43]. These systems can be used to simulate systems where atoms are closely trapped to nanostructures. These nanostructures can be waveguides which carry photons that can be absorbed or emitted by the closely trapped atoms. These systems have already been realized, where atoms enter a strong coupling regime by experiencing an evanescent electric field at the nanostructure [76]. Trapping of the atoms at this close distances to these surfaces comes with many difficulties, preventing these systems to fully explore this strong coupling regime.

Note that driving an interaction between the g and e state in the absence of strong magnetic fields requires us to work with ^{87}Sr as bath particles. To mimic photons, which are bosons, one can assume that we need bosonic particles to avoid influences on the tunneling dynamics due to Pauli's exclusion principle. However, ^{87}Sr provides 10 different spin states which can be evenly populated. In this case the probability of finding two bath particles having the same spin state at adjacent lattice sites is dramatically reduced. Therefore, ^{87}Sr is a good candidate to simulate photons as bath particles and we call this metallic phase involving many spin states a "quasi-superfluid" phase.

In Fig. 1.7 we display the principle of such a quantum simulation in more detail. An emitter in the ground state simply corresponds to an empty e state lattice site [Fig. 1.7 (a)], whereas an emitter in the excited state corresponds to an atom trapped in the e state lattice [Fig. 1.7 (b)]. The bath particles can move with tunneling rate $J/\hbar$, like particles in photonic waveguides [Fig. 1.7 (c)]. One or two-dimensional arrangements of these quantum emitters can be realized [Fig. 1.7 (d)], leading to variety of different dynamics. The corresponding band structure for 2D is shown in Fig. 1.7 (e), where the energy levels of both, the g state and e state bands, versus the quasi-momentum q are displayed. The motional ground state of the deep e state lattice is almost completely flat, while the shallow lattice shows a certain dispersion relation. When Ω is chosen to be negligible versus the bandwidth $W = 4dJ$ of the motional ground state band, the detuning Δ of the clock laser allows us to choose in which part of the band structure the quantum emitter will emit, and thus to resolve the band structure. Higher motional
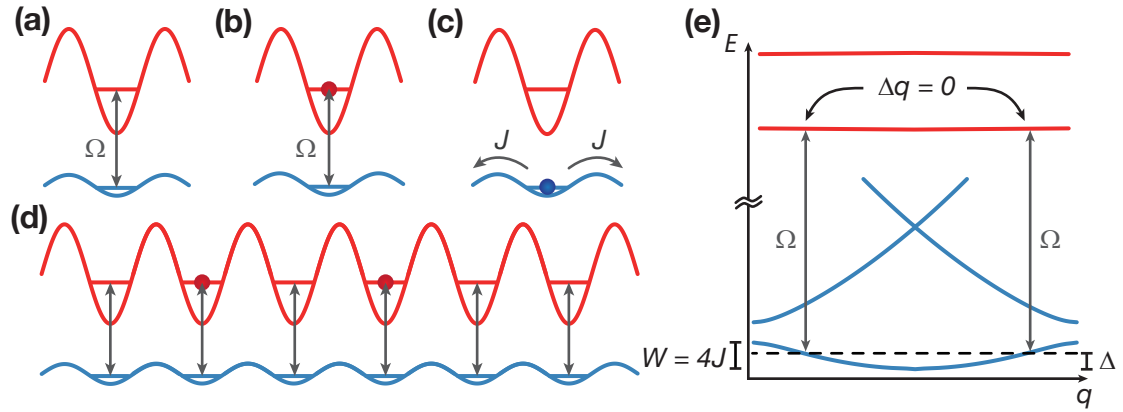
Fig. 1.7 Quantum emitter simulation scheme. The red color refers to the e state and the blue color to the g state, respectively. (a) The quantum emitter is in the ground state, when no atom is trapped in the e state potential. This is analogous to an atom, which cannot emit a photon since it is in the ground state. (b) The quantum emitter is in the excited state when an atom in the e state is trapped. Clock laser light mediates an interaction with Rabi frequency Ω between the two lattices. This is analogous to an excited state atoms that "carries" a photon, which can be "emitted". (c) A bath particle is moving in the shallow lattice. This is analogous to a photon traveling in a photonic waveguide. (d) A chain of quantum emitters with two excitations. (e) Energy band structure of the g and e state lattice which are coupled via clock laser light with Rabi frequency Ω. When $\Omega \ll W$, the ground state band structure can be resolved.
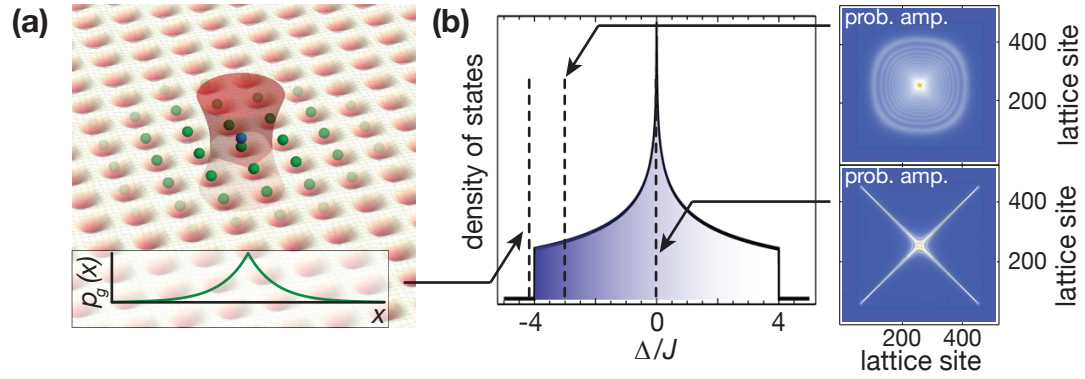
Fig. 1.8 (a) Depiction of a single-site resolved bound state with the projected bath-particle probability in one dimension $p_g(x)$. (b) The density of states in a 2D lattice can be probed via the clock laser detuning Δ. At $\Delta = 0$ a singularity in the density of states leads to non-Markovian dynamics which show a non-isotropic behavior in the probability amplitude of the emitted bath particle. Large systems are necessary to capture the full probability amplitude.

states also could be resolved in the same way.

Furthermore, the existence of bound states of the bath particles at the corresponding emitter have been proposed with these systems. In fact, these bound states have been observed in a photonic crystal [76] as well as with a rubidium-based quantum simulator in one dimension [44]. By realizing these systems in a 2D square lattice together with single-site resolved atom detection schemes, the probability density distribution of these bound states could be measured in real space [Fig. 1.8 (a)]. While the bound states are realized in the far-detuned regime of the density of states of a square lattice, other regimes with certain probability amplitudes exist [Fig. 1.8 (b)]. At the singularity of the density of states, a breakdown of the valid regime of Fermi's golden rule is expected and non-Markovian dynamics accompanied with non-isotropic emission patterns can be explored [40–43]. To detect these non-isotropic emission patterns, large systems are necessary to capture the full probability density, as in smaller systems finite size effects and particle reflections at the boundary would destroy the emission pattern.

1.6 Thesis outline

This thesis we report on the status of building the world's first strontium quantum gas microscope with single-site resolution. We aim to employ ultracold (fermionic) strontium atoms in large, homogeneous, 2D systems generated by a crossed optical buildup cavity with two optimally overlapping modes.

In chapter 2, we give an overview of the strontium machine that was built by explaining the experimental cycle and its most important modules. The functionality of the most important components of this apparatus are explained in detail together with encountered difficulties and employed solutions during building and operation. This regards the vac-

uum chamber design, the strontium oven, the blue laser system and magnetic trapping of strontium. A coarse overview of the red laser system and further plans of atomic transport are given.

Chapter 3 discusses first spectroscopic measurements with strontium in 1D, state-dependent lattices. Measurements of the $^1S_0$ ground state tune-out wavelength and the polarizability of the $^3P_0$ state are presented. This allowed a first proof-of-principle trapping of $^3P_0$ atoms and a reevaluation of atomic lifetimes of the $^1P_1$ and the $^3S_1$ state.

Chapter 4 is fully devoted to the crossed buildup cavity. Starting from initial ideas and system size calculations, we present the building procedure and characterization of the mode overlap. The power enhancement in the buildup cavity is measured and different approaches of mounting the cavity inside the vacuum chamber are discussed.

The implementation of state-dependent lattices in the crossed cavity is discussed in chapter 5. Parameter regimes for the realization of the quantum simulation scheme presented in section 1.5 are given.

We conclude and give an outlook of planned modules and experiments in the near future in chapter 6.

Chapter 2

Towards a Strontium Quantum Gas Microscope

W$^{\text{E}}$ plan to build the world's first quantum gas microscope to perform site-resolved quantum simulation in large systems of about $\sim$200 $\times$ 200 lattice sites. These system sizes will be realized in a monolithic in-vacuum buildup cavity, which provides almost perfect overlap of two crossed optical lattices. In this chapter we take a journey through the experimental apparatus, starting with a hot, high-velocity strontium atom, passing through a long vacuum chamber, where it is slowed down, captured, laser-cooled to ultra-low temperatures, and optically transported to end up in the center of the crossed cavity.

We begin the introduction to this chapter with a brief overview of the experimental cycle which describes all necessary components and stages implemented. This helps us to understand the working principle of the entire machine before we elaborate on each part in detail. An overview of the experimental setup is shown in Fig. 2.1.

Oven

The experimental cycle starts with a solid chunk of strontium in a hot in-vacuum oven, leading to a high vapor pressure and hot strontium gas in the oven crucible. Strontium atoms leave the oven with at high velocities in form of an atomic beam and arrive in the main chamber after about one meter.

Blue MOT stage

The atomic beam is collimated in the transverse cooling region and the atoms are slowed down by a Zeeman slower on their way to the main chamber. It uses radiation pressure induced by shining blue light about one linewidth detuned from the broad $^1S_0$– $^1P_1$ transition. In the main chamber the atoms are captured and cooled in a "dim" blue magneto-optical trap (MOT), which is a MOT without optical repumping, such that they decay into the $^3P_2$ state. Here, atoms are trapped in the present magnetic field, which is why we call this process magnetic trap loading. The atoms loaded into the magnetic trap end up with a final temperature of $\sim$1 mK.

(a)

(b)

(c)
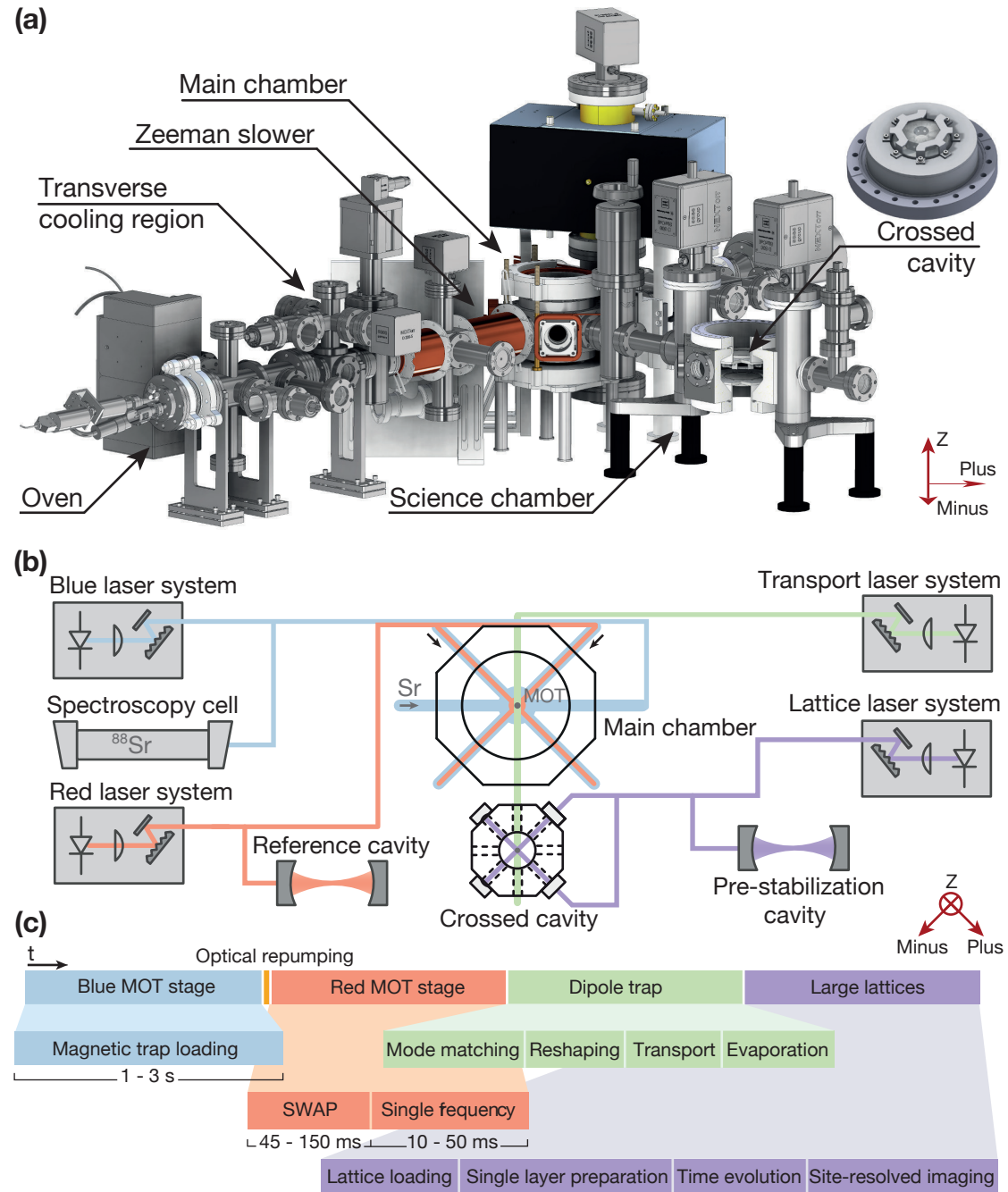
Fig. 2.1 (a) Overview of the vacuum chamber of the experimental setup. (b) Schematic overview of the essential components of the (planned) strontium quantum gas microscope. With the blue and red laser system generate a MOT with any strontium isotope in the main chamber. A $1064\,\mathrm{nm}$ laser transports the atoms into the crossed cavity located in the science chamber. From here, atoms are trapped and imaged in lattices. Spectroscopy cell and cavities provide references for laser stabilization. (c) Overview of the experimental cycle describing the purpose of all laser systems presented.

Optical repumping

To release the atoms from the magnetic trap and transfer them back to the $^1S_0$ ground state, we apply repump lasers acting on the $^3P_2$– $^3S_1$ and $^3P_0$– $^3S_1$ transitions. Here, the $^3P_2$ atoms are transferred to the $^3P_1$ state, where they decay to the $^1S_0$ state. From here, these atoms will be further cooled in the red MOT stage.

Red MOT stage

At temperatures of the atoms achieved with the blue MOT, the velocity of the atoms is already low enough to transfer a large fraction to the red MOT. We need to increase the capture velocity artificially by scanning the red laser in frequency, from far red detuned to slightly across the $^1S_0$– $^3P_1$ resonance to achieve a sawtooth-wave-adiabatic passage (SWAP), which has a higher cooling efficiency compared to traditional MOT schemes [77]. The red laser is then set to a single frequency operation where a final temperature of the atoms of $\sim 1~\mu K$ is achieved.

This is the current status of the experiment, as following stages are prepared but not fully implemented, yet. Keep in mind, that none of the following components are tested in the experiment and we use the following explanations to illustrate the (planned) experimental sequence.

Dipole trap

At this point atoms will be transferred to a dipole trap, which can move its focus from the main chamber to the science chamber and thereby transporting the atoms into the crossed cavity over a distance of about half a meter. The tunability of the focus is based on focus-tunable lenses.

Lattice loading

At the end of the transport, the atoms will enter the crossed cavity, which is used to generate a two-dimensional lattice at many different trap wavelengths. The lattice light will be ramped up adiabatically, such that the atoms will be transferred to the crossed cavity while minimizing heating effects to reduce atom loss. On top of the cavity, outside of the vacuum chamber, a microscope objective is mounted to reflect a third lattice beam and also capture scattered photons to take a fluorescence image of single atoms in a plane which will be imaged with a CCD camera.

From this point on, the chapter is structured as follows: we start to explain the oven design and discuss a selection of complications we experienced with it. We use this opportunity to briefly discuss the resulting vacuum pressure we have in our vacuum chamber. The next section provides an in-depth explanation of our power-scalable blue-laser system. Consequently, we describe the design and functionality of our Zeeman slower and the blue MOT stage. In that regard, we show magnetic trap lifetime measurements and

relate them to our vacuum pressure. Next, we give an overview to the red laser system, the red MOT stage, and other components of the setup and provide the reader with references for further interest. In the final section, we describe the design and implementation of the science chamber.

2.1 Oven

The oven is the entire structure which we use to generate a hot, directed strontium atomic beam. We use a commercial oven from CREATEC (dual-filament effusion cell) which we run in a horizontal orientation [Fig. 2.2 (a)]. Inside the oven structure, a crucible containing strontium is surrounded by tantalum wires which are mounted on ceramic discs and can radiatively heat the crucible. At the front end of the crucible a nozzle is inserted to transmit a collimated atomic beam, in which strontium atoms with velocities ~ 400 m/s leave the oven. The nozzle consists of a frame including 700 micro-tubes each with an inner diameter of 200 μm and a length of 10 mm.

2.1.1 Loading and operation

Initially the oven is loaded with ~ 3 g of a naturally abundant strontium isotope mixture, which we place in the crucible. The strontium chunks are placed in the crucible in a glove bag environment which is filled with argon, such that the strontium hardly oxidizes. When all of the strontium chunks are placed in the crucible, we close it by inserting the nozzle in the front and fixing it with a steel wire.

During the operation and the heat ramps of the oven, the temperature of the nozzle is always kept 50 °C higher with respect to the crucible to avoid condensation of strontium at the nozzle which thus should prevent clogging. We run the oven at 500 °C and 600 °C to work with ⁸⁸Sr and ⁸⁷Sr, respectively. This allows us to compensate for the factor ~ 10 lower abundance of ⁸⁷Sr to keep the loading time of the MOT below 3 s, as the loading time is one of the biggest contributors to our experimental cycle time. An atomic shutter blade driven by an electric motor allows us to turn the atomic beam on and off.

2.1.2 Pressure in the vacuum chamber

We measured the pressure in our vacuum chamber in the oven region, the TC region, the ZS region, and the main chamber with hot-wire vacuum gauges versus the oven temperature [Fig. 2.2 (b)]. With the oven at room temperature, the base pressure was at the 2×10^{-10} mbar level. We are not satisfied with the vacuum pressure measurements and assume they could be influenced by increased outgassing of the hot-wire vacuum gauges. A better indication of the vacuum level will be given with lifetime measurements in atomic traps. The oven region, the TC region and the ZS region are separated with differential pumping tubes, which have an inner diameter of 5 mm. The pressure in the oven region is increasing with rising temperature, followed by a pressure increase in the TC region. In the main chamber, the pressure hardly rises above the base pressure at any

(a)

(b)
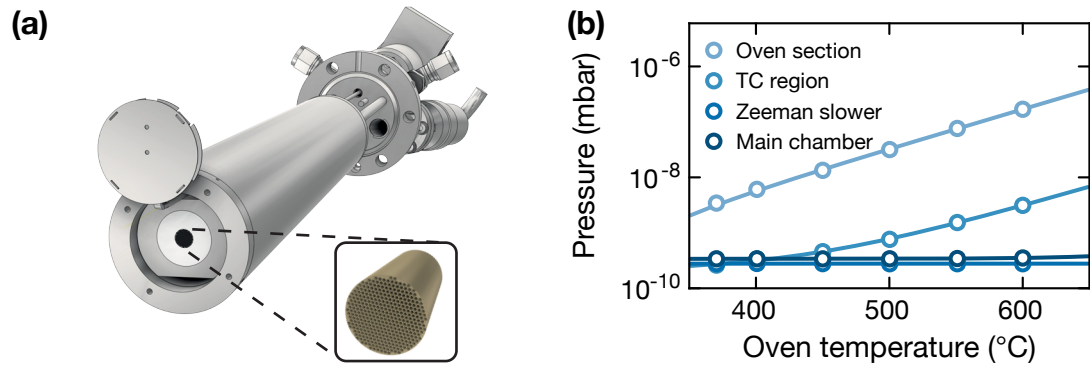
Fig. 2.2 (a) A CAD model for the strontium oven we use. An atomic shutter blade is integrated which is driven by an electric motor. The collimator for the atomic beam is a titanium nozzle, which consists of roughly 700 micro-tubes, which have an inner diameter of $200\ \mu\mathrm{m}$ and a length of $10\ \mathrm{mm}$. (b) Vacuum pressure measurement with hot-wire vacuum gauges in several regions in the vacuum chamber. Two differential pumping tubes separate the oven region, the TC region, and the ZS region from each other.

temperature, because gas contributions from the other regions are too small due to the differential pumping tubes. For each differential pumping tube, we find a attenuation in pressure increase by about a factor of 50.

2.1.3 Atomic beam collimation and nozzle clogging

To get an idea of the collimation angle and the flux, we made absorption measurements with light scanning over the ${}^1\mathrm{S}_0$– ${}^1\mathrm{P}_1$ resonance one centimeter after the oven nozzle and after the first differential pumping tube in the TC region. For every time we loaded or placed new strontium in the oven, we found that the oven to be in two different conditions: "unclogged" and "clogged". Every time we reloaded the oven with strontium, we observed absorption spectra on the first operation as shown in Fig. 2.3 (a) and (b) in the oven region and TC region, respectively, which correspond to an unclogged oven. After ramping the oven temperature down to room temperature and up to operating temperature again for very few times, we measured absorption spectra with a wider collimation angle and higher flux for the following times until we had to reload the oven again [Fig. 2.3 (c) and (d)], which correspond to a clogged oven.

We investigated this clogging issue, as we had to break vacuum at the oven region a few times to reload the oven. Right after removing the nozzle from the crucible, which included some struggle, we found a about one centimeter thick layer of strontium sticking at the nozzle [Fig. 2.4]. It was an open question to us, whether the strontium was condensing at the nozzle, when cooling down, or partly melting and creeping up the nozzle before it became solid again. Both explanations seemed unlikely in the first place, as the $50\,^{\circ}\mathrm{C}$ hotter nozzle should have avoided strontium condensing there, as well as the $600\,^{\circ}\mathrm{C}$ hot crucible should have been below the strontium melting point of $777\,^{\circ}\mathrm{C}$ [78].

As for melting, different materials, such as stainless steel and titanium have been used
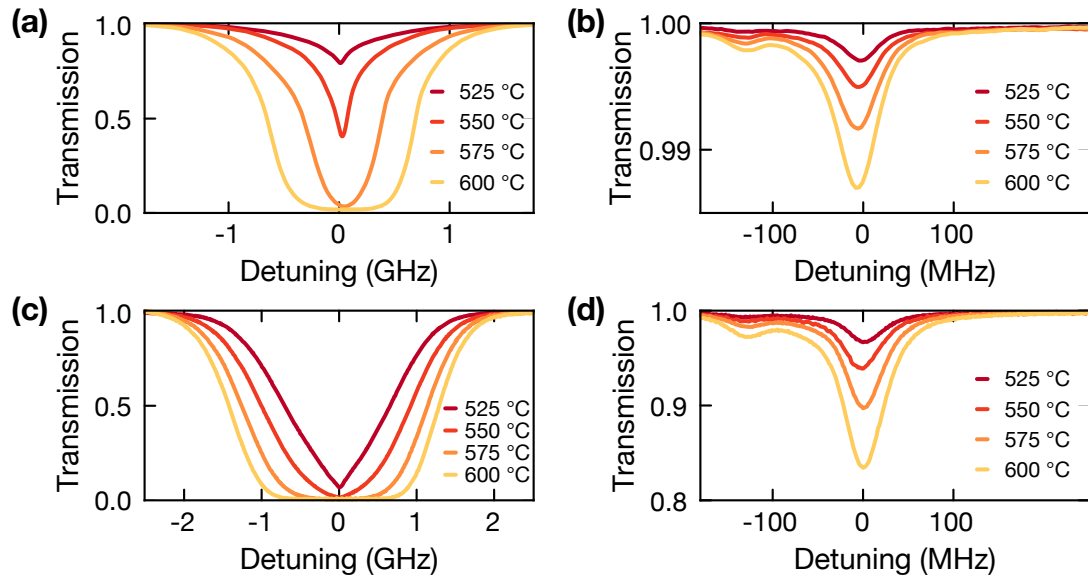
Fig. 2.3 Curves for absorption measurements for an unclogged oven nozzle in the oven region (a) and the TC region (b). After heating up and ramping down the oven a few times, we observe absorption curves for a clogged oven in the oven region (c) and the TC region (d). We see that the collimation angle as well as the atomic flux seem to increase in the clogged oven case.
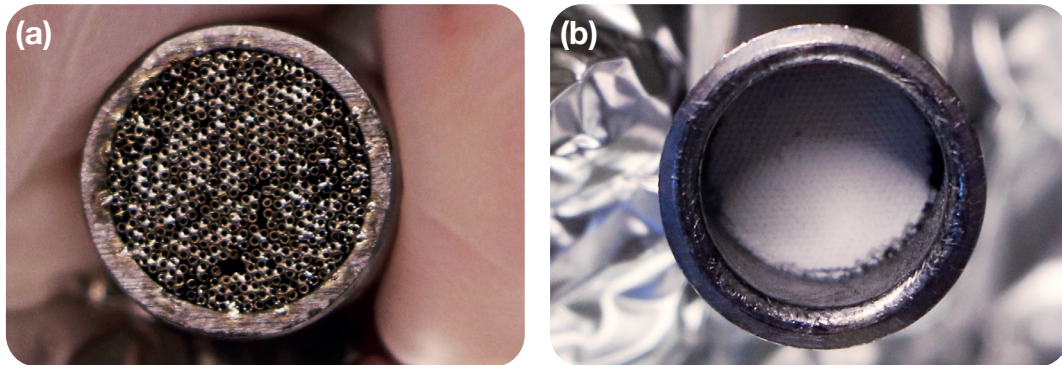
Fig. 2.4 (a) Stainless steel nozzle before the first implementation. The micro-tubes are welded together. (b) Perspective into the crucible after removing the titanium nozzle. A thick layer of white strontium-oxide reveals that strontium has accumulated at the backside of the nozzle.

as a crucible or a nozzle material, as we suspected strontium to have different creeping properties on each of them. However, all measurements showed the same behavior. In addition, we tried placing the solid strontium chunks once in a tantalum and once in a stainless steel boat such that molten strontium cannot flow towards the nozzle. However, also here no difference in the clogging behavior was visible. As for the condensation issue, we could have tried to employ a larger temperature gradient between the nozzle and the crucible, or heating up the nozzle up to the strontium melting point and try to unclog it (at least with the titanium nozzle and crucible, which have a melting point at $1670\ ^\circ$C [78]). However, we were afraid of the temperature gradients to cause other malfunctions of the oven. A new oven design, in which creeping is impossible, was built on the side. Test runs showed clogging by condensation only when the temperature gradient between nozzle and crucible was not large enough. An in-depth discussion on this can be found in Ref. [79].

As Fig. 2.3 (d) compared to (b) shows, the clogging seemed to improve the flux, after all. Thus, we determined the flux after clogging of the oven to be $10^{15} - 10^{16}$ 1/s of ^{88}Sr at the temperatures where we are operating at [80]. The flux increases by a factor of 10 from $500\ ^\circ$C to $600\ ^\circ$C, which is crucial to keep the loading time of the MOT lower for a rare isotope, such as ^{84}Sr. After the first differential pumping tube, in the TC region we observe a much lower flux of $10^{12} - 10^{13}$ 1/s for ^{88}Sr [Fig. 2.3 (c) and (d)]. We account the lower flux to the low solid angle of the differential pumping tube with respect to the oven, as alignment of the angle of the oven did not improve the flux in the TC region any further.

However, when running the oven at $600\ ^\circ$C on a day-to-day basis, we found that we are running out of strontium within 3 months. We attribute the rather short operation time to the increased flux and wider collimation angle due to the clogging issue, which is why we think it is worthwhile to solve it.

2.2 Blue laser system

In this section we present our blue laser design, which is frequency tunable and suitable to trap all strontium isotopes in a MOT, while it can be upgraded in power, whenever needed. The design consists of an ECDL master laser, which is locked to the ^{88}Sr ^{1}S$_0$–^{1}P$_1$ transition in a spectroscopy cell and seeds several injection lock modules, the slave lasers [Fig. 2.5]. We measure the wavelength of the laser at the spectroscopy cell with a wavemeter, to ensure the laser is locked to the correct transition. The slave lasers are injection lock modules, which are built on a compact breadboard in an enclosure to enhance the stability of the lock [Fig. 2.6]. Each injection lock module can add about $100\,\mathrm{mW}$ power in free space, such that the overall output power can be stacked whenever more is needed. Note that this power is reduced afterwards by being coupled to optics, such as acousto-optical-modulators (AOMs) and optical fibers.

Compared to frequency doubled infra-red lasers, the downside of the injection lock modules is that one never ends up with more than the output power of the laser diode in a single beam, since two beams stemming from two injection locks cannot be merged easily
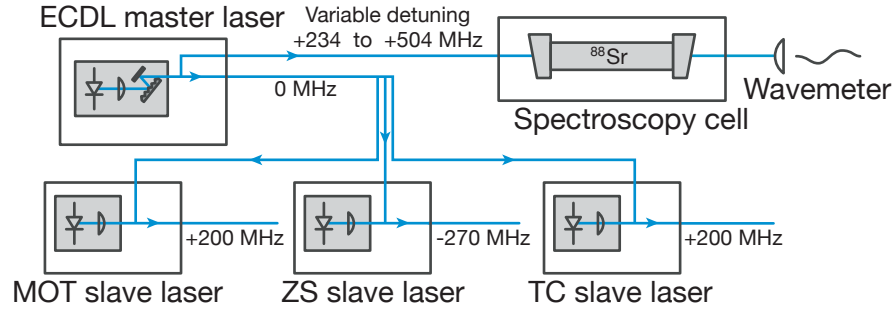
Fig. 2.5 Overview of the blue laser design. An ECDL master laser is locked to the ^{88}Sr $^1S_0$– $^1P_1$ transition in a strontium spectroscopy cell and used to generate seed light for several slave lasers. Each slave laser module can generate $100\ \mathrm{mW}$ such that the power can be simply increased by adding more modules. The output light of the master laser can be tuned in frequency to generate a frequency offset of the atomic frequency reference to cover the isotope shifts of all available strontium isotopes, which are provided by our strontium source. With this scheme, we address and cool each of the isotopes separately in the blue MOT.

(with the same polarization). In our case, we were limited to $\sim\!100\ \mathrm{mW}$ since we are using NICHIA NDB4216E laser diodes, which were the only available single mode laser diode available at this wavelength at this time. It could be useful to have more power in very wide ZS beams to slow down more atoms and increase the magnetic trap loading rates. To combine two laser beams from injection lock modules with the same polarization, good phase control, phase mismatch detection, and a PID lock would be necessary, leading to a class of techniques which is called "coherent beam combining" [81]. However, with the available output power for the MOT, ZS and TC, we were able to achieve a suitable blue laser design to generate MOTs with all available isotopes.

In following subsections, we will describe the blue master laser setup including the large frequency tunability in more detail. The next two subsections will focus on the injection lock module design and the spectroscopy cell setup, respectively.

2.2.1 Master laser

In this subsection, we describe the master laser optics setup in more detail and how we achieve a large frequency tunability of the locked laser to provide laser cooling in a MOT for all available isotopes.

The output power of the master laser is $\sim\!50\ \mathrm{mW}$ on the desired wavelength for the ^{88}Sr $^1S_0$– $^1P_1$ transition, where we split off $\sim\!40\ \%$ of the power to the locking arm and distribute most of the remaining power on three seed light ports. As shown in Fig. 2.7, we separate the rest of the light into two probe beam arms and the oven absorption section, where we need beams of roughly $50\ \mu\mathrm{W}$ of optical power. Note that the coupling efficiencies in this figures are relatively low compared to coupling efficiencies with other visible and near-IR wavelengths ($\sim\!70\ \%$). One reason for this a relatively inhomogeneous mode shape caused by the laser diode which becomes worse with larger distances from

(a)

(b)
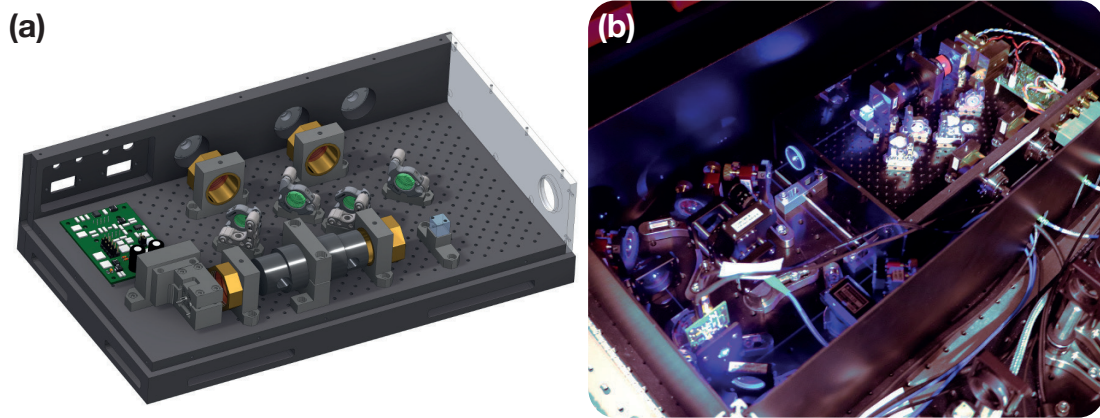
Fig. 2.6 (a) A CAD model of the final version of our injection lock modules. The output light is transmitted through an anti-reflection coated window inserted in the acrylic wall. (b) Image of our TC injection lock module. We transmit the output light onto another breadboard, where for instance, an AOM accounts for frequency shifts and mechanical shutters are implemented.

the laser. Another reason is a relatively large Rayleigh scattering of blue light in the optical fibers, which is indicated by scattered blue light along any curvature of the fiber and already visible at a few milliwatts of input power.

For now, let us take a closer look into the frequency shifts, which we control by tuning only the frequency of a single AOM and thus achieve MOTs with all availabe isotopes. Usually, the frequency of an AOM can be tuned within a certain bandwidth while changing the diffraction angle of the frequency-shifted first order mode. Although this behavior might be beneficial in some situations, it is not, whenever we require frequency tunability and at the same time want to maintain the beam direction for fiber coupling. A solution to this challenge is given by using a double-pass AOM configuration [82].

The idea of the design is close to the idea described in reference [83], by tuning the frequency offset of the laser with respect to the ^{88}Sr $^1S_0$– $^1P_1$ transition. By providing large enough tuning range, isotope shifts of the $^1S_0$– $^1P_1$ transition for all available isotopes over $270\,\mathrm{MHz}$ can be covered, while providing the same amount of power to the MOT, ZS and TC region. Here, the key ingredient is a broadband (BB) $350\,\mathrm{MHz}$ AOM[1] used in a double-pass (DP) configuration. The aperture is only $150\,\mu\mathrm{m}$ and therefore requires focusing a $\sim1\,\mathrm{mm}$ wide collimated laser beam with a $f = 100\,\mathrm{mm}$ lens through the AOM, before its first diffraction order is sent back into the AOM via a cat-eye configuration including another $f = 100\,\mathrm{mm}$ lens.

Here, the challenge is to align the AOM such that the DP efficiency of the first order diffraction is maximized, while minimizing the transverse beam movement during frequency sweeps to maintain fiber coupling. Keep in mind that the shifted light after

---

[1]We use the Gooch and Housego, model 3350-199, here. All attempts to achieve a tuning range over $\sim300\,\mathrm{MHz}$ with the model 3350-125 have failed, as the model 3350-199 offers 3 times more bandwidth at the expense of diffraction efficiency and aperture size. Note that the bandwidth is stated as a $-10\,\mathrm{dB}$ return loss, which is the frequency range before $10\,\%$ of the RF power are reflected.
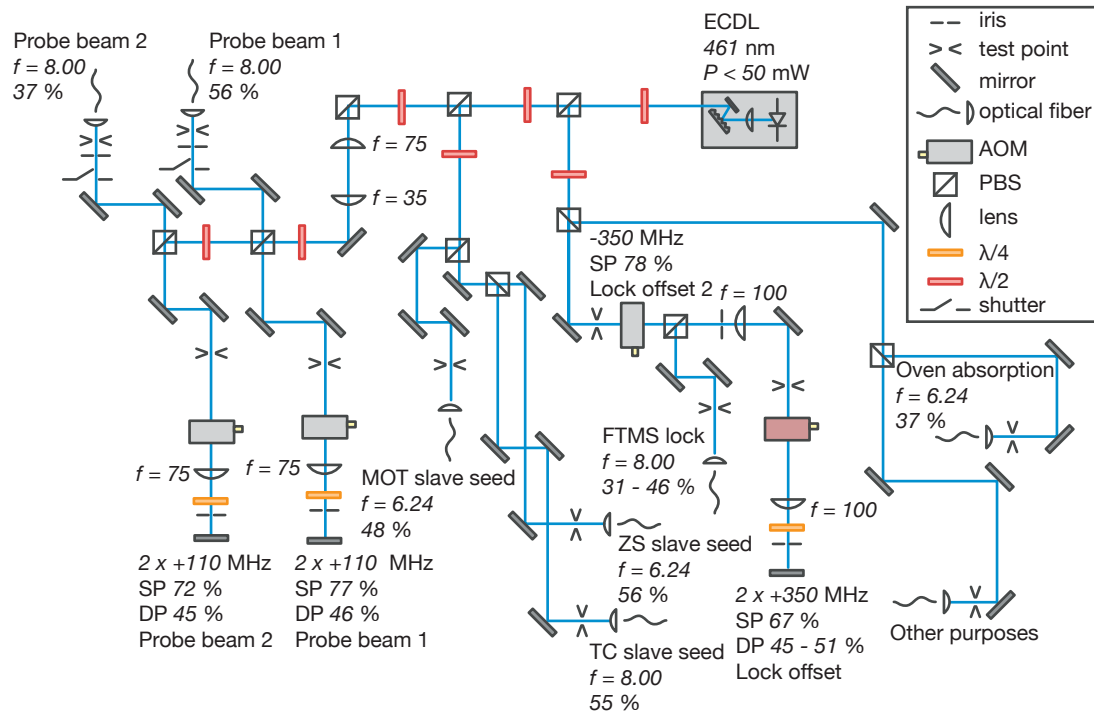
Fig. 2.7 Overview of the blue master laser system. The red AOM is the broadband $350\,\mathrm{MHz}$ AOM used in the DP regime to enable large frequency tunability. The fiber coupling rates are comparably low as the blue laser mode is unfavorable. With longer beam paths the coupling efficiencies decrease. All focal lengths f are given in mm.

	Isotope shift (MHz)	BB AOM (MHz)	SP AOM (MHz)	Detuning (MHz)
^{84}Sr	-271	427	-350	-234
^{86}Sr	-125	353	-350	-234
^{87}Sr	-47	313	-350	-234
^{88}Sr	0	292	-350	-234

Tab. 2.1 The (estimated) frequency settings for the BB and SP AOM used to generate the frequency shifts of the blue master laser to cool all isotopes in the blue MOT. The isotope shifts are taken from reference [83].

this configuration theoretically does not move anymore with a perfect cat-eye configuration, but careful alignment is necessary to diminish the transverse beam movement and maintain fiber coupling in practice: first, we need to pre-align the cat-eye setup, which consists of a $f = 100 \, \mathrm{mm}$ lens, $\lambda/4$ waveplate, an iris, and a $0\,°$ reflective mirror mounted on a THORLABS cage system. We transmit a collimated beam through a polarizing beam splitter cube (PBS) and send it centered on the optics through the cat-eye. The distance of the lens to the $0\,°$ mirror has to be adjusted such that the reflected beam at the beam splitter cube matches the size of the input beam at the same position. Also, it has to be ensured that the retro-reflected beam is centered on the almost completely-closed iris and lens again by adjusting the $0\,°$ reflective mirror. Then, without the cat-eye system, we align the AOM in the single-pass (SP) configuration first, together with the first lens and maximize the SP efficiency of the first order diffraction. With that, the position of the AOM and the first lens is determined. A frequency sweep has to be turned on to see the transverse beam movement. The cat-eye setup then has to be brought into place to retro-reflect the first-order diffraction of the AOM such that we minimize the transverse beam movement on a CCD camera at the position of the fiber, where we want to couple light in. This can be done, depending on the length of the beam path on the order of micrometers at a sweep over a full bandwidth at this wavelength and center frequency of the AOM. With this procedure, we achieve AOM DP diffraction efficiencies of $45 - 51 \, \%$ and maintained fiber coupling efficiencies of $36 - 40 \, \%$ for a single-pass frequency range of $292 - 428 \, \mathrm{MHz}$.

With this in mind, we take a look at the frequency budget: the tuning range of the BB AOM described in the passage above in the DP configuration leads to a total range from 584 to $854 \, \mathrm{MHz}$. A SP AOM before subtracts $-350 \, \mathrm{MHz}$ such that we end up with a frequency offset from 234 to $504 \, \mathrm{MHz}$. This positive offset frequency is then sent to the spectroscopy cell where it is locked onto the ^{88}Sr ^{1}S$_0$– ^{1}P$_1$ transition such that the detuning of the laser output is negative with respect to this transition. The detuning of the BB AOM is then set such that for each isotope including the isotope shift, the laser output is detuned by $-234 \, \mathrm{MHz}$ to the corresponding isotope in total (Tab. 2.1). As for the MOT, another AOM after the injection module adds $200 \, \mathrm{MHz}$ such that we end up with a total detuning of the MOT laser beams of $-34 \, \mathrm{MHz}$, about one linewidth away from the ^{1}S$_0$– ^{1}P$_1$ transition frequency. Analogously, this is done for the ZS beam to achieve a total of $-504 \, \mathrm{MHz}$ and TC beams to achieve a total of $-34 \, \mathrm{MHz}$ detuning.

The AOMs in the DP configuration for the probe beams are set to $+117\,\mathrm{MHz}$, such that the probe beams are on resonance for absorption imaging. The oven absorption section is only used with the laser in an unlocked state, which is frequency-scanned over a range of several GHz to obtain spectra as shown in Fig. 2.3 (a) and (c). This is crucial so we can check the flux after reloading the oven or to check if the whole strontium load is used up. In situations, where more power on the $^1S_0$– $^1P_1$ resonance is required, we set the BB AOM to a frequency of $272\,\mathrm{MHz}$, such that the MOT beams are on resonance with a total of 5 to $7\,\mathrm{mW}$ per beam.

2.2.2 Injection lock modules

As mentioned before, we can stack the power of our blue laser system by adding more injection lock modules, with an optical power of $100\,\mathrm{mW}$ for each. In this subsection, we want to give the main ideas and construction features which went into the design of our injection lock modules.

Every injection module is equipped with a blue laser diode, which is seeded by a port with light stemming from the master laser [Fig. 2.8]. The injection lock laser diode is pumped by an electric current to generate population inversion in the diode semiconductor material, as it is done in other diode lasers. The difference is, that the population inversion is not brought to stimulated emission via optical feedback of the laser diode light itself, but by seed light [84, 85]. The seed light is inserted to the optical isolator from the side, which lets the seed beam pass through the isolator against its allowed propagation direction, because of the orthogonal polarization. At the injection lock laser diode, the seed light generates stimulated emission such that the laser diode emits all available power with an identical optical spectrum as the seed light. The output of the laser diode is sent through the isolator, along its allowed propagation direction. We split off a small fraction of this light to a scanning "monitor cavity" at another polarizing beam splitter, where we find a narrow transmission peak versus the typical $\sim$1 nm wide broadband spectrum of the laser diode itself, only when the seed beam is well mode-matched to the laser diode (at the corresponding electric current). In this case, we speak of the injection lock laser to be "locked", for which a minimum amount of $\sim$1 mW of seed light is necessary. With more power in the seed beam, the alignment is less sensitive to keep the laser locked, which is why we have about three times as much power in each seed beam available than necessary.

Our injection lock modules are designed to be as compact and stable as possible. An earlier version was equipped a breadboard with holes for dowel-pins, such that the optic components could be simply plugged in and removed. As the tolerance of the dowel-pin diameter to the whole diameter was kept extremely tight, the dowel-pins offered a higher repeatability with respect to only fixing the mounts in place with screws. This preserved any alignment to a large fraction, even fiber coupling. Another feature of this design was that placing optics with the pins aligned all components in an orthogonal orientation. Mirrors were aligned at $45\,^{\circ}$ angles. The breadboard offered an about four times higher compactness of optics than achieved with typical breadboards and optic
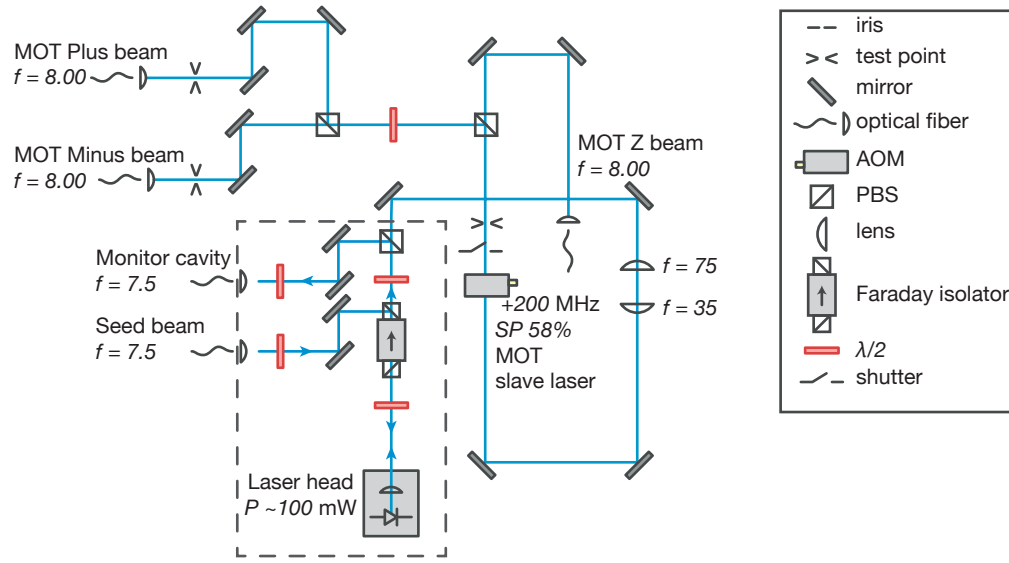
Fig. 2.8 Sketch of the MOT injection lock module. Injection lock modules for the ZS and the TC region are structured similar.

sizes, such as standard Thorlabs parts. The entire module was enclosed in a black acrylic enclosure to provide laser safety as well as isolate the setup from air exchange with the environment, such that no turbulences can interrupt the lock. This feature together with the seed beam power we use, requires us to relock the injection lock lasers by retuning the electric current only about once a day. A more detailed explanation of this design and optic components can be found in reference [80].

After the first prototype, we realized that precision machining of dowel-pins to holes was too time-consuming and costly for our purposes. We decided to drop the concept of the pins and stayed with the compact size and the acrylic enclosure. The output beam in the module can pass through a window. From this point on, we can shift the frequency of the output beams via AOMs, which where hard to implement into the module because of the induced diffraction angles. Additionally, we found that we were able to achieve a fiber coupling efficiency of only ~35 % with the fiber ports in the box (Thorlabs; PAF2-7). Coupling the output beam outside of the box to our usual fiber couplers, with coupling efficiencies of ~50 %, enabled us to use more power for the experiment.

Also, it was important to us to have an AOM after each injection lock to use it as a switch together with a mechanical shutter (as blocking the seed light would not stop the emission of the laser diode). The AOM switches the light on and off within fast ramps <500 ns, while the shutter needs several milliseconds to close. Opposed to the AOM, the shutter completely blocks any scattered light which still can be transmitted by the AOM. We calibrate each AOM together with the corresponding shutter, such that the AOM is turned on most of the time, to maintain a steady-state temperature by keeping the injected RF input power. By doing that, we obtain relatively sharp switching times while we avoid drifts of the beam pointing caused by temperature changes of the AOM,
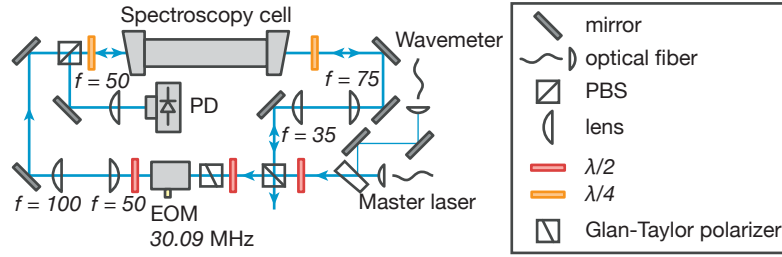
Fig. 2.9 Spectroscopy cell setup used in our experiment. A traditional FMTS lock is employed to lock the master laser. We pick off some light here and send it to the wavemeter to have a reference for the lock.

which affects fiber coupling.

2.2.3 Spectroscopy cell

We built a spectroscopy cell setup to employ a Doppler-free lock of our blue master laser to the ^{88}Sr $^1S_0$– $^1P_1$ transition [Fig. 2.9]. In principle, a cathode lamp could be used for this purpose, but is typically more affected by noise from the pump current [86, 87]. The cell consists of standard vacuum nipple with angled, AR viewports attached and is filled with 10 g of strontium [83]. The cell is wrapped in heating tapes and thermally isolated by fiber glass strips with several layers of aluminum foil. The cell is then operated at a constant temperature of 400 °C to create a sufficiently high vapor pressure of strontium inside, so we can probe the (Doppler-broadened) $^1S_0$-$^1P_1$ transition with resonant 461 nm light. As want to lock the master laser to a Doppler-free signal, we employ a traditional frequency modulation transfer spectroscopy (FMTS) lock [88, 89]: a pump beam together with a counter-propagating probe beam generate a Doppler-free absorption peak, a "lamb-dip", within the collision-broadened absorption signal. By phase modulating the pump beam via an electro-optic modulator (EOM) at 30.09 MHz, the modulation can be transfered to the probe beam and detected by a photodetector. This signal is demodulated with a mixer at the modulation frequency and we obtain an error signal. Using this error signal, we employ a PI lock to the master laser. In addition, we measure the wavelength exactly at the probe light with a wavemeter to confirm we are locked to the transition of ^{88}Sr and the lock is at the expected wavelength of 460.8618 nm to have a day-to-day reference.

2.3 The Bitter-coil Zeeman slower design

Very often, Zeeman slowers are long tubes with manually-wound conically-shaped coils. A downside for traditional Zeeman slowers is, that all winding has to be done before the bakeout procedure and cannot be changed with the Zeeman slower integrated in the vacuum chamber. This was of particular importance to us, as we had a NEG coating inside the ZS nipple, where the coils should be mounted to. For the activation of this coating
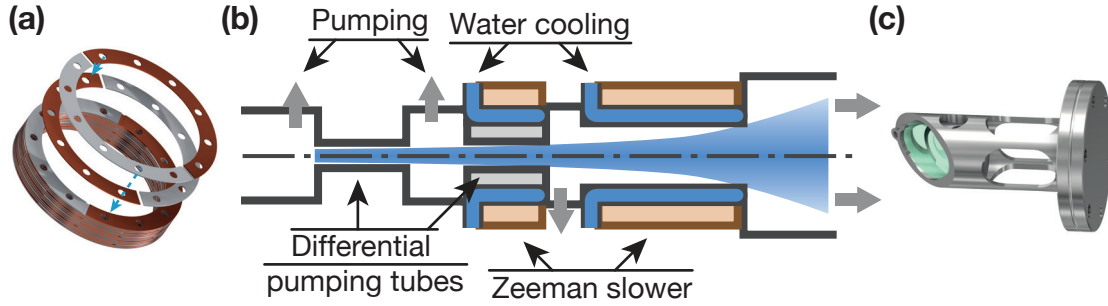
Fig. 2.10 Overview of our ZS design. (a) Exemplary demonstration of our coil assembly with half-circular isolating (gray) and conducting sheets (brown). (b) Cross-section of our ZS region. Beneath the coils water cooling shells are stacked on a vacuum nipple. Also shown is the position of both differential pumping tubes. (c) A CAD model of our reflective ZS mirror, which redirects the ZS slower light beam into the vacuum chamber.

it is absolutely crucial, that the heating tapes could be mounted directly to the vacuum part to reach the required activation temperature inside the nipple, during the bakeout process.

For theses reasons, we thought of a more versatile ZS design, which affected our ZS coils: we adapted an already existing design which was already used in cold atom experiments [90]. The idea of the design was to build coils by stacking it on a (in two-pieces-separated) vacuum nipple and alternately stacking "conducting and isolating arcs". The isolating arcs had a very small conducting region, such that the current can pass through the whole stack of arcs.

However, our design was slightly modified. Instead of having completely conducting and isolating arcs we planned to implement half-circular arcs, where we created fully-circular sheets by combining an isolated piece with a conducting piece [Fig. 2.10 (a)]. The conducting and isolating parts are made from copper and glass fiber-isolated plastic, respectively. The sheets have clearance holes such that they can be stacked on rods. By controlling the overlapping, conducting area of two neighboring sheets, we can control the winding density, which however only allows a limited number of winding densities for the whole system. By combining the half-circular sheets around the vacuum nipple, we can mount the ZS coil even after the baking process and also unmount and mount it again, if we want to make changes to the magnetic field.

The theoretical expectation of the calculated magnetic field together with the winding density is shown in Fig. 2.11 (a). The slope of the magnetic field gets steeper as the distance to the MOT decreases, while we see a deviation in the homogeneity of the field in the region of the zero-crossing. This deviation is due to spatial constraints affecting the coils, induced by a four-way cross where a NEG pump and a hot-wire vacuum gauge are attached to. At the end of the ZS coils, we have an additional coil with a reversed current to locally cancel out the far-reaching magnetic field from the MOT coils. However, with and without this coil connected, we did not see a large difference in the MOT loading rates.
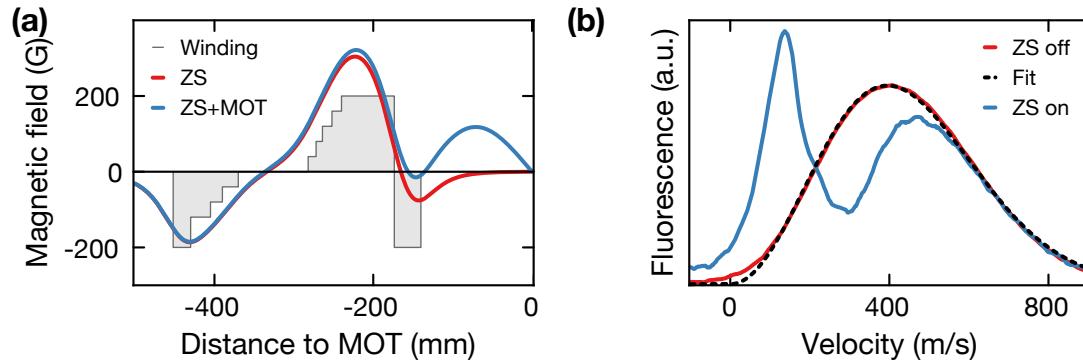
Fig. 2.11 (a) Theoretical results of the ZS magnetic field we used for an older configuration with $-584\,\mathrm{MHz}$ absolute detuning from the ${}^1\mathrm{S}_0$– ${}^1\mathrm{P}_1$ transition. The blue (red) curve shows the ZS magnetic field with (without) influences by the MOT coils. (b) Measured longitudinal velocity distribution with the ZS switched on and off at an oven temperature of $550\,{}^\circ\mathrm{C}$ with $-584\,\mathrm{MHz}$ absolute detuning from the ${}^1\mathrm{S}_0$– ${}^1\mathrm{P}_1$ transition. The fit funciton is a Maxwell-velocity distribution at $550\,{}^\circ\mathrm{C}$.

We water cool the ZS system via a copper water cooling shell, which is mounted underneath the coils. This prevents melting of the isolating pieces and electrical shorts, when the coil is in operation [Fig. 2.10 (b)]. On top of the water cooling shell, a Kapton isolation layer prevents electrical shorts bypassing the ZS coil. The ZS light beam is sent into the vacuum chamber via a reflective mirror mounted at the very end of our vacuum chamber [Fig. 2.10 (c)]. We were afraid that the mirror will be coated with strontium over time and therefore its reflectivity would decrease. However, the remaining question was, how much strontium actually reached the mirror and was sticking to it. After three years of operating our strontium machine, we find our ZS to be as efficient as in the first days which lets us conclude that no significant reflectivity changes of the mirror have happened.

2.3.1 Longitudinal velocity distribution measurement

To get an idea of the performance of the Zeeman slower, we performed longitudinal velocity distribution measurements [Fig. 2.11 (b)]. This helped us to see what fraction of the initial Maxwell-velocity distribution is slowed down and can be captured by our blue MOT. The ZS was designed to slow down all atoms with velocities up to $400\,\mathrm{m/s}$ below the capture velocity of $\sim 30\,\mathrm{m/s}$ [59] which lead to the initial ZS configuration consistent with a detuning of the ZS light beam of $-584\,\mathrm{MHz}$. Furthermore, we used this measurement to optimize the magnetic field strength and the detuning of the ZS light beam initially. Later, these settings were confirmed by optimizing for the atom numbers in the magnetic trap and the red MOT.

The measurement was done with an oven at $550\,{}^\circ\mathrm{C}$ with the blue laser system set up to capture ${}^{88}\mathrm{Sr}$ in the MOT (together with the ZS without employing TC). The power of the ZS light beam used in this measurement was $50.3\,\mathrm{mW}$ and the beam radius at the

oven was on the order of 1 mm. As the blue master laser frequency was already stabilized to generate a blue MOT, we were not able to use it as probe laser and scan it over several GHz at the same time. Therefore, we used a titanium-sapphire laser (Ti:Sapph) and employed second-harmonic generation to convert 922 nm light into 461 nm light. With that, we sent a probe beam with a power of 0.5 mW at a 45 ° angle through the main chamber to measure the velocity distribution of the atoms entering the main chamber. The probe beam $1/e^2$ radius was 2 mm to collect fluorescence from as many atoms as possible without causing power broadening on the frequency spectrum. The fluorescence was collected with a lens two-inch in diameter to focus the collected light onto an avalanche-photodetector (APD). To convert the timescale to frequency, we observed an error signal at the spectroscopy cell during the laser scan, where we referenced the scan speed to the ^{86}Sr - ^{88}Sr isotope shift of 125 MHz.

As shown Fig. 2.11 (b), we took measurements with and without the Zeeman slower (light and magnetic field): as expected, we observed a Maxwell-velocity distribution with the ZS turned off and fitted it to determine the temperature. The temperature was consistent with the oven setting of 550 °C, instead of the nozzle temperature of 600 °C, as one could have expected with the clogged oven we were operating.

When turning on the ZS we saw very similar velocity distributions induced by the ZS light beam with and without the magnetic field. In both cases, we saw a cut in the initial Maxwell-velocity distribution at 400 m/s which corresponds to a Doppler shift of 867 MHz. At the detuning we used, the Doppler broadened transition together with contributions of near-resonant scattering lead to this velocity cut-off. However, the velocity distribution below the relevant capture velocity of the blue MOT below 30 m/s [59] does not change significantly when switching the ZS magnetic field on and off, and improves the fluorescence and atom number of the blue MOT only by ~ 10 %. The ZS light beam alone, however, improves the MOT by more than a factor of 10. After all, we were not satisfied with the little influence of the magnetic field.

Further changes of the magnetic field strength and the laser detuning within a range of 40 MHz did not show significant differences. Hoping for an increased influence of the magnetic field, we reconfigured the coils and set the laser beam detuning to -504 MHz to have a lower velocity cut-off. However, the results of the longitudinal velocity distribution measurement and fluorescence of the blue MOT were similar compared to the previous configuration. After all, we are not sure why the magnetic field does not have a larger influence on the atomic velocity distribution.

2.3.2 Zeeman slower power optimization

As mentioned in section 2.2.2, we implemented a shutter AOM together with a mechanical shutter after each injection lock module. However, the -270 MHz AOM we wanted to include into the ZS slave laser setup yielded only 71 % diffraction efficiency. To check whether we still had enough optical power available, we decided to measure how the blue MOT fluorescence, and with that the atom number, changes in dependence of optical power in the ZS beam. We expected to find plateau regions which happen at a critical

value for the intensity in the oven region. The maximum power we had available in the ZS beam at this time was $51\,\mathrm{mW}$ without and $36\,\mathrm{mW}$ with the switching AOM in the beam path, respectively. Depending on the result of this measurement, we would have thought about alternative solutions to increase the optical power in the ZS beam.

We tried different ZS beam sizes in the oven region by varying the beam size via different telescopes in the Zeeman slower beam path. As we could not measure the absolute beam size in the vacuum chamber, we tried telescopes with magnifications of 2.5 up to 5 while focusing the ZS beam in the oven region. The focus was determined by minimizing the extent of the fluorescing atoms right in front the oven. With a motorized $\lambda/2$ waveplate and a PBS we scanned the power for all configurations, while we optimized the ZS beam alignment for each telescope for two power options, with $36\,\mathrm{mW}$ and $51\,\mathrm{mW}$, respectively. The fluorescence of the MOT was captured with a lens and sent to an APD.

We found a saturation for all configurations at about $40\,\mathrm{mW}$ power with a comparable fluorescence differing by less than $28\,\%$, opposed to our hope of finding immense improvements. For this reason, we decided to use a 3.75 telescope and the $-270\,\mathrm{MHz}$ AOM, as this curve showed the highest fluorescence compared to the other configurations at this power and $93\,\%$ of the measured maximal fluorescence.

2.4 Blue MOT stage

Our blue MOT stage consists of a combination of TC, ZS, and blue MOT in operation. A good reference to get familiar with the working principle of MOTs is their first realization [91].

The dim blue MOT is the first constituent of our experimental sequence [Fig. 2.1 (c)]. Here, we benefit from the $^1P_1$– $^3P_2$ decay channel to trap and accumulate atoms in the magnetic trap, where they have long lifetimes solely determined by collisions with the background gas. After the magnetic trap loading and turning off any blue light, we apply repump lasers to optically pump the population from the $^3P_2$ state to the $^1S_0$ state. From this point on, we continue with the red MOT stage.

When applying repump lasers together with the dim blue MOT, we pump atoms from the $^3P_2$ state back to the $^1S_0$ state, such that they can still be trapped in the blue MOT. As these atoms scatter blue photons during the MOT, the fluorescence signal increases by a factor of $\sim$10, which is why we call this the "bright blue MOT". The fluorescence signal is captured with an APD mounted on the top of the chamber and serves us as a day-to-day reference.

The following subsections will give a quick overview on the beam parameters, the optical repump scheme and lasers we use to achieve a blue MOT. We demonstrate how efficiently we can load all available isotopes and extract the natural abundance for our strontium mixture in the following subsection. Next, we present the magnetic trap loading process and lifetime measurements followed by a discussion on our vacuum pressure. The final subsection will focus on the optical beam setup, which displays how we merge the red MOT and absorption imaging beams with the blue MOT beam setup.

2.4.1 Beam parameters and magnetic field

Our beam parameters for the MOT beams were set such, that we apply similar intensities as in Ref. [83], where the authors use a 5 mm and 4 mm beam radius with 4 mW of power for the horizontal beams and 1 mW for the vertical beam, respectively. We scaled our beam sizes accordingly to a 6.2 mm beam radius, as we had more than 6 mW for the horizontal beams and 4 mW for the vertical beam available. As described in section 2.2.1, the MOT beam detuning was set to roughly one transition linewidth below the actual transition frequency, yielding a detuning of -34 MHz.

We operate the Zeeman slower with a -504 MHz detuned light beam with 36 mW of optical power. In the TC region we have a horizontal and vertical beam with a detuning of -34 MHz, as we did not see significant differences in the performance after trying different detunings. The power of each TC beam is 2.5 mW at a ~ 3 mm $1/e^2$ beam radius.

To obtain a better understanding of the magnetic field gradients in the Z direction applied to the blue and red MOT, we made a careful calibration by observing the red MOT position for different MOT beam detunings. As we did these checks for different applied gradients, we were able to scale the calibrated value for our blue MOT and found a magnetic field gradient in Z direction of 63.7 G/cm. A more detailed description of our coil configuration can be found in Ref. [92].

2.4.2 Repump scheme and lasers

The purpose of our repump scheme is mostly to transfer the $^3P_2$ state population to the $^1S_0$ state, such that these atoms can further be part in the blue MOT cycle or to be transferred from the magnetic trap to be further cooled in the red MOT.

Strontium atoms in the $^1P_1$ state can decay via the $^1D_2$ state to the $^3P_2$ state, which is a metastable state with a long lifetime. To optically pump atoms from this state to the $^1S_0$ ground state, we have to optically pump atoms to another state first, while accounting for decays into meta-stable states. In our case we use a 707 nm laser to transfer atoms to the $^3S_1$ state, from where they can decay to all of the ^3P_J triplet states. If the excited atoms decay to the $^3P_2$ state, they will again be pumped to the $^3S_1$ state. If the decay ends in the metastable $^3P_0$ state, we have a 679 nm laser pumping the atoms up the $^3S_1$ state again. After the atoms eventually end up in the $^3P_1$ state, they will relatively quickly decay to the $^1S_0$ state with a decay time of $21.28(3)$ μs [48] without escaping the trap region due to gravity. The 689 nm and 707 nm laser are not locked to any reference and have optical powers of ~ 4 mW at a $1/e^2$ beam waists of 3 mm.

Alternatively, a popular repump scheme is to optically pump atoms from the $^3P_2$ state to the *5s5d* $^3D_2$ state [Fig. 1.1]. From there, atoms can only decay back to the $^3P_2$ or $^3P_1$ state, where they will eventually decay to the $^1S_0$ state [83].

A 688 nm laser beam can be used on the $^3P_1$–$^3S_1$ transition to enhance the atom number in the magnetic trap for bosonic isotopes by 65 % and for fermions by 30 % [93]. As the benefit for the fermionic ^{87}Sr, which we will mainly work with, seemed to be rather small to us, we decided to not spend the effort on implementing this beam into our setup.

2.4.3 Loading different isotopes

Once we had a working blue MOT, we checked whether we were able to load and lasercool all isotopes as planned with the blue master laser in subsection 2.2.1. Therefore, we maximized the fluorescence on an APD by changing the BB AOM frequency starting from the values we expected from Tab. 2.1. For each isotope we observe a loading process with a different loading time and a saturated signal of fluorescence by opening the atomic shutter (which has a negligible switching time on the order of 10 ms). We turn off the oven by closing the shutter and observing a decay time.

As the loading rate $\kappa = 1/\tau_{\mathrm{load}}$ is coupled to the loss rate in the trap by photo-association, the fluorescence signal $\Delta V \propto N$ gives us an idea of the number of atoms trapped. We can combine these two quantities in a single differential equation

$$\dot{N} = \phi - \kappa N \, . \tag{2.1}$$

Here, ϕ denotes the fraction of the flux which increases the atom number N until it equals the total atom loss rate κN. The solution for this differential equation is well-known and we find

$$N(t) = \frac{\phi}{\kappa} \left(1 - \exp(-\kappa t) \right) \, , \tag{2.2}$$

in the case of the loading process. For times $t \to \infty$ we find an expression for the flux

$$\phi = N_{t \to \infty} \kappa \, , \tag{2.3}$$

with $N_{t \to \infty}$ as the saturated atom number. With this in mind, we measure the fluorescence in terms of an APD voltage ΔV_i for each isotope i of strontium. Here, we assume that the fluorescence is proportional to the atom number as the total intensity of all the MOT beams ($I = 16$ mW/cm^2) is well below the $^1S_0$– $^1P_1$ saturation intensity of $I_{\mathrm{sat}} = \frac{\pi h c}{3 \lambda^3} \Gamma_{^1P_1} = 41$ mW/cm^2 [58], for $\lambda = 461$ nm. We then can relate the fluxes ϕ_i with the corresponding APD voltages and the loading rates κ_i we measure.

$$\frac{\phi_i}{\phi_j} = \frac{\Delta V_i}{\Delta V_j} \frac{\kappa_i}{\kappa_j} \tag{2.4}$$

By receiving relations of ϕ_i, we can assume that these are proportional to the abundances $\chi_{i,\mathrm{meas}}$, which have to add up to one. From that, we can derive the absolute abundance, for instance for ^{88}Sr via

$$\chi_{^{88}\mathrm{Sr,meas}} = \frac{1}{\frac{\phi_{^{84}\mathrm{Sr}}}{\phi_{^{88}\mathrm{Sr}}} + \frac{\phi_{^{86}\mathrm{Sr}}}{\phi_{^{88}\mathrm{Sr}}} + \frac{\phi_{^{87}\mathrm{Sr}}}{\phi_{^{88}\mathrm{Sr}}} + 1} \, . \tag{2.5}$$

With the help of Eq. (2.4) we then find $\chi_{i,\mathrm{meas}}$ for the other isotopes.

The results of the loading times and abundances, together with decay times $\tau_{i,\mathrm{decay}}$ are shown in Tab. 2.2. As we can judge these results without an error bar, we find very good agreement on the second and even third digit of the measured abundance

	BB AOM freq. (MHz)	$\tau_{i,\text{load}}$ (s)	$\tau_{i,\text{decay}}$ (s)	$\chi_{i,\text{meas}}$ (%)	$\chi_{i,\text{nat}}$ (%)
^{84}Sr	424	0.881	0.960	0.621	0.56
^{86}Sr	351	0.263	0.314	9.48	9.86
^{87}Sr	318	-	-	-	7.00
^{88}Sr	290	0.132	0.261	82.9	82.58

Tab. 2.2 Resulting frequencies of the BB AOM used to generate MOTs for all available isotopes. For all MOTs we show loading times $\tau_{i,\text{load}}$ and decay times $\tau_{i,\text{decay}}$, which we measure by observing exponential fluorescence ramps on an APD, while blocking and unblocking the atomic beam with a shutter. From these fluorescence signals, we derive abundances of the isotopes $\chi_{i,\text{meas}}$ and compare them to measured natural abundances $\chi_{i,\text{nat}}$.

compared to the natural abundance stated in Ref. [94]. As the signal-to-noise ratio of the fluorescence signal was too small for ^{87}Sr we were not able to obtain a large enough signal-to-noise ratio to extract a loading time and included the literature value for the corresponding abundance. We find longer decay times than loading times for all isotopes. An explanation for this observation is given by a higher loss rate in the MOT due to atomic collisions with the presence of the atomic beam. However, it is important to consider the loading times for the extraction of the abundances as the additional losses are limiting the atom number in the MOT and thus the fluorescence signal.

In the experiment later, a potential cooling method for ^{87}Sr would be sympathetic cooling with ^{84}Sr. To minimize the magnetic trap loading time, we thought of parallel loading process which would need two detunings at the same time in the MOT, ZS and TC beams at the cost of available power for each isotope. As the abundance differs by a factor of 12.5, the loading process would be dominated by the magnetic trap loading of ^{84}Sr and therefore not be significantly shorter. Therefore, we aim for a sequential loading process where one isotope is loaded to the magnetic trap before the other isotope. Our blue master laser lock presented in subsection 2.2.1 is able to switch from one isotope to another within one millisecond, which can make sequential loading to the magnetic trap possible.

2.4.4 Magnetic trap loading and atom number measurement

As mentioned before, the main purpose of the blue MOT stage is the loading of the magnetic trap. We decided to use our MOT field gradient to create a magnetic quadrupole potential which traps atoms with a magnetic moment larger than zero, which is true for atoms in states with the electronic angular momentum $J > 0$. This condition is fulfilled for atoms in the ^{3}P$_2$ state. In this subsection, we want to introduce a sequence, which we used to measure the number of atoms captured in the magnetic trap at various instances. In particular, we maximized the atom number in the magnetic trap for the blue MOT beam alignment at a fixed loading time, used it to verify the magnetic field parameters and alignment of the ZS, and performed magnetic trap lifetime measurements to get a better idea of our vacuum level.

To measure the number of atoms captured in the magnetic trap, we run a sequence as shown in the schematic pulse diagram in Fig. 2.12. At the beginning of each cycle, we
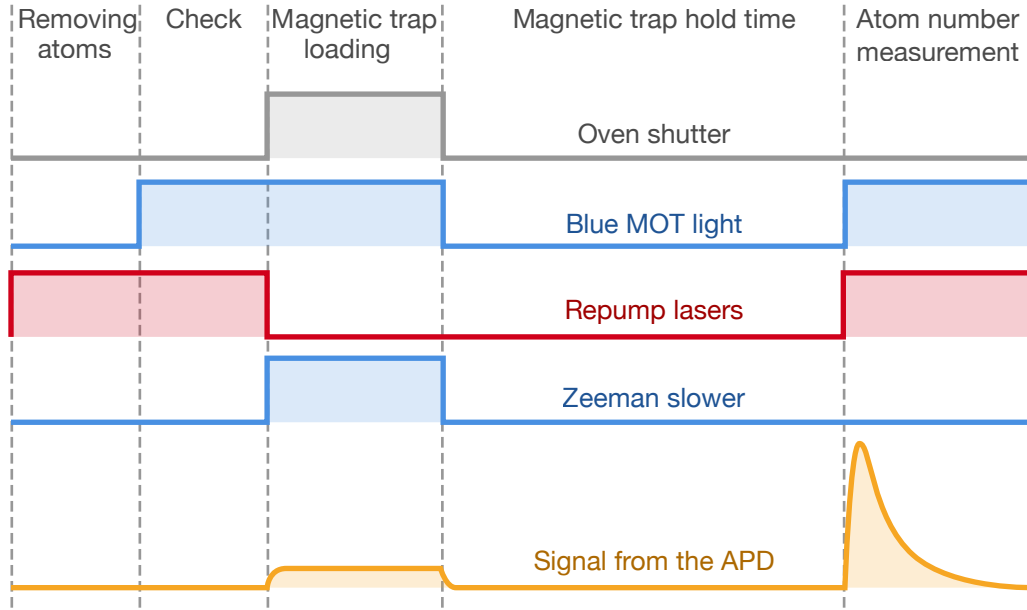
Fig. 2.12 Schematic overview of the magnetic trap lifetime measurement sequence.

remove any remaining atoms from previous cycles by shining $679\,\text{nm}$ and $707\,\text{nm}$ repump laser light for one second. Any remaining atoms in the $^3P_2$ state will then be pumped to the $^3P_1$ state, and eventually decay to the $^1S_0$ state such that they are not trapped any more. In the next step, a pulse with additional blue MOT light will create fluorescence on an APD which only serves us to check whether all remaining atoms are gone and our sequence is not faulty. The actual measurement then starts with magnetic trap loading, which happens during a blue MOT without repump lasers, and ends up with $^3P_2$ state atoms trapped in the magnetic trap.

In a typical experimental cycle, we would continue the trap loading to reach a certain atom number in the trap, before we transfer the atoms with repump light back to the $^1S_0$ state to start the red MOT stage.

In an atom number measurement in the magnetic trap, we stop the trap loading typically after $1\,\text{s}$ by closing the atomic shutter. The atoms are held for a certain time, typically only tens of milliseconds to wait for the shutter to close completely. The sequence ends with an atom number measurement of the remaining atoms by shining repump and MOT light at them. The resulting fluorescence peak is measured via an APD on the oscilloscope and integrated to determine the fluorescence signal of all atoms.

2.4.5 Magnetic trap lifetime

To convince ourselves of the pressure measurements taken with the hot-wire gauges presented in section 2.1, we decided to measure the atomic lifetime in the magnetic trap, which is limited by the background pressure. In more detail, the trapping potential in
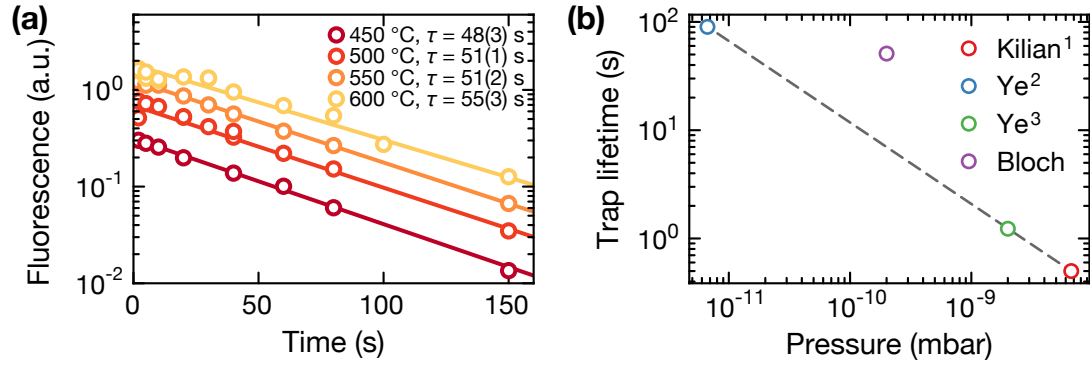
Fig. 2.13 (a) Fluorescence signals to extract magnetic trap lifetimes for different oven temperatures for ^{88}Sr. (b) Vacuum lifetime comparison to other groups. Magnetic trap lifetimes taken from Refs. [1] [95] and [3] [96]. In Ref. [2] [97] the number was obtained from a dipole trap.
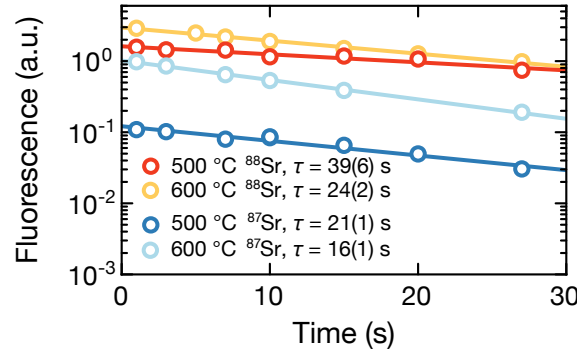
Fig. 2.14 Fluorescence signals to extract magnetic trap lifetimes for ^{88}Sr and ^{87}Sr after the atomic shutter broke.

the magnetic trap can be assumed to have a depth in the order of $k_B \times 100$ mK. The average kinetic energy of a particle at room temperature is $k_B \times 440$ K, so we assume that every collision with such a (thermal) particle of the background gas leads to direct loss of the trapped atom. Consequently, this atom loss from the magnetic trap can be directly related to the background particle density.

For the magnetic trap lifetime measurements, we use the sequence described in subsection 2.4.4 with a loading time of 6 s and different hold times, ranging from 2 to 150 s. Our results are shown in Fig. 2.13 (a). Measurements at different oven temperatures show magnetic trap lifetimes around 51 s which seem (relatively) independent from the oven temperature.

We compare our measured magnetic trap lifetime of 51(2) s obtained at an oven temperature of 550 °C with ^{88}Sr in the ^{3}P$_2$ state to the measured vacuum lifetime values of other groups [Fig. 2.13 (b)]. Here, we compare the same element and isotope as the cross-section for collisions with different background gas elements differ [98]. The underlying assumption here is that the vacuum in other experiments is limited by the
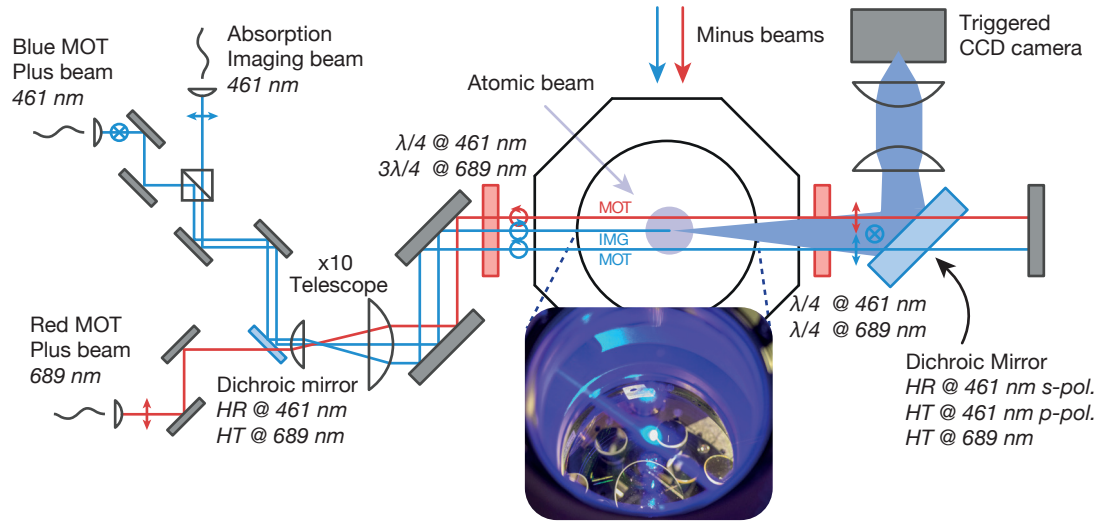
Fig. 2.15 Sketch of the MOT beam setup. We magnify all beams with a $\times 10$ telescope, prepare and select all beams via custom-made dual-wavelength waveplates and dichroic mirrors.

same elements, which is typically hydrogen. Excluding the data point from our group, we drew a line through the remaining data points to visualize the lifetime dependence on the pressure. Judging from that, we think that our pressure measurement obtained with the hot-wire vacuum gauges in subsection 2.1.2 is not accurate enough and should be rather around $\sim 2 \times 10^{-11}$ mbar.

In Fig. 2.14 we show measurements of the magnetic trap lifetime with ^{88}Sr we did after the shutter of our atomic oven broke. The atomic beam was now constantly turned on during the measurement and thus induces collisions and a faster decay of the atom number in the trap. Here, we find reduced lifetimes for higher oven temperature due to the increased flux of the atomic beam. In addition, we also measured the atomic lifetime of ^{87}Sr. The reduced lifetimes could be explained by a higher effective cross section of the fermion with the atoms (mostly ^{88}Sr) in the atomic beam.

2.4.6 Beam merging and imaging setup

To implement the second MOT stage into our setup, the red MOT stage, we needed to design breadboards for the beams of both MOTs. On the same breadboard, we implemented absorption imaging beams from two axes to properly extract the temperature from time-of-flight absorption images: vertical and horizontal absorption images allow us to observe the expansion of the atomic cloud in all three directions. On the top layer, we merge the two repump beams originating from a single fiber collimation port with the red light so they are applied on Z direction on the atoms.

An examplaric depiction of the MOT beam setup in plus direction [indicated in Fig. 2.1] is shown in Fig. 2.15. We merge a relatively weak absorption beam ($\sim 50 \mu$W)

with the blue plus MOT beam with different polarizations via a PBS. Both beams are reflected at a dichroic mirror, where the red MOT beam is transmitted and therefore merged with the blue beams just before a $\times 10$ telescope. From there, the beams are relatively large and well collimated, such that they are aligned to the main chamber with two two-inch mirrors. Just in front of the chamber they pass a dual-wavelength $\lambda/4$ waveplate, where the polarization of the MOT beams and imaging beams is converted to σ^+ and σ^- polarization, respectively. As the polarization of the blue and red MOT beams before was orthogonal, it is matched after the waveplate.

The MOT beams pass the trap center (while picking up a little shadow from the atomic cloud) and are transmitted through another custom $\lambda/4$ waveplate, after which the polarization is linear again. To image the atoms for instance after the red MOT sequence, we apply a weak absorption imaging beam: a small region (of uniform intensity) in the absorption imaging beam shows a shadow of the atomic cloud due to scattering on the $^1S_0$– $^1P_1$ transition. The power of the absorption beam has to be sufficiently weak to not nearly operate in saturated regimes of scattering. The shadow of the MOT is imaged on the plus axis (Z axis) with a telescope with focal lengths of $350\,\mathrm{mm}$ ($500\,\mathrm{mm}$) and $250\,\mathrm{mm}$ ($250\,\mathrm{mm}$) yielding a magnification of 0.7 (0.4) on a CCD camera. We use these images to extract the size and optical density of the shadow to determine the atom number.

We found a fraction of 5 to $10\,\%$ of the blue MOT beams leaking into the imaging path and therefore onto the CCD camera causing blooming and smearing effects on the camera images[2] [99]. The custom-made dichroic mirrors showed the specified behavior (as long as the incident beam was well collimated at the corresponding mirror surface). Further, investigation of the custom-made dual-wavelength waveplates showed well-aligned slow and fast axes for both wavelengths. Starting with a linear polarization, the polarization of $689\,\mathrm{nm}$ light generated with these waveplates was found to be circular of $\geq 98\,\%$[3], whereas we found only $87\,\%$ and $81\,\%$ for $461\,\mathrm{nm}$ light for the $\lambda/4 - \lambda/4$ and $\lambda/4 - 3\lambda/4$ waveplates, respectively. For this reason, we found that the MOT beams, opposed to the image of the atomic cloud, were focused between the lenses of the telescope, such that we could block them with a thin wooden stick. The image was not affected by this.

2.5 Red laser system

In addition to the frequency versatility of our blue MOT laser setup, we set the basis to generate red MOTs with all isotopes with our red laser setup. This section and the following section will be explained in further detail in the PhD thesis by Annie Jihyun Park. As the isotope shifts on the $^1S_0$– $^3P_1$ transition span over a range of more than $350\,\mathrm{MHz}$, it would be harder to enable large frequency tunability with a single DP BB AOM setup. The tunability of the frequency is reached by having seperate optical arms for each isotope with the desired net frequency. The power, which is amplified by a

---

[2]This effect was still present, even though the blue MOT light was switched off shortly before the camera image was taken. It is caused by residual electric charge, which requires transport times on the order of tens of milliseconds and is remaining on the chips of the corresponding pixels at this time.

[3]Here, we used the ratio of the major and minor axes of the elliptical polarization.

injection lock and is about 90 mW, is then sent through the desired optical arms to obtain the desired frequency shifts before it is split into three different beams to be sent to the vacuum chamber to form a red MOT.

In addition MOT beams, we have fairly weak stirring laser beam which is used exclusively for the fermionic isotope ^{87}Sr: here, the ^{3}P$_1$ $F = 9/2$ state shows three different hyperfine states due to the non-zero nuclear spin, namely $F' = 7/2, 9/2$ and $11/2$. The narrow-line MOT operates on the ^{1}S$_0$– ^{3}P$_1$ $F = 9/2 - F' = 11/2$ hyperfine transition, where the Clebsch-Gordan coefficients favor rather small values of m_F to be populated [100]. The stirring laser addresses the ^{1}S$_0$– ^{3}P$_1$ $F = 9/2 - F' = 9/2$ hyperfine transition which helps to distribute the population on the magnetic sublevels more uniformly and improves the overall trap performance, as some m_F levels are suited better for certain locations in the MOT.

The narrow 7.4 kHz transition also requires extreme frequency stability for the red MOT, which is why we feed our red frequency shifters only with a direct digital synthesis system (DDS) instead of using amplified voltage-controlled-oscillator (VCO) signals. The laser frequency has to be stabilized via a Pound-Drever-Hall (PDH) lock to a reference cavity as the absorption signal of this forbidden transition is extremely weak and therefore not suitable to apply a FMS or FMTS lock.

2.6 Red MOT stage

As the Doppler limit of our blue MOT is ~ 0.7 mK, we want to cool atoms further to get closer to quantum degeneracy. As strontium is an earth-alkaline atom, the narrow parity-forbidden ^{1}S$_0$– ^{3}P$_1$ transition allows us to use a second MOT stage with a Doppler limit of 180 nK, which is actually limited to the recoil of strontium trapped with 689 nm light at 230 nK. As the difference in the linewidth of the ^{1}S$_0$– ^{1}P$_1$ transition compared to the ^{1}S$_0$– ^{3}P$_1$ transition is ~ 4000, certain effort has to be spend to transfer a large fraction of the atoms, ideally all of them, to the red MOT to end up with a cool and condensed atomic cloud.

We describe the red MOT sequence briefly to give the reader an idea how we achieve dense clouds in short times: after we load atoms into the ^{3}P$_2$ state and capture them with our magnetic trap, we turn off the blue light and use repump light to optically pump atoms within 2 ms into the ^{3}P$_1$ state. During this repumping process, we ramp down the magnetic field (within ~ 100 μs with an IGPT circuit) from the gradient used in the blue MOT of 63.7 G/cm to 1 G/cm to prevent atom loss due the isotropic expansion of atoms. From this point on we turn on red MOT light while sweeping the laser frequency (slowly enough) in a sawtooth-pattern slightly over the resonance of the $F = 11/2$ state, which is also called "sawtooth-wave adiabatic-passage" (SWAP). The sweeping creates sidebands in frequency space with spacing of the sweeping frequency while the frequency range is given by the sweep amplitude to increase the capture velocity effectively and thereby transfer as many atoms as possible.

The SWAP increases the excitation probability during the ramping process upwards in frequency close to one. The ramp downwards is fast enough such that no stimulated

emission occurs. Thereby, the atom can spontaneously decay and the net momentum change of the atom is within the direction of the cooling beam. This method is more efficient and thus faster than traditional methods, which also induce stimulated emission to a large extent.

In our experimental cycle, we employ a combination of different cooling schemes during the red MOT stage [Fig. 2.1]: The stage starts with a SWAP MOT cooling applied on all three MOT beams for 40 ms, which we denote as "SWAP-3", to slow down atoms initially. The reduced velocity will pay off in the next step. As in the 3D scheme heating processes due to momentum transfers between orthogonal beams are present, we switch on only one MOT beam at a time, which we call "SWAP-1", to achieve faster cooling and reduction of the phase space density. For efficient SWAP-1 cooling, we apply it for 15 ms on ⁸⁸Sr and for 100 ms on ⁸⁷Sr before the red MOT stage ends with a single frequency MOT, where we turn off the laser sweeping and thus the additional laser linewidth broadening. The single frequency MOT takes 50 ms for ⁸⁸Sr and 10 ms for ⁸⁷Sr, where we end up with atom numbers of 6×10^7 and 1×10^7, respectively.

2.7 Other experimental components

In this section we give a higher level overview on the experiment and use this opportunity to point out the most important aspects of other laser systems and our red MOT. Many components which we briefly describe here, will be referenced to several master thesis' and explained in more detail in the PhD thesis by Annie Jihyun Park.

2.7.1 Clock laser and reference cavity

As our red 689 nm laser is operating on the narrow forbidden $^1S_0$–$^3P_1$ transition, and we need a very narrow 698 nm clock laser to interact with strontium atoms on the doubly-forbidden $^1S_0$–$^3P_0$ transition, we lock our lasers to a high-finesse ultrastable cavity. Detailed description of the setup and its characterization can be found in Refs. [80, 101, 102]. The frequency of both lasers are locked via a traditional PDH scheme, while their laser beams are sent to the cavity in counter-propagating directions. To combine and separate the laser beams we employ dichroic mirrors. The finesse of the cavity is $270\,000$ while the cavity is thermally isolated from the environment by several stages and actively temperature stabilized at the most outer stage. Without temperature stabilization, we find cavity drifts of 2.5 kHz per day [102]. From excitation spectra with the clock laser with $^1S_0$ state atoms, we find a laser linewidth of ~ 1 kHz. As the first cavity seemed to have troubles with unknown outgassing sources and vacuum seals, we built a second, improved reference cavity [102].

2.7.2 Dipole trap and transport laser

Ultracold, bosonic atom clouds of red strontium MOTs have shapes similar to slightly curved pancakes [83]. When transferring atoms from such a MOT into a dipole trap,
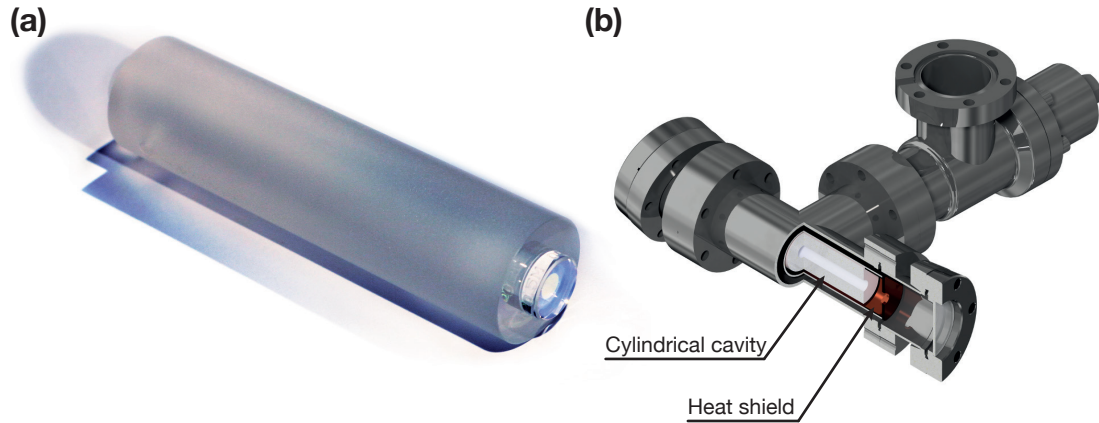
(a)

(b)

Cylindrical cavity

Heat shield

Fig. 2.16 (a) Optically-contacted cylindrical pre-stabilization cavity. (b) A CAD model for the whole
pre-stabilization cavity in a heat shield and vacuum chamber.

matching the trap shape to the atomic cloud shape increases the transfer efficiency and
prevents unnecessary heating. For this reason, we designed a dipole trap at a 1064 nm
laser system to provide dynamically-shaped optical trap potentials generated with an
acousto-optic deflector (AOD) [103]. The time-averaged trap potential can be tuned to
vertical waists of 23 μm at a horizontal waist of 541 μm yielding an aspect ratio of 23.5.

The trap can be reshaped to a Gaussian with a waist of 148 μm at the focus and shift this
focus over a distance of 92 cm while maintaining the waist of the focus. As our transport
distance is 51 cm, we reduce the waist to 30 μm. This increases the trap frequency from
0.2 Hz to 6 Hz, which would dramatically reduce the transport time, as the inverse of
the trap frequency sets the timescale on which the adiabatic transport process can be
performed. A setup which uses three tunable lenses allows us to perform the shift of the
focus over such a distance and will help us to transport as many atoms as possible from
the main chamber to the science chamber into the cavity.

2.7.3 Pre-stabilization and other cavities

The crossed cavity and the two reference cavities are not the only cavities in our lab. We
encountered several other challenges in the lab, where filter, monitoring (section 2.2.2),
and pre-stabilization cavities were useful. As filter and monitoring cavities require a
piezo, pre-stabilization cavities do not. In principle, they are similar to reference cavi-
ties, but do not provide the same frequency stability. We use pre-stabilization cavities to
stabilize the frequency of our lattice lasers, as the lattice lasers could hinder the optical
transport of the atoms when they stay locked to the crossed cavity.

With the skill of optical contacting in our toolbox, we designed and bought multiple
cylindrical cavity spacers made from ultra-low-expansion glass[4]. With these spacers, we

---

[4]A larger amount of glass substrates hardly changes the total price, as long as all of them are processed
in the same run. For instance, this regards cavity spacers, mirror substrates and coating runs of mirror

were able to build most of the required cavities together with flat and $50\,\mathrm{cm}$ radius-of-curvature mirror substrates, which were IBS coated together with the $10.2\,\mathrm{m}$ radius-of-curvature substrates we used for the crossed cavity. All of these mirrors were suitable for optical contacting and their multi-band coating offered a large reflectivity for the wavelengths of the lasers we were working with.

An optically contacted pre-stabilization cavity is shown in Fig. 2.16 (a), which we use to stabilize our titanium-sapphire lasers at the $^1S_0$–$^3P_0$ and the $^1S_0$–$^3P_1$ magic wavelengths ($813\,\mathrm{nm}$ and $914\,\mathrm{nm}$). We designed a simple vacuum setup imitating our reference cavity design to isolate the cavity spacer from temperature changes by ruling out convection. The vacuum housing consists of a standard CF40 vacuum-tee with angle-brackets together with anti-reflection coated viewports [Fig. 2.16 (b)]. To provide another layer of thermal isolation, a (closed) polished copper heat shield is resting on viton half-rings inside the tee, while the spacer is resting on viton half-rings inside the heat shield. All dimensions are chosen such that we optionally can fit a $\sim 1\,\mathrm{cm}$ long piezo tube between the spacer and one of the mirror substrates. The vacuum tee is pumped out with a turbo-pump, before we close the angle valve. This still yields a $10^{-4}\,\mathrm{mbar}$ vacuum level for a few years.

We estimate the frequency stability of the pre-stabilization cavities according to the $10\,\mathrm{cm}$ long spacer with a thermal expansion coefficient of $3\times 10^{-8}\,\mathrm{m/Km}$ to be $11\,\mathrm{MHz/K}$ at a wavelength of $813\,\mathrm{nm}$. With this coefficient and the layers of thermal isolation, we achieve a frequency stability on the few megahertz level. We improve this by stabilizing the temperature of the vacuum housing to $30\,^\circ\mathrm{C}$ with heating wires, a thermistor and thermal isolation by aluminum foil around it.

For filter and monitoring cavities (which include a piezo), we designed a separate mount, which is isolated from vibrations by a sand and lead filling, while the spacer is gently clamped on viton pads. The whole mount comes with an acrylic enclosure, which has two anti-reflection coated windows to transmit laser beams.

2.8 Science chamber

Many quantum gas microscopes are using glass cells [13, 16, 19], since they come with great optical access and compactness. The implementation of the crossed cavity into a glass cell however would have come with increased difficulty. It would be possible to optically contact the crossed cavity at one of the glass cell walls and then assemble the cell via optical contacting. However, it seemed to be more of a challenge to us to weld the glass to a steel flange, while keeping the inside clean. An approach like this would be possible, but requires careful planning in cooperation with a company.

Furthermore, it is questionable how the optical access would have been beneficial for a setup with the crossed cavity. The cavity modes require specific beam paths to achieve good mode matching, while laser beams with angles up to $45\,^\circ$ with respect to the plane spanned by the cavity modes would be blocked by the cavity spacer. The aperture of
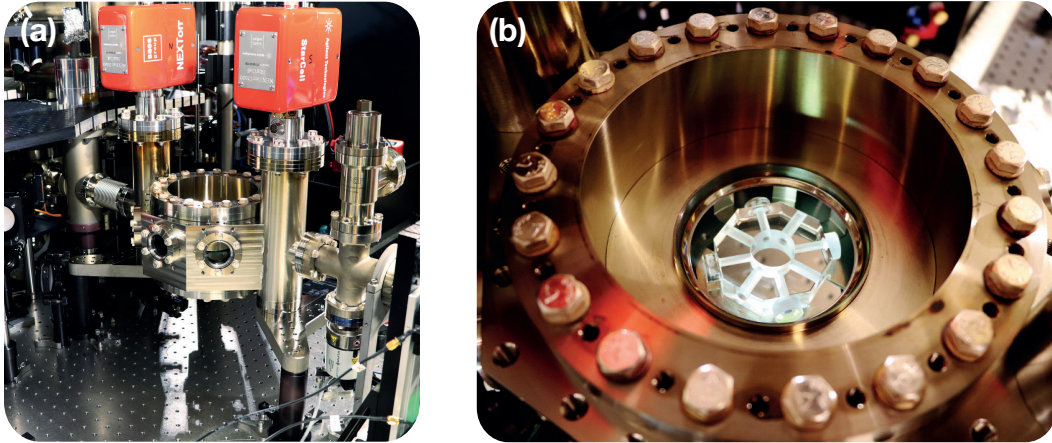
---

substrates.

Fig. 2.17 (a) The science chamber after the bakeout and activation of the ion and NEG combination pumps. (b) The crossed cavity mounted in the science chamber. It is highlighted with a white-light source.

the viewports can be chosen large enough to not restrict the numerical aperture of the microscope objective (apart from spherical aberrations).

For these reasons we chose a custom-made steel chamber as our science chamber. The CF40 viewports provide optical access to the cavity mirrors as well as one clearance hole of the spacer for other laser beams. The wide viewports on top and the bottom of the chamber are so-called "bucket windows" which have 75 mm wide glass windows. The construction of these custom made viewports was tricky, due to the large window diameter as a large contacting area for the crossed cavity: the uncoated window had to be welded into the steel bucket first, where it formed a slight saddle shape under stress from the steel frame. The flatness of the windows had to be restored on best effort with magnetorheological finishing (MRF), a technique where a polishing liquid jet is guided with magnetic fields. After repolishing the windows, the surface profile of the window had a peak-to-valley of $3.6 \ \mu\text{m}$ and an ion-beam sputtered (IBS) anti-reflection coating was applied to both sides of the window to transmit lattice and imaging wavelengths.

At the top-window the cavity spacer is resting about $\sim\!100 \ \mu\text{m}$ underneath the glass surface constrained in a stainless-steel cage (which avoids virtual leaks caused by entrapped air bubbles). This configuration allows close optical access of the microscope objective to the atoms in the optical lattice mainly constrained by half of the thickness of the crossed cavity. The microscope objective takes into account spherical aberrations of the glass viewport. Due to the uneven, saddle-shaped surface profile of the bucket window optical contacting of the cavity spacer to the viewport was not possible.

The inside of the science chamber is coated with a non-evaporative-getter (NEG) coating, which provides pumping and improves the vacuum we achieve at UHV about one order of magnitude. The coating itself can keep the vacuum pressure at a 10^{-10} mbar level without any additional pumping. By adding ion and NEG pumps, we achieved a vacuum below 10^{-11} mbar.

2.9 Conclusion

We showed design and construction of a strontium machine from the beginning, with the aim of achieving a strontium quantum gas microscope. It is kept to be as versatile as possible, to work with mixtures of different isotopes and different lattice wavelength. To reduce cycle times and thus improve classical averaging for quantum simulation, further optimization of components such as the ZS would be beneficial to improve loading rates of atoms into the magnetic trap. However, as our machine is still missing loading of atoms into lattices in the crossed cavity and single-site-resolved imaging, we decided to move on to complete the system. If necessary, further optimization of these components can be done at later times.

Chapter 3

State-Dependent Optical Lattices for the Strontium Optical Qubit

As the science chamber together with the crossed cavity was planned to be the second and final module to be attached to the vacuum chamber, we were left with some time to generate lattices and perform spectroscopy in the main chamber. This opportunity helped us to get more familiar with strontium, our experimental sequences and the implementation of lattice lasers.

In chapter 1 we already introduced the notion of qubits which are quantum-mechanical two-level systems. In contrast to a classical bit, the information in a qubit is not only 0 or 1, but can also involve superpositions and carry phase information between the two states. In addition to that, we discussed that the clock states of strontium, the $^1S_0$ and $^3P_0$ state, are great candidates to store information and can be treated as a two-level system under certain conditions. Ignoring the nuclear spin of ^{87}Sr for now, we can think of the $^1S_0$ ground (g) state as $|0\rangle$, and of the $^3P_0$ excited (e) state as $|1\rangle$ of the qubit.

Trapping strontium in state-dependent lattices for the clock states allows us to obtain differential control over the corresponding states. To our knowledge no state-dependent lattice wavelength for strontium has been measured so far, which is why we used this opportunity to measure the g state tune-out wavelength around $689.2\,\mathrm{nm}$. The content of this chapter is associated with Ref. [104].

We start this chapter by introducing a novel measurement technique to measure tune-out wavelengths with thermal gases of atoms. We discuss the measurement framework, analysis and results in detail. In addition to that, the implementation and a measurement of the $^3P_0$ state polarizability is presented. The next section takes a brief glance at an attempt to measure the $633\,\mathrm{nm}$ e state tune-out wavelength and highlights difficulties we experienced with it. Proof-of-principle trapping and a lifetime measurement of e state atoms in a one-dimensional g state tune-out lattice is shown. Finally, we explain how our experimental results were used for a reevaluation of lifetimes in the strontium atom.

3.1 Measuring the ground state tune-out wavelength

Many approaches for measuring tune-out wavelengths already exist, but all of them are based on measurements with degenerate gases [105, 106] or atom interferometry [107, 108]. We tried to think of a new method which is easy to implement using thermal atoms in an optical (lattice) trap. Most importantly, the method should be suitable to measure
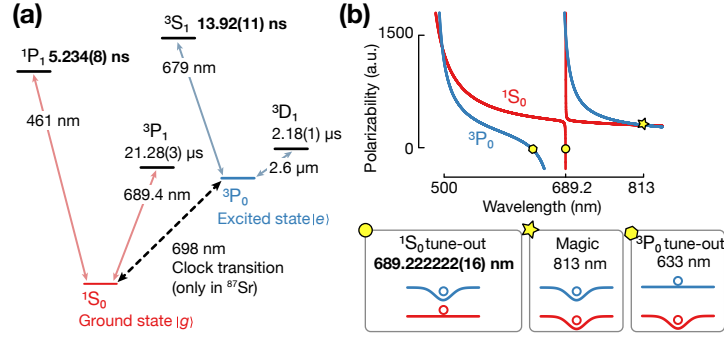
Fig. 3.1 (a) Simplified strontium energy level diagram to show the most dominant transitions contributing to the polarizabilities of the g and e state. (b) The trap depth, which is proportional to the dynamic dipole polarizability, versus wavelength. At the magic wavelength (star) both, the g and e state, experience the same trap depth. For the g state tune-out wavelength an atom in the g state is free to move, while an atom in the e state can still be trapped. All quantities with bold lettering are determined in this work.

the 689.2 nm g state tune-out wavelength and the 633 nm e state tune-out wavelength, respectively. As degenerate gases in the $^3P_0$ state would not be feasible due to inelastic collisions [109, 110] and atom interferometers would require a large effort to build, we tried to think of a simple method which can be applied to thermal gases of atoms in any state and thus avoid these difficulties.

Our measurement technique will be based on a heating process called "parametric heating", which we achieve by modulating the amplitude of the lattice potential. As the potential depends linearly on the polarizability [Eq. (1.2)], the potential and therefore the polarizability vanish when the trap light is at the tune-out wavelength. This also means, that any modulation and heating effects are minimized at this wavelength. For this reason, we introduce the basic concept of parametric heating in the next subsection.

3.1.1 Parametric heating

As a starting point, we look at a process called parametric heating, or amplitude-noise-induced heating [111–113]. When we shake the amplitude of a trap potential for a single atom with a fractional fluctuation of the form $V_x(1 + \epsilon(t))$, the Hamiltonian which is left to solve is

$$\hat{H}_\epsilon = \frac{\hat{p}_x^2}{2m} + \frac{1}{2}m\omega_{\text{trap}}^2(1 + \epsilon(t))x^2 \,, \tag{3.1}$$

which corresponds to fluctuations of the spring constant in a classical system. Here, $\hat{p}_x$ is the momentum operator acting on the coordinate x, m is the mass of the atom and ω_{trap} is the trap frequency in absence of modulation. By applying first-order time-dependent perturbation theory can be used to calculate the average transition rates between the quantum states of the trap, which allows us to determine the heating rate Γ_ϵ. We find [111–113]

$$\Gamma_\epsilon = \pi^2\nu_{\text{trap}}^2 S_\epsilon(2\nu_{\text{trap}}) \,, \tag{3.2}$$
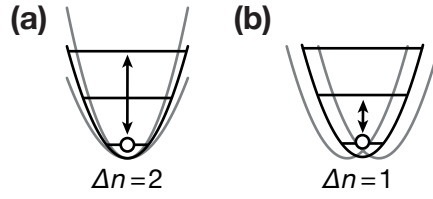
Fig. 3.2 A visualization of parametric heating (a) and phase-noise induced heating (b) in optical traps. The change of the number of motional quanta is given by Δn.

where $S_\epsilon(2\nu_{\text{trap}})$ is the power spectrum at two times the trap frequency $\nu_{\text{trap}} = \omega_{\text{trap}}/2\pi$, and is given in units of $1/\text{Hz}$. Hence, shaking of the trap potential amplitude at two times the trap frequency leads to heating to higher motional states, which are two quanta apart [Fig. 3.2 (a)].

A similar equation can be found for shaking of the trap center, which we call phase-noise induced heating [111–113]. The Hamiltonian for this system reads

$$\hat{H}_\delta = \frac{\hat{p}_x^2}{2m} + \frac{1}{2}m\omega_{\text{trap}}^2(x - \delta(t))^2\,, \tag{3.3}$$

where the amplitude of the lattice well shaking is $\delta(t)$. The resulting heating rate is [111–113]

$$\Gamma_\delta = \pi^2\nu_{\text{trap}}^2 S_\delta(\nu_{\text{trap}})\,, \tag{3.4}$$

where $S_\delta(\nu_{\text{trap}})$ is the power spectrum of the relative position fluctuations at ν_{trap}. Here, shaking the trap center at the trap frequency leads to heating to higher motional states which are one quantum apart [Fig. 3.2 (b)].

3.1.2 Idea of the measurement

As parametric heating does not require quantum degeneracy, we used it for our considerations. Usually, this is an unwanted effect in most trapping schemes and to be avoided, whereas it can be used to measure trap frequencies and has been used to characterize state-dependent lattices [114]. In our case, we will employ it to measure tune-out wavelengths: we intentionally generate parametric heating by modulating the amplitude of the trap potential of light close to the tune-out wavelength, such that any heating vanishes when the wavelength matches the tune-out wavelength.

The trap potential created by light which is close to the tune-out wavelength is extremely shallow and becomes more shallow, as the lattice wavelength approaches the tune-out wavelength. For this reason, atoms would be easily lost from the trap due to gravity such that the precision of this measurement would be limited by this effect. To keep the atoms trapped, even when the modulated light is exactly at the tune-out wavelength, we need a separate trap to prevent this atom loss. For this reason, we overlap our "shallow tune-out lattice" with another trap, a "deep magic-wavelength lattice".

In each experimental sequence, we measure an exponential atom loss rate Γ_{loss}, which
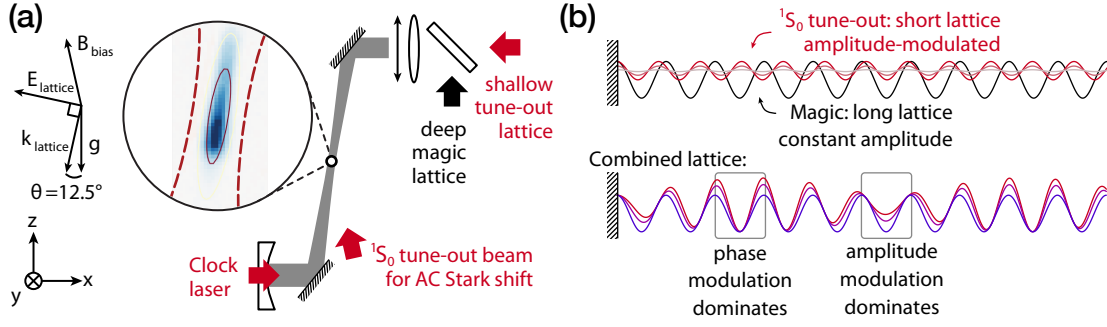
Fig. 3.3 (a) Experimental setup and optical lattice geometry. A shallow lattice close to the tune-out wavelength is overlapped with a deep magic-wavelength lattice to trap atoms in this combined trap. (b) Modulation of the full shallow-lattice amplitude leads to heating of the atoms caused by phase- and amplitude modulation of the wells of the combined optical lattice.

is the result of heating an atom over all bound states in the lattice well, which is proportional to the parametric heating rate from Eq. (3.2). To motivate this expression, we start with a modulation of the form $\epsilon(t) = \epsilon_0 \cos(\omega t)$ with an angular modulation frequency ω, a dimensionless modulation depth ϵ_0, and time t. It can be shown that the power spectral density then takes the form [111–113]

$$S_\epsilon(\omega) = \frac{2}{\pi} \int_0^\infty \mathrm{d}\tau \cos(\omega\tau)\langle\epsilon(t)\epsilon(t+\tau)\rangle = \epsilon_0{}^2\delta(\omega)\,. \tag{3.5}$$

As $\epsilon(t)$ describes the relative modulation depth of the optical lattice potential, we can determine the modulation depth as $\epsilon_0 = V_{\mathrm{mod}}/V$, where V_{mod} is the modulation amplitude of the shallow tune-out lattice and V is the optical lattice depth of the deep magic wavelength lattice. In the supplemental material of Ref. [104], we show that the shallow tune-out lattice does not influence the total lattice depth due to a vanishing polarizability around the tune-out frequency. With the trap frequency from Eq. (1.9) and the Stark shift from Eq. (1.2), we find the proportionality of the atom loss rate

$$\Gamma_{\mathrm{loss}}(\omega) \propto \nu_{\mathrm{trap}}^2 \left(\frac{V_{\mathrm{mod}}}{V}\right)^2 \propto \alpha_g{}^2(\omega)I_{\mathrm{mod}}^2\nu_{\mathrm{trap}}^{-2}\,, \tag{3.6}$$

where we introduced the ${}^1S_0$ g state polarizability α_g. Here, I_{mod} is the intensity amplitude of the modulated shallow tune-out lattice. From this expression, we see that the atom loss rate caused by amplitude modulation grows quadratically with α_g and vanishes when it equals zero. For this reason we modulate the shallow lattice with a close-to-unity modulation amplitude, while ν_{mod} is given by two times the trap frequency of the deep lattice.

3.1.3 Optical lattice setup

Before we measure the tune-out wavelength, we need to build and align the optical lattice setup. Therefore, it is important to load the atoms into the 813 nm deep magic-wavelength lattice and match the waists, or foci, of the input and retro-reflected lattice beams with the atomic cloud to achieve maximal intensity and trap frequencies. This is even more important for the 689 nm tune-out lattice to improve the signal-to-noise ratio of the measurement later on, which thus has to be well overlapped with the magic-wavelength lattice.

We designed two custom constructions mounted above and underneath the main chamber, which we call "beam crown". It provides a collection of one-inch and two-inch mirrors to direct beams into the main chamber. This construction allows us to send the Z axis MOT and imaging beams (which are shaped on a breadboard layer) through the center of the chamber without any angular deviations. We use the other mirrors, to form retro-reflected lattices and shine clock laser light under a small angle of 12.5 ° with respect to the perpendicular axis of the optical table.

A depiction of the vertical optical lattice setup is given in Fig. 3.3 (a). As for the vertical lattice, we send a magic-wavelength lattice input beam at 813 nm through the main chamber with the help of the beam crown. Underneath the vacuum chamber, we retro-reflect the lattice beam with a 35 cm radius-of-curvature half-inch mirror at a position 35 cm away from the focus, such that the retro-reflected beam has a focus at the same position. Similarly, we implement the 689 nm tune-out lattice beam, which is merged with the help of a dichroic mirror with the magic wavelength lattice beam and is retro-reflected at the same retro-reflector.

To align the 813 nm lattice, we started by making a steady-state blue MOT and observing its fluorescence signal on an avalanche-photodetector (APD). We used the 689 nm optical path to send a frequency-modulated 689.4 nm probe beam, which was scanning over the ${}^1S_0$– ${}^3P_1$ resonance, onto the blue MOT and maximized the modulated signal visible on the APD. In the next step, we ran our standard experimental sequence, while the frequency of the probe beam now was set to the ${}^1S_0$– ${}^3P_1$ resonance and turned on during the red MOT operation. It is easy to see an influence of the probe beam (starting with ~ 1 mW) onto the red MOT by removing atoms using radiation pressure. The effect is largest when the beam is directly hitting the center of the cloud. In successive steps, we lowered the probe beam power (down to the 1 μW level) to enhance the sensitivity of the beam position to the atoms and repeated the process when aligning the retro-reflector angle. The 813 nm input beam is then overlapped with the probe beam (by matching the beam path with index cards).

To ensure that the 813 nm and 689 nm optical paths and the retro-reflector are optimally aligned, we place a polarizing beam splitter (PBS) in front of the fiber of each wavelength which leads to the optical lattice setup. The polarization of the input light incident on the PBSs is set such that all of the light is transmitted and coupled to the fibers. The retro-reflected light, which travels back through the fibers, might pick up impurities on the polarization such that some light is reflected at the PBS and can be detected with a power meter. When both input beams are roughly overlapped, some 813 nm light
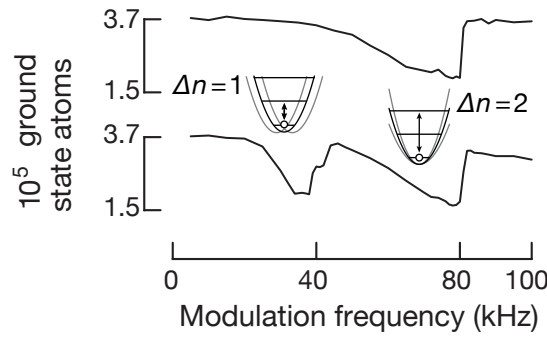
Fig. 3.4 Measured lattice modulation spectrum when modulating the magic-wavelength lattice without the shallow lattice (top), and when modulating the shallow lattice in the combined trap (bottom).

leaks into the 689 nm path, coupled through the fiber and is visible on the corresponding power meter. When the retro-reflecting mirror is roughly aligned, the signal is visible on the corresponding other power meter. From here, both signals just have to be maximized by tuning the 813 nm input mirrors and the retro-reflector, to ensure optimal overlap of both lattice axis in the main chamber.

To ensure that also both waists, of the retro-reflected 813 nm lattice are overlapping, the retro-reflected signal would theoretically be maximized when both waists are overlapping and the retro-reflector is in the correct position. However, the mentioned polarization impurity drifts over time and the signal obtained is not long-term reliable. Therefore, we needed to try different positions (with 5 mm step size) of the retro-reflector on a rail, while maximizing the retro-reflection and each time measure the size of the atomic cloud. The atomic cloud size is minimized, but relatively insensitive to the case when both waists are at the atomic position. Of course, a rough range of the 35 cm distance from the MOT is required and a ABCD matrix calculation of the sensitivity of the retro-reflector positioning is helpful. According to our calculation, the optimal retro-reflector position for both wavelengths differs by a relatively small chromatic displacement of the focus of ~ 50 μm, which has no significant influence on our experimental setup. When all of these steps are clear, the whole alignment procedure can be done within a day.

3.1.4 Measurement framework

Overlapping both the shallow tune-out and deep magic-wavelength lattice leads to a combined, incommensurate lattice as shown in Fig. 3.3 (b). When modulating the shallow tune-out lattice in this configuration, in some lattice sites phase modulation dominates, while in other lattice sites amplitude modulation dominates. By sweeping the modulation frequency over a range of 100 kHz, we obtain spectra as shown in Fig. 3.4. To find the modulation frequency for the tune-out lattice, we first take a reference spectrum by turning the shallow lattice off and modulating only the deep lattice with a modulation amplitude of 2 %, which is shown on the top panel. In this case, we find a single minimum

in the spectrum at $\nu_{\mathrm{mod}} \approx 80$ kHz, which corresponds to the amplitude modulation and parametric heating that results in transitions between lattice bands that are two motional quanta apart [111]. From this measurement, we deduce the trap frequency of the lattice, which is half of ν_{mod} and reads $\nu_{\mathrm{trap}} = 40$ kHz. We find this value to be unchanged when turning on and only modulating the shallow lattice with a 100 % modulation amplitude as shown in the bottom panel. In this spectrum, we find an additional minimum at the trap frequency which corresponds to phase modulation and transitions between adjacent lattice bands [111].

In addition to that, we measure the transverse, or radial trap frequency of the lattice by taking modulation spectra up to 1 kHz with the magic-wavelength lattice and find $\nu_{\mathrm{radial}} = 100$ Hz. The ratio of the radial and longitudinal trap frequency from Eqs. (1.9) and (1.10) allows us to determine the $1/e^2$ beam radius w at the atoms via

$$ w = \frac{\sqrt{2}}{k} \frac{\nu_{\mathrm{trap}}}{\nu_{\mathrm{radial}}} = 73 \ \mu\mathrm{m} \,. \tag{3.7} $$

As shown in Fig. 3.3 (a), about 2×10^5 g state atoms occupy a ~ 60 μm long and ~ 20 μm wide ellipsoid in this near-vertical one-dimensional deep magic-wavelength lattice at $813.4274(2)$ nm. We use these in-situ and time-of-flight images to determine atom numbers and temperatures [77].

The power of both lattices is stabilized to 290 mW and 4.5 mW of the deep lattice and shallow lattice, respectively. The power of each laser beam is stabilized via a PI circuit which receives an error signal from the difference of a set point and the voltage of a photodetector, which measures a constant fraction of the optical power. The power, or intensity, is adjusted with an acousto-optical modulator (AOM), such that we modulate the intensity of each laser beam by switching from a constant to a sinusoidally-modulated set point at the intensity stabilization circuit. We write down the modulation amplitude of the tune-out light in terms of voltage ($\propto I_{\mathrm{mod}}$) obtained at the corresponding photodetector which we use to rescale data points according to Eq. (3.6).

During the measurements, we found that amplified spontaneous emission (ASE) on the tune-out laser light would induce systematic shifts in our measurement. Especially around the $^1S_0$– $^3P_1$ transition, where the polarizability diverges, it was important to achieve a good suppression of the ASE. Although noise levels seemed to be negligible on our optical spectrum analyzer (OSA) and a beat with a frequency comb, a higher suppression increased the lifetime in the combined lattice and reduced unknown heating effects, which were not easily accounted for.

For this reason, we minimize the light away from the carrier by Fourier filtering it with a grating as a dispersive element. We expand the beam to a $1/e^2$ waist of 2 cm, diffract it from a holographic grating with 2400 lines/mm, propagate it over ~ 6 m, before finally coupling it into a single-mode polarization-maintaining fiber. By measuring the Gaussian suppression lineshape after the fiber and taking into account the ASE background of the unfiltered light, we determine the overall suppression of the tune-out light spectrum at the $^1S_0$– $^3P_1$ transition to be -90 dB compared to the carrier.
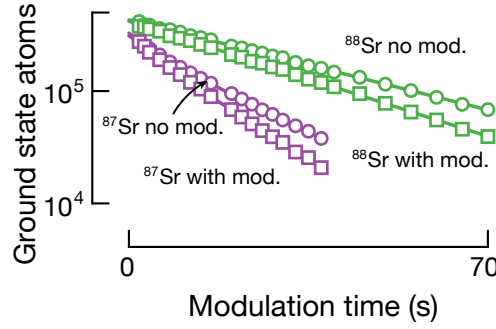
Fig. 3.5 Lifetime measurements for the bosonic ^{88}Sr and fermionic ^{87}Sr, with and without modulation of the shallow lattice show clear differences in the lifetime for each isotope.

3.1.5 Data taking and analysis

The goal for taking a single data point is measuring the atom loss rate caused by modulation at a certain wavelength of the tune-out laser. Therefore, we first set the wavelength of the shallow tune-out laser, lock it to a wavemeter and measure the absolute frequency with a self-referenced femtosecond frequency comb, resulting in an absolute frequency error of 3 MHz. As the full measurement run took about three weeks, the wavelength setting is done in a random manner across the entire wavelength range of interest to avoid systematic errors due to long-term drifts, for instance of the wavemeter. Then, we measure the modulation frequency ν_{mod} as described in the passage before, which is applied to the shallow lattice modulation. This is crucial, as the lattice alignment can slightly drift and thus, comes with slight changes in the trap frequency (on the order of kilohertz). We use ν_{mod} to rescale Γ_{loss} in Eq. (3.6) to obtain comparable loss rates.

In the next step, two spectra of exponential atom loss versus time are taken, with and without the modulation of the tune-out lattice [Fig. 3.5 (b)]. It is important to understand that the background atom loss rate (without tune-out lattice modulation) differs for different wavelengths, as residual-intensity noise (RIN) of the tune-out laser can lead to larger or smaller scattering on the ^{1}S$_0$– ^{3}P$_1$ transition, which is roughly -143 GHz detuned from the tune-out light. The RIN of the unfiltered tune-out laser light showed strong wavelength-dependent signatures, which led to significant differences in the background atom loss spectrum. Other contributions to the background atom loss are RIN of the magic-wavelength lattice, and collisions with background gas atoms.

The atom loss rate is then extracted with a fit. For ^{88}Sr we use the solution

$$N(t) = N_0 \exp\left(-\Gamma_{\mathrm{loss}}t\right) , \tag{3.8}$$

of a single-body decay process corresponding to the differential equation $\dot{N} = -\Gamma_{\mathrm{loss}}N$. Here, N is the atom number at time t with the initial atom number N_0 and Γ_{loss} is the loss rate corresponding to the observed decay, with or without modulation. Based on a

χ^2 test we found that we need to use a super-exponential decay for ⁸⁷Sr

$$N(t) = N_0 \frac{\exp\left(-\Gamma_{\text{loss}}t\right)}{\Gamma_{\text{loss}} + N_0 b(1 - \exp(-\Gamma_{\text{loss}}t))} \,, \tag{3.9}$$

as we find an additional two-body decay process, which is described by the two-body loss coefficient b stemming from the additional two-body loss term of the differential equation $\dot{N} = -\Gamma_{\text{loss}}N - bN^2$.

As for data taking, we ran into a challenge that we could not quantify the overlap of both lattices correctly, although we tried different calibration methods based on parametric heating. This effect led to error bars, which were too small for a fit later on, as the data points varied too much in their value for Γ_{loss} from day to day. For this reason, we take about 3 to 5 data points for the tune-out laser around a certain wavelength, each at a different day, to quantify the variations in the overlap. Using a standard deviation modified with the student-t distribution does not seem reasonable to us as the absolute frequency of each data point slightly differed as measured with the frequency comb. In total, we take about 80 data points for each isotope and we use all data points with their individual error bars for a fit.

3.1.6 Results

The rescaled data for ⁸⁸Sr and ⁸⁷Sr are shown in Fig. 3.6 (a) and (b), respectively, as a function of $\Delta/2\pi \equiv (\omega - \omega_{³P_1})/2\pi$, the detuning from the $^1S_0$– $^3P_1$ transition of the corresponding isotope. The induced loss rate Γ_{loss} shows a minimum at detuning $\Delta_t/2\pi$ corresponding to the tune-out wavelength for each isotope. For ⁸⁷Sr the induced two-body coefficient b is obtained by the difference of the two-body coefficients extracted from the underlying atomic decay curves and shows the same behavior with respect to the detuning as Γ_{loss}. This behavior can be explained by an increased tunneling rate in the second lattice band, leading to increased evaporation, correlated one-body and two-body decay rates, and an increased uncertainty for Δ_t^{87}.

We model the induced loss rate as

$$\Gamma_{\text{loss}}(\Delta) = c_0 \left(1 - \frac{\Delta_t}{\Delta}\right)^2 \,, \tag{3.10}$$

where the fit parameter c_0 relates the parametric heating rate to the trap loss rate. A detailed derivation of this expression can be found in the supplemental material of reference [104]. We find

$$\begin{aligned} \Delta_t^{88} &= 2\pi \times 143.009(8) \text{ GHz}\,, \\ \Delta_t^{87} &= 2\pi \times 142.86(8) \text{ GHz}\,. \end{aligned} \tag{3.11}$$

Considering the empirical two-body loss model used for ⁸⁷Sr, we find these numbers to be in good agreement. An upper limit of the difference of the corresponding Δ_t due to hyperfine splitting, tensor and vector shifts is derived by us to be $|\Delta_t^{88} - \Delta_t^{87}| <$
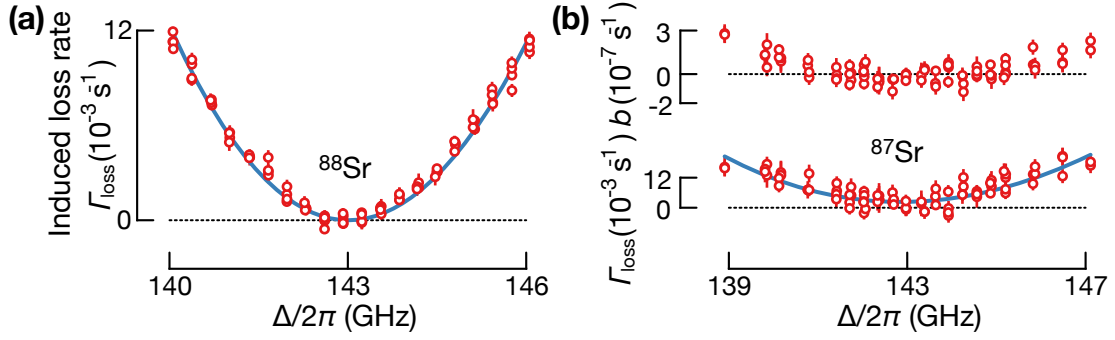
Fig. 3.6 (a) The induced exponential atom loss rate Γ_{loss} versus the detuning from the $^1S_0$–$^3P_1$ transition for ^{88}Sr. The detuning at the minimum of Γ_{loss} corresponds to the tune-out wavelength. (b) For ^{87}Sr, interactions lead to an induced two body loss rate b and an increased uncertainty.

$2\pi \times 23$ MHz [104]. For this reason, we use the measured value for Δ_t^{88} for ^{87}Sr in the following discussions, and suppress the superscript for clarity. This choice leads to a residual polarizability of the g state $\alpha_g = \pm0.05$ a.u. from the 2.4 a.u./GHz polarizability slope around Δ_t. Here, 1 a.u. $= 4\pi\epsilon_0 a_0^3$ is the atomic unit of polarizability, where a_0 is the Bohr radius.

The measurement range is limited to a few GHz, to work with the same I_{mod} and avoid saturation effects of Γ_{loss}. Reducing the measurement range did not change Δ_t, such that we can assume that saturation effects are negligible. Fitting the data for the induced loss rate with our model [Eq. (3.10)] and additional offset, showed statistically significant offsets of $2(1)\times10^{-4}$ 1/s and $2.3(4)\times10^{-3}$ 1/s for ^{88}Sr and ^{87}Sr, respectively. Although the offset for ^{87}Sr can be explained by contributions from vector and tensor polarizabilities, these cannot occur in ^{88}Sr. The offset for ^{88}Sr causes a systematic shift of 2 MHz. In conclusion, this leads to a resulting tune-out frequency for ^{88}Sr of

$$\omega_t^{88}/2\pi = (434,972,130 \text{ MHz}) \pm (8 \text{ MHz}_{\mathrm{stat}}) \pm (2 \text{ MHz}_{\mathrm{sys}}), \tag{3.12}$$

and tune-out wavelength

$$\lambda_t^{88} = 689.222222(16) \text{ nm}, \tag{3.13}$$

using $\omega_{^3P_1}^{88} = 2\pi \times 434,829,059,124,500$ Hz for the $^1S_0$–$^3P_1$ transition [115].

For ^{87}Sr we use the isotope-shifted transition frequency $\omega_{^3P_1}^{87} = 2\pi \times 434,829,059,124,500$ Hz obtained from literature [115, 116] together with Δ_t^{88} and find

$$\omega_t^{87}/2\pi = (434,972,149 \text{ MHz}) \pm (8 \text{ MHz}_{\mathrm{stat}}) \pm (2 \text{ MHz}_{\mathrm{sys}}), \tag{3.14}$$

and the corresponding tune-out wavelength

$$\lambda_t^{87} = 689.222320(16) \text{ nm}. \tag{3.15}$$

This result is the most precise measurement of a tune-out wavelength to date, if we take

into account the small sensitivity to a change in optical frequency [117, 118, 105, 107, 106, 119]. In other words, we considered the slope of the polarizability of the corresponding measurement and compared it to the frequency uncertainty of the measurement. This gives us a polarizability value which is a measure for sensitivity of the corresponding tune-out measurement.

3.2 Measuring the excited state polarizability

With the vanishing g state polarizability at the tune-out wavelength, the AC Stark shift of the clock transition is solely determined by the e state polarizability. This enables a direct measurement of the e state polarizability $\alpha_e(\omega_t)$ by Stark shift spectroscopy: the concept here is to trap strontium atoms in a magic-wavelength lattice, which does not induce a differential and measurable Stark shift. The transition frequency of the clock transition is then measured with and without an overlapping tune-out beam, such that the Stark shift can be determined by the difference of the two measured frequencies of the clock transition. This is performed for different intensities of the tune-out light, which shows a linear behavior and allows an extraction of the polarizability from the slope of a linear fit.

3.2.1 Clock laser beam implementation

For this measurement, we need to excite strontium atoms from the g to the e state to measure the Stark shift on the clock transition, which required us to work with ⁸⁷Sr, the fermionic isotope. Therefore, we prepare a sample of atoms in the same lattice setup as described in 3.1.4, but with a larger tune-out beam, with a $1/e^2$ waist of 300 μm, to ensure a more uniform AC Stark shift over the atomic cloud. In addition, we need to apply clock laser light to the atoms, which would be ideally sent parallel to the lattice axis to ensure reliable excitation of the e clock state. As the lattice retro-reflector at the bottom did not transmit clock light and sending it from the top would thus cause an unwanted standing wave, it seemed favorable to us too apply the clock light from the bottom along the magic-wavelength lattice [Fig. 3.3 (a)]. In that scenario, the clock laser beam had to pass the mirror in free-space at the cost of a $3.5\,°$ angle with respect to the lattice axis. We overlap the clock laser light with the magic-wavelength lattice at the position of the atoms. In Fig. 3.7 (a), we show a typical sideband spectrum of the clock transition, which is consistent with a ~ 1 μK temperature of the atoms.

3.2.2 Stark shift measurement

Attempts to observe Rabi oscillations on the carrier of the clock transition showed strongly damped Rabi oscillations [Fig. 3.7 (b)]. We attribute this to the $3.5\,°$ angle between the clock laser wave vector and lattice axis, driving transition between a variety of different motional states in the trap, which consequently leads to dephasing of the Rabi oscillations. However, from this data we determined a 0.3 ms illumination time to excite as many
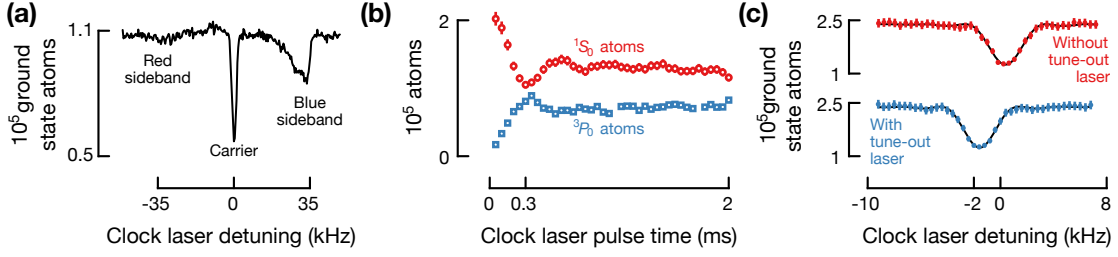
Fig. 3.7 (a) Clock line spectrum in the magic-wavelength lattice. The suppression of the red to the blue sideband is consistent with a temperature of $\sim 1\ \mu\text{K}$. (b) The relative angle of the $3.5\,^\circ$ between the lattice axis and the clock laser wave vector leads to quick dephasing of Rabi flops on the carrier. (c) The large-waist tune-out laser beam shifts the clock line (pulse time $300\ \mu\text{s}$) homogeneously. Fits are shown in black.

atoms as possible. As shown in Fig. 3.7 (c), this illumination applied over a spectrum of $20\ \text{kHz}$ leads to dips in the g state atom number, which we fit with a solution to the optical Bloch equations to extract the corresponding center frequency of the transition with and without the overlapping tune-out lattice [120].

3.2.3 Intensity calibration

The Stark shift spectroscopy heavily relies on the applied intensity of the tune-out light: the corresponding shift at the tune-out frequency $\omega_t/2\pi$ is given by the product of the real part of the polarizability at the tune-out wavelength $\alpha_e(\omega_t)$ with the intensity I according to [60]

$$\hbar\Delta\omega = -\frac{1}{2\epsilon_0 c}\alpha_e(\omega_t)I\,. \tag{3.16}$$

As power measurements and beam size calculations would be too imprecise at the position of the atoms, we directly determined the intensity by measuring the Rabi frequency of Rabi oscillations on the $^1\text{S}_0$–$^3\text{P}_1$ transition with the atoms. Actually, we will show that the intensity does not have to be determined directly and we use the measured Rabi frequency to extract the polarizability $\alpha_e(\omega_t)$.

As the data shown in Fig. 3.7 (b) was not suitable to extract (at least a single) Rabi frequency, we chose to drive Rabi oscillations on the $^1\text{S}_0$–$^3\text{P}_1$ transition on ^{88}Sr (at the same position as the ^{87}Sr atomic cloud) with a resonant probe beam of $689\ \text{nm}$ light. The Rabi frequency measurement is performed after releasing the atoms from the trap by diabatically switching off the lattice. The choice of the bosonic isotope simplified this measurement significantly due to the lack of hyperfine structure. The probe beam had a power of $P_0 = 112\ \mu\text{W}$ and was using the same optical path as the clock laser light. Before measuring the Rabi frequency, we aligned a bias magnetic field of $3.6\ \text{G}$ such that the quantization axis of the atoms was orthogonal to the clock laser polarization. As a result (or indicator for the magnetic field orientation), Rabi oscillations on the π transition completely vanished and we were left with the effect solely on the σ^+ and σ^- transition, which where Zeeman-split by applying $3.5\ \text{G}$ along the z axis [Fig. 3.8 (a)].
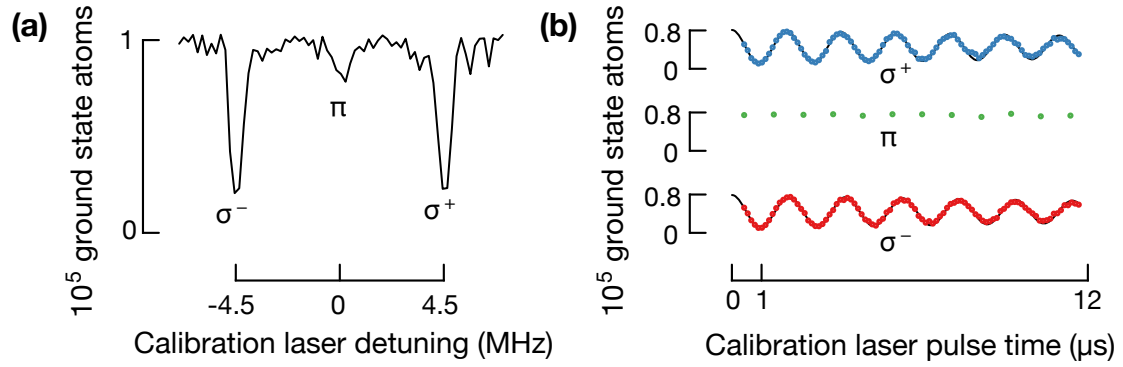
Fig. 3.8 (a) Free-space spectrum of the ${}^1S_0$– ${}^3P_1$ transition using the same optical path as the tune-out beam with a bias magnetic field of 3.5 G. The relative strength of the three transitions is determined by the driving beam polarization with respect to the quantization axis. (b) Rabi oscillations on the ${}^1S_0$– ${}^3P_1$ transition: after aligning the magnetic bias field with the driving beam wave vector, the π component vanishes, while the $\sigma^\pm$ components have well-matched amplitudes. Fits are shown in black.

Fitting the Rabi oscillations with a damped-oscillation model yielded Rabi frequencies Ω_+ and Ω_- [Fig. 3.8 (b)]. Combining these two in a quadratic manner to a probe beam Rabi frequency $\Omega_0{}^2 = \Omega_+{}^2 + \Omega_-{}^2$ allowed us to determine the Rabi frequency Ω by measuring the power P of the applied tune-out light via

$$\Omega = \Omega_0 \sqrt{\frac{P}{P_0}} \,. \tag{3.17}$$

Note that for the measurement of P it is important to suppress background light and use a precise power meter which you can trust. We additionally measure the Rabi frequency Ω_0 without bias magnetic field as a consistency check.

3.2.4 Extraction of the polarizability

To extract $\Delta\omega$ from the Stark shifts, we briefly derive a relation between the measured shift and applied power of the tune-out light: our goal is now to express I in Eq. (3.16). Thus, we use the definition of the saturation parameter [58]

$$s_0 = \frac{I}{I_{\text{sat}}} = \frac{2\Omega^2}{\Gamma_{{}^3P_1}{}^2} \,, \tag{3.18}$$

where $\tau_{{}^3P_1}$ is the $1/e$ lifetime of the ${}^3P_1$ state, which is reciprocally related to the decay rate of the ${}^3P_1$ state $\Gamma_{{}^3P_1}$. The saturation intensity of a two-level system is [58]

$$I_{\text{sat}} = \frac{\pi h c}{3\lambda^3 \tau_{{}^3P_1}} \,, \tag{3.19}$$
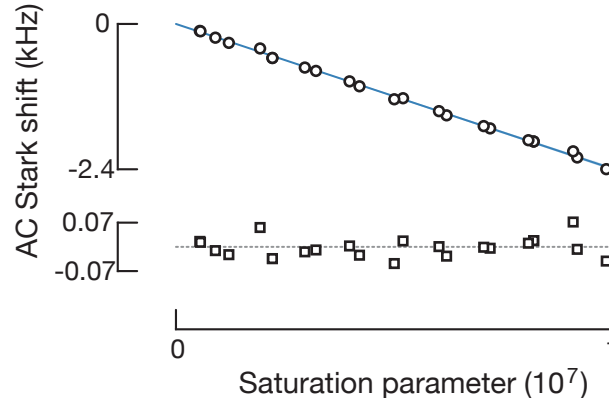
Fig. 3.9 The AC Stark shift on the $^3P_0$ state due to the tune-out laser beam versus the saturation parameter (circles), obtained from Rabi flops. The polarizability α_{3P_0} can be extracted from the slope of the fit shown in blue. Resisudals are shown in squares.

which we use as an approximation for driving the $^1S_0$– $^3P_1$ transition in ^{88}Sr. Here, λ is the wavelength of the $^1S_0$– $^3P_1$ transition. When both equations are combined and solved for I, Eq. (3.16) becomes

$$\Delta\omega = -\frac{1}{12\pi\epsilon_0 c^3}\omega_{3P_1}{}^3\tau_{3P_1}\alpha_e(\omega_t)\Omega_0{}^2\frac{P}{P_0}.$$

(3.20)

All quantities in this expression are measured: we use $\tau_{3P_1} = 21.28(3)$ ns and $\omega_{3P_1} = 2\pi \times 434,829,059,124,500$ Hz from literature [115, 48, 116], while Ω_0, P_0 and P are measured by us. We calculate $\omega_{3P_1}/2\pi$ by taking the ^{88}Sr $^1S_0$– $^3P_1$ transition frequency and adding the ^{88}Sr $\rightarrow$ ^{87}Sr isotope shift. A plot of the Stark shift versus the saturation parameter is shown in Fig. 3.9, which allowed us to extract the polarizability from the slope of the fit. We found

$$\alpha_e(\omega_t) = 1555 \pm 8_{\text{stat}} \pm 2_{\text{sys}} \text{ a.u.}$$

(3.21)

Our measurement agrees well with the theoretical prediction of $1546(14)$ a.u., which M.S. Safronova and S.G. Porsev based on reference [121].

3.3 Attempts to measure the excited state tune-out wavelength

As our method to measure the tune-out wavelength could be applied to thermal gases and did not require quantum degeneracy, we tried to measure the $^3P_0$ tune-out wavelength with ^{88}Sr at 632.83 nm [30]. As Bose-Einstein condensates with $^3P_0$ strontium atoms would suffer from inelastic e-e collisions [109, 110], methods such as Kapitza-Dirac scattering cannot be applied [106].

Additional to the setup described in subsection 3.1.3 we implemented a horizontal deep magic-wavelength lattice beam. We wanted to be able to work with a 2D lattice setup to

reduce the strong e state collisions, of which we have seen indications before. In the 2D lattice atoms are trapped in tubes instead of pancake-shaped lattice sites and therefore cannot interact with atoms on adjacent lattice sites as tunneling processes at this lattice depth are strongly reduced. We implemented the horizontal lattice beam with a power of $540\,\mathrm{mW}$. By taking modulation spectra as shown in Fig. 3.4, we found a longitudinal trap frequency of $\nu_{\mathrm{trap}} = 60\,\mathrm{kHz}$ and a transverse trap frequency of $\nu_{\mathrm{radial}} = 160\,\mathrm{Hz}$ which yields a beam radius at the atoms of $69\,\mu\mathrm{m}$.

For comparison, we measured the atomic lifetime of e state $^{87}\mathrm{Sr}$ atoms in the horizontal 1D lattice first. By using clock laser pulses as described in 3.2.1, we initially excited 1×10^5 atoms to the e state and cleared out remaining g state atoms by scattering with resonant $461\,\mathrm{nm}$ light. Without any modulation, decay spectra for the 1D lattice showed dominating two-body losses which we fit with a solution for the rate equation $\dot{N} = -bN^2$, i.e.

$$N(t) = N_0 \frac{1}{1 + N_0 bt} \, . \tag{3.22}$$

Here, N_0 is the initial atom number, b the two-body loss coefficient and t is time. In the one-dimensional lattice, we found $b_{\mathrm{1D}} = 6.23(13) \times 10^{-5}\,\mathrm{1/s}$. When turning on the near-vertical magic-wavelength axis we found a reduced two-body loss coefficient $b_{\mathrm{2D}} = 3.23(7) \times 10^{-5}\,\mathrm{1/s}$. The improvement of the two-body coefficient by a factor of $1/2$ is marginal. It can be explained by reduced tunneling opportunities in the 2D lattice, while the density in the tube-shaped lattice sites is increased and atoms can still collide.

In addition to that, we assumed that atoms in the outer trap region could still be trapped in pancakes and therefore show the same loss behavior as before. We introduced a "handover" lattice sequence where we ramped both lattice beams after each other down and up again, while keeping the other lattice beam on. By this, we dropped the atoms trapped in pancakes in outer regions and kept the atoms that actually stayed in the tubes. However, after this sequence the atoms had a final temperature of $\sim 2\,\mu\mathrm{K}$, which was independent of the ramp time $1 - 10\,\mathrm{ms}$ and linear or exponential ramp shapes. We found an increased two-body loss coefficient of $b_{\mathrm{ho}} = 1.29(6) \times 10^{-4}\,\mathrm{1/s}$ due to the higher temperatures, a higher tunneling rate in higher motional states and thus an enhanced collision rate.

As heating would lead to a higher temperature, we tried obtaining a signal for heating based on the two-body loss coefficient b. In this experiment, we used a 2D lattice without the handover sequence and modulated the horizontal beam by a small fraction ε, as shown in Fig. 3.10. The two-body loss coefficient changes with the varying relative modulation depth ε, but the signal has to be related to the $^3\mathrm{P}_0$ polarizability slope at the e state tune-out wavelength.

From Fig. 1.2, we find a (negative) slope of $\sim 12.5\,\mathrm{a.u./nm}$ at $633\,\mathrm{nm}$ and the polarizability of the magic wavelength to be at $\sim 250\,\mathrm{a.u.}$. From Fig. 3.10 we find that the relative modulation depth at the tune-out wavelength has to be roughly $\varepsilon = 1\,\%$ to distinguish the two-body loss coefficient with the modulated lattice by roughly an error bar from the atom loss without modulation. With lattice beam parameters and Eq. (1.9), we find the lattice depth of the magic lattice to be $\sim 75\,\mathrm{E_{rec}}$ yielding a necessary modulation depth of $0.75\,\mathrm{E_{rec}}$. At the same beam radius we need to detune the $633\,\mathrm{nm}$ laser with an
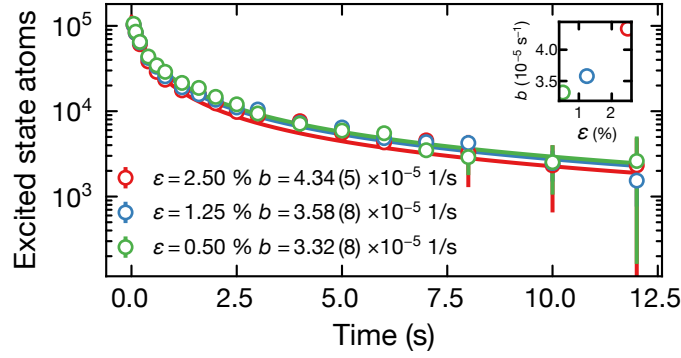
Fig. 3.10 Lifetime measurements of $^3P_0$ atoms when modulating a 2D magic-wavelength lattice with relative modulation depth ε. Inelastic two-body collisions are dominating the decay process, but show significant differences in the two-body coefficient b.

available power of $20\,\mathrm{mW}$ by $17\,\mathrm{nm}$ to obtain a comparable signal. The laser diode of our $633\,\mathrm{nm}$ laser (or any other diode laser) is not tunable by such a large range and the resolution of our spectroscopic measurement would still be on the $\sim 1\,\mathrm{nm}$ level when fitting suitable functions to the data. For these reasons, we decided to not further pursue this method and it might be better to use the theoretical value from Ref. [30]. In conclusion, we found the strong two-body collisions to be a limiting factor of our novel measurement technique.

3.4 Trapping excited atoms at the tune-out wavelength

At the tune-out wavelength, g state atoms cannot be trapped anymore due to the vanishing g state polarizability. As the polarizability of the e state is non-zero and well-known from our measurements in section 3.2, it is important to check how well e state atoms can be controlled, or in other words, how long we can trap them. Therefore, we prepare a sample of ^{87}Sr atoms in the magic-wavelength lattice, of which we excite about $70\,\%$ to e state using a $10\,\mathrm{ms}$ long adiabatic-rapid-passage pulse.

After another $2\,\mathrm{ms}$, we diabatically switch on the tune-out lattice, where we have $64\,\mathrm{mW}$ of optical power available for this experiment. To achieve this optical power, we send the tune-out laser beam through a tapered amplifier (TA) and filter it by the same grating as mentioned in subsection 3.1.4, send it trough an AOM and into an optical fiber, which leads to the lattice setup.

After an additional $1\,\mathrm{ms}$, we ramp down the magic-wavelength lattice over $10\,\mathrm{ms}$ and retain $80\,\%$ of the e state atoms in the tune-out lattice. We hold the atoms in the tune-out lattice for a given time, before we turn it off diabatically. Next, we repump the atoms over $2\,\mathrm{ms}$ [77] to the g state and take an absorption image to determine the final atom number.

Note that care was taken to match the trap frequencies of the tune-out and magic-wavelength lattices to $\sim 40\,\mathrm{kHz}$, as well as overlapping the both lattices, such that the
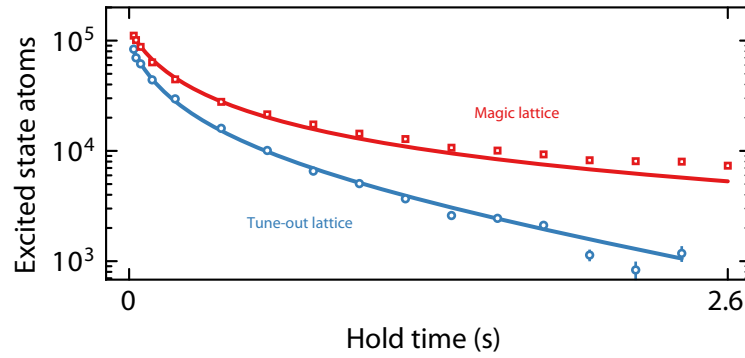
Fig. 3.11 Number of e state atoms versus hold time in a one-dimensional optical lattice at the magic wavelength (squares) and at the tune-out wavelength (circles). Both lattices exhibit the expected losses due to inelastic collisions, while the tune-out lattice additionally exhibits exponential one-body decay due to light scattering.

position and size of the trap region matches on the order of micrometers. As a result, the temperature increase during the transfer of the e state atoms was moderate with a final temperature of $3\ \mu$K in the tune-out lattice.

The e state atom number for different hold times in the tune-out and magic-wavelength lattice is shown in Fig. 3.11. In both cases, we observe superexponential decays due to e-e state atom collisions. In the magic-wavelength lattice this inelastic loss dominates, while the atoms in the tune-out lattice experience additional exponential loss with a $1/e$ lifetime of ~ 1.2 s in a $\sim 17\ \mathrm{E_{rec}}$ lattice. The scattering process of tune-out lattice photons of e state atoms is dominated by the 10 nm detuned $^3\mathrm{P}_0$– $^3\mathrm{S}_1$ transition. With a branching ratio of $\sim 1{:}9$ of this transition, almost every scattered photon leads to an atom lost to a different electronic state. Our estimate takes also other excited states into account and yields a lattice lifetime of 1.4 s, which is consistent with the measured lifetime. As the scattering rate would linearly decrease with the intensity of the lattice, a compromise between lattice depth and tunneling rate needs to be found depending on the application. For instance, trapped e state atoms in a two-dimensional tune-out lattice in a Mott insulator state would have a lifetime of ~ 1 s.

3.5 Determination of atomic lifetimes

Our measurement of the tune-out wavelength strongly constrains the relationship between the $^1\mathrm{S}_0$– $^1\mathrm{P}_1$ and $^1\mathrm{S}_0$– $^3\mathrm{P}_1$ matrix elements. An explanation for this can be given by understanding that the tune-out wavelength is determined by the two mentioned transitions as the main contributors: the $^1\mathrm{S}_0$– $^1\mathrm{P}_1$ transition causes an overall polarizability background, while the contribution from the $^1\mathrm{S}_0$- $^3\mathrm{P}_1$ transition cancels it in the ~ 143 GHz-detuned vicinity of the tune-out wavelength. Note that other minor contributions to the polarizability background from the core shells and other accessible transitions from the g state exist, which are on the few percent level and need to be included for

completeness.

This allows us to cross-check the $^1\mathrm{P}_1$ and $^3\mathrm{P}_1$ lifetimes, $\tau_{1\mathrm{P}_1}$ and $\tau_{3\mathrm{P}_1}$, respectively. While the best experimental determination for $\tau_{3\mathrm{P}_1}$ results from a direct measurement [48], $\tau_{1\mathrm{P}_1}$ comes from photoassociative spectroscopy [122, 123]. Combining our measurement with the directly measured $\tau_{3\mathrm{P}_1}$ [48] and other background contributions, we find $\tau_{1\mathrm{P}_1} = 5.234(8)$ ns. This yields a 7σ discrepancy with the currently accepted value [123].

With M.S. Safronova's and S.G. Porsev's help, we were able to use our result for the polarizability in section 3.2 to revise the $^3\mathrm{P}_0$– $^3\mathrm{S}_1$ lifetime. In fact, this transition is the main contributor with a portion of 87 %. Other contributions were determined with an uncertainty of 4 a.u. by using a high-precision relativistic method [121]. The matrix element of $^3\mathrm{P}_0$– $^3\mathrm{S}_1$ transition was then determined with the usage of our measurement of α_e, which was presented in section 3.2. The lifetime $\tau_{3\mathrm{S}_1}$ is extracted from a calculation of the $^3\mathrm{S}_1$– $^3\mathrm{P}_\mathrm{J}$ branching ratios with 0.1 % accuracy. The very similar electronic correlation effects for these transitions, which largely cancel their ratios, make this accurate prediction of branching ratios possible. A lifetime $\tau_{3\mathrm{S}_1} = 13.92(11)$ ns was found, which is an improvement over one order of magnitude compared to prior measurements that ranged from $10.9(1.1)$ ns to $15.0(8)$ ns [124–126]. The branching ratios have been calculated for the $^3\mathrm{S}_1$ decay to the $^3\mathrm{P}_2$, $^3\mathrm{P}_1$, and $^3\mathrm{P}_0$ state to be 0.1162, 0.3402, and 0.5433, respectively.

The lifetime $\tau_{3\mathrm{D}_1}$ of the $^3\mathrm{D}_1$ state and $\tau_{3\mathrm{S}_1}$ are correlated, as both are extracted from a single data set [48]. This is of particular importance since the lifetime $\tau_{3\mathrm{D}_1}$ directly determines the dynamic contribution to the strontium lattice clock blackbody radiation shift [121], its currently largest systematic uncertainty. These results combined with a new direct measurement of $\tau_{1\mathrm{P}_1}$ and Ref. [48] directly improve this uncertainty. From our measurements it becomes evident that direct measurements of atomic lifetimes with improvements on atomic structure calculations are essential in pushing optical clock accuracy to the 10^{-19} level.

3.6 Conclusion

In conclusion, we have shown a novel technique to measure the g state tune-out wavelength for the strontium optical qubit. As a modulation technique for particles, this method benefits from the suppression of systematic errors and long integration times. As an evidence of that, we achieved the highest suppression in lattice depth for the g state with respect to the e state with almost five orders of magnitudes (48 dB). This method can be applied to thermal gases, molecules [127] or trapped ions.

In a one-dimensional lattice, we did not succeed in measuring the tune-out wavelength of the $^3\mathrm{P}_0$ state at 633 nm [30] due to a low signal-to-noise ratio caused by inelastic collisions of e state atoms. Applying this method in a three-dimensional lattice together with band mapping [128], however, can enable a successful measurement even in the presence of interactions. Inelastic collisions will be suppressed due to the higher lattice dimensionality. Only a single e state atom can exist during the time of the measurement per lattice site, such that we need band mapping to improve the signal-to-noise ratio to compensate for the resulting lower atoms numbers.

The high-fidelity control of the strontium optical qubit, which we have shown, removes the main obstacle for the realization of quantum computation schemes with two-valence-electron atoms [28]. Finally, new opportunities are created for quantum simulations of nanophotonics [129, 42, 44] and quantum chemistry [130].

Chapter 4

Optical Lattices in a Crossed Cavity

Cavities are a valuable and widely spread tool with many different applications in the field of atomic, molecular, and optical physics (AMO). By circulating light between mirrors thousands over thousands of times, cavities can enhance the intensity in atomic traps. The light circulation process between the cavity mirrors leads to two counter-propagating light beams which form an optical lattice potential. In this part of our work we will learn how to design and assemble buildup cavities with crossed, large, homogeneous modes, which we will use in the future to generate wide atomic traps with minimized harmonic confinement.

This chapter starts with a theoretical introduction to optical cavities to provide all necessary basics to understand the work presented in the following sections. Next, we will discuss the atomic system size at the example of a Mott-insulator. This section presents the results of a Fourier optics simulation for cavity modes and, from this, a resulting estimate for the expected system size. Next, the design and assembly of a crossed buildup cavity is described in detail and followed by the discussion of characterization methods for the mode overlap including the results, which have been achieved. The next section provides results on finesse measurements as well as a discussion of the achieved power enhancement. In the final section, different mounting methods of the cavity to the inside of a vacuum chamber as well as corresponding test results are presented.

4.1 Theory of optical cavities

To understand the wide range of applications and advantages of cavities, it is useful to take a closer look from the theoretical side first. In the first subsection we introduce the Fabry-Pérot interferometer. We use this interferometer to describe the cavity transmission and how we can relate it to the intensity circulating inside the cavity. During this derivation, we will naturally discover the concepts of the free spectral range and the finesse. We will derive the reflection at cavities in the second subsection, which cannot be trivially deduced from the transmission. The next subsection illuminates the concept of the cavity ring-down time and relates it to the cavity finesse. We briefly introduce higher-order Hermite-Gaussian modes in the following subsection. The focus will be on the lowest order mode, the Gaussian mode, which introduces the concept of Gaussian beams as well. The next subsection explains the causes of mode shifts in cavities, and, in the final subsection, we focus on loss measurements and power enhancement inside the cavity.

4.1.1 Transmission and finesse

We take a look at the light transmission through the cavity first. This and the following derivations are based on models which are well-covered in textbooks such as Refs. [131, 132]. We introduce a typical Fabry-Pérot interferometer with two flat mirror surfaces, 1 and 2. Each of them has an amplitude reflection, transmission, and loss coefficient, r_j, t_j and l_j, respectively[1] [Fig. 4.1 (a)]. In general, we keep all quantities complex to handle passage through a medium with finite thickness or a finite penetration depth when reflected. Note that we always have to check if light gets reflected at an optically denser surface and manually change the sign in front of the corresponding reflection amplitude coefficient r_j. For any mirror surface j, the following relation holds

$$|r_j|^2 + |t_j|^2 + |l_j|^2 = 1 \,. \tag{4.1}$$

With this framework in mind, we can now take a detailed look at the following transmission process: to observe any transmission, we initially require an electric light field $E_i(t) = E_0 \exp(i2\pi\nu t)$ that is incident on the first mirror surface, where E_0 is the amplitude of the field, ν is the optical frequency, and t is time. The electric field $E_i(t)$ is transmitted through the first mirror, where it is multiplied by an amplitude transmission coefficient t_1. Inside the cavity, the field travels along an effective distance of nL, where n is the index of refraction in the medium between the mirrors and L the distance between both reflecting mirror surfaces. The field is then reflected with an amplitude reflection coefficient r_2, and it travels back along nL once more before getting reflected again with an amplitude reflection coefficient r_1. From that point on the cycle repeats, while a fraction t_2 of the electric field is coupled out of the cavity on the second mirror surface. During each round trip, the field is multiplied by a factor of $r_1 r_2 \exp\left(i2\pi\frac{2nL}{\lambda}\right) = r_1 r_2 \exp\left(i2\pi\frac{2nL}{c}\nu\right)$, where λ is the wavelength of the light and we converted it to the optical frequency via $\nu = c/\lambda$. Note that we assume that no light is lost in the medium. The transmitted field can be expressed in terms of a geometrical series:

$$\begin{aligned} E_t(t) &= t_1 t_2 E_0 \exp(i2\pi\nu t) \sum_{m=0}^{\infty} r_1^m r_2^m \exp\left(i2\pi\frac{2nL}{c}\nu m\right) \\ &= \frac{t_1 t_2}{1 - r_1 r_2 \exp\left(i2\pi\frac{\nu}{\nu_{\text{FSR}}}\right)} E_0 \exp\left(i2\pi\nu t\right) \,. \end{aligned} \tag{4.2}$$

In the last step we identify the free spectral range (FSR)

$$\nu_{\text{FSR}} = \frac{c}{2nL} \,, \tag{4.3}$$

which is a fundamental property of cavities and can be understood as the number of round trips a photon undergoes inside the cavity within one second. Since optical electric

---

[1]Note that we refer to the quantities r_j, t_j and l_j as "amplitude coefficients" and to $|r_j|^2$, $|t_j|^2$ and $|l_j|^2$ as "coefficients".
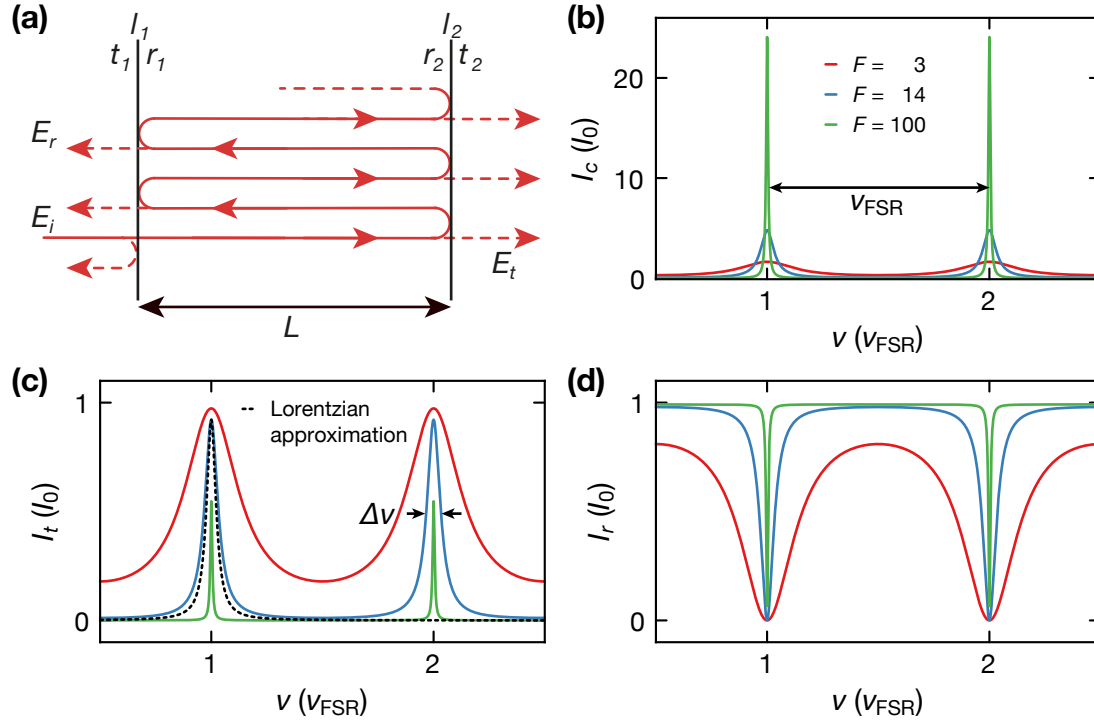
Fig. 4.1 (a) Illustration of a Fabry-Pérot interferometer with two flat mirror surfaces. An incident electric field E_i is (partly) coupled into the cavity, which then undergoes infinitely many round trips inside. At each mirror, some light is coupled out and contributes either to the transmitted field E_t or reflected field E_r via constructive or destructive interference. (b) Circulating intensity I_c inside the cavity. Red, blue and green curves show spectra for different finesses and reveal Lorentzian-like resonance peaks which are separated by ν_{FSR}. Our model assumes a symmetric cavity with reflectivities of $r^2 = (0.4, 0.8, 0.9693)$ with a fixed loss coefficient of $l^2 = 0.8\,\%$. The highest reflectivity (finesse) yields the highest enhancement. (c) Transmitted intensity spectrum I_t for the Fabry-Pérot interferometer. Shown are resonance peaks with a full-width-maximum (FWHM) of $\Delta\nu$ (shown on the blue graph). The dotted curve shows the Lorentzian approximation for the blue curve. We see that I_t is reduced when l becomes comparable to t. (d) The reflected light intensity I_r is not influenced by the loss as much as I_t, since most of the light loss happens inside the cavity after light is coupled in.

fields are difficult to measure directly, we need to compute the transmitted intensity $I_t(t) = \frac{1}{2}cn\epsilon_0|E_t(t)|^2$. We find

$$I_t(\nu) = \frac{|t_1|^2|t_2|^2}{1 + |r_1|^2|r_2|^2 - 2|r_1||r_2|\cos\left(2\pi\frac{\nu}{\nu_{\text{FSR}}} + \phi_1 + \phi_2\right)}\frac{1}{2}cn\epsilon_0|E_0|^2\,, \tag{4.4}$$

where we have separated the complex reflection coefficients into amplitude and phase, i.e. $r_j = |r_j|\exp(i\phi_j)$. In the following we assume ideal mirrors and set all transmission and reflection amplitudes to be real numbers, yielding $\phi_1 = \phi_2 = 0$ in Eq. (4.4). Another important aspect to understand is that the maxima, or better, the resonances of this function are periodic in ν with periodicity ν_{FSR}, because of the periodicity of the cosine function [Fig. 4.1 (b)]. We illustrate this behavior by recalling that photon round trips periodically repeat in time which thus leads to a FSR-spaced grating in frequency space. For future purposes, we approximate the denominator in Eq. (4.4) up to second order around the resonance (a multiple of ν_{FSR}) and factorize it

$$I_t(\delta) = \frac{t_1{}^2 t_2{}^2}{(1 - r_1 r_2)^2 + r_1 r_2\left(\frac{2\pi\delta}{\nu_{\text{FSR}}}\right)^2}I_0\,, \tag{4.5}$$

where we replaced $\frac{1}{2}cn\epsilon_0|E_0|^2$ with I_0 and $\delta \equiv \nu - s\nu_{\text{FSR}}$ ($s \in \mathbb{N}_0$), is the frequency deviation from the n-th cavity resonance. Here we recognize that the lineshape I_t close to the resonance $\delta = 0$ is Lorentzian with a full-width-half-maximum (FWHM) of $\Delta\nu = \nu_{\text{FSR}}\frac{1-r_1 r_2}{\pi\sqrt{r_1 r_2}}$. This means that for narrow linewidths, i.e. $\Delta\nu \ll \nu_{\text{FSR}}$, we can treat cavity resonances as Lorentzian functions [Fig. 4.1 (c)]. In this case we can define the finesse as

$$\mathcal{F} \equiv \frac{\nu_{\text{FSR}}}{\Delta\nu} = \frac{\pi\sqrt{r_1 r_2}}{1 - r_1 r_2}\,, \tag{4.6}$$

where the second equal sign leads to the well-known expression of the finesse in terms of the mirror reflectivities. Keep in mind that this expression is a result of an approximation and does not apply to low finesse cavities. In the high finesse regime it is a quantity solely stemming from the reflectivity of the mirror pair and is independent of transmission and losses. From Eq. (4.4) we directly see, as t_1 and t_2 approach zero, that the amount of transmitted light will be reduced while the finesse is unchanged.

For buildup cavities in particular, we want to know what the circulating intensity I_c inside the cavity is. It can be determined from

$$I_c = I_t/t_2{}^2\,, \tag{4.7}$$

where we use the fact that light is coupled out by passing the second mirror. This seems like a trivial step, but is actually very powerful: from Fig. 4.1 (b) and (c) we can compare the transmission I_t through a cavity against the circulating intensity I_c inside. We look at symmetric (low finesse) cavities with a fixed loss coefficient. To increase the finesse, we increase the reflection coefficient, which consequently decreases the transmission coeffi-

cient and leads to a significant reduction of the transmitted intensity I_t. In other words, the losses are becoming more and more comparable to the transmission and we lose light in the cavity rather than transmitting it. However, I_c greatly benefits from the higher reflectivities. This emphasizes that buildup cavities profit from large reflectivities to build up the intensity I_c. On the other hand, for filter cavities which filter and transmit as much light as possible, negligible losses are necessary.

Be aware that any derivation so far relied on the assumption of a plane wave, which can be extended by adding a transverse field distribution to the field (which usually depends on the position in the cavity). We can easily convert Eq. (4.2), (4.4) and (4.7) to obtain equations for power by integrating over the transverse cross section, i.e. $P = \int I(A)\mathrm{d}A$, which is the quantity we measure.

4.1.2 Reflection

For completeness, we also want to deduce the reflected part of the field from the cavity. Here we have to take into account that there is already a part of the field directly reflected at the first mirror which is multiplied by the amplitude reflection r_1. The light which passes through the first mirror is multiplied by t_1, than travels a distance nL and is reflected at the second mirror inside the cavity (where it is multiplied by r_2) before it travels back. As a fraction t_1 of the light field is transmitted at the first mirror again, the reflected part undergoes another round trip. Just as before, the electric field is multiplied by a factor $r_1 r_2 \exp\left(i2\pi \frac{2nL}{c}\nu\right)$ for each round trip. We find the reflected electric field

$$
\begin{aligned}
E_r(t) &= r_1 E_0 \exp\left(i2\pi\nu t\right) + \frac{r_2 t_1{}^2 \exp\left(i2\pi \frac{\nu}{\nu_{\mathrm{FSR}}}\right)}{1 - r_1 r_2 \exp\left(i2\pi \frac{\nu}{\nu_{\mathrm{FSR}}}\right)} E_0 \exp\left(i2\pi\nu t\right) , \\
&= \frac{r_1 + r_2(r_1{}^2 + t_1{}^2) \exp\left(i2\pi \frac{\nu}{\nu_{\mathrm{FSR}}}\right)}{1 - r_1 r_2 \exp\left(i2\pi \frac{\nu}{\nu_{\mathrm{FSR}}}\right)} E_0 \exp\left(i2\pi\nu t\right) .
\end{aligned}
\tag{4.8}
$$

For a typical cavity with glass mirror substrates and reflective surfaces facing each other, the input light would have to pass through the glass first before it gets reflected and thus would experience no π-phase shift. Since parts of the light field, that are coupled out of the cavity always undergo an odd number of reflections in the cavity, the minus sign is always present. For this case we have to change the sign in front of $r_2 t_1^2$ in the first line and in front of $(r_1^2 + t_1^2)$ in the second line.

For completeness, we give the reader the reflected intensity $I_r(\nu)$. To keep it simple, we again set all transmission and reflection amplitudes to their modulus, to only deal with real values. We find

$$
I_r(\nu) = \frac{r_1{}^2 + r_2{}^2(r_1{}^2 + t_1{}^2)^2 + 2r_1 r_2(r_1{}^2 + t_1{}^2)\cos\left(2\pi \frac{\nu}{\nu_{\mathrm{FSR}}}\right)}{1 + r_1{}^2 r_2{}^2 - 2r_1 r_2 \cos\left(2\pi \frac{\nu}{\nu_{\mathrm{FSR}}}\right)} I_0 .
\tag{4.9}
$$

An illustration of I_r can be found in Fig. 4.1 (d). Note that for losses which are non-zero, I_t and I_r never add up to I_0. For every transmission through a mirror and, more importantly, for every round trip, some light is lost. The relative amount of lost light grows with higher loss coefficients or, when we keep the losses fixed, an increase of the number of round trips (which scales with the finesse).

4.1.3 Cavity ring-down time

In this section we briefly derive an important estimate for the cavity ring-down time, since it is often used to measure the finesse of cavities. We refer to the cavity ring-down time as the $1/e$ lifetime of a photon inside the cavity before it is lost. Consequently, we need to understand how the finesse is related to the cavity ring-down time. We consider the Fabry-Pérot interferometer as before, but directly start our derivation with a circulating intensity $I_c(t_0)$ inside the cavity. We are not interested in the phase of the field and can directly focus on the process of on-resonant light intensity being coupled into and out of the cavity. Therefore, we relate the difference in circulating intensity for one round trip $\Delta I_c(t) = (1 - |r_1|^2|r_2|^2)I_c(t)$ to the time for one round trip $\Delta t = \frac{2L}{c} = 1/\nu_{\text{FSR}}$ and obtain the differential equation

$$\dot{I}_c(t) \approx \frac{\Delta I_c}{\Delta t} = -\left((1 - |r_1|^2|r_2|^2)\nu_{\text{FSR}}\right) I_c(t), \tag{4.10}$$

with the well-known solution

$$I_{\text{in}}(t) = \left(1 - \exp\left(-\frac{t}{\tau}\right)\right) I_{0,\text{in}}$$

$$I_{\text{out}}(t) = \exp\left(-\frac{t}{\tau}\right) I_{0,\text{out}}, \tag{4.11}$$

where $I_{0,\text{in}} = I_{\text{in}}(t \to \infty)$ and $I_{0,\text{out}} = I_{\text{out}}(t_0 = 0)$. We identify the cavity ring-down time

$$\tau = \frac{1}{\kappa} = \frac{1}{(1 - |r_1|^2|r_2|^2)\nu_{\text{FSR}}} \approx \frac{1}{2(1 - |r_1||r_2|)\Delta\nu\mathcal{F}} \tag{4.12}$$

where we used the assumption $|r_i|^2 \approx 1$, Eq. (4.6), and wrote the cavity ring-down time in terms of a decay rate κ. Looking at this expression and comparing it with Eq. (4.6) where we can approximate $\sqrt{|r_1||r_2|} \approx 1$, we find

$$2\pi\Delta\nu = \kappa. \tag{4.13}$$

This result shows that the width of the cavity resonance is a direct measure of the photon decay rate in the cavity. To measure the finesse of a cavity, one can observe an exponential decay $I_{\text{out}}(t)$ as a leakage through the cavity to perform a well-known "cavity ring-down measurement". With the cavity ring-down time the finesse can be calculated via

$$\mathcal{F} = 2\pi\tau\nu_{\text{FSR}}. \tag{4.14}$$

It is interesting to consider the Fourier spectrum of $I_{\text{out}}(t)$. This requires a Fourier transform of the signal, yielding

$$\mathcal{F}_t \left[I_{\text{out}}(t) \right](\nu) = I_{0,\text{out}} \int_{-\infty}^{\infty} \exp\left(-\kappa|t|\right) \exp\left(-i2\pi\nu t\right) \mathrm{d}t = \frac{1}{\pi} \frac{\kappa/2\pi}{\nu^2 + (\kappa/2\pi)^2} I_{0,\text{out}} \,, \quad (4.15)$$

where we also see that cavity resonances in frequency space are Lorentzians with width $\kappa/2\pi$.

With Eq. (4.14) we deduce how many round trips a photon will undergo in the cavity on average, before it is lost: τ is the lifetime in the cavity, while $1/\nu_{\text{FSR}}$ is the time a photon needs for a full round trip. When we divide these two quantities, we find $\mathcal{F}/2\pi$ as the average number of round trips of a photon in the cavity.

4.1.4 Hermite-Gaussian modes

In the previous sections we focused on basic resonances in the cavity which were derived with the assumption that light is reflected at two plane mirrors. In fact, two plane mirrors would neither restrict nor select any transverse field or extent. Two plane mirrors, however, do not form a stable cavity as any relative angle between the mirrors leads to a walk-off of the light beam which eventually escapes from the cavity by geometrical constraints. Since instable cavities are not very useful in most cases it is practical to break this transverse symmetry by using concave mirror shapes. These geometries cause light to circulate in the cavity and provide spatial confinement which allows more round trips for photons and therefore higher achievable finesses. As one can guess there might be different beam paths which are resonant in the cavity by including the transverse geometries. An accurate description of these resonances is given by the theory of Hermite-Gaussian modes. At this point we omit a full derivation since it can be found in any standard optics textbook, for example reference [131]. The solution for an nm higher-order Hermite-Gaussian mode electric field propagating in the Z-direction is given by

$$E_{nm}(\boldsymbol{r}) = E_0 \frac{w_0}{w(z)} \frac{1}{\sqrt{2^{n+m}n!m!}} H_n\left(\frac{\sqrt{2}x}{w(z)}\right) H_m\left(\frac{\sqrt{2}y}{w(z)}\right) \exp\left(-\frac{r^2}{w^2(z)}\right) \exp\left(i\phi_{nm}\right) \,,$$

$$\phi_{nm} = kz - (1+n+m)\arctan\left(\frac{z}{z_R}\right) + k\frac{r^2}{2R(z)} \,,$$

$$(4.16)$$

which we call transverse-electric-modes-nm (TEM_{nm}) from now on. Note that the term "transverse" refers to the polarization of the light which, in the derivation, is assumed to be orthogonal with respect to the propagation axis. Here, w_0 is the waist of the mode,

which is the smallest value of the $1/e^2$ beam (intensity) radius

$$w(z) = w_0 \sqrt{1 + \left(\frac{z}{z_R}\right)^2}, \tag{4.17}$$

and is found at $z = 0$ by convention. Here, H_j are the Hermite polynomials and $R(z)$ is the phase front curvature which is given by

$$R(z) = z \left(1 + \left(\frac{z_R}{z}\right)^2\right), \tag{4.18}$$

where we introduced the Rayleigh range

$$z_R = \frac{\pi w_0^2}{\lambda}. \tag{4.19}$$

Note that z_R is a fundamental property which is only determined by the waist w_0 and wavelength λ, and it sets a spatial scale on which beam parameters change significantly. For this reason, z_R is important to determine the sensitivity for positioning optics.

Examples of the lowest TEM intensities can be found in Fig. 4.2. The fields E_{nm} provide a complete basis to describe any transverse electric field which can be approximated to only change slowly along its propagation axis. Note that TEM$_{00}$ is often referred to as the "fundamental mode" or "Gaussian mode" due to its Gaussian beam profile, which becomes clear from Fig. 4.2. The solution for the Gaussian mode stemming from Eq. (4.16) is identical to the treatment of Gaussian laser beams and is described by

$$E_{00}(\boldsymbol{r}) = E_0 \frac{w_0}{w(z)} \exp\left(-\frac{r^2}{w^2(z)}\right) \exp\left[-i\left(kz + k\frac{r^2}{2R(z)} - \psi(z)\right)\right], \tag{4.20}$$

with the Guoy phase $\psi(z) = \arctan\left(\frac{z}{z_R}\right)$.

To describe eigenmodes of a certain cavity, we first have to match the beam properties with the cavity geometries. In particular this means that we have to match the radius-of-curvature (ROC) to the phase curvature of the beam, i.e. $R(z_j) = R_j$ for each mirror with ROC R_j at position z_j. For a linear cavity with two mirrors at position z_1 and z_2 we can find an expression for the mode waist in the cavity by combining Eqs. (4.17), (4.18), and (4.19). For two fixed ROCs R_1 and R_2 separated by a cavity length L, the $1/e^2$ beam waist reads [133]

$$w_0 = \sqrt{\frac{\lambda L}{\pi}} \left(\frac{g_1 g_2 (1 - g_1 g_2)}{(g_1 + g_2 - 2g_1 g_2)^2}\right)^{\frac{1}{4}}, \tag{4.21}$$

where $g_j = 1 - L/R_j$. We simplify this expression for a cavity with a curved mirror with ROC R and a flat mirror with a ROC of infinity. The equation then becomes

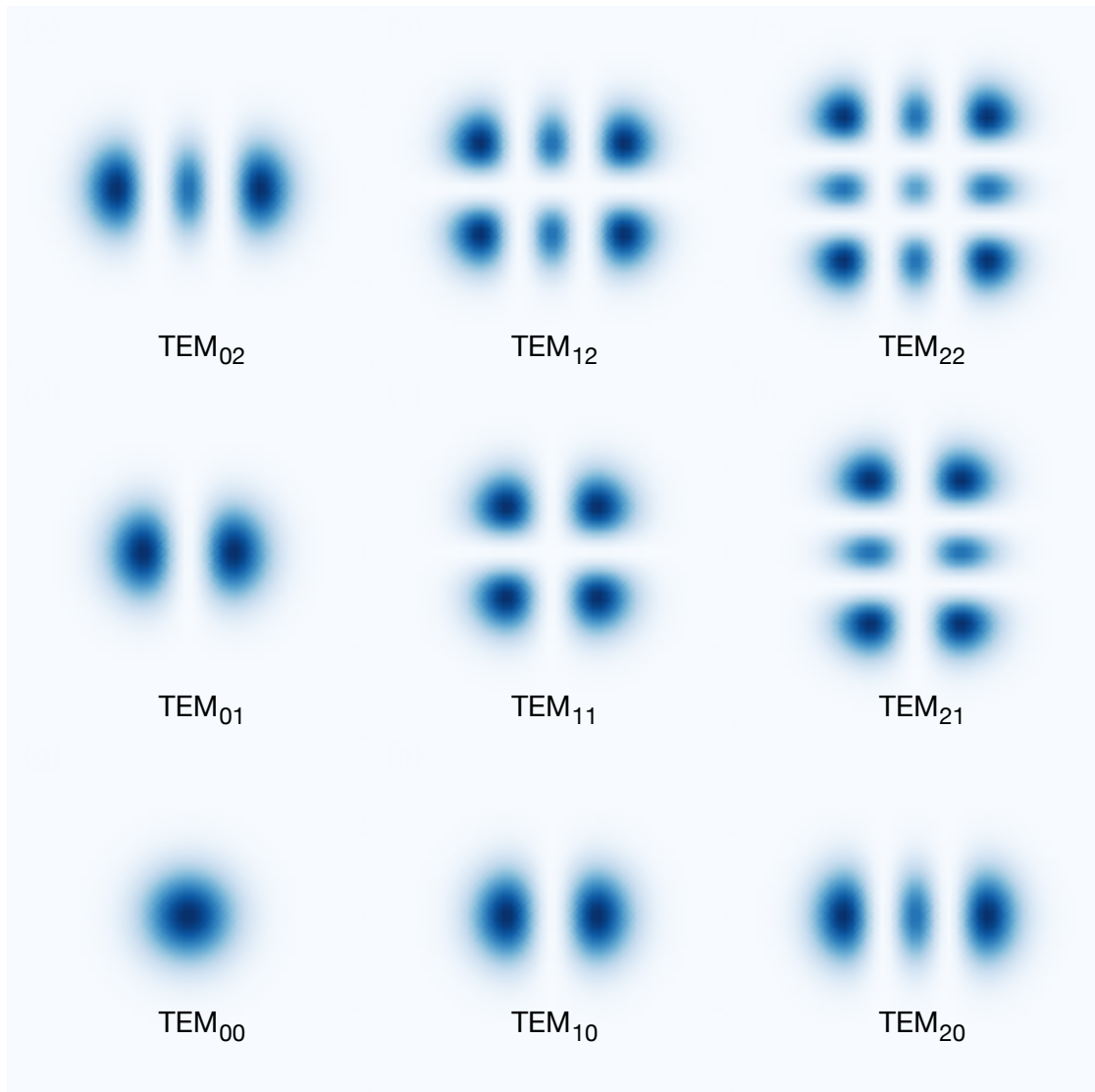$$w_0 = \sqrt{\frac{\lambda L}{\pi}} \left(\frac{R - L}{L}\right)^{\frac{1}{4}}. \tag{4.22}$$

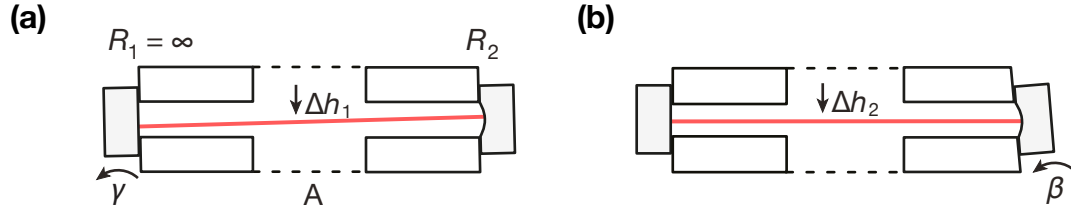**Fig. 4.2** Examples of transverse intensity distributions of higher-order Hermite-Gaussian modes.

(a) **(b)**

Fig. 4.3 A plano-concave cavity design. (a) Even with perfectly parallel surfaces, a common angle γ on both surfaces shifts the mode in the center by Δh_1. (b) A mode shift Δh_2 caused by a relative angle β between opposite surfaces on which mirrors are attached to.

For a cavity of this kind the waist will be at the flat mirror due to the flat wavefront. As an example, for a cavity with $L = 50$ mm and $R = 50$ cm we find a waist of $w_0 = 181\ \mu$m for $\lambda = 689$ nm. With the same parameters, but $R = 10.2$ m, we find $w_0 = 395\ \mu$m.

Another important aspect in this section is the mode separation. Higher-order modes very often play an important role and it is important to know their position in frequency space. It can be shown that the absolute frequency of a higher order mode nm is given in a linear cavity by [133]

$$\nu_{nmq} = \nu_{\text{FSR}} \left(q + \frac{1}{\pi}(1 + m + n) \arccos\left(\sqrt{g_1 g_2}\right) \right) , \tag{4.23}$$

Here, q indexes the corresponding resonance and we identify the mode separation frequency $\nu_{\text{sep}} = \frac{1}{\pi} \arccos\left(\sqrt{g_1 g_2}\right) \nu_{\text{FSR}}$. Note that this expression is completely independent of λ.

For a linear cavity with a flat and a curved mirror, where $L = 50$ mm we find $\nu_{\text{FSR}} = 3$ GHz in vacuum [Eq. (4.3)]. The mode separation for $R = 50$ cm of the curved mirror $\nu_{\text{sep}} = 307$ MHz, which is a fraction of 10 % of the free spectral range. For $R = 10.2$ m the mode separation is $\nu_{\text{sep}} = 66.9$ MHz, which is a fraction of 2.2 % of the free spectral range. We see that the mode frequencies become more and more degenerate, the more we approach the plane-parallel cavity regime.

4.1.5 Spatial mode shifts

In this section we address spatial mode shifts caused by angle imperfections in the specific case of plano-concave cavities. As indicated by the name, plano-concave cavities consist of a flat mirror and a curved mirror, forming a mirror pair. The plane mirror only reflects the mode at a right angle, but does not determine the position of a cavity mode. It solely sets the angle γ of the mode in space with respect to the reference surface [Fig. 4.3 (a)]. The curved mirror, however, determines the position of the mode by finding the spot in the curved region which maximizes the distance with respect to the flat mirror. Since both mirrors have separate influences on the mode position in space, we discover that individual angles of these mirrors lead to two different sources of mode shifts.

A less critical mode shift is caused by a common tilt of the two parallel surfaces which

carry the mirror pair. We can imagine tilting each mirror around an axis through its mirror center by an angle γ [Fig. 4.3 (a)]. As the mode will always be orthogonal to the flat mirror and fixed by the curved mirror, the mode center in the middle of the cavity will be shifted by

$$\Delta h_1 = L/2 \tan \gamma \,. \tag{4.24}$$

The second and more important case, is the mode shift induced by the relative angle between the two mirrors of a mirror pair. A part of this quantity is a direct contribution of the relative angle of the surfaces that the mirrors are attached to. Displacements of the spherical surface center with respect to the mirror center lead to an effective tilt, which is referred to as "wedge error". This error can also be caused by polishing imperfections assuming the mirror has a flat annulus. As shown in Fig. 4.3 (b), we visualize this relative angle case by leaving the flat mirror fixed and only imagine a tilt β of the curved mirror. We realize that only the center point of the radius-of-curvature shifts, which then determines the new spot with the maximum distance with respect to the flat mirror and thus, determines the new mode position. The expression for the mode shift is

$$\Delta h_2 = R \sin \beta \,, \tag{4.25}$$

where R is the radius-of-curvature of the curved mirror. Note that this expression is completely independent of the cavity length. Although Eq. (4.25) shows a linear dependence in R and small angles of β, we display the significance of Δh_2 by stating a few numbers: For a typical $50\,\mathrm{cm}$ radius-of-curvature we obtain a sensitivity of $2.4\,\mu\mathrm{m/arcsec}$ whereas a $10\,\mathrm{m}$ radius-of-curvature yields $48\,\mu\mathrm{m/arcsec}$. Thus, large ROCs set much tighter constraints on β when we try to carefully position cavity modes (compared to typical mode sizes of a few hundred micron).

Knowing these two causes for mode shifts, we can always split individual angles on each mirror (with respect to the reference plane A) into a common and a relative tilt. The common tilt is only given by the angle of the flat mirror with respect to reference plane A, and the relative tilt by the angle difference of the curved and flat mirror. For small angles γ, we approximate the two contributions to be decoupled and treat them separately.

4.1.6 Power enhancement and losses

We conclude this brief theory review with a few insights on power enhancement and how it is influenced by losses. This section will give a deeper understanding of buildup cavities in particular and we present a few tools to design and think about this type of cavities.

We start the discussion by looking at the cavity transmission coefficient T_cav and cavity reflection coefficient R_cav of the cavity by normalizing Eq. (4.5) and (4.9) to the input intensity while fulfilling the resonance condition. We will treat all amplitudes as real
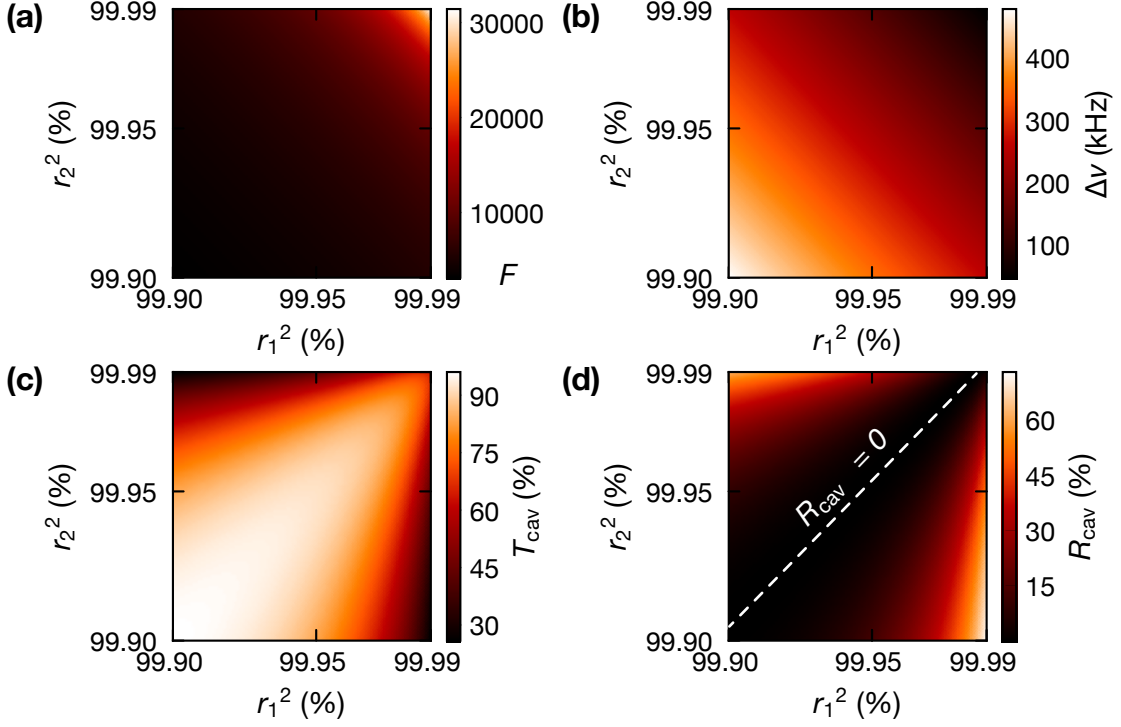
Fig. 4.4 (a) The finesse $\mathcal{F}$ of an asymmetric cavity model plotted against individual reflection co-efficients $r_1{}^2$ and $r_2{}^2$. (b) The linewidth $\Delta\nu$ of a cavity with $\nu_{\mathrm{FSR}} = 1.5\,\mathrm{GHz}$ in vacuum. For filter cavities, this linewidth directly yields its spectral filtering bandwidth. (c) The cavity transmission coefficient T_{cav} through a cavity, which is always maximal for $r_1 = r_2$. Since the model assumes losses of $20\,\mathrm{ppm}$, T_{cav} never reaches $100\,\%$. (d) The cavity reflection coefficient R_{cav} is non-zero for $r_1 = r_2$, however shows a shifted $R_{\mathrm{cav}} = 0$ contour line in which case the impedance matching condition is fulfilled.

numbers from now on. We arrive at

$$T_{\mathrm{cav}} = \frac{t_1{}^2 t_2{}^2}{(1 - r_1 r_2)^2}, \tag{4.26}$$

$$R_{\mathrm{cav}} = \frac{r_1{}^2 + 2 r_1 r_2 (r_1{}^2 + t_1{}^2) + r_2{}^2 (r_1{}^2 + t_1{}^2)^2}{(1 - r_1 r_2)^2}. \tag{4.27}$$

These expressions do *not* neglect losses and carry important information about the system, which we plot in Fig. 4.4. We find reduced values for T_{cav} for a higher asymmetry in r_1 and r_2, as well as when the loss coefficients become comparable to the transmission and reflection coefficients, respectively, i.e. $l^2 \lesssim 1 - r^2$. In fact, T_{cav} only equals one when we consider symmetric cavities, i.e. $t_1 = t_2$ and $r_1 = r_2$, without losses, i.e. $l_1 = l_2 = 0$.

Note that for asymmetric cavities it is always possible to make R_{cav} vanish completely by fulfilling the impedance matching condition $t_1{}^2 = t_2{}^2 + l_1{}^2 + l_2{}^2$, which can be understood as follows [134]: the light which is coupled into the cavity, has to be equal to the sum

of every other transmission and loss inside the cavity. Even if the reflection is zero, the transmission is not equal one, since light is lost by scattering and absorption processes in the glass substrate and coatings of the mirror.

Applying Eq. (4.7) to (4.26) leads to the enhancement coefficient

$$\Lambda = \frac{t_1{}^2}{(1 - r_1 r_2)^2} \, , \tag{4.28}$$

which allows us to simply calculate the circulating intensity I_c and power P_c in the cavity via

$$I_c = \Lambda I_i = I_t / t_2{}^2 \qquad \text{and} \qquad P_c = \Lambda P_i = P_t / t_2{}^2 \, , \tag{4.29}$$

respectively. Keeping these results in mind, we appreciate the benefits of symmetric cavities, which is why we set $r_1 = r_2 = r$, $t_1 = t_2 = t$ and $l_1 = l_2 = l$ for the rest of this subsection. With this simplification we reduce Eq. (4.28) to $\Lambda = \mathcal{F}/\pi$ whenever losses are negligible ($l^2 \ll 1 - r^2$) to be able to do quick estimates. However, losses very often are not negligible, especially when dealing with visible or UV light and $\mathcal{F} \gtrsim 10^4$.

With Eq. (4.6) we have already shown that a large value of $\mathcal{F}$ only depends on r. This means that an accurate measurement of $\mathcal{F}$ implicitly is a measurement of r, which we can extract via

$$r^2 = \left(\frac{\pi}{2\mathcal{F}} - \sqrt{\left(\frac{\pi}{2\mathcal{F}} \right)^2 + 1} \right)^2 . \tag{4.30}$$

Note that this equation does not neglect any losses or assumes further approximations, as it was already done in the derivation of Eq. (4.6). In addition, measurement of t^2 can be done, for instance by doing a transmission measurement through the mirror (or using a spectrometer). For small transmissions, an accurate power meter and a careful elimination of the background light is necessary. In addition, the power meter should be placed at a distance large enough such that scattering light at the mirror can be neglected. We then calculate the losses via

$$l^2 = 1 - r^2 - t^2 . \tag{4.31}$$

Keep in mind, that this an indirect measurement of t^2, and so is the enhancement factor, since we measure t^2 for individual mirrors. However, t^2 can also be measured directly: a laser is stabilized to a cavity and the input P_i, the transmitted $T_c P_i$ and reflected power $R_c P_i$ are measured. From Eq. (4.26) and (4.27) we use the simplification

$$\begin{aligned} T_{\text{cav}} &= \frac{t^4}{(1 - r^2)^2} \, , \\ R_{\text{cav}} &= \frac{l^4}{(1 - r^2)^2} r^2 \, , \end{aligned} \tag{4.32}$$

to determine t and l. By knowing all three quantities, r, t, and l, we then calculate Λ or just use $\Lambda = \sqrt{T_{\text{cav}}}/(1 - r^2)$ to determine the enhancement. Here, R_{cav} scales with l^4,

assuming we keep r constant. This results in a negligible reflection for small losses which strongly grows as the losses increase. We understand this behavior by recalling that the power buildup in the cavity is caused by constructive interference, while the reflection is dominated by destructive interference. The contrast of these interferences is strongly affected by the mismatch of amplitudes of each contribution, which then leads to higher reflections and lower transmissions (or circulating intensity).

4.2 Expected system size

Before we show and discuss the crossed buildup cavity design, it is useful to get an idea of the expected system size. The Mott insulator (MI) phase is very often used as an initial state in quantum simulation experiments, especially when working with optical lattices in quantum gas microscopes. In addition, MIs are experimentally well understood, which is why we use the underlying framework to define our system size as the size of a MI.

4.2.1 Mott-insulator size

In subsection 1.3.3, we already discussed the condition for a MI transition in a red-detuned trap. Here, we compared the bandwidth of the lowest energy band $W = 4dJ$ with tunneling matrix element J to the on-site interaction U_{00} in a d-dimensional optical lattice [Eq. (1.23)]. We assume a 3D lattice, where the center region of each beam have required lattice depth for a MI phase, as calculated in Tab. 1.1. Note that the third lattice beam potential will be deep enough such that tunneling to other planes is prevented and the condition which actually needs to be applied here reads $U_{00}/J = 8$. However, we did not observe dramatic differences in the obtained system sizes.

For our estimate, we obtain an envelope from a Gaussian beam [Eq. (4.20)] by calculating the intensity $I \propto |E_{00}|^2$, which yields $\exp(-2r_i^2/w_i^2)$ with r_i being the distance from the optical axis of the corresponding beam and w_i the $1/e^2$ cavity beam radius at the position of the atoms[2]. We use this envelope for lattice depths V_i and find

$$V_{3D}(\boldsymbol{r}) = -V_x \exp\left(-2\frac{y^2 + z^2}{w_x^2}\right) - V_y \exp\left(-2\frac{x^2 + z^2}{w_y^2}\right) - V_z \exp\left(-2\frac{x^2 + y^2}{w_z^2}\right) . \quad (4.33)$$

For a red-detuned lattice ($V_i > 0$) the boundary of a MI is at the point when the negative potential envelope has grown by an interaction energy, i.e. the solution for all $\boldsymbol{r}_s$ in $V_{3D}(\boldsymbol{r}_s) = V_{3D}(\boldsymbol{0}) + U_{00}$. We call the resulting surface described by $\boldsymbol{r}_s$ the "MI shell". We plot the MI shell for a $813\,\mathrm{nm}$ magic-wavelength lattice in Fig. 4.5.

We find that any reduction of the beam size in one or more lattice beams change the effective size of the MI. If all beams are reduced by the same amount, the shell changes linearly with the waist of the beams. Furthermore, displacements between the beams seem to increase the system size at the expense of higher power on each displaced beam.

---

[2]Keep in mind that w_i is almost identical with the waist w_0 of the beam due to an almost vanishing divergence of these large Gaussian beams in the cavity.
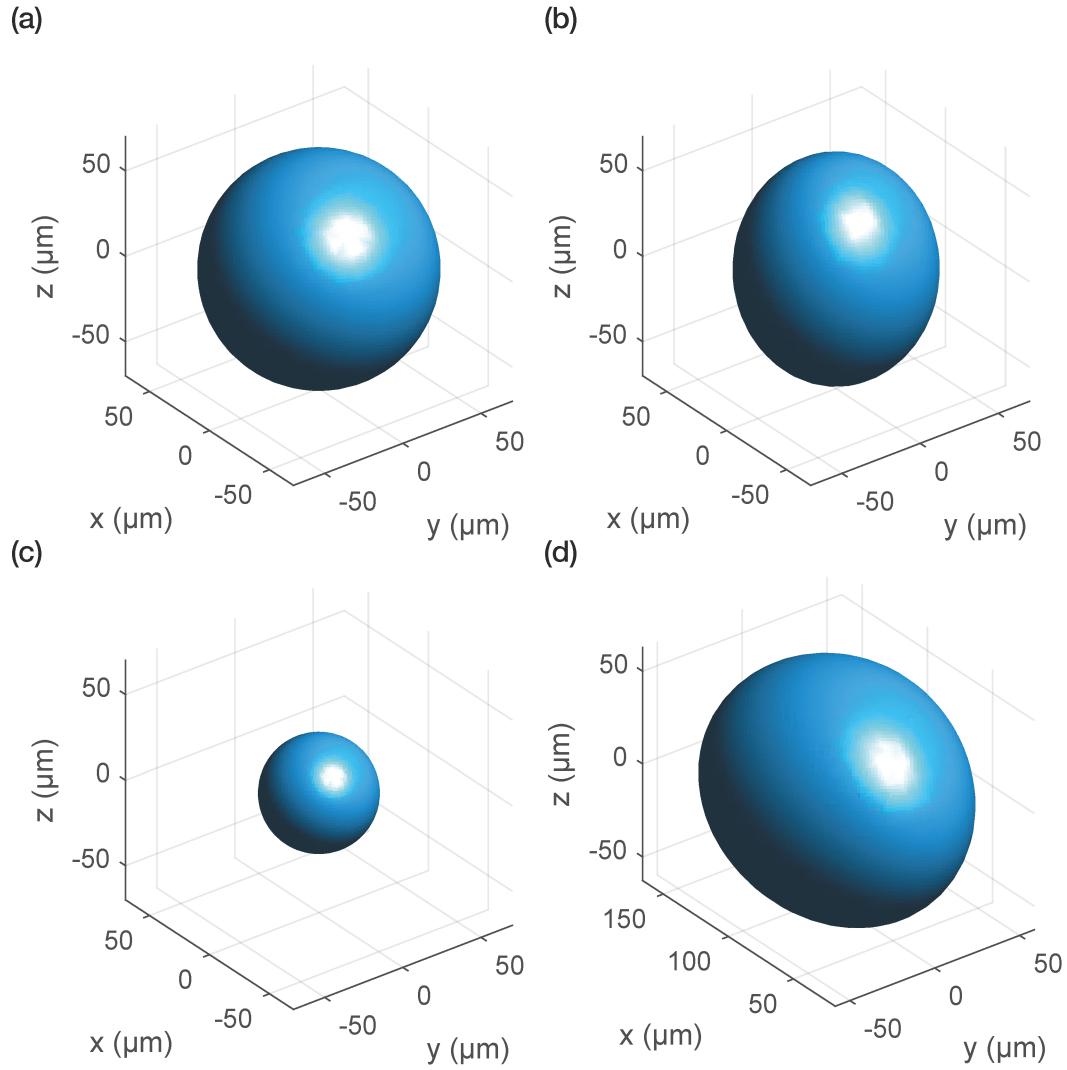
Fig. 4.5 (a) The MI shell in a $813\,\mathrm{nm}$ lattice. All three lattice beams have a (cavity mode) $1/e^2$ beam radius of $430\,\mu\mathrm{m}$ and are aligned to the center. The size of the shell is $124\,\mu\mathrm{m}$ and an atomic plane at $z = 0$ yields 305×305 lattice sites. (b) A MI shell under the same conditions as in (a), but the z-axis beam radius is reduced to $75\,\%$. We find a plane with 261×261 lattice sites. (c) A MI shell under the same conditions as in (a), but with the half of the waist. The MI size is exactly half as large. (d) A MI shell under the same conditions as in (a), but the y-axis beam is displaced by half a waist. Judging from the shell, this leads to 354×305 lattice sites.

We find that the envelope still has a single, homogeneously looking maximum as long as the displacements are not larger than half of a beam waist of displacement. In practice however, careful alignment seems to be necessary to obtain a homogeneous MI phase, which is why we are skeptical about this finding.

Independent of the wavelength and U_{00}/J ratio, the size of the MI shell stays relatively constant around 124 μm. However, the size of the lattice spacing changes with the wavelength and is given by $\lambda/2$ as shown in section 1.2.2. Taking this into account, we find 392×392 and 242×242 lattice sites for 633 nm and 1064 nm, respectively.

Another, but important question is the applicability of this MI size estimate. Considering an example given in Ref. [69], with ^{6}Li in 1064 nm lattice: the lattice was generated with angled beams with a $1/e^2$ beam radius of 125 μm leading to a lattice spacing of 1.15 μm and lower tunneling rates. With $U_{00} = h \times 2.8$ kHz we find a $U_{00}/J = 7.3$ ratio and a MI size of 16×16 lattice sites in the experiment [Fig. 1.5 (b)]. Our estimate with these parameters leads to a MI size of 26×26, differing by a factor of 0.62 from the experimental observation. Applying this corrections to our findings with 813 nm, we can expect system sizes of roughly 200×200 which we think are more realistic due to the non-zero temperature of the atoms.

4.2.2 Fourier Optics Simulation

Fourier optics (FO) simulations are a versatile tool to calculate transverse fields which propagate through many instances, such as round trips in cavities. As our curved cavity substrates have a transition region between the spherical surface and the annulus which deviates from an ideal spherical surface, we simulate our cavity mode to check whether the transition region shows any influence on the cavity mode. The cavity mode shape ideally is a Gaussian, such that no inhomogeneity can influence the MI shape.

We start the simulation with a Gaussian field $U(x, y, z)$, which already has the width of the Gaussian mode we expect. To simulate the case of a resonant mode in the cavity, we calculate the resonant wavelength λ which is as close as possible to the wavelength we initially chose, such that the cavity length L is a multiple of $\lambda/2$.

To calculate the propagation of the field $U(x, y, z)$, we express it in plane waves such that we can evaluate the propagation of each. Hence, we calculate the angular spectrum $A(f_X, f_Y; z)$ via a Fourier transform of $U(x, y, z)$ over the transverse directions, X and Y [135]

$$
\begin{aligned}
A(f_X, f_Y; z) &= \int_{-\infty}^{\infty} \int_{-\infty}^{\infty} U(x, y, z) \exp\left(-i2\pi(f_X x + f_Y y)\right) \mathrm{d}x\mathrm{d}y\,, \\
U(x, y, z) &= \int_{-\infty}^{\infty} \int_{-\infty}^{\infty} A(f_X, f_Y; z) \exp\left(-i2\pi(f_X x + f_Y y)\right) \mathrm{d}f_X\mathrm{d}f_Y\,.
\end{aligned}
\tag{4.34}
$$

Here, f_x and f_y are the corresponding frequencies in Fourier space. We maintain the z axis since we are interested in the propagation of the transverse field in the Z direction. The field $A(f_X, f_Y; z)$ is called the angular spectrum of $U(x, y, z)$, of which we determine
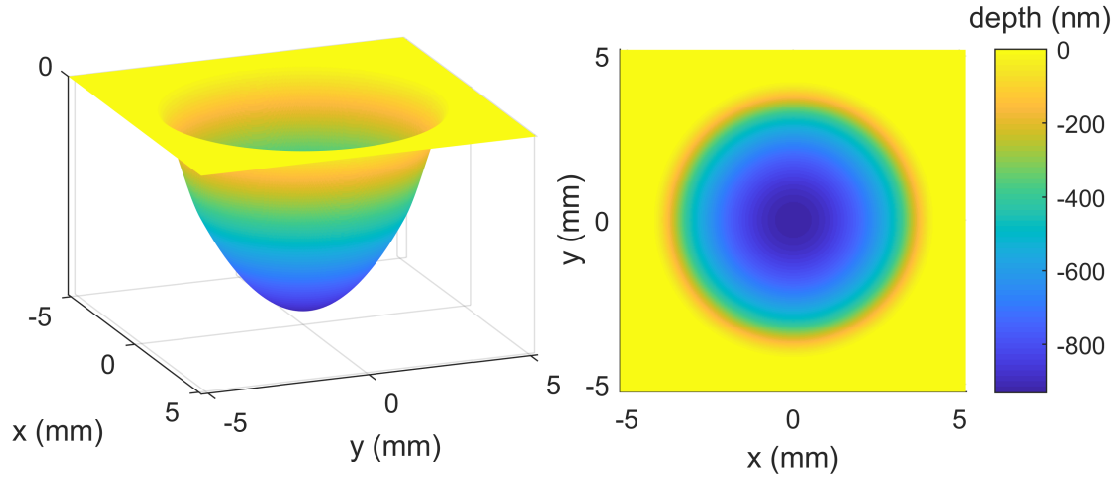
Fig. 4.6 The model for a $10.2\,\mathrm{m}$ mirror, which we used in the FO simulation. We approximated the spherical region from the center to $3\,\mathrm{mm}$ radius with a parabolic function. In the left picture we see small kink, where the transition region starts. We modeled this region by a third order polynomial which ends at zero, at the flat annulus region.

the propagated part over a distance Δz

$$A(f_X, f_Y; z + \Delta z) = A(f_X, f_Y; z) \exp\left(ik\Delta z\sqrt{1 - f_X{}^2 - f_Y{}^2}\right) \qquad (4.35)$$

by a simple multiplication of a phase factor at each point $(f_X, f_Y; z)$.

We assume that our simulation starts with the field at the flat mirror, where we know the beam waist exactly (and couple light into the cavity in practice). From this point on, we can propagate the field over the cavity length L, multiply the field by a reflection coefficient r^2 and add a phase induced by the mirror where the field is reflected. For this operation, we have to transform the angular spectrum A back to U and multiply it by a phase factor of $M \exp\left(-i2\pi 2S/\lambda\right)$. Here, M is a matrix with entries of one and zero, where the field is allowed and not allowed, respectively. S is a matrix which contains information about the real space surface profile of the mirror. The surface profile has to be zero at the annulus and has to have positive values elsewhere, because the phase of a plane wave is accumulated by passing an additional distance, which the light has to travel (twice) at each point of the mirror. The modeled mirror shape of a curved mirror substrate is shown in Fig. 4.6.

The field U is then transformed to the angular spectrum A and propagated back to the flat mirror, where we add the new field shape to the existing shape already. Note that this contribution becomes weaker with every round trip, because of the reflection coefficient r^2, which it is multiplied with in each round trip. We found 50 round trips and an $r^2 = 0.92$ to be sufficient to obtain a converging field distribution, where the last round trip changes the field distribution by $0.12\,\%$. The size of one pixel in our simulation is $\sim 20\,\mu\mathrm{m} \times 20\,\mu\mathrm{m}$ while U and A are calculated on 512×512 pixels (which yields an

area of $10.4 \times 10.4 \text{ mm}^2$). Furthermore, the flat mirror only adds a uniform phase of π, which is why we omit a Fourier transform at this point.

We show different results for U in Fig. 4.7 for different cases: figure 4.7 (a) shows an ideal Gaussian mode shape. When we include imperfections, such as relative angle between the mirrors and add an offset due to a centering error, we receive a mode like in Fig. 4.7 (b). Here, we do not observe any deviations from a Gaussian mode shape such that we can accept these imperfections for our design. In Fig. 4.7 (c) we observe a clipped mode at the mask, which shows a slight interference pattern. A possible explanation could be that clipping from the mask accompanied by diffraction acts effectively like a mirror and causes standing-wave-like patterns. In Fig. 4.7 (d) we increased the mask such that it does not have an influence on the mode shape anymore and increased the tilt further. The mode is now influenced by the transition region and looks squeezed by the aberrations. By tilting the mirror even further, we see rippled mode shapes next to each other (not shown in the Figure). Note that all modeshifts caused by the relative angle are in agreement with the prediction of Eq. (4.25).

We obtain a potential envelope from the FO simulation and compare the resulting MI shell with the result from before. We get the potential envelope by propagating A along the Z direction in 25λ steps and adding angular spectrum contributions for the corresponding minima and maxima. Transforming the resulting fields back to real space and subtracting them, leads to the envelope [Fig. 4.8 (a)]. Rotating the envelope in space yields two more beams in X and Y direction and creates the situation of a 3D lattice. The resulting MI shape is shown in Fig. 4.8 (b) which looks very similar to the result in Fig. 4.5 (a) and yields almost the same MI size with 300×300 lattice sites. The more pronounced polygonic shape of the shell is caused by the limited pixel resolution.

Specifications for a spacer and cavity mirrors probably could have been obtained with back-of-the-envelope calculations, such as the spatial mode shift that was discussed before. However, design and manufacturers, and with them the predictions for the glass pieces, changed during the design process several times. Therefore, this simulation was a good tool to exclude unforeseen influences, for instance by an increased width of the transition region. Furthermore, the FO simulation is very helpful to understand our overlap measurement techniques, as we will see.

4.3 The crossed cavity design

Harmonic confinement leads to finite size effects and discrepancies of tunneling rates and interaction energies in quantum simulation experiments as discussed in subsection 1.3.1. Although an in-vacuum buildup cavity is an obvious solution to increase the available laser power it comes with many different technical challenges. The crossed cavities, or "crossed cavity" is the core of this thesis and took three years of development, to figure out necessary specifications and companies to work with. We give a brief review on the crossed cavity design in this section.

An image of a finished crossed cavity is shown in Fig. 4.9. The final cavity design consists of an octagon-shaped spacer, with a hole on each side connecting pairwise opposite
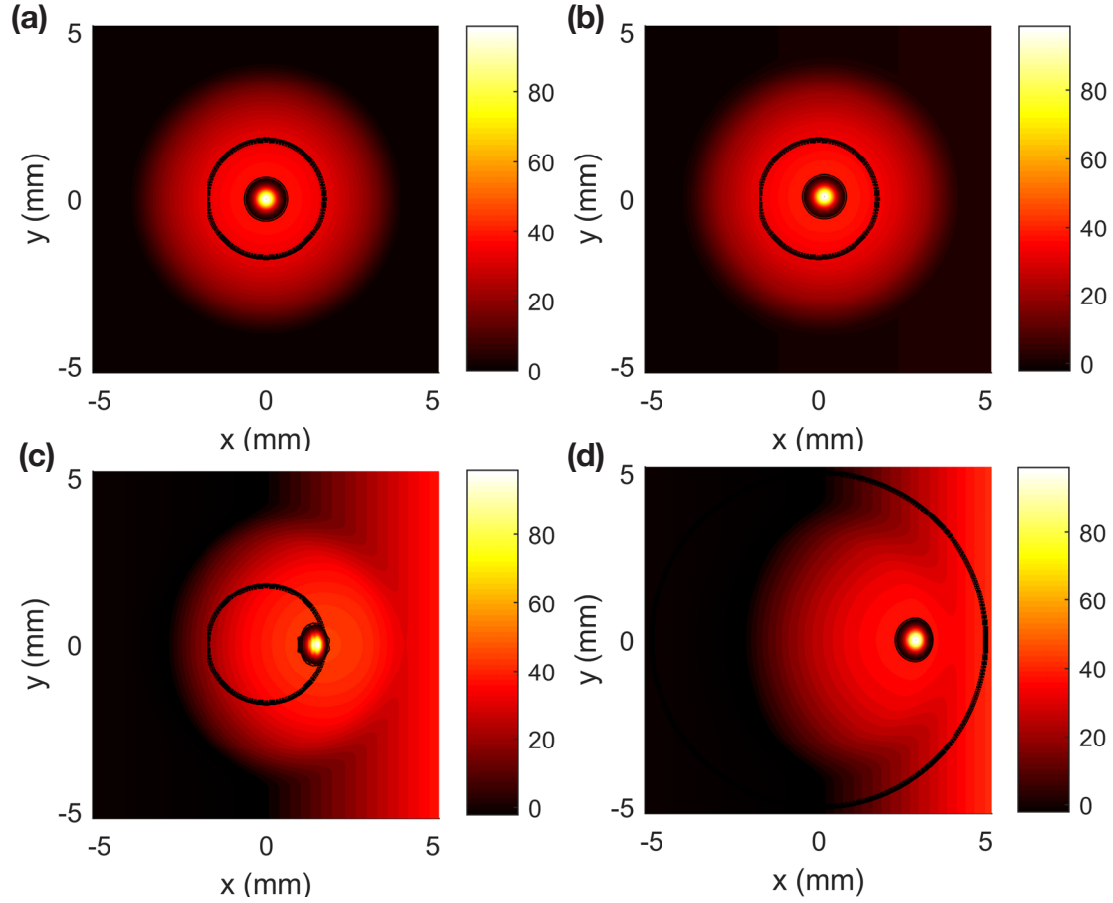
Fig. 4.7 Different cases of Gaussian mode fields produced by the FO simulation. The red-to-black color gradients in the background resemble the (tilted) mirror shape. The black circles indicate the mask at the curved mirror, where the field cannot enter. The intensity fields are shown by the yellow-red-black color gradients, which normalized intensity is given by the colorbar in percent. (a) The ideal case. The mirrors are perfectly centered and parallel. A Gaussian mode forms in the center. (b) Tilt of $2\ \mathrm{arcsec}$ between the mirrors, while the spherical mirror is shifted by $100\ \mu\mathrm{m}$ diagonally into the upper right direction. The tilt and the offset can be translated into mode shifts. (c) The tilt is $35\ \mathrm{arcsec}$ such that the mode is clipped at the mask. Slightly visible interference fringes appear. (d) The tilt is $60\ \mathrm{arcsec}$ such that the mode is formed at the edge of the transition region, which induces aberrations visible by a squeezed mode shape.

(a)

(b)
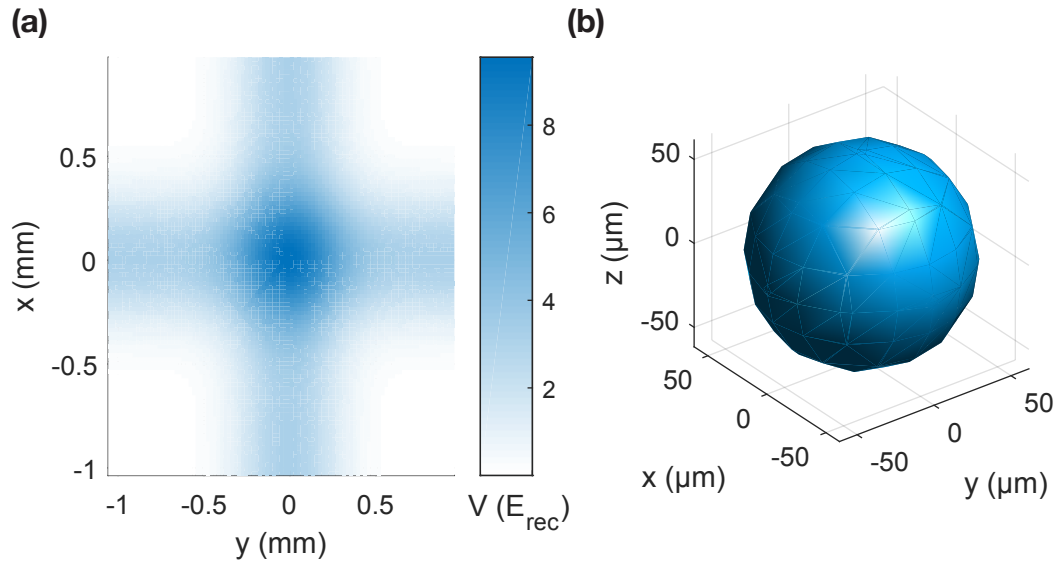
Fig. 4.8 (a) The resulting potential envelope V without imperfections on the mirrors. (b) The MI shape without imperfections yields 300×300 lattice sites.

surfaces and a large center bore through the two large surfaces. Four half-inch mirror substrates are attached to the sides, such that two mirrors each form a pair, which lead to two orthogonal optical cavity modes.

The cavity design was not obvious from the beginning. Early on, we knew that the design has to be monolithic to avoid differential vibrations and mechanical shifts of the cavities to each other. Furthermore, it has to be made from ultra-low-expansion (ULE) glass, to minimize frequency shifts of the resonances caused by temperature changes. As the monolithic design is advantageous to preserve the overlap, the frequency drifts have to be minimized such that the cavity resonance precisely stays on particular trapping wavelengths, such as magic wavelengths. This is especially important to excite long-lived states (with a narrow linewidth).

To obtain and preserve a good overlap of both modes, long-term mechanical and temperature stability turns out to be crucial. Regarding the mirrors, we came up with the following question: would gluing the mirrors be easier than attaching them via optical contacting[3], and yet be sufficient? The answer is no. Simple estimates lead to the conclusion that the expansion of the glue would easily be a factor 10 times larger than the expansion of the spacer and could induce relative angles, which would be hard to control. Since optical contacting leads to a direct bonding of the mirror to corresponding surface, we can estimate the maximal mode shift by knowing the specifications of our spacer and mirrors. This gives an upper bound of how much the mirror position needs to be corrected by to achieve a good overlap.

---

[3]Optical contacting is a process where two very clean and flat polished glass-surfaces bond together, mostly via van der Waals forces.
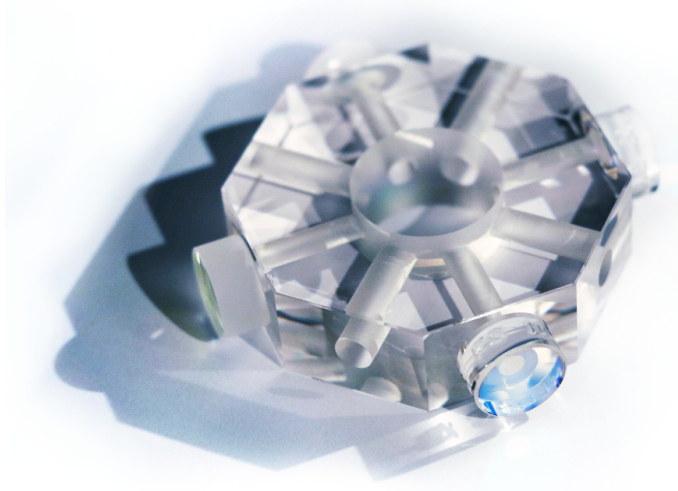
Fig. 4.9 A finished monolithic octagon-shaped crossed cavity.

First, we take a look at the choice of the mirror geometry and walk the reader through our first idea of using a plane-parallel mirror pair. Next, we will justify our choice of an quasi-plane-parallel mirror geometry, consisting of a flat mirror and 10.2 m ROC mirror. In the end of this section, we explain the design specifications of our spacer in detail.

4.3.1 Initial idea of a plane-parallel mirror pair

Another crucial decision we had to make was the geometry of the mirrors. First, we considered cavities with two plane mirrors, a plane-parallel cavity design. The advantage of these cavities is that beams of any size can be coupled in. However, by the transverse symmetry, there is no mode selection which leads also to coupling of beam aberrations into the cavity. Furthermore, a plane-parallel cavity design is at the border of the stability region: the two plane mirrors have to be perfectly parallel, which is practically impossible to achieve as there will always be a residual relative angle between the mirrors.

For example, we can think of two flat mirrors which are contacted to a spacer with two parallel surfaces. The residual angle of these surfaces can be minimized nowadays to about $\alpha = 1$ arcsec. Starting with a perfectly orthogonal beam with respect to the first mirror surface, we can calculate the walk-off between those mirrors. At each reflection at the second mirror an angle of 2α is added to the orientation of the beam propagation. We set the condition, that the beam leaves the cavity mode when it traverses the initial

beam waist w_0[4]. With the length L of the cavity, we evaluate the walk-off

$$\Delta h \approx 2\alpha L \sum_{n=0}^{n_{\max}} (2n+1) = 2\alpha L(n_{\max}^2 + 3n_{\max}) \,, \tag{4.36}$$

where we assume small angles α and $n_{\max}$ is the number of round trips to be determined. Assuming a beam waist of $w_0 = 400\,\mu\mathrm{m}$, $\alpha = 1\,\mathrm{arcsec}$, and $L = 50\,\mathrm{mm}$ we find $n_{\max} = 55$. Taking into account the number of round trips $n_{\max}$ and our results from section 4.1.3, we can estimate a maximum finesse of 340 and enhancement of 110, respectively. Especially to obtain deep lattices for imaging, we require the enhancement to be at least a factor of 1000 for imaging wavelengths, which is why did not choose this mirror configuration.

4.3.2 Plano-concave mirror pair

As a plane-parallel design did not satisfy our requirements, we decided to use a plano-concave cavity design, consisting of a flat and a curved mirror. The curved mirror breaks the transverse symmetry of the plane-parallel cavity and rules out the beam walk-off. With much higher achievable round trips, we achieve a higher finesse and, thus, higher power enhancement. As two plane-parallel mirrors do not select mode size and shape, a slightly curved second mirror allows a large mode, which is why we decided to use a ROC of $10.2\,\mathrm{m}$[5]. However, mirror pairs with these ROCs are very similar to plane-parallel mirror pair and therefore are very sensitive to wedge errors and relative angles, as already described in Eq. (4.25).

As an overall compact crossed cavity design seemed beneficial to us because we need to get the microscope objective close to the atoms, we decided to use mirror substrates with a diameter of $12.7\,\mathrm{mm}$. Despite the relatively small mirror size, a flat annulus of about $2\,\mathrm{mm}$ width has to be polished into the mirror substrate to allow optical contacting. However, the smaller the mirror diameter, less material can be removed from the curved mirror, and thus, the harder the polishing process of the annulus becomes. This difficulty can be illustrated by calculating the depth d of the spherical region with diameter D and a ROC R. We find

$$d \approx \frac{D^2}{8R} \tag{4.37}$$

by approximating the spherical region up to the second order in D. For a $12.7\,\mathrm{mm}$ diameter mirror substrate with a $10.2\,\mathrm{m}$ ROC and a $2\,\mathrm{mm}$ annulus, we find a depth less than a micrometer and less than a micrometer of glass can removed. Comparing this to a typical $25.4\,\mathrm{mm}$ mirror substrate used in standard ULE reference cavities, with a ROC of $50\,\mathrm{cm}$ and the same diameter of the spherical region, about $160\,\mu\mathrm{m}$ of material can be

---

[4]Here, we assume that the beam is well collimated, which means that the growth of the beam radius is negligible to the beam waist.

[5]Note that a ROC at this size is one of the largest a glass-manufacturing company specialized on polishing can sell. Very often, tools for such inquiries are not available and have to be bought (and payed by the customer) first. "Coastline Optics Inc." in the United States or "WZWOPTIC AG" in Switzerland are manufacturers that were willing to produce such mirrors.
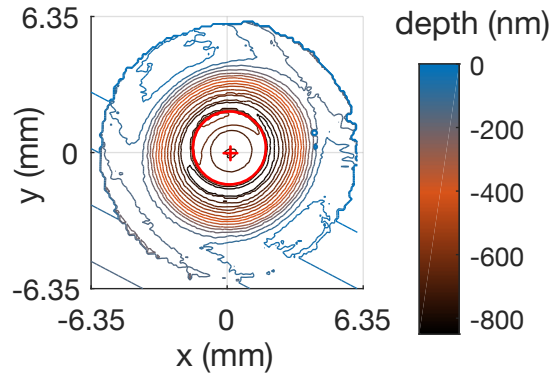
Fig. 4.10 A contour plot calculated from an interferogram of a coated 10.2 m ROC mirror substrate with annulus. The red cross indicates the deepest point of the spherical region and the red circle the edge of the coated region. The deepest point of the spherical region is shifted by $175(25)$ μm in x direction and corresponds to a wedge error of about 3 arcsec.

removed. This demonstrates, that polishing an annulus into a large ROC substrate has to be done with extreme care, also, to no scratch the spherical region in the center.

Note that an even width of the annulus guarantuees the deepest point of the spherical region to be in the center. The more even the width of the annulus is, the smaller is the wedge error, which is the displacement of the deepest point in the spherical surface with respect to the mirror center. This can be visualized by looking at an example surface profile of such mirror substrate in Fig. 4.10. Also, if more material for the annulus is removed and one practically polishes the annulus deeper "into the glass", then the reference might be lost, such that the spherical surface has no local minimum anymore. In that case, the wedge error is too large to generate a mode in the cavity later on. The only company we found to polish an annulus without removing one micrometer of material (and if necessary repolish the spherical surface) is "Coastline Optics Inc". One out of twenty of these custom made mirrors is displayed in Fig. 4.10, where we specified a wedge error of 2 arcsec.

As we already mentioned possible scratches on the spherical region, we decided to add a masked IBS coating to the mirrors after the annulus polishing had been done successfully. The main reason is that this multi-band reflective coating consists of 51 layers and has a total height of $\sim$5 μm. Therefore, it sticks out of the one-micrometer-deep spherical surface and would most likely be scratched when the annulus would be polished into the mirror after applying an IBS coating run. To guarantee optical contacting, the 3.5 mm wide mask of the coating has to be smaller than the 4 mm wide hole of the spacer. Therefore, we had 250 μm room to correct for the mirror position. According to our specifications, this was tough to adjust the mirror position such that the resulting mode positions could yield a good overlap, as we will elaborate on in the next section.

After working through all these specifications and tolerances, we want to emphasize the benefits of the large ROC of 10.2 m: with a cavity length $L = 50$ mm and the red-detuned magic wavelength $\lambda = 813$ nm, Eq. (4.22) predicts a mode waist of 430 μm

located at the flat mirror. At these mode waists, it can be shown that beam divergence is less than one micrometer larger at the curved cavity mirror and thus negligible [133]. As the atoms will be located in the center of the cavity, we will use the term beam radius while quoting numbers for the mode waist in that regard.

4.3.3 Spacer

As the mirror pairs were the first main ingredient, a spacer with the correct specifications is the second main ingredient to complete our monolithic crossed cavity. We aimed for a compact, temperature-stable, geometry, which was polished such that optical contacting was possible. A technical drawing of the spacer can be found in Fig. 4.11.

We chose to machine the spacer from ULE glass to minimize thermal expansion, similar to high-finesse reference cavities, which are typically used to achieve narrow-linewidth lasers. Not only does this minimize frequency drifts, which should be avoided to stay on magic wavelengths or might exceed the bandwidths of frequency shifters to lock the laser later on onto the cavity, but it also reduces the effect of thermal gradients. These are present, when a heat source, for instance a laser, heats the cavity spacer while it is heat-sunk by touching steel or a glass window. In vacuum, the other surfaces then only can cool via radiation. Heat conduction of glass is rather low, which is why the temperature would not equilibrate fast enough. Thermal gradients therefore could lead to a larger expansion in regions with higher temperature and change the relative angle of the spacer. However, with ULE glass we can estimate that the mode shift would be about $5 \ \mu\text{m}/°\text{C}$.

In the drawing in Fig. 4.11 we see two surface pairs denoted by B and C, where the mirror pairs will be attached to. These require better polishing conditions than the other surfaces, such as a maximum number and depth of scratches, to ensure optical contacting. A flatness in fractions of λ[6] at the contactable surface is essential, such that a few-millimeter thick glass mirror can slightly deform and adjust to the spacer surface to maximize the contact area, when optically contacted. Also, reference surface A is polished such that optical contacting of the whole spacer to a suitable window is still possible.

We specified the surface pairs B and C to have a parallelism of $1 \ \text{arcsec}$, which reduces the mode shift for our curved mirrors to $49 \ \mu\text{m}/\text{arcsec}$ according to Eq. (4.25). The orthogonality of the surface pairs B and C with respect to reference surface A is specified to be $30 \ \text{arcsec}$ which reduces to mode shifts described by Eq. (4.24) to a maximum of $4 \ \mu\text{m}$. The orthogonality of the surface pairs B with respect to C is specified to be $10 \ \text{arcsec}$, but does not have an influence on the overlap. It sets an error of less than $2 \ \mu\text{m}$ of how centered the mode crossing will be with respect to the center of the spacer, which could help with the alignment of the microscope objective later on.

To exploit long lattice lifetimes and thereby long coherence times of the atoms in the experiment, it makes sense to take a look at possible sources of heating, which might lead to atom loss. Vibrational modes cause oscillations of the mirrors with respect to

---

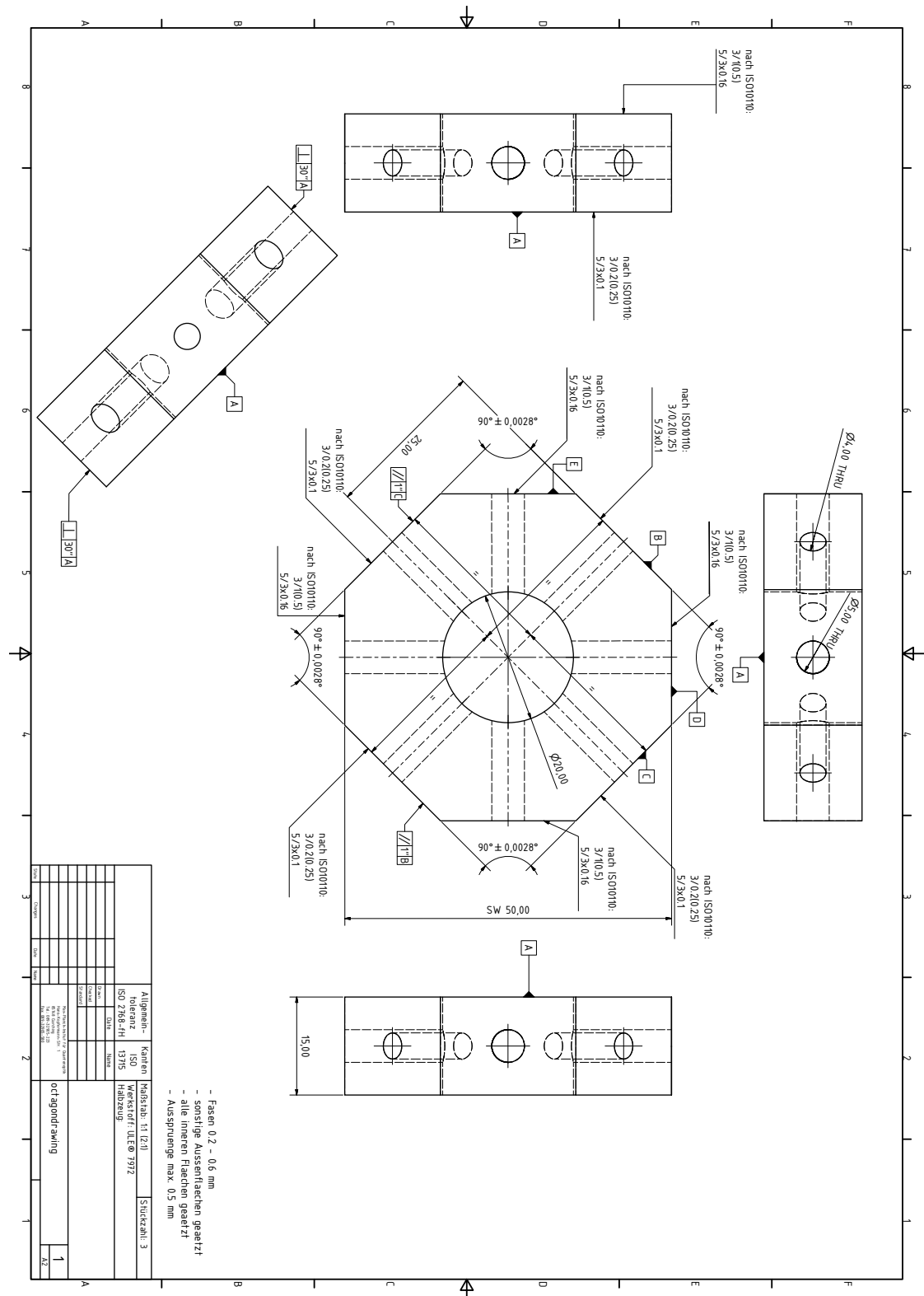[6]The unit λ is standard to characterize glass surfaces and is given in terms of a $633 \ \text{nm}$ measurement laser.

Fig. 4.11 Technical drawing of the octagon-shaped spacer.

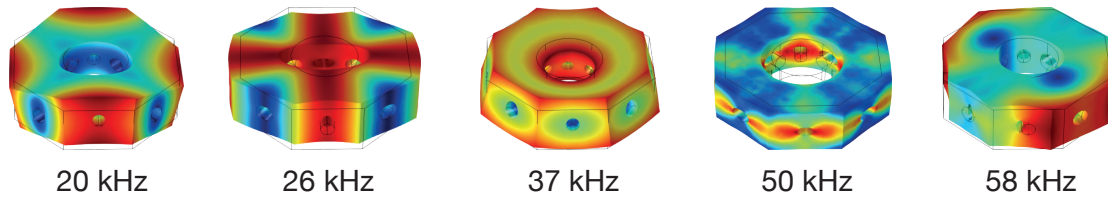| 20 kHz | 26 kHz | 37 kHz | 50 kHz | 58 kHz |

Fig. 4.12 A selection of vibrational modes of the cavity spacer. The first, third and fifth mode lead to transverse oscillations of the mirrors, which convert to intensity fluctuations and thus parametric heating at the atoms. The second mode leads to oscillations of the cavity length, and thus the resonances, which also causes parametric heating. Therefore, the dimensions of this compact design are chosen such that the lowest vibrational mode is at $20\,\mathrm{kHz}$. Red and blue regions indicate more and less squeezed regions, respectively.

the input beam. The mode matching and therefore the intensity in the cavity is then modulated with the same vibration frequency which leads to amplitude noise. When this noise matches two times the trap frequency, a process called parametric heating enhances the atom loss rate [111]. Although typical trap frequencies in optical lattices for strontium can reach tens of kilohertz, it makes sense to find a design with vibrational frequencies as large as possible to reduce the risk of parametric heating. Regarding the geometry of the spacer, we varied the dimensions of the spacer while simulating its vibrational modes with a finite elements simulation [Fig. 4.12]. The same effect happens when the cavity length oscillates, which converts to vibrations of the cavity resonances. Note that also higher order vibrational modes play a role and the vibrational frequencies we calculated only set a lower limit. Also keep in mind, that mounting the spacer will dampen and therefore smear out the vibrational modes in frequency space and increase the risk of increased parametric heating later on. The influence on the atomic lifetime in the lattice eventually has to be measured in the experiment.

Increasing the length of the spacer or the size of the holes leads to lower vibration frequencies and inspired us to choose a more compact design with a length of $50\,\mathrm{mm}$ and a height of $15\,\mathrm{mm}$. The holes for the cavity modes have a diameter of $4\,\mathrm{mm}$ to avoid mode clipping at the glass. Optical access (for instance for fluorescence imaging beams) and atomic transport is given by the other holes with a diameter of $5\,\mathrm{mm}$. The top hole provides pumping for vacuum and provides optical access to the microscope with a diameter of $20\,\mathrm{mm}$. As the atoms will be in the center of the spacer, the height of the spacer together with the center bore diameter sets an upper bound for the numerical aperture (NA) of the microscope. We find a maximum NA of 0.77, which is large enough to not prevent single-site resolution at typical trapping and imaging wavelengths.

4.4 Assembling the crossed cavity

In the following section we want to describe the assembly of the crossed cavity in detail and show the most important keypoints which are necessary to build it. We summarize the cleaning procedure before we describe the contacting process. The contacting of all

four mirrors is done by following a certain strategy and successive alignment steps to achieve a satisfying overlap, i.e. $> 95\,\%$ according to our estimation.

4.4.1 Cleaning

In this subsection we focus on preparations before optical contacting, which involves the process of cleaning and building a cleanroom-grade working environment. To conduct optical contact later on, we emphasize that both spacer and mirrors have to be exceedingly clean to enable a bond between two flat and smooth glass surfaces. In practice, special repolishing agents exist which can facilitate the bond between both surfaces instead. Since their outgassing properties in ultra-high vacuum (UHV) are unknown to us, we decided to not use them. Our approach is similar to cleaning procedures which are used in semiconductor fabrication [136].

Cleaning of the octagon spacer is done by suspending it on a stainless steel wire in a beaker of RCA1 solution consisting of unstabilized hydrogen peroxide ($30\,\%$), ammonium hydroxide ($28 - 30\,\%$), and HPLC-grade or semiconductor-grade water with a mixing ratio of 1:1:5 [136]. The beaker with the spacer in it is boiled at $80\,°\mathrm{C}$ in a fume hood. After about 15 minutes of boiling, most of the hydrogen peroxide has become water and oxygen, such that less bubbles are ascending. At this point, we take out the hot beaker, put it in a pre-heated sonicator bath and sonicate it for three more minutes. Next, the spacer is removed from the beaker and suspended in another beaker filled with pre-heated HPLC-grade water to remove residues of the cleaning solution. In this manner, the spacer is transported without being exposed to dust. Afterwards, the spacer is taken out and residual water droplets are blown off with particle-filtered nitrogen.

The assembly described in the following sections takes place in a enclosure, which is built around a HEPA filter. We keep this environment as clean as possible, work only with gloves, hair caps and a full-body clean-room suit, which is why we refer to this environment as "mini-cleanroom". This minimizes the dust which can settle on the surfaces and prevent optical bonding.

4.4.2 Contacting strategy

Before we talk about the contacting itself, we give the reader the strategy we used to assemble the crossed cavity. Therefore, we have to recall that the flat mirror only determines the angle of the cavity mode in space, but not the position. The position is thus only determined by the curved mirror. For further details we advise the reader to refer to subsection 4.1.5. Taking this into account, we contact first the two flat mirrors and one curved mirror. The first complete mirror pair, therefore, determines the position of one mode. From that point on, we need care to attach the second curved mirror at the optimal position to achieve a satisfying overlap of both modes. For this reason, the next subsection elaborates on this step and explains, how we find the ideal mirror position before we bring the mirror into contact with the spacer. Nevertheless, sometimes the resulting overlap is not satisfying and the mirror is removed and we repeat the previous step.

4.4.3 Preparations

To assemble a crossed cavity matching our requirements, we had to develop custom procedures and tools. A "contacting stage" is the core of our working environment, where controlled positioning of the mirror substrates and the optical contacting of them to the corresponding surface of the spacer is performed. The working principle of this stage is shown in Fig. 4.13 (a). The mirror substrate, which we want to contact, and the spacer are mounted separately, while the horizontal position and two angles of the mirror and the vertical position of the spacer can be adjusted. With the help of an interferometer on top of the stage we measure the parallelism between the annulus of the mirror and the top-surface of the spacer, where the mirror will be attached to. We couple light from a frequency-scanned laser into the cavity to observe the cavity resonances on two photodetectors. With a slit measurement we measure the overlap of the two modes before and after the contacting process. We apply corrections to the transverse mirror position to improve the overlap, before we press it down and optically bond it with a punch.

In more detail the stage consists of a four-axis stage which allows translation in two spatial dimensions as well as the adjustment of two angles [Fig. 4.13 (b)]. In a center hole of the stage, the mirror substrate is mounted in a tube, where it is lightly clamped at its circumference. The octagon-shaped spacer is mounted on an optical rail which can be used for coarse vertical adjustments. The posts of the top-part as well as the optical rail are filled with lead, to damp out vibrations and improve the differential stability of the interferogram between the spacer and the mirror surfaces. A translation stage between the slit on the rail and the mount of the spacer allows for fine adjustments of the vertical position of the spacer to bring it as close as necessary to the mirror (a few hundred micrometer in practice).

The interferometer at the top of the stage produces interferograms between the front surface of the mirror and the top surface of the spacer [Fig. 4.14]. We can think of this as a Fizeau-type interferometer, where we exchange the flat Fizeau plate with the front surface of the mirror. The back surface of the mirror is wedged and therefore does not contribute to the interferograms we see. We image the interferograms with a camera and an objective, which is focused on the front-surface of the mirror, where the interferogram is produced. The beam splitter mirror of the interferometer is mounted on a flip mount, such that we can remove it to insert the tube with the mirror substrate and the punch to press the mirror down to optically contact it.

The next preparations are thoroughly cleaning the corresponding surfaces before mounting both parts on the stage: therefore, we place the mirror on the spin coater, where it is held to an O-ring of the rotating chuck by a membrane pump. The spin coater then spins the mirror substrate with about $8000\,\mathrm{rpm}$, while we spray HPLC-grade isopropanol and water onto it, and wipe it from the inside out with a lint-free Q-tip. Residual water droplets are blown off with particle-filtered dry nitrogen. By that we receive a clean surface of the mirror. We carefully grab the mirror with clean tweezers, place it in the tube and clamp it lightly [Fig. 4.15 (a)]. The tube is then inserted into another tube on top of the four-axis stage and fixed. Then, the mirror is clean and in its initial position.

Next, the spacer is lightly clamped in its mount on the optical rail [Fig. 4.15 (b)]. We
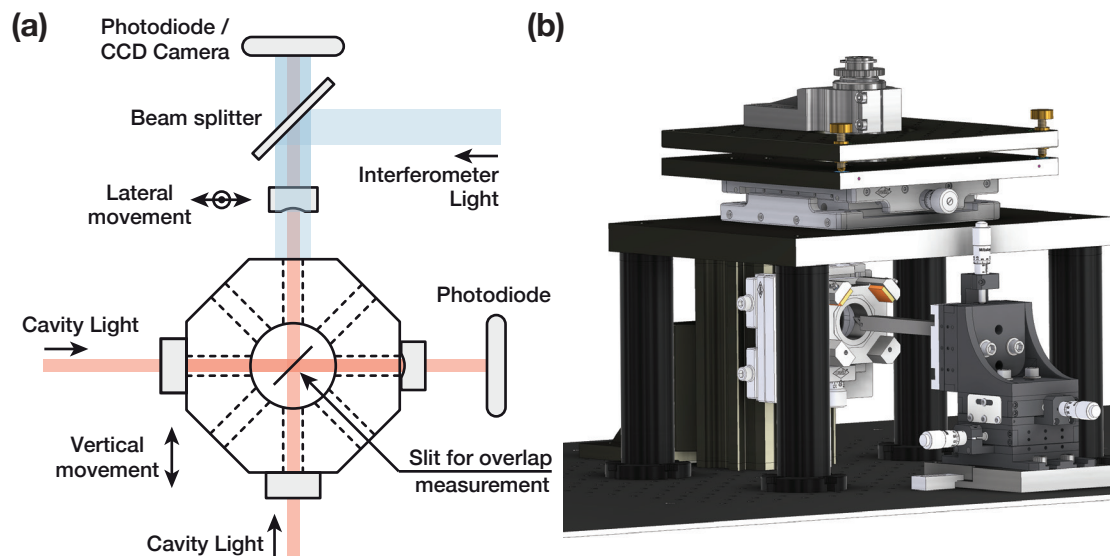
Fig. 4.13 (a) Sketch of the working principle of the contacting stage. The mirror substrate and the spacer are mounted vertically, while the position of the spacer can be adjusted. An interferometer above measures the parallelism between the annulus of the mirror and the spacer surface, where the mirror will be attached to. Light is coupled into the cavity, while the laser is scanning over the resonances. With a slit measurement, the overlap of the two modes is measured before and after the contacting process. Corrections for the overlap are done by moving the mirror transversely, before it is pressed down and contacted with a punch. (b) A CAD-drawing of the mechanical parts of the contacting stage. The black pillars are filled with lead to damp vibrations and improve the stability on the top layer of the stage.
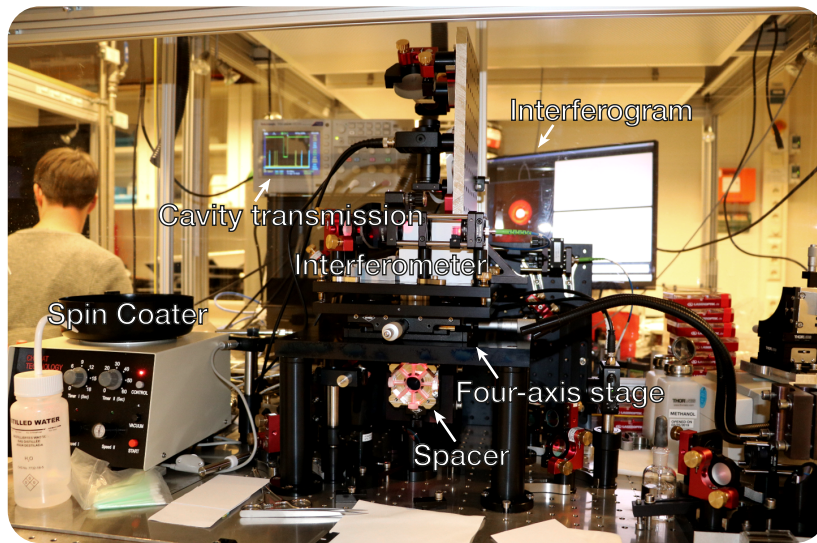
Fig. 4.14 An image of the working environment we used to assemble the crossed cavity. The spin coater serves to clean the mirror substrates. The spacer is mounted on a translation stage on a rail on the lower part of the contacting stage. The mirror which will be contacted to spacer is mounted slightly above it, lightly clamped in a tube. On top of the four-axis stage (two transverse movements + two angles to adjust) we built a Fizeau-type interferometer to measure the parallelism of the mirror to the spacer surface. The interferograms are taken with a camera and displayed on-line on a screen behind the mini-cleanroom. Light is coupled into the cavity where photodiodes measure the transmission and, together with a slit on a translation stage, to measure the overlap.

(a)   **(b)**   **(c)**
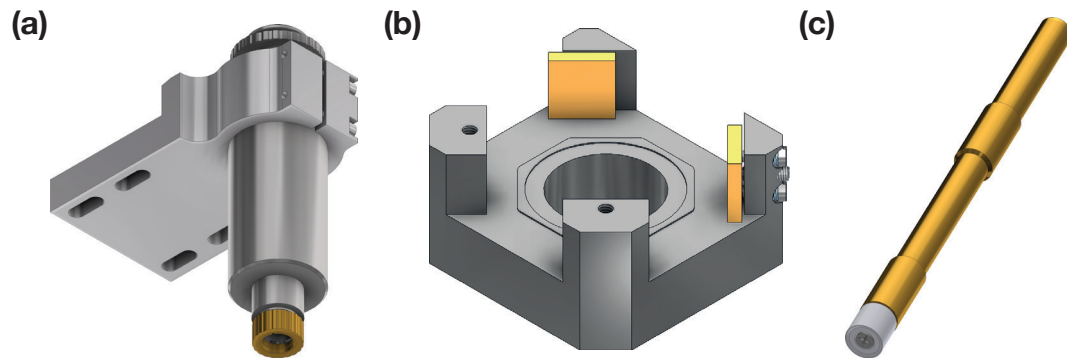
Fig. 4.15 (a) Mount for the mirror substrate. The mirror is clamped homogeneously around the mirror circumference at the bottom with a contractible ring. On top of the mirror a tube is machined into the mount and open on the top, such that interferometric light and a punch can be used to release the mirror from the mount. (b) Mount for octagon-shaped spacers. The mount is made from stainless steel to prevent scratches on the spacer surface. From two sides, Vespel pads can be used to clamp the spacer gently. The mount of the contacting stage can be exchanged to also contact mirrors to differently-shaped spacers. (c) The punch which is used to release the mirror from the mount. The tip is made from teflon to not cause scratches and provide uniform pressure onto the mirror back surface.

use a cotton cloth with HPLC-grade methanol to wipe the top-surface of the spacer and remove any (organic) dirt, which could have accumulated after the RCA cleaning procedure. However, the cotton wipe is not lint-free, which is why we need a lens-tissue and remove residual lint and dust of the surface with the "drag'n'drop method". Afterwards, the spacer is clean and ready for contacting. A cross-check on residual dust can be done by shining white light from the side onto the surface with a bright light source. The spacer can then be moved up on the optical rail and with the translation stage up to a few hundred micrometer close to the mirror.

4.4.4 Mirror positioning

With the mirror and spacer in place, we observe an interferogram which is imaged onto a CCD camera and shown on the screen of a computer [Fig. 4.14]. The interferogram shows fringe patterns which are produced by $689\,\mathrm{nm}$ light [Fig. 4.16 (a)]. The height difference of a maximum (minimum) to the next maximum (minimum) is then $\lambda/2$ of the wavelength used. Taking all fringes over the whole half-inch diameter of the mirror into account, we can derive the relative angle between the annulus of the mirror and the top-surface of the spacer. With these considerations, we find the relative angle per fringe to be $5.6\,\mathrm{arcsec}$.

As we want to predict the overlap before we contact the fourth mirror, we want to align the annulus of the mirror to the top-surface of the spacer to be as parallel as possible to simulate the situation when the mirror is attached later on. Any residual angle will lead to an unpredictable mode shift after the contacting process. This means, if we are able
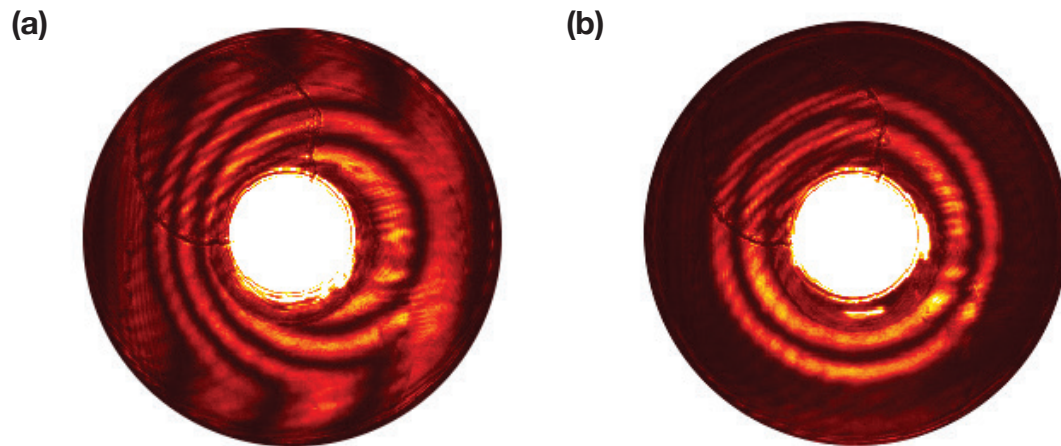
(a) **(b)**

Fig. 4.16 (a) Interferogram of a tilted mirror towards the spacer surface. Fringes across the annulus are visible and can be used to determine the tilt. (b) Interferogram of a optimally parallel mirror to the spacer surface. Across the annulus we see the fraction of a fringe, which corresponds to the smallest possible angle we achieved.

to align the mirror substrate such that we see a very homogeneous fringe, which still might be a fifth of a total fringe, we still can expect a mode shift of at least $50\ \mu$m after attaching the mirror. An example of best effort alignment is displayed in Fig. 4.16 (b). We tried to improve the alignment procedure by writing software which shows integrated signals over both transverse directions, as well as a polar plot of the signal on the fringe. However, turbulences in air as well as differential movements between the top-part of the stage with respect to the rail, lead to significant fluctuations on the order of a fringe on the interferogram.

When we are satisfied with the interferometric alignment, we insert a slit mounted on a translation stage to measure the mode overlap. We will elaborate on the method of the slit measurement in the following section. Nevertheless, the slit measurement reveals the vertical displacement of the two modes. By vertical displacement we mean the distance of the optical axis of the two modes taken at the crossing of the modes (projected on the plane which is spanned by them). By knowing the vertical displacement, we know the distance which we have to correct the mirror position by. Usually, we have to repeat the preceding steps up to this point a few times, starting from the alignment of the mirror to the spacer surface. This has to be done successively and after about 3 - 5 steps, we cannot measure a relevant mode displacement anymore.

4.4.5 Optical contacting

After this preparation, we use a punch with a teflon tip to push down the mirror substrate, release it from the clamping structure and press it uniformly onto the spacer surface. During this process, the glass substrate then slightly deforms such that a large enough contact between the two surfaces is facilitated. If a residual particle is left between the

surfaces, it will, depending on the size of the particle, reduce the contact region and therefore the bonding strength [136]. After some practice with cleaning and carefully mounting the parts, a success rate of the contacting process of $100\,\%$ was achieved.

However, after contacting, the angle between the curved mirror annulus and the spacer surface might have changed with respect to its previous position and thus lead to a significant mode shift. Therefore, the final mode displacement has to be remeasured carefully, after which a decision has to be made: if the overlap is not satisfying, we take a cleaned stainless steel razor blade, place it in the gap formed by the bevel of the mirror and the spacer surface and push it in between. With a little bit of force and training, the parts can be separated from each other without causing scratches. By cleaning both parts again, we repeat the whole step described in this subsection until we find a satisfying overlap. After achieving satisfying overlaps several times, we experienced that once, even after the first trial, we had a satisfying overlap. Another time, it took us two days to finish a crossed cavity with a satisfying overlap. So, it definitely involves a little bit of luck as the optical resolution is not high enough to measure angles of $1\,\mathrm{arcsec}$ over a range of $12.7\,\mathrm{mm}$. Nevertheless, the optical resolution could be improved to narrow down the unpredicted mode shift by using interferometric light with a shorter wavelength.

During the design process of the contacting stage, we wondered how much the mirror would shift from the desired position when it is released from the clamp and optically contacted afterwards. To get an idea of this, we installed two compact USB microscopes, as close as possible, but such that we still saw the surface of the spacer and the edge of the mirror substrate. An image was taken with each microscope before and after the contacting process [Fig. 4.17]. We removed the spacer and took images of a ruler in the focus, such that we could convert pixels into length. To determine the displacement, we stacked the two images and used a differential edge detection algorithm to count the pixels of displacement. After several measurements, we found an average of total displacement of $30(5)\,\mu\mathrm{m}$. During the contacting process, the mirror was moving downwards by about half of a millimeter or less.

4.4.6 Removing optically bonded mirrors

Throughout our work with glass pieces, we got to know and to try different ways of removing optically bonded mirrors. During a visit at WZWOPTIC AG we were introduced to different ways to break optical bonds: Firstly, a short exposure of the mirror substrate to a flame can lead to a fast thermal expansion of the substrate and the mirror will come off. As this method would only strengthen the bond of quartz glass, such as ULE glass and UV fused silica, we did not try this method. Secondly, squeezing one of the pieces in a vise will lead to a reversible deformation of the entire piece and a deformation of its surfaces with it. When this deformation reaches the order of λ (at $633\,\mathrm{nm}$) the optical bond is reduced and eventually breaks. Lastly, the most efficient way to separate two bonded glass pieces is to push an exceedingly clean razor blade in between. With a little bit of practice, the bond breaks without having produced scratches, which reduce the probability of successful optical contacting.
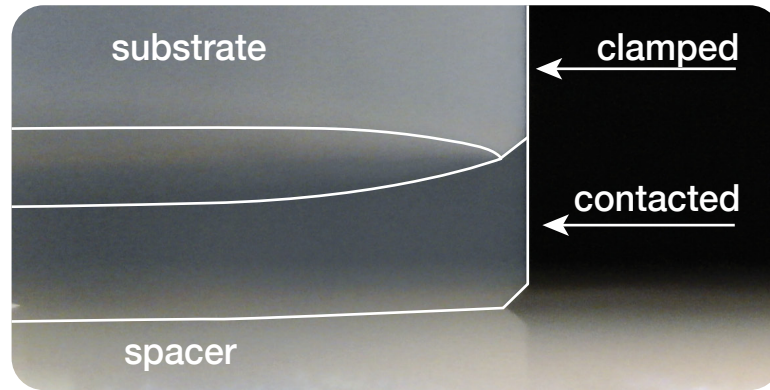
Fig. 4.17 Two stacked images of the spacer surface and a mirror taken before and after the con-
tacting process. We increased the transparency of the top image, such that both mirror
positions are visible. The edges drawn here only serve the reader clarification.

4.5 Characterization of the mode overlap

As already pointed out in the previous subsection, we need to perform a careful charac-
terization of the overlap, before a spacer can be placed in a vacuum chamber. For this
reason, we came up with two main ideas for an overlap measurement, a knife edge and
a slit measurement.

4.5.1 Knife edge or slit measurement?

Our initial idea was based on a typical knife edge measurement, which is usually applied
to measure laser beam sizes rather than beam positions. However, to measure an overlap,
we need to determine the position of two modes with respect to each other. We define
the position of the mode as the center of the Gaussian TEM_{00} mode. Translation stages
provide reliable movements on the micrometer scale, but the numbers read off from them
need to be referenced, if we want to measure an absolute position. Also, regions where
we care about a beam position are usually not accessible, for instance laser beams in
vacuum chambers. In our case this is different: we can reference the position of one
mode in the crossed cavity with respect to the other one and thereby determine their
vertical displacement.

   Therefore, we started the first measurements on a provisorily-built prototype crossed
cavity. This cavity was made of a discarded piece of glass from manufacturing, to which
we glued flat and $20\,\mathrm{cm}$-ROC mirrors. A $633\,\mathrm{nm}$ laser beam was split into two beams,
which were coupled to the cavity. The laser was scanned over the cavity resonances,
while two photodetectors detected the TEM_{00} transmission through the cavities. The
maximum of the peak heights were recorded for each point of the translation stage, which
was moved in equidistant steps through the cavity mode. The results were repeatable and
promising in the first place, but revealed some difficulties.

   Naively, we expected an error-function-like signal, just as for a typical knife edge mea-
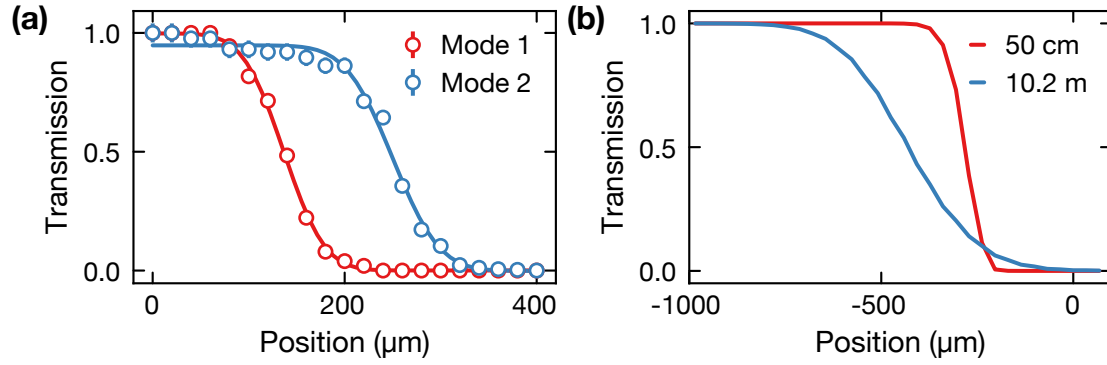
Fig. 4.18 (a) First knife edge measurements on a prototypical crossed cavity. The signals show an error-function-like behavior. (b) Simulation of knife edge measurements for different ROC mirrors in a plano-concave cavity with 50 mm length. The zero point of the x-axis is referenced to the center of the mode and shows almost no transmission for the slit at the center of the mode.

surement on an ideally-Gaussian beam. According to our expectation, we model any taken data with the function

$$S(x) = a \, \text{erf} \left(\sqrt{2} \frac{x - x_0}{\sigma} \right) + b \, . \tag{4.38}$$

Here, a is an amplitude, b an offset, and σ is the width (which is the width of a Gaussian beam for a typical knife edge measurement at a beam propagating in free space). In practice, we consider x_0 as the position of the mode, which is the point of $50\,\%$ transmission. This would be true for a knife edge measurement on an ideal Gaussian beam.

In Fig. 4.18 (a) we plotted the data from the prototypical measurement. The region where we expect a flat plateau shows fluctuations in the signal, which might be explained by changes in laser power over time. This could possibly be fixed by including intensity stabilization of each laser beam close to the cavity. By performing the measurement even in different laboratories, we found a repeatability of the displacement of both modes within $10 - 20 \; \mu\text{m}$. However, we were not sure if systematic errors were affecting this measurement.

For this reason, we used the FO simulation to obtain a better understanding of the measurement. In Fig. 4.18 (b) we see a signal obtained by moving a sharp mask, a limit in space above which the light field cannot pass, in equidistant steps through the cavity mode. The curves show a transmission of zero at the actual center of the modes. If we imagine the light as circulating inside the cavity to form a cavity mode, it becomes clear that blocking half of the mode ceases most of the circulation process.

Taking this into account, we decided to use two edges, forming a slit [Fig. 4.19 (a)]. This method does not rely on intensity stable plateaus, although intensity stable laser input beams definitely lead to a better signal-to-noise ratio. Most importantly, the slit will allow most the light in the cavity to pass when it is placed symmetrically around the
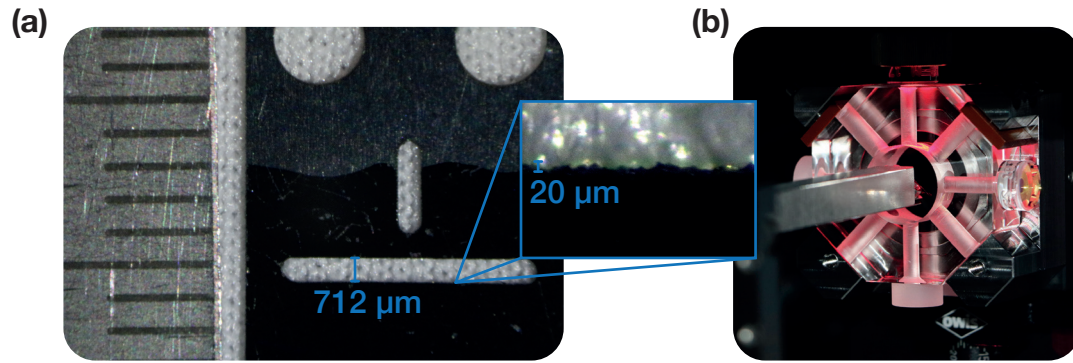
(a)

(b)

20 µm

712 µm

Fig. 4.19 (a) A slit together with a ruler for calibration purposes. We obtain a micrometer-to-pixel conversion and find a slit width of $712~\mu$m. The inset is taken from another image, zoomed into the slit. By using the just measured slit size as a reference, we find a roughness of the edge with a peak-to-valley of $20-50~\mu$m. (b) The slit mounted on a translation stage and moved into the cavity to measure the mode displacement. The red illumination is stemming from interferometric light.

mode center and thereby showing a maximum in the signal.

Intuitively, we expect lower transmission signals for narrower slits and a plateau at the signal maximum, for slits which are multiple times larger than the mode diameter. To figure out the ideal slit size, we measured signals for a slit measurement on a Gaussian mode of 689 nm light with a mode size of $396~\mu$m, which is the result of a plano-concave cavity with 50 mm length and a 10.2 m-ROC mirror. The results are plotted in Fig. 4.20. Slit sizes of $600-1400~\mu$m show a distinct local maximum with increasing maximum for larger slit sizes. Measurements with slit sizes of $700-800~\mu$m showed signal shapes which were close to a Gaussian and therefore we used these slit sizes for most overlap measurements.

In Fig. 4.20, we also show the results of a FO simulation for the slit measurement. Here, for each position of the slit, we let the field propagate 150 times until we see the field converging and assume this to be the eigenmode of the system. In the end, we integrate over the field to receive a measure for the power. We see some qualitative agreement with the data, but find deviations especially in low transmission regions. This can be explained by diffraction of the edges of the slit, around which the light can find a slightly longer resonant path in the cavity. In the experiment we observe transmission in these regions, as the laser scans over a large range of frequencies, and we see a shift of the mode resonance. The FO simulation always starts with infinitely narrow resonant frequency to the cavity without the slit, and therefore cannot account for this. The deviations around high transmission regions, could be explained by an effectively smaller slit size caused by the rough cutting edges of $20-50~\mu$m [Fig. 4.19 (a)], as they might scatter more light than the smooth edges in the simulation.
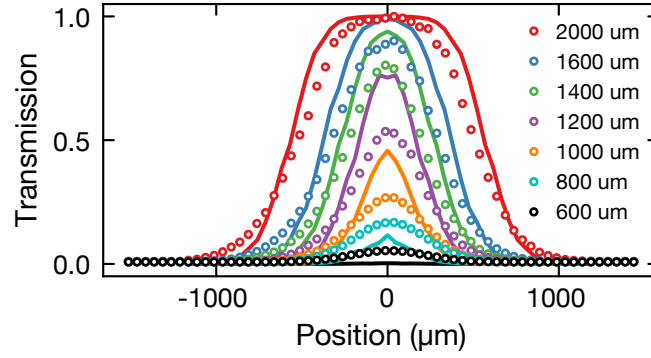
Fig. 4.20 Cavity transmission measurements versus the position of a slit, which is moved through the cavity. The signal shows a Gaussian shape with a maximum at the mode center. For the largest slit size of $2000\ \mu$m, we see a plateau forming at the center of the mode.
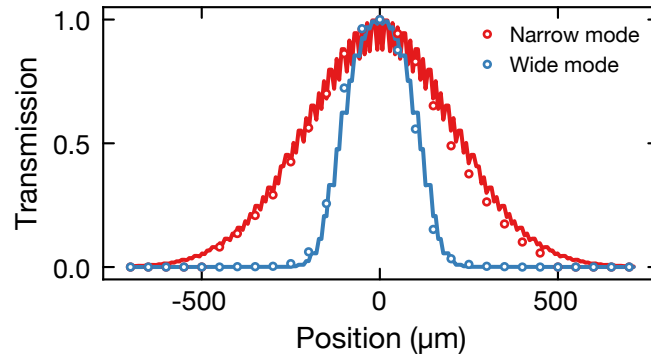

Fig. 4.21 Signal shapes of slit size measurements of two cavities with $50\ \mathrm{mm}$ length. The narrow and wide modes are stemming from a cavity with a $50\ \mathrm{cm}$ and $10.2\ \mathrm{m}$-ROC mirror, respectively. The FO simulation can reproduce the width of the signals, while the fluctuations on the signal of the wide mode are probably unresolved interferences which only occur when the slit size is relatively small compared to the mode diameter.

Slit measurement of narrow and wide modes

As already mentioned, we expected to see a plateau in each signal, when the slit is multiple times larger than the beam waist. However, we did several overlap measurements on a "test spacer", with a narrow and a wide cavity mode. One surface pair of the spacer did not fulfill the specifications and, therefore, a $50\ \mathrm{cm}$-ROC substrate had to be attached, yielding a mode diameter at the center of the cavity of $186\ \mu$m[Eq. (4.22)]. The orthogonal cavity mode is generated with a flat and a $10.2\ \mathrm{m}$ mirror which leads to a mode diameter of $396\ \mu$m[Eq. (4.22)]. The slit size we chose for the measurement was $700\ \mu$m.

In Fig. 4.21 we display the results of the measurement together with the results of the FO simulation. Contrary to our assumption, the width of the narrow mode also leads to a much narrower signal compared to the larger mode. The FO simulation agrees with

the measurement. However, the wide mode shows a noisy curve, as the combination of mode and slit size leads to extremely low field intensities and would need to be resolved with higher pixel resolution. This finding is related to the stronger radius of curvature of the 50 cm-ROC mirror. We assume that the stronger curvature leads to a larger spatial spread of circulating light which is constrained by the slit. Light could still be present in regions a few waist sizes away from the mode, where it destructively interferes and only constructively interferes in the center. Clipping only the outer regions of the mode, which affects only 0.03 % of the field intensity, therefore might have a larger effect on the reduction of the signal. With a flat and a 10.2 m-ROC mirror, however, we can think of a plane-parallel cavity where light can travel back and forth without involving (much) angular spread. Therefore, the signal of the wide mode is wider than the signal of the narrow mode as it is less influenced by clipping through the slit.

Measurement of mode sizes

Another aspect to consider is, if these measurements can be used for an extraction of the mode size. In Fig. 4.20 we saw a rather bad agreement of the FO simulation with the data. We think, that a knife edge measurement performed on a mode and extracting the width σ via the fit function in Eq. (4.38) would be possible way to measure the mode size. However, we cannot compare the simulation with the data taken directly. In that sense, a calibration with well known mode sizes to find a relation $w(\sigma)$ would be necessary.

However, we measured σ of a cavity with a 10.2 m mirror, before and after optical contacting. Before contacting, the mirror was less than half a millimeter close to the spacer surface, such that we can neglect mode size changes by length changes in this case. We found a σ of $349(5)$ μm before and $378(7)$ μm after contacting, which could hints on a mode size increase of 8.3 %. As our mirrors have a ROC of 10.2 m, which we verified by interferometric measurements, this could lead to a mode size from $396(6)$ μm to $429(8)$ μm and would correspond to a new ROC of 14 m, caused by induced mechanical stress and deformation of the substrate by the optical contacting process.

This however, would need more investigation of width measurements before and after optical contacting. Also, this indication could be supported by the measured MI size in the experiment later on.

4.5.2 Systematics

Throughout our work with overlap measurements, we discovered possible systematic errors and eliminated them. The slit is mounted on a long extension on a three-axis translation stage. The whole construction of the translation stage is shown in Fig. 4.13 (b). The slit is mounted at a 45 ° angle with respect to the table, such that it can obstruct both modes equally [Fig. 4.19 (b)].

The first systematic, is orthogonal movement of the slit to the modes. Each translation stage has an angular deviation, which means that the angle of the translation stage changes within this range when being moved. A typical value we infer from knife edge measurements is 100 μrad (for the PT3/M sold by Thorlabs). Unfavorable mounting of

the slit can therefore lead to $10\ \mu\mathrm{m}$ movement, when the slit is mounted on a $10\ \mathrm{cm}$ long rod. In other words, the angular deviation of the translation stage can lead to slit movements along the moving direction. However, mounting of the slit as shown in Fig. 4.19 (b) only leads to micrometer movements within the plane spanned by the modes, but not within the measurement direction.

Secondly, the slit is supposed to be moved through the crossing of the modes. This eliminates systematics which would be caused by a slightly tilted slit, which would clip modes at different positions lower or higher than the other mode. For a slit, which would cut the modes $1\ \mathrm{mm}$ away from the crossing, the displacement would be influenced by $25\ \mu\mathrm{m}/°$. Also, if the modes are not oriented completely orthogonal to the direction of the slit movement this would lead to same systematic. A method to circumvent this problem is the integration of a vertical slit in the metal sheet. With that, we can maximize the transmission through the vertical slit first, before we do the measurement with the horizontal slit. By this procedure, we ensure that we move the slit through the modes at the crossing and minimize the effect of this systematic.

Last and most importantly, we observed systematics by imperfections of the alignment of the input beam at each cavity. As our flat and $10.2\ \mathrm{m}$-ROC mirrors are almost plane-parallel, a slightly shifted input beam can yet circulate between the mirror surfaces through the slit and show a maximum at the position given by the input beam. A larger input beam leads to a wider signal. For that reason we improved the mode matching to the TEM_{00} mode to $96\ \%$, while making sure that the odd modes vanish. In this case, the input beam is perfectly centered on the Gaussian mode and incident with the right angle. Under this condition, we minimize the effect of this systematic to $\pm 20\ \mu\mathrm{m}$, leading to the largest uncertainty of the measurement.

4.5.3 Definition of the overlap

To characterize the overlap of the crossed cavity later on, we need to define it first: we define the overlap by considering the cross section of the intensities $I_1(z)$ and $I_2(z)$ of both modes at the position of the atoms. Therefore, we define the intensities with amplitudes I_{01} and I_{02} and Gaussian envelope of both, which have widths w_{01} and w_{02}, respectively. The overlap is then the integral over the overlapping functions

$$O(z_1, w_{01}, z_2, w_{02}) = \frac{\int_{-\infty}^{\infty} \min\left(I_1(z), I_2(z)\right) \mathrm{d}z}{\int_{-\infty}^{\infty} I_1(z)\mathrm{d}z + \int_{-\infty}^{\infty} I_2(z)\mathrm{d}z} . \tag{4.39}$$

Here, z_1 and z_2 are the center position of the Gaussian envelopes along the Z axis. We can evaluate this expression and obtain

$$
\begin{aligned}
O(z_1, w_{01}, z_2, w_{02}) &= \frac{2}{\sqrt{\pi}(w_{01}I_{01} + w_{02}I_{02})} \int_{z_{\text{int}}}^{\infty} I_{01} \exp\left(-2\frac{(z-z_1)^2}{w_{01}{}^2}\right) \mathrm{d}z \\
&+ \frac{2}{\sqrt{\pi}(w_{01}I_{01} + w_{02}I_{02})} \int_{-\infty}^{z_{\text{int}}} I_{02} \exp\left(-2\frac{(z-z_2)^2}{w_{02}{}^2}\right) \mathrm{d}z \\
&= \frac{w_{01}I_{01}}{w_{01}I_{01} + w_{02}I_{02}} \left[1 - \mathrm{erf}\left(\sqrt{2}\frac{z_{\text{int}} - z_1}{w_{01}}\right)\right] \\
&+ \frac{w_{02}I_{02}}{w_{01}I_{01} + w_{02}I_{02}} \left[1 - \mathrm{erf}\left(\sqrt{2}\frac{z_2 - z_{\text{int}}}{w_{02}}\right)\right] .
\end{aligned}
\tag{4.40}
$$

So far, we only could evaluate both integrals up to a intersection point z_{int} of both functions, which we also find analytically

$$
z_{\text{int}} = \frac{z_1 w_{02} \pm z_2 w_{01}}{w_{02} \pm w_{01}} .
\tag{4.41}
$$

We see that there are actually two intersection points. If we assume that both Gaussians have similar widths, we find one point close to the maxima of both functions, and one point at very small values, which we neglect since it would hardly influence the result. Since we match the mode sizes and intensities in the cavity in the experiment, we set $I_{01} = I_{02}$ and $w_{01} = w_{02} = w_0$, where we find $z_{\text{int}} = (z_1 + z_2)/2$ to be exactly in the middle of both modes. Note that the other intersection point diverges in this case. By taking the solution z_{int} into account, we find for the overlap

$$
O(z_1, z_2, w_0) = 1 - \mathrm{erf}\left(\frac{d}{\sqrt{2}w_0}\right) \approx 1 - \sqrt{\frac{2}{\pi}}\frac{d}{w_0} ,
\tag{4.42}
$$

where we introduced the mode displacement $d = z_2 - z_1$ and approximated the error function for small arguments in the last step. Keep in mind that we always have to consider positive numbers for d such that the overlap is a value smaller than one. The equations here are based on our assumption on the position of the modes 1 and 2 without loss of generality. Concluding, we always need to compare the mode displacement d to the width w_0 of both modes. To do so, we use a calculated value for w_0 depending on the cavity geometry and wavelength. To be even more precise, we would have to measure the width of both cavity modes and use Eq. (4.40) and (4.41).

4.5.4 Results

In this subsection we present our results after going through theory, preparation, building and the definition of the overlap: We built two suitable crossed cavities with a satisfying overlap. The second best one had a mode displacement of $15(5)\ \mu\mathrm{m}$, which we express as an overlap of $97.0(1.7)\ \%$. The number for the overlap is obtained with expression (4.42)
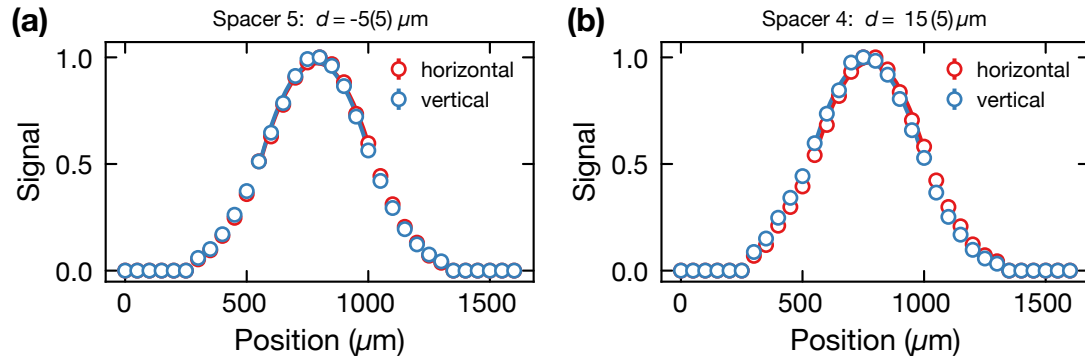
Fig. 4.22 Examples for final characterization measurements for the best crossed cavity (a) and the second best crossed cavity (b).

	rotation angle	reference surface A	mode displacement (μm)	overlap (%)
	0 °	front	2(4)	99.6
	90 °	front	-3(4)	99.4
	180 °	front	9(6)	98.2
	270 °	front	2(4)	99.6
	0 °	back	9(4)	98.2
	90 °	back	-18(6)	96.4
	180 °	back	8(7)	98.4
	270 °	back	-5(5)	99.0
Result			1(2)	99.8(7)

Tab. 4.1 Results of overlap measurements of the final crossed cavity in eight different orientations. The resulting displacement is a weighted average.

with a waist 396 μm which we obtain in our cavity design at a wavelength of 689 nm, which is the wavelength we used for the measurements.

The results of our best crossed cavity are shown in Tab. 4.1. An image of this crossed cavity is shown in Fig. 4.9. We find a displacement of 1(2) μm of the two modes with a corresponding overlap of 99.8(7) % after measuring the overlap in eight different orientations of the crossed cavity. These eight orientations were obtained by employing four 90 ° rotations around the center bore, and once again after one 180 ° rotation around a diagonal passing between the two flat and the two curved mirrors. By measuring in different orientations we hoped to cancel out systematics, which were depending on geometry, for example an error on the angle of modes with respect to the measurement coordinate system which could be caused by imperfections of the mount. Furthermore, we obtained eight independent values of the displacement to evaluate the weighted mean and thereby determined the overall displacement. We have to admit that this result exceeded our expectations as this crossed cavity seems to perfect. However, we are looking forward to see if overlap measurements with atoms show comparable results, in whatever way they may be performed.

Note that we used the overlap measurements to determine the frequency separation between the TEM_{00} modes of both orthogonal cavity arms $\Delta\nu_{00,689}$. This is important to determine the frequency offsets for each laser beam which is locked to one of the cavity arms in the experiments, as we will see in section 5.1. Therefore, we frequency-scanned a laser over both TEM_{00} modes while observing a transmission peak of higher-order Gaussian modes separated by $2\nu_{\text{sep}} = 2 \times 66.9$ MHz [subsection 4.1.4], which we fitted with Lorentzians and used the resulting time interval as a time-to-frequency conversion. Consequently, the time interval obtained from the two TEM_{00} modes yielded $\Delta\nu_{00,689}$.

4.6 Power enhancement

A buildup cavity enhances the circulating intensity or power inside its optical resonator. After discussing design specifications and features, we take a look at the corresponding power enhancement achieved by our reflective multiband coating.

4.6.1 Measurement procedure

After we worked out the basics in section 4.1.6, we want to turn these into a recipe of how to measure the enhancement Λ for the cavity. As we prefer a direct measurement, we need to set up a laser lock and measure the finesse $\mathcal{F}$, the input P_i and the transmitted power $P_t = T_{\text{cav}}P_i$. In addition, we have to estimate the power in the sidebands, which are needed for a PDH lock and the power left in other cavity modes [137]. This can be done by taking the peak height of the sidebands and higher order modes, to relate them to the sum of all peaks, and thus to obtain the fraction ξ of the power which is lost from P_i'. Thus, we have $P_i = (1 - \xi)P_i'$. With that, we

1. measure the Finesse $\mathcal{F}$ to obtain r^2,

2. measure the cavity transmission coefficient T_{cav}, which yields $\Lambda = \sqrt{T_{\text{cav}}}/(1 - r^2)$.

4.6.2 Finesse and enhancement

Depending on the trapping wavelength we chose enhancement factors of $10 - 1000$. For wavelength where we use diode lasers (typically with only few ten milliwatts of optical power and no tapered amplifiers available), we need a larger enhancement, whereas for visible red to IR wavelength in the range of $780 - 920$ nm our TiSapph can provide several Watts of optical power.

We show the specified and measured finesse values together with the expected and measured enhancement coefficients in Tab. 4.2. We specify relatively high finesses of 3000 for the initially planned imaging wavelength 389 nm and 914 nm, where extremely deep lattices are necessary, and for the 633 nm diode laser, which has an output power of $\sim$20 mW and no good options to amplify this power are available. At the other wavelengths, we aim for a moderate finesse value of 300 to provide enough power for the

	λ (nm)	$\mathcal{F}_{\text{spec}}$	$\mathcal{F}_{\text{meas}}$	Λ_{spec}	Λ_{meas}
blue magic ${}^1S_0$- ${}^3P_0$, ${}^3P_1$	389	3000	4693(171)$*$	955	117(5)$*$
tune-out ${}^3P_0$	633	3000	4183(168)$*$	955	660(62)$*$
tune-out ${}^1S_0$	689.2	300	522(19)	95	147(5)
red magic ${}^1S_0$- ${}^3P_0$	813	300	572(14)	95	161(5)
red magic ${}^1S_0$- ${}^3P_1$	914	3000	5025(58)	95	1132(13)
high power	1064	30	-	9	-

Tab. 4.2 Specified and measured finesse values $\mathcal{F}_{\text{spec}}$ and $\mathcal{F}_{\text{meas}}$ together with the corresponding enhancement Λ_{spec} and Λ_{meas} are shown for the state-dependent wavelengths of our multiband coating. Errors are standard deviations taken from a set of $5-10$ measurements. Numbers marked with an asterisk are measured on the former test coating.

large lattice beams, while the 1064 nm wavelengths comes with high power lasers and only requires a small finesse value to form homogenous cavity modes.

The finesse measurements for 689.2 nm and 813 nm are done by linewidth measurements on TEM$_{00}$ cavity mode with time-to-frequency calibration obtained by EOM-generated sidebands. The 914 nm value is taken with a cavity ringdown measurement, as the finesse for this wavelengths is sufficiently large to not be influenced by systematics originating from the AOM switching time. For these wavelengths, the finesses exceed the specifications.

The same statement remains true for the enhancement factors of these three wavelengths. As described in 4.6.1, we measure the input and output power at the cavity at each wavelength to receive a value for the enhancement. To average our results and confirm a linear enhancement behavior, we measure the enhancement for different input powers and obtained satisfying results.

The finesse measurements for 389 nm and 633 nm are taken on the previous test coating. The 633 nm finesse value was obtained with a cavity ringdown measurement, while the enhancement factor was determined indirectly by calculating it with r from the finesse measurement, and t from a standard transmission measurement of a single mirror. Locking the laser to determine T_{cav} is difficult as our one-body Littrow laser design, we used at this time, showed a hideous frequency stability. We suspect, that our new linear laser design will perform better to do these measurements, but our near-future plans do not include this wavelength.

The 389 nm finesse measurement was taken by observing an interference pattern, which forms when the laser is scanned fast enough over the cavity resonance. A good description of this measurement is provided by Ref. [138]. At this time, this was easier for us as we did not have suitable high-power EOM to lock the laser to the cavity. Note that, from our experience these measurements rely on a good signal-to-noise ratio and can easily underly systematics, such as strong jittering of the laser frequency. Hence, we advice to take a cavity ringdown measurement when you need to know the frequency of the cavity precisely and you have the time and capabilities to do so.

The enhancement coefficient at the 389 nm wavelength turned out to be disappointing
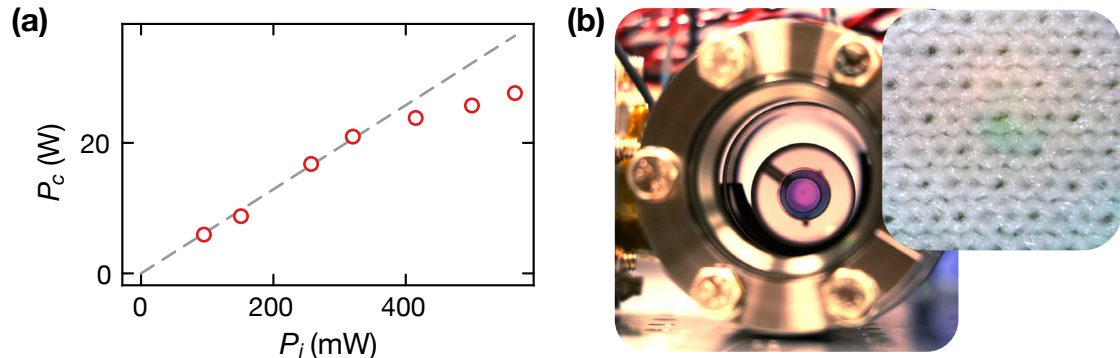
(a)

(b)

Fig. 4.23 Complications with high-power UV light in cavities. (a) Intracavity power P_{cav} versus input power in a 10 cm long cavity with a flat and 50 cm ROC mirrors. (b) Dark spots appear on the cavity mirrors and viewports after locking the UV laser for a total of two hours. On a white background, we observe the dark spot on the reflective mirror surface under a microscope.

due to unexpected high loss coefficients, which we found to be $l^2 \approx 600$ ppm (instead of ~ 100 ppm). We obtained this result by transmission measurements through the cavity yielding $T_{cav} \approx 3.5$ %. At this point, we elaborate on this and discuss a few more issues with the 389 nm wavelength in the next section.

4.6.3 Limitations on the UV lattice

One of our initial plans was to use the UV lattice as an imaging lattice with a wavelength of 389 nm with a small lattice spacing. To do so, we required ~ 200 W of circulating power in a cavity mode with a $1/e^2$ beam radius of 297 μm to achieve a ~ 1000 E_{rec} deep lattice, which can be used for direct sideband cooling with sufficiently large scattering rate for imaging on the narrow $^1S_0$–$^3P_1$ transition. The buildup measurements were useful to see how much circulating power we can achieve.

To perform this measurement, we locked the frequency doubled titanium-sapphire laser to an in-vacuum test cavity with different levels of input power P_{in}, and measured the transmitted power as usual. The test cavity provided a smaller mode diameter (157 μm $1/e^2$ waist at the flat mirror), as we used a 10 cm long cavity with a flat and 50 cm ROC configuration. The resulting buildup measurement for the 389 nm wavelength is shown in Fig. 4.23 (a).

We repeatedly found deviations from a linear enhancement above an input power of ~ 350 mW, which showed a decrease in Λ_{meas} from $117(5)$ to $103(5)$. The circulating power P_c is calculated by taking into account the transmission of only the first four points, which are also used to draw the linear fit. We assume that this behavior can be attributed to local heating in the coating surfaces, which is on the order of 10 mW assuming half of our losses are absorption losses in the mirror coating, leading to potential changes in the reflectivity coefficient r^2 rather than the transmission coefficient t^2. Nevertheless, it seemed that we were not able to achieve more than 25 W of power in this cavity

setup. Translating this value to the large cavity modes by leaving the maximum intensity constant, we could potentially achieve $\sim$90 W in the crossed cavity, which would still not fulfill our imaging requirements. A similar saturation behavior of the enhancement coefficient in a green enhancement cavity was observed in Ref. [139].

Along with this, we found another issue: When setting up the test cavity setup for the first time, we did not a very careful job of cleaning it. When the UV laser was locked to the cavity for about two hours with an input power of $\sim$500 mW, we found an immediate degradation of the finesse from $4693(171)$ to $1535(350)$, which manifested a significant decrease in transmission of the TEM_{00} mode. After some investigation, we found dark spots on the inside of the vacuum chamber viewports and on the inside and outside of the cavity mirrors [Fig. 4.23 (b)]. This could be UV-light-induced breakup of residual carbohydrates in vacuum, similar to what was observed in Refs. [140, 141, 139], although the dark spots did not vanish in air and had to be cleaned off with solvents.

We concluded from this, that working with UV light requires cavity mirrors which are exclusively optimized for this wavelength. Our multiband test coating was also optimized for this wavelength and the corresponding Bragg layers for the shortest wavelength are always on top to minimize Rayleigh scattering, but compromises to fulfill the other specifications were made.

4.7 Mounting the cavity inside the science chamber

Not only was building a crossed cavity a challenge, but so was the mounting structure a maybe even more challenging and important task. During the contacting procedure we already realized how prone the crossed cavity was to mechanical stress: in our initial contacting trials we clamped the spacer with moderate stress in its mount, such that it could not move anymore and was held by friction [Fig. 4.15 (b)]. After we found a satisfying overlap, we released the cavity and remeasured the overlap with the cavity resting in the mount, without applying clamping force. We found that the overlap had changed on the order of $50 - 100 \ \mu\text{m}$.

With that in mind, we invented different mounting structures. All of these were designed such that we were able to mount the cavity on a bucket window (which is part of the science chamber). All tests were performed with a test spacer, consisting of narrow and a wide cavity mode, generated by a flat and 50 cm-ROC mirror pair and flat and 10.2 m-ROC mirror pair, respectively. As the narrow mode is almost insensitive to relative angles of the mirror pair, we can individually measure the influence on mechanical stress on the wide mode, which will be present in the final crossed cavity. An overview of the most important structures we tested is given in Fig. 4.24.

Our requirements to the mounting structure were simple: not influencing the overlap, and if it would, the overlap should not be prone to thermal changes. In other words, a mount that influences the overlap could be used to tune it, if it is not satisfying already. In that sense, the entire assembly needs to show the same overlap in a measurement after a bakeout procedure at which the setup is heated up to $200\,^\circ\text{C}$ for a at least a few hours and is ramped down to room temperature again. Furthermore, the mount should constrain

(a)   **(b)**   **(c)**
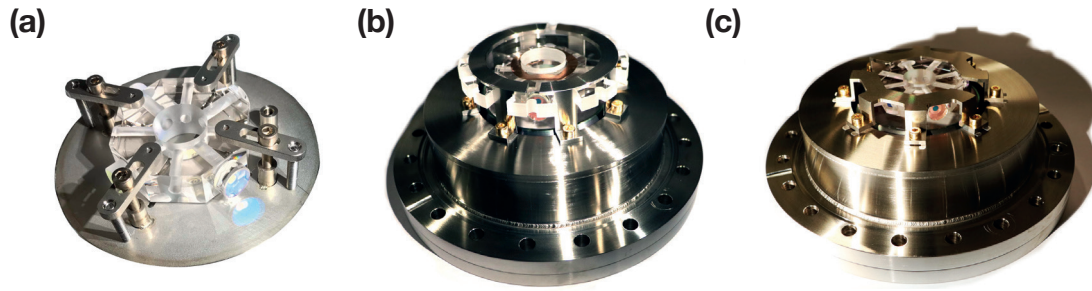

Fig. 4.24 Different cavity mounting structures. (a) The first mount was based on clamps which transmitted a spring force via stainless steel spheres to generate friction and prevent the crossed cavity from moving. (b) One of the later versions. A stainless steel cage is holding a glass plate in place. A circular spring underneath the glass plate generates friction and thus prevents the crossed cavity from moving. (c) The crossed cavity is resting in a cage without clamping.

the cavity, such that it cannot move over time. A movement of the cavity would mean a movement of the atomic system position and would require re-optimization of the input beams, the transport laser beam, and microscope objective alignment (if even possible).

4.7.1 Clamping force transmitted by steel spheres

The first idea we had was simple. This structure was built on a "test bucket window" which we solely designed to test mounting structures and their behavior during bakeout procedures. The mount consisted of four clamps where stainless steel spheres transmitted the force between the clamps and the cavity spacer [Fig. 4.24 (a)]. A steel wire of $200\ \mu$m thickness is placed between the crossed cavity and the test bucket window, to avoid virtual leaks in vacuum later on. By the friction force, generated by the steel spheres, the spacer was constrained in position. We expected that a symmetrically distributed force at four points of the spacer, matching the symmetry of the optical axes of the cavity modes, would preserve the overlap. However, mounting the spacer showed that even marginal turns of the screws lead to overlap changes up to $200\ \mu$m (when we tightened the screws, we measured the overlap at the same time).

After we were satisfied with the overlap, we enclosed the test bucket window in a vacuum chamber, also designed for testing. We followed a bakeout procedure by heating the chamber up to $200\ °$C, kept this temperature for a few hours, and ramped the temperature down to room temperature again. By taking the test bucket window out of the chamber, we found that one of the steel spheres was not even touching the spacer anymore. The overlap measurement yielded $165(3)\ \mu$m. After unmounting the crossed cavity and remeasuring the overlap several times, we found the overlap to be the same as before. From this test we learned, that pointed clamping led to a large sensitivity to the overlap in general and therefore the mount to be prone to temperature changes. Furthermore, it was hard to match the symmetry of the octagon with four individual points. A finite

elements simulation to study the existence or position of points, where the relative angle of mirror pairs is preserved, would be helpful for mounting structures of this kind.

4.7.2 Clamping force with a circular spring

In Fig. 4.24 (b) we show the version of a mount, which uses clamping force of a circular spring to constrain the crossed cavity in position. The circular spring is $7 \, \mathrm{mm}$ wide and has four contact points, which match the symmetry of the octagon-shaped spacer. The width of the spring provides a more homogeneous clamping force, while it can maintain the friction during thermal expansion of the mount during bakeout procedures. The spring itself is made out of beryllium-copper or stainless steel, to ensure vacuum-compatibility, and pressed down by a glass plate. Here, we use glass to avoid Eddy currents and minimize the amount of metal we use. A metal cage, which consists out of two half-rings, to keep the glass plate in position and to not favor the existence of Eddy currents, is screwed down tightly by vacuum-vented gold-plated screws.

Mounting the cross-cavity showed a sensitive behavior of overlap changes to the contact points of the spring on the spacer. Reducing the spring force, however, did not reduce the influence on the overlap significantly in our experience. Several bakeout tests with slightly different variations on the mounting structure were performed. The overlap measurements before and after showed displacements of $\pm 30 \, \mu\mathrm{m}$. From these results, including the sensitivity of the overlap to the contact points, we could not conclude if these changes were only stemming from the systematics, described in section 4.5.2, or actual changes of the overlap of $\sim 10 \, \%$.

4.7.3 Resting in a cage

After realizing that clamping force always led to sensitivities and therefore overlap changes, we concluded to build a mounting structure, where the crossed cavity can rest without being clamped. The challenge which was left to solve here was the spatial constraint of the cavity. Therefore, we had V-shaped lips at the bottom side of the flat sheet at the top of each part of the cage, which can be moved closer to the cavity and therefore constrain it. We found that a tolerance of about $200 \, \mu\mathrm{m}$ left the crossed cavity just enough space, such that it was not clamped by friction at the sides when tightening the screws on the cage.

After mounting the final crossed cavity, it had a little gap to the mount, such that we could check whether the cavity was clamped or not by moving it slightly. This was the case before and after the bakeout test, which also yielded a result of $-11(7) \, \mu\mathrm{m}$ before and $+20(5) \, \mu\mathrm{m}$ after the bakeout test, respectively. With this as a final test, we inserted the bucket window together with the cavity into the science chamber and closed it.

ν_{FSR}	3 GHz		$w_{689.2}$	396 μm
ν_{sep}	66.9 MHz		w_{813}	430 μm
$\Delta\nu_{00,689}$	19.9(4) MHz		w_{914}	456 μm
d	1(2) μm		$O(396\ \mu\mathrm{m})$	99.8(7) %
$\mathcal{F}_{689}$	533(19)		Λ_{689}	147(5)
$\mathcal{F}_{813}$	572(14)		Λ_{813}	161(5)
$\mathcal{F}_{914}$	5025(58)		Λ_{914}	1132(13)

Tab. 4.3 The most important parameters summarized. All measured quantities are shown with an error. The mode separation frequency ν_{sep} was calculated in section 4.1.4.

4.8 Conclusion

In hindsight, we found that choosing a 10.2 m-ROC for the curved mirror substrate led to increased sensitivity and thus an increased effort during the contacting procedure. Following our contacting procedure and strategy, a ROC of 2 m (5 m) would decrease the sensitivity to relative angles between the mirrors of the mirror pair and would enable a deterministic prediction of the overlap before the mirror is attached. According to Eq. (4.22) the suggested ROCs would reduce the mode diameter only by 33 % (16 %) while reducing the sensitivity to relative angles by a factor of 5 (2). Combining this with a shorter wavelength for the interferometric light, we believe that a deterministic prediction of the overlap before contacting is possible and thus would dramatically reduce the number of trials necessary to achieve a satisfying overlap. Also, keeping all other specifications, such as the parallelism of the spacer surfaces and wedge error of the mirrors, we presume that methods focusing on positioning the mirror well-centered on a spacer bore, would also produce overlaps > 90 % within only a few trials.

Nevertheless, we achieved a crossed cavity with an overlap close to 100 %. Whether this measurement represents the actual overlap has to be checked with a measurement including atoms. By doing that, we want to make sure, no other systematic has influenced our overlap measurement such that the result was better than it actually should be. For convenience, we summarize the most important parameters in Tab. 4.3.

We propose that this invention can be implemented to achieve an enlargement of the system size in quantum simulation with a factor of a 40 more atoms in a two-dimensional array, comparing our predictions to state-of-the-art fermionic quantum gas microscopes with a MI size of 30×30 atoms [21, 20].

Next to achieving a larger system size in quantum simulation, a monolithic crossed cavity with an overlap like this could be useful for optical lattice clocks. Constrained by optical power requirements, the $1/e^2$ beam radius is also around 100 μm, which would be improved to ~ 400 μm per beam using our crossed cavity design. The number of probed atoms thus increases by a factor of 16 leading to an improvement of the signal-to-noise ratio using classical averaging alone (as is scales with $1/\sqrt{N}$ with the atom number N). By employing quantum metrological techniques, the signal-to-noise ratio can be improved by the full factor of 16 (as the Heisenberg limit is given by $1/N$ [142]). Note that, an

implementation of the crossed cavity in optical clock setups would most likely require additional fine-tuning of the cavity length to match the cavity resonances better with required magic-wavelengths.

Our monolithic crossed cavity design would also be beneficial by implementing it in optical lattice clocks in space missions, which are of interest for fundamental research as well as for future-generation GPS satellites. For example, a space-compatible optical lattice clock is a challenge which is specifically encountered by the ISOC project [143]. To our knowledge, transportable clocks which for instance are used for geodesy missions on earth still rely on retro-reflected lattices, such as the transportable optical lattice clock by the Physikalisch-Technische Bundesanstalt (PTB) [144–146]. We believe that our crossed cavity design is not prone to strong acceleration, such as during rocket launches or being transported in a moving truck, or any temperature changes associated with that. In other words, no re-alignment of the lattice (afterwards) is necessary.

Taking all of these advantages into account, the crossed cavity design currently is object of an international patent application (MI 1202-5819 - vB 22530/PCT).

Chapter 5

State-Dependent Lattices in the Crossed Cavity

ONE of the goals in our experiment is the generation of large, state-dependent optical lattices in the crossed cavity. We came closer to achieving this goal by performing measurements of and with the $^1S_0$ ground state tune-out wavelength in chapter 3 and by building the crossed cavity throughout chapter 4. We now take a brief look at the combination of the knowledge we gained during our work and see how the realization of state-dependent optical lattices will look like after the planned implementations over the next few months.

We start this brief chapter by proposing a laser stabilization scheme for the lattice lasers to the crossed cavity in the first section. This prospect is followed by a discussion about frequency-to-amplitude noise conversion in the cavity and related to potential parametric heating of the atoms. The next section describes a frequency uncertainty for the state-dependent lattice, which is set by the free spectral range of the cavity, and investigates its effects at the example of the $^1S_0$ tune-out wavelength. Having collected all these tools, the last section discusses possible parameter regimes for a quantum simulation of light-matter interfaces with our setup.

5.1 Lattice laser stabilization scheme

First, we focus on the implementation of the lattice lasers. We have a titanium-sapphire laser to generate magic-wavelength lattices in the near-infrared spectrum, and several diode lasers to produce laser light for state-dependent lattices. The beams of each laser will be split into two and coupled to the cavity. If necessary, the beams of two or more lasers have to be merged beforehand. Most likely, we will combine a physics lattice with an imaging lattice, in which the simulated physics model will evolve in time, and a deep imaging lattice, which provides strong trapping conditions during the imaging process. We will first implement the $689\,\text{nm}$ $^1S_0$ tune-out lattice together with the $813\,\text{nm}$ $^1S_0$–$^3P_0$ magic wavelength lattice.

During the experimental cycle, the atoms will be transported into the cavity via a dipole trap beam [103]. When the atoms enter the trapping region in the center of the cavity, the lattices will be turned off, such that the optical lattice potential does not hinder loading the atoms. Potentially, the lattice lasers could be locked during the whole cycle to the crossed cavity, if the power of the lasers can be lowered sufficiently while the laser stays locked.
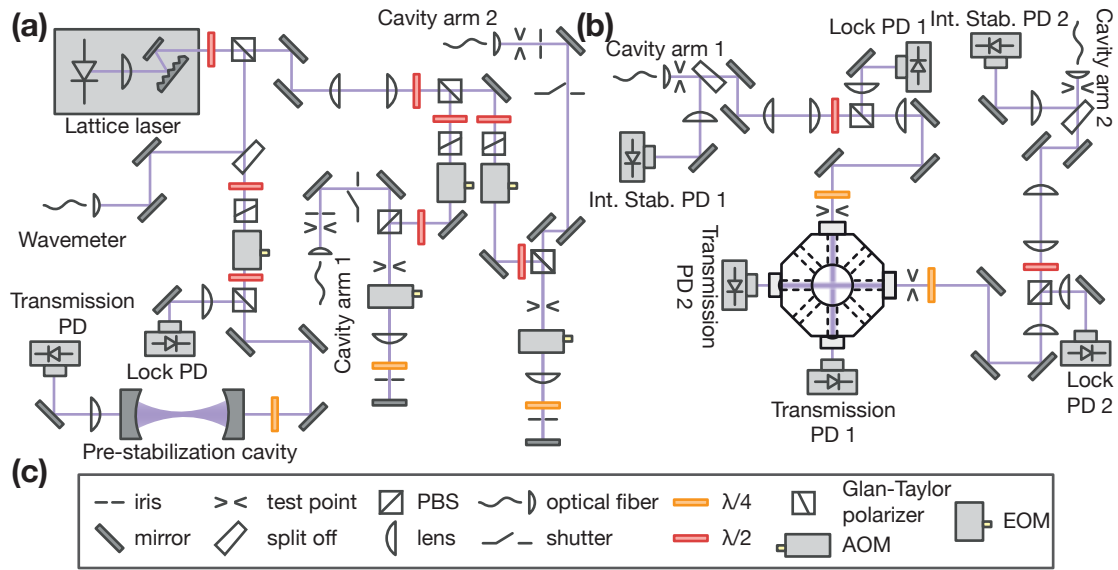
Fig. 5.1 (a) Lattice laser beam setup. The lattice laser is locked to a pre-stabilization cavity. The output beam is split into two beams, while the phase and frequency of each is modulated via an EOM and a double-pass AOM setup, respectively. (b) Lattice beam setup at the crossed cavity. (c) Legend of the displayed optical components.

Another option would be to lock the lattice lasers to a pre-stabilization cavity, which has to fulfill the same stability requirements as the crossed cavity. When the lattices need to be ramped up in the crossed cavity, a switch can turn on the lattice laser light, the cavity resonance will be found to apply a laser lock. The scheme we propose is shown in Fig. 5.1.

The lattice laser is depicted as an external-cavity-diode laser symbol, but can be replaced by other laser types. A small fraction of the laser output light is sent to the locking arm and the wavemeter. A standard Pound-Drever-Hall (PDH) lock is applied to a pre-stabilization cavity as presented in subsection 2.7.3. The transmission photodetector (PD) helps with cavity alignment and monitors the transmission level.

The beam size of the output beam of the lattice laser is adjusted with a telescope, before the beam is split into two, and sent through an EOM each. The beam shaping achieved with the telescope ensures that the full aperture of both EOMs is used, and the intensity damage threshold of the EOM crystals is not exceeded. We propose to use two EOMs after splitting the beam into two, as this reduces the applied intensity per EOM by another factor of two. The EOMs add a phase modulation to the beams, which will be used to apply PDH locks to the crossed cavity.

The phase-modulated beams are then sent to two double-pass acousto-optical modulator setups, which allows shifting the frequency of the beams by two times the AOM frequency, and allows to tune the power of each beam. The frequency shifting of each beam can compensate for the frequency detuning of both fundamental cavity modes,

which is 19.9(4) MHz at 689 nm[1] (section 4.8). The power adjustment of each beam is used to implement intensity stabilization of the lattice beams, which is crucial to avoid changes in the trap depth and trap frequency.

Both beams are coupled to fibers and sent to the cavity arms on different breadboards. After each fiber, a pick-off sends a small fraction of light onto a PD which is used in the intensity stabilization circuit. Then, a three lens combination, i.e. a telescope and a lens to focus the beam, is used to optimize the mode matching to the TEM$_{00}$ mode of the cavity. In principle, only a telescope or a lens with a suitable focal length and distance could also be used to achieve reasonable mode matching, but a three-lens system offers more versatility for adjusting the beam parameters.

Placing a polarizing beam splitter for PDH locking after the telescope seems best to us, as the incident and reflected beam will be collimated and the focus will be at the flat mirror surface of the crossed cavity. With a collimated beam, the beam splitter works well according to any specifications and an optimal amount of light is reflected and sent to the lock PD. However, for instance for 813 nm the input power into the cavity has to be quite large and attenuating the power in front of the PD will be necessary. This is due to the low saturation power of our intensity stabilization PDs of $\sim$50 μW.

As for the pre-stabilization cavities, the transmission needs to be monitored for checking the day-to-day cavity alignment and to check the transmitted power levels when the lasers are locked.

5.2 Parametric heating in the cavity

As we already pointed out in subsection 4.3.3, we have to consider parametric heating in the cavity, which can be by caused vibrations of the cavity length leading to conversion of frequency noise into amplitude noise. In addition to that, phase noise of the laser can be converted into amplitude noise. In the following, we briefly discuss the frequency-to-amplitude conversion.

In subsection 4.1.1, with Eq. (4.5) we revealed the Lorentzian nature of the cavity resonances. When the laser is locked to a resonance, the control loop keeps the frequency of the laser on the peak of the Lorentzian lineshape. Especially when the laser is locked, we can assume that our laser linewidth is narrow compared to the $\sim$1 MHz wide resonances, which means that we do not have to take the laser linewidth into account for now. The optical lattice potential in the cavity is proportional to the circulating intensity I_c, which we derived in Eq. (4.7). We use these two equations to approximate the Lorentzian peak at the resonance to second order and find that the circulating intensity changes by

$$\Delta I_c(\delta_L) = I_c(0) - I_c(\delta_L) \approx I_0 \frac{4\pi^2 r^2 t^2}{(1-r^2)^4} \frac{\delta_L{}^2}{\nu_{\text{FSR}}{}^2} = 4I_c(0) \frac{\delta_L{}^2}{\Delta\nu_C{}^2} , \qquad (5.1)$$

with a frequency deviation of δ_L of the laser frequency from the cavity resonance. Here,

---

[1]Coincidently, this value is fairly small as the frequency detuning could have been anything within half of a free spectral range, due to the large length tolerances of the spacer compared to the optical wavelength.

r and t are the amplitude reflection coefficients of both cavity mirrors, $I_c(0)$ is the peak of the circulating intensity, I_0 the initial intensity coupled to the cavity, ν_{FSR} the free spectral range, and $\Delta\nu_C$ the linewidth of the resonance[2]. In the last step we used Eq. (4.6). We see that the converted amplitude linearly depends on the circulating intensity, but grows quadratically with a narrower cavity resonance and larger detuning δ_L from the resonance. This was also one of the reasons, why we did not choose $\Delta\nu_C$ too small (and the finesse too high), as we were not sure about the resulting heating effects.

To obtain a number for the parametric heating rate Γ_ϵ in Eq. (3.2), we need to get an idea of the power spectral density S_ϵ which is a result of the converted frequency noise into amplitude noise in the cavity. In section 3.1.1, we saw that a relative modulation $\epsilon(t)$ in dependence of time t of the optical lattice depth leads to parametric heating. Our optical lattice potential in the cavity is directly proportional to I_c in the cavity and we find

$$\epsilon(t) = \frac{\Delta I_c}{I_c(0)} = 4\frac{\delta_L^2(t)}{\Delta\nu_C{}^2} \,, \tag{5.2}$$

which is a dimensionless frequency-to-amplitude-noise conversion. At this point we have to make an assumption on $\delta_L(t)$. For simplicity, we assume that $\delta_L(t)$ can be described by a single Fourier component, and reads

$$\delta_L(t) = \mathcal{A}\cos(\omega t) \,, \tag{5.3}$$

with $\mathcal{A}$ being a frequency amplitude and ω the modulation frequency. To determine $\mathcal{A}$, we relate $\delta_L(t)$ to the angular frequency noise power spectral density of the laser $S_{\omega\omega}(\omega)$ via defining

$$\langle\delta_L{}^2(t)\rangle \equiv \int_0^\infty \mathrm{d}\omega S_{\omega\omega}(\omega) \,. \tag{5.4}$$

We assume that $S_{\omega\omega}(\omega)$ has a frequency noise background b_0 up to a cut-off frequency ν_c and is 0 otherwise. The right side of our expression becomes $b_0\nu_c$ and we know from Ref. [147] that the (Gaussian) full-width-half-maximum laser linewidth $\Delta\nu_L$ of lasers with this characteristic frequency noise spectrum reads $\Delta\nu_L = 2\sqrt{2\ln(2)b_0\nu_c}$. The left side of our expression yields $\mathcal{A}^2/4$ and we can relate $\mathcal{A}$ to the laser linewidth via

$$\mathcal{A} = \frac{\Delta\nu_L}{\sqrt{2\ln(2)}} \,. \tag{5.5}$$

At this point, we need the amplitude noise power spectral density to at $2\omega_{\mathrm{trap}}$, which we calculate via [111]

$$\begin{aligned} S_\epsilon(2\omega_{\mathrm{trap}}) &\equiv \frac{2}{\pi}\int_0^\infty \mathrm{d}\tau\cos(2\omega_{\mathrm{trap}}\tau)\langle\epsilon(t)\epsilon(t+\tau)\rangle \\ &= \frac{32}{\pi\Delta\nu_C{}^4}\int_0^\infty \mathrm{d}\tau\cos(2\omega_{\mathrm{trap}}\tau)\langle\delta_L{}^2(t)\delta_L{}^2(t+\tau)\rangle \,, \end{aligned} \tag{5.6}$$

---

[2]Note that we use the subscript L and C for "Laser" and "Cavity", respectively.

where we used Eq. (5.2). We can use our assumption for $\delta_L(t)$ to evaluate the second-order auto-correlation function and find

$$\langle \delta_L{}^2(t)\delta_L{}^2(t+\tau)\rangle = \frac{\mathcal{A}^4}{4}\left(1 + \frac{1}{2}\cos(2\omega\tau)\right) . \tag{5.7}$$

The constant offset will cancel when evaluating the time integral and we find for the power spectral density

$$S_\epsilon(2\omega_{\text{trap}}) = \frac{1}{\ln(2)^2}\frac{\Delta\nu_L{}^4}{\Delta\nu_C{}^4}\left(\delta(2\omega_{\text{trap}} - 2\omega) + \delta(2\omega_{\text{trap}} + 2\omega)\right) , \tag{5.8}$$

where we used the Dirac-Delta distribution $\delta(\omega) = \frac{1}{2\pi}\int_0^\infty dt\exp(i\omega t)$. When $\omega = \omega_{\text{trap}}$, the first Delta distribution contributes and heating to higher energy states in steps of two quanta occurs. We consider the other Delta distribution as unphysical, as it requires a negative frequency. Investigating this expression, the component of our laser at frequency ω_{trap} leads to parametric heating with frequency $2\omega_{\text{trap}}$ due to the quadratic nature of frequency-to-amplitude conversion coefficient. This finding is crucial and means that the laser lock has to be optimized to suppress the lower frequency noise components at ω_{trap} instead of $2\omega_{\text{trap}}$, as one could initially assume, which is easier in practice for typical trap frequencies (of several $10\,\text{kHz}$).

Using this expression, we calculate the heating rate with Eq. (3.2) and find

$$\Gamma_\epsilon = \frac{\pi^2\nu_{\text{trap}}{}^2}{\ln(2)^2}\frac{\Delta\nu_L{}^4}{\Delta\nu_C{}^4} . \tag{5.9}$$

We can use this expression now to estimate a heating rate: our Ti:Sapph is specified to have a linewidth of $50\,\text{kHz}$ (measured over a period of $100\,\mu\text{s}$) and the cavity resonance at $813\,\text{nm}$ is $5.2\,\text{MHz}$. In a lattice with a depth of $9.6\,\text{E}_{\text{rec}}$ (corresponding to a Mott-insulator phase) we find $\nu_{\text{trap}} = 21.5\,\text{kHz}$, yielding a $\Gamma_\epsilon = 81\,1/\text{s}$. This number seems rather high, but keep in mind that we used the linewidth of a free-running laser, which will reduce when the laser is locked. The heating rate Γ_ϵ then will reduce dramatically as it scales with $\Delta\nu_L{}^4$. Getting to a laser linewidth of $\Delta\nu_L = 10\,\text{kHz}$ would sufficiently suppress the heating rate to $\Gamma_\epsilon = 0.1\,1/\text{s}$, but would probably require locking the lattice laser to a high-finesse pre-stabilization cavity. Also, the assumption made in Eq. (5.5) describes a frequency modulation with an amplitude with almost the full laser linewidth and is completely independent of frequency ω, which in reality is surely not true and rather is given by a complicated structure of frequency noise sources on the order of several $10\,\text{kHz}$ (such as vibrations and resonances in the laser gain medium).

Note that, a similar approximation can be done for frequency-to-amplitude modulation due to vibrations in the cavity as discussed in subsection 4.3.3. Here, we need to find a different expression for the amplitude of the form $\mathcal{A}' = \frac{\omega}{2\pi}\frac{\Delta L}{L}\mathcal{A}$, where L is the cavity length and the ΔL the amplitude of the acoustic vibration, which has to be determined.

5.3 Precision of state-dependent lattice frequency

When a lattice laser is locked to the crossed cavity, the laser frequency is a multiple of the free spectral range. For instance for red light around ~600 nm, we can estimate with the help of Eq. (4.3), that 1 nm of length change of a 5 cm long cavity, leads to a frequency shift of 10 GHz. As polishing techniques offer control over the cavity length with best effort on the order of 1 μm, it becomes clear that the absolute frequency of a cavity resonance cannot sufficiently be controlled. In addition, an uncontrolled phase shift in the high-reflective mirror coating needs to be compensated. Even if it could, it would only be useful for a single wavelength. Other wavelengths would be close to resonances at other multiples of the free spectral range and might require a different absolute cavity length. From these arguments we conclude that the cavity resonance, close to any wavelength, will have a practically "random" position. In the worst case, the lattice frequency we want to address is exactly in between two cavity resonances, which leads to a maximal uncertainty of 1.5 GHz.

This uncertainty can be used to estimate the effect it will have on our state-dependent lattices. Therefore, we have to estimate the slope of the (real part of the) polarizability first, as it determines the difference in the atomic potential according to Eq. (1.2). When the lattice wavelength is far detuned, the polarizability of a state k can be estimated via Eq. (1.4).

We find the curve shown in Fig. 5.2 for the ${}^1S_0$ and ${}^3P_0$ polarizability. We use the numbers presented in Fig. 1.1 for the ground state by taking into account the ${}^1S_0$–${}^3P_1$ and ${}^1S_0$–${}^1P_1$ transition, and contributions from the inner shell $\alpha_c = 5.30(5)$ a.u. and valence electrons $\alpha_v = 6.57(14)$ a.u. received from M. Safronova. For the excited ${}^3P_0$ state we used the transition wavelengths and transition matrix elements to the *5s6s* ${}^3S_1$, *5s5d* ${}^3D_1$, and *5p^2* ${}^3P_1$ states taken from Ref. [121] based on M. Safronova's recommendation. In addition, we added a contribution of 51 a.u. due to other transitions and another 5.6 a.u. originating from contributions of the core and the other valence electron from M. Safronova's theory calculations. The ${}^3P_0$ polarizability stays relatively constant compared to the ${}^1S_0$ polarizability, which is dominated by the only ~143 GHz detuned ${}^1S_0$–${}^3P_1$ transition. Fitting the slope at the zero-crossing yields 2.44 a.u./GHz, which leads to a maximum polarizability of 3.67 a.u. at a detuning of 1.5 GHz from the zero-crossing.

From the initial -48 dB suppression, which was limited by our measurement precision, we arrive at a -26 dB suppression in the worst case.

5.4 Parameter regimes for quantum simulation of light-matter interfaces

In this section we give an explicit example for parameters of the quantum simulation of light-matter interfaces, which we proposed in section 1.5. We would like to resolve the energy band structure shown in Fig. 1.7 (e). With that, the parameter regimes turn out to be similar for the observation of bound states and matter-wave emission patterns,
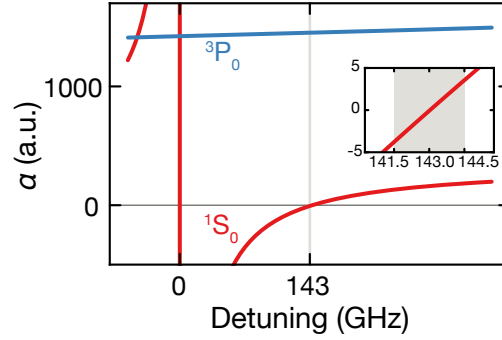
Fig. 5.2 The $^1S_0$ ground state and $^3P_0$ excited state polarizability in dependence of the detuning from the ^{88}Sr $^1S_0$–$^3P_1$ transition. At a detuning of $143\,\mathrm{GHz}$, the $^1S_0$ state polarizability crosses zero. The inset shown zooms into the $^1S_0$ state polarizability at the tune-out region. The uncertain frequency range in which the fundamental cavity modes will exist is shaded in light-gray.

as precise addressing of certain regions in the band structure, and thus, the density of states is required [Fig. 1.8]. In addition, we include the cavity enhancement factor, the available optical power of our laser at $689.2\,\mathrm{nm}$, the cavity mode size and the lifetime limitation in the $^3P_0$ state shown in section 3.4.

To simulate light-matter interfaces, we require atoms in the excited $^3P_0$ (e) state, which cannot tunnel to adjacent lattice sites during the time τ_{sim} of the simulation. During τ_{sim}, tunneling in the shallow lattice is necessary. About 100 tunneling processes should be enough to cover a large range of bound state sizes, which can be tuned by the detuning of the clock laser with respect the upper and lower band edge [42].

With the parameters we have, we need to determine the input power of the tune-out light for each cavity arm, which determines the e state lattice depth. From this we find the detuning from the tune-out frequency which is necessary to achieve a certain lattice depth for the $^1S_0$ (g) state, while ensuring that enough tunneling processes can happen during τ_{sim}.

5.4.1 One dimension

With the polarizability α_e of the e state from section 3.21, we can calculate the lattice depth V_e with the cavity buildup factor Λ_{689}, the cavity beam radius w and the input power P_i for one dimension (1D) via

$$V_e = \frac{4\Lambda_{689}P_i}{\pi c \epsilon_0 w^2}\alpha_e \,. \tag{5.10}$$

Here, we combined Eq. (1.2) with Eq. (4.29) and converted the related input intensity to power via $I_i = \frac{2P_i}{\pi w^2}$. In the following discussion, we express V_e in units of the recoil energy E_{rec}.

With a deeper lattice at the $689.2\,\mathrm{nm}$ tune-out wavelength, the occupation time $\hbar/J_e$

of a particle in a single lattice site increases. Here, J_e is the tunneling matrix element in the excited state lattice as explained in subsection 1.3.1. At the same time, the lifetime τ_e of atoms in the e state linearly decreases with the lattice depth by scattering of lattice photons from the ${}^3S_1$ state. In one dimension, we find a tunneling rate $J_e/\hbar = 1.2$ s^{-1} for a 50 E$_{\rm rec}$ deep lattice using the methods from subsection 1.3.2. The scattering rate in the lattice can be scaled via $\Gamma_{\rm sc} = 0.049$ s$^{-1} \frac{V_e}{E_{\rm rec}}$ by taking into account the results from section 3.4. Thus, for this lattice depth we find a scattering rate of $\Gamma_{\rm sc} = 1/\tau_{\rm sc} = 2.5$ s^{-1}. We assume Gaussian statistics for these two independent decoherence processes and limit the lifetime for the experiment to $\tau_{\rm sim} = 1/\sqrt{\Gamma_{\rm sc}^2 + (J_e/\hbar)^2} \approx 0.37$ s, after which a $\sim 1/e$ fraction of the e state atoms has been lost.

We achieve this lattice depth with an input power of ~ 13.8 mW, which is less than the available power we can achieve with the use of injection locks or tapered amplifiers. In the shallow lattice, we want bath particles to be mobile and g state atoms to be in a quasi-superfluid phase, respectively. This happens within a range of $\sim 1 - 9$ E$_{\rm rec}$, before the Mott-insulator phase forms (Tab. 1.1). Via the analogous expression to Eq. (5.10), we find

$$V_g = \frac{4\Lambda_{689}P_i}{\pi c\epsilon_0 w^2} \frac{\partial \alpha_g}{\partial \nu} \Delta\nu \,, \tag{5.11}$$

for the g state lattice, where we use the slope of the polarizability $\frac{\partial \alpha_g}{\partial \nu}$ from section 5.3 to determine the required detuning $\Delta\nu$ from the tune-out frequency. With the power levels stated above, we need to detune the 689.2 nm laser by $12.7 - 114$ GHz, which corresponds to $\sim 4 - 38$ free spectral ranges of the crossed cavity, respectively. To ensure about 100 tunneling processes, the typical tunneling time must not exceed 3.7 ms, taking into account $\tau_{\rm sim}$ from above, which is fulfilled for the whole range of lattice depths with tunneling rates of $J_g/\hbar = 5900 - 730$ s^{-1}, respectively.

The lowest energy band can be resolved with the Rabi frequency being ~ 10 % of the bandwidth $W = 4J_g$ of the lowest energy band. We obtain values of $\Omega = 2\pi \times 94 - 12$ Hz, which are attainable, but require a clock laser with a linewidth ideally around 1 Hz to achieve these Rabi-frequencies. The Rabi-frequency also determines the emitter excitation and emission dynamics, which have to sufficiently large to explore these dynamics.

5.4.2 Two dimensions

In two dimensions (2D), the total lifetime of the e state atoms $\tau_{\rm sim}$ reduces by a factor of two to 0.21 s. One reason is a doubled scattering rate due to a factor of two higher light intensity on each lattice site. The second reason is a doubled tunneling rate of e state atoms due twice as many opportunities to tunnel caused by the additional dimension.

The shallow lattice depth requires a range of $\sim 1 - 9$ E$_{\rm rec}$ in each dimension, such that the bath particle tunneling rate $J_g/\hbar$ and the bandwidth of the lowest energy band also increase by a factor of two. The factor of two higher tunneling rate in the g state band leads to faster dynamics and compensates directly for the factor of two lower experiment lifetime.

The input power into the cavity and the corresponding detuning is therefore unchanged.

The resulting interactions are also doubled due to the doubled bandwidth of the lowest energy band, and read $\Omega = 2\pi \times 188 - 24$ Hz.

5.5 Conclusion

We have presented a scheme of how to lock lattice lasers to the crossed cavity and pointed out possible complications with parametric heating effects. Furthermore, we estimated the influence of the frequency limitations set by the crossed cavity and investigated possible parameter regimes for a quantum simulation scheme. With attainable input powers, detunings and Rabi frequencies, this quantum simulation scheme seems absolutely feasible to us with the system we have. However, we require an overhaul of the clock laser lock setup such that a narrow laser linewidth of about 1 Hz can be achieved.

Chapter 6

Conclusion and Outlook

$\mathbb{W}$E discussed the concept and benefits of a quantum gas microscope with strontium, which is a versatile tool to study state-dependent lattice physics with long coherence times. By using the $^1S_0$ ground and $^3P_0$ excited state of strontium as a two-level system in combination with state-dependent lattices, we presented a quantum simulation model which mimics individual matter-wave emitters. In this context, we discussed the necessity of a large system and proposed an in-vacuum build up cavity to achieve the required system size.

In this thesis we reported on our progress to realize such a quantum simulator. We started by describing the building process of the world's first strontium quantum gas microscope. The trapping and cooling process of ^{88}Sr and ^{87}Sr was demonstrated, including all necessary components, such as the entire vacuum system and lasers for the blue and red MOT stages. At this point, we find reasonable atom numbers at a temperature of $\sim 1~\mu$K.

Before we implemented the in-vacuum buildup cavity to the setup, we measured the first state-dependent lattice wavelength for the strontium clock states, the $^1S_0$ ground state tune-out wavelength. With a novel measurement technique, we demonstrated the most precise measurement of a tune-out wavelength to date, if we take into account the small sensitivity to a change in optical frequency. In addition to that, we measured the polarizability of the $^3P_0$ state which allowed a reevaluation of the $^1P_1$ and $^3S_1$ state lifetimes and the $^3S_1$ decay branching ratios. In a proof-of-principle experiment, we trapped $^3P_0$ atoms in a one-dimensional lattice at the tune-out wavelength and measured the lifetime limitation of the trapped atoms due to scattering on the 10 nm-detuned $^3P_0$– $^3S_1$ transition.

After that, we demonstrated the design and building process of a monolithic in-vacuum crossed cavity, with large, optimally overlapping modes for different trapping wavelengths of strontium. With $1/e^2$ beam radii up to $456~\mu$m of the cavity modes, we estimated the Mott-insulator size and found $\sim 200 \times 200$ lattice sites. The mode overlap was characterized and measured, after which we achieved an almost perfect overlap of $99.8(7)$ %. We measured the power enhancement in the cavity for three different wavelengths and found enhancement factors up to $1132(13)$, which look promising to generate deep lattices for imaging. Different approaches of mounting of the crossed cavity on a bucket window were discussed and tested. We used the most promising approach to mount the crossed cavity in the science chamber.

Based on these numbers we are optimistic about our experimental goals. Whether the

cavity mode overlap is really almost perfect is a question that has to be answered with measurements using atoms. An idea of such a measurement could be as follows: after transporting the atoms in the dipole trap, we measure atomic transfer rates into each of the lattice arms. These measurements can be repeated for different vertical dipole trap positions. The transfer rate should show a symmetric distribution around each mode center. In addition, a vertical dimple beam would be necessary to confine the atoms at the cavity mode crossing.

Another question is if large circulating powers during imaging will have short or long-term influences on the power enhancement factor, as we have seen buildup power limitations with $389\,\mathrm{nm}$ light. The losses in the near-infrared are much lower compared to the ultraviolet regime, mostly due to Rayleigh scattering in the mirror coating. The unknown here is the absorption loss of these wavelengths, which in our opinion leads to the (indicated) saturation in the intra-cavity power.

We are excited to see if the crossed cavity design will be applied in other experiments. The expected system size enhancement would be beneficial in both many-body quantum simulation and quantum metrology, leading to more homogeneous systems and an improvement of the signal-to-noise ratio. The signal-to-noise improvement can be as large as a factor of 16 in experiments by the enhanced system size alone.

We proposed a laser locking scheme for the lattice laser to the crossed cavity in the science chamber, which we are implementing at the moment. In parallel, the transport laser setup is tested and built in. After that, we will try to transfer the first atoms to the dipole trap and see if we can get atomic transport to the cavity. The position of atoms in the cavity can be checked with a simple fluorescence imaging setup and lifetime measurements will be conducted to check on the vacuum quality inside the cavity. In addition to that, we need to measure the atomic temperature after the transport and try to cool the atoms to quantum degeneracy via evaporative cooling. Another ingredient which is still missing and about to be built in, is the magnetic field gradients and a single-layer preparation scheme before we mount and align the microscope objective and try to image the first single-site resolved atoms in a $813\,\mathrm{nm}$ magic wavelength lattice within the next months. An update on the implementation of these components will be given in the next PhD thesis by Annie Jihyun Park.

The accessible parameter space of the presented light-matter interface quantum simulation scheme is strongly limited by the scattering loss of trapped $^3P_0$ atoms in the $689\,\mathrm{nm}$ tune-out wavelength lattice. In particular, a compromise has to be found of making the excited state lattice not too deep, while not losing too many quantum emitters by tunneling processes in the excited state lattice. The resulting driven interactions tend to be rather small and call for an overhaul of the clock laser setup to achieve a narrower laser linewidth. We are confident that such quantum simulations are feasible with our strontium machine, the $^1S_0$ ground state tune-out wavelength and the buildup cavity.

Besides this particular quantum simulation scheme, we can think of many other interesting physics to study with this setup. So far, collisional phase gates have not been realized and are still an interesting challenge for quantum computing and simulations. We look forward to see in which direction our experiment will develop and what physics

will be conducted in the near future.

References

[1]   R. P. Feynman. *Simulating physics with computers*, International Journal of Theoretical Physics **21**., 467–488 (June 1982). DOI: 10.1007/BF02650179.

[2]   C. Gross and I. Bloch. *Quantum simulations with ultracold atoms in optical lattices*, Science **357**., 995–1001 (Sept. 2017). DOI: 10.1126/science.aal3837.

[3]   S. Lloyd. *Universal Quantum Simulators*, Science **273**., 1073–1078 (Aug. 1996). DOI: 10.1126/science.273.5278.1073.

[4]   I. M. Georgescu, S. Ashhab, and F. Nori. *Quantum simulation*, Rev. Mod. Phys. **86**, 153–185 (Mar. 2014). DOI: 10.1103/RevModPhys.86.153.

[5]   A. Aspuru-Guzik and P. Walther. *Photonic quantum simulators*, Nature physics **8**., 285–291 (Apr. 2012). DOI: 10.1038/nphys2253.

[6]   A. A. Houck, H. E. Türeci, and J. Koch. *On-chip quantum simulation with superconducting circuits*, Nature Physics **8**., 292 (Apr. 2012). DOI: 10.1038/nphys2251.

[7]   R. Blatt and C. Roos. *Quantum simulations with trapped ions*, Nature Physics **8**, 277–284 (Apr. 2012). DOI: 10.1038/nphys2252.

[8]   I. Bloch, J. Dalibard, and W. Zwerger. *Many-body physics with ultracold gases*, Rev. Mod. Phys. **80**, 885–964 (July 2008). DOI: 10.1103/RevModPhys.80.885.

[9]   I. Bloch, J. Dalibard, and S. Nascimbène. *Quantum simulations with ultracold quantum gases*, Nature Physics **8**, 267 (Apr. 2012). DOI: 10.1038/nphys2259.

[10] J. L. Bohn, A. M. Rey, and J. Ye. *Cold molecules: Progress in quantum engineering of chemistry and quantum matter*, Science **357**., 1002–1010 (Sept. 2017). DOI: 10.1126/science.aam6299.

[11] T. Esslinger. *Fermi-Hubbard Physics with Atoms in an Optical Lattice*, Annual Review of Condensed Matter Physics **1**., 129–152 (May 2010). DOI: 10.1146/annurev-conmatphys-070909-104059.

[12] M. Greiner, O. Mandel, T. Esslinger, T. Hänsch, and I. Bloch. *Quantum phase transition from a superfluid to a Mott insulator in a gas of ultracold atoms*, Nature **415**, 39–44 (Jan. 2002). DOI: 10.1038/nphys2259.

[13] W. S. Bakr, J. I. Gillen, A. Peng, S. Fölling, and M. Greiner. *A quantum gas microscope for detecting single atoms in a Hubbard-regime optical lattice*, Nature **462**, 74 (Nov. 2009). DOI: 10.1038/nature08482.

[14]   J. F. Sherson, C. Weitenberg, M. Endres, M. Cheneau, I. Bloch, and S. Kuhr.
       Single-atom-resolved fluorescence imaging of an atomic Mott insulator, Nature
       467, 68 (Aug. 2010). DOI: 10.1038/nature09378.

[15]   C. Weitenberg, M. Endres, J. F. Sherson, M. Cheneau, P. Schauß, T. Fukuhara,
       I. Bloch, and S. Kuhr. *Single-spin addressing in an atomic Mott insulator*, Nature
       471., 319–324 (Mar. 2011). DOI: 10.1038/nature09827.

[16]   A. Omran, M. Boll, T. A. Hilker, K. Kleinlein, G. Salomon, I. Bloch, and C. Gross.
       Microscopic Observation of Pauli Blocking in Degenerate Fermionic Lattice Gases,
       Phys. Rev. Lett. **115**, 263001 (Dec. 2015).
       DOI: 10.1103/PhysRevLett.115.263001.

[17]   L. W. Cheuk, M. A. Nichols, M. Okan, T. Gersdorf, V. V. Ramasesh, W. S. Bakr,
       T. Lompe, and M. W. Zwierlein. *Quantum-Gas Microscope for Fermionic Atoms*,
       Phys. Rev. Lett. **114**, 193001 (May 2015).
       DOI: 10.1103/PhysRevLett.114.193001.

[18]   E. Haller, J. Hudson, A. Kelly, D. A. Cotta, B. Peaudecerf, G. D. Bruce, and
       S. Kuhr. *Single-atom imaging of fermions in a quantum-gas microscope*, Nature
       Physics **11**, 738 (July 2015). DOI: 10.1038/nphys3403.

[19]   M. F. Parsons, F. Huber, A. Mazurenko, C. S. Chiu, W. Setiawan,
       K. Wooley-Brown, S. Blatt, and M. Greiner. *Site-Resolved Imaging of Fermionic*
       ^{6}Li *in an Optical Lattice*, Phys. Rev. Lett. **114**, 213002 (May 2015).
       DOI: 10.1103/PhysRevLett.114.213002.

[20]   M. Boll, T. A. Hilker, G. Salomon, A. Omran, J. Nespolo, L. Pollet, I. Bloch, and
       C. Gross. *Spin- and density-resolved microscopy of antiferromagnetic correlations*
       in Fermi-Hubbard chains, Science **353**., 1257–1260 (Sept. 2016).
       DOI: 10.1126/science.aag1635.

[21]   A. Mazurenko, C. S. Chiu, G. Ji, M. F. Parsons, M. Kanász-Nagy, R. Schmidt,
       F. Grusdt, E. Demler, D. Greif, and M. Greiner. *A cold-atom Fermi–Hubbard*
       antiferromagnet, Nature **545**., 462–466 (May 2017).
       DOI: 10.1038/nature22362.

[22]   C. S. Chiu, G. Ji, A. Bohrdt, M. Xu, M. Knap, E. Demler, F. Grusdt, M. Greiner,
       and D. Greif. *String patterns in the doped Hubbard model*, Science **365**.,
       251–256 (July 2019). DOI: 10.1126/science.aav3587.

[23]   G. Salomon, J. Koepsell, J. Vijayan, T. A. Hilker, J. Nespolo, L. Pollet, I. Bloch,
       and C. Gross. *Direct observation of incommensurate magnetism in Hubbard*
       chains, Nature **565**., 56–60 (Dec. 2019). DOI: 10.1038/s41586-018-0778-7.

[24]   J. Koepsell, J. Vijayan, P. Sompet, F. Grusdt, T. A. Hilker, E. Demler, G. Salomon,
       I. Bloch, and C. Gross. *Imaging magnetic polarons in the doped Fermi–Hubbard*
       model, Nature **572**., 358–362 (Aug. 2019). DOI: 10.1038/s41586-019-1463-1.

[25] J. Vijayan, P. Sompet, G. Salomon, J. Koepsell, S. Hirthe, A. Bohrdt, F. Grusdt, I. Bloch, and C. Gross. *Time-resolved observation of spin-charge deconfinement in fermionic Hubbard chains*, Science **367**., 186–189 (Jan. 2020). DOI: 10.1126/science.aay2354.

[26] S. L. Campbell *et al. A Fermi-degenerate three-dimensional optical lattice clock*, Science **358**., 90–94 (Oct. 2017). DOI: 10.1126/science.aam5538.

[27] E. Oelker, R. Hutson, C. Kennedy, L. Sonderhouse, T. Bothwell, A. Goban, D. Kedar, C. Sanner, J. Robinson, G. Marti, *et al. Demonstration of 4.8×10^{-17} stability at 1 s for two independent optical clocks*, Nature Photonics **13**., 714–719 (July 2019). DOI: 10.1038/s41566-019-0493-4.

[28] A. J. Daley. *Quantum computing and quantum simulation with group-II atoms*, Quantum Information Processing **10**., 865 (Sept. 2011). DOI: 10.1007/s11128-011-0293-3.

[29] J. Ye, H. J. Kimble, and H. Katori. *Quantum State Engineering and Precision Metrology Using State-Insensitive Light Traps*, Science **320**., 1734–1738 (June 2008). DOI: 10.1126/science.1148259.

[30] M. S. Safronova, Z. Zuhrianda, U. I. Safronova, and C. W. Clark. *Extracting transition rates from zero-polarizability spectroscopy*, Phys. Rev. A **92**, 040501 (Oct. 2015). DOI: 10.1103/PhysRevA.92.040501.

[31] R. Yamamoto, J. Kobayashi, T. Kuno, K. Kato, and Y. Takahashi. *An ytterbium quantum gas microscope with narrow-line laser cooling*, New Journal of Physics **18**., 023016 (Feb. 2016). DOI: 10.1088/1367-2630/18/2/023016.

[32] *Florian Schreck group webpage*. http://www.strontiumbec.com/. Accessed: 2020-01-30.

[33] *Cheneau group webpage*. https://www.lcf.institutoptique.fr/en/groups/quantum-gases/experiments/quantum-dynamics. Accessed: 2020-01-30.

[34] *Weld lab webpage*. http://web.physics.ucsb.edu/~weld/research/. Accessed: 2020-01-30.

[35] A. Cooper, J. P. Covey, I. S. Madjarov, S. G. Porsev, M. S. Safronova, and M. Endres. *Alkaline-Earth Atoms in Optical Tweezers*, Phys. Rev. X **8**, 041055 (Dec. 2018). DOI: 10.1103/PhysRevX.8.041055.

[36] M. A. Norcia, A. W. Young, W. J. Eckner, E. Oelker, J. Ye, and A. M. Kaufman. *Seconds-scale coherence on an optical clock transition in a tweezer array*, Science **366**., 93–97 (Oct. 2019). DOI: 10.1126/science.aay0644.

[37] S. Saskin, J. T. Wilson, B. Grinkemeyer, and J. D. Thompson. *Narrow-Line Cooling and Imaging of Ytterbium Atoms in an Optical Tweezer Array*, Phys. Rev. Lett. **122**. (Apr. 2019). DOI: 10.1103/physrevlett.122.143002.

[38] H. Ozawa, S. Taie, Y. Takasu, and Y. Takahashi. *Antiferromagnetic Spin Correlation of* SU($\mathcal{N}$) *Fermi Gas in an Optical Superlattice*, Phys. Rev. Lett. **121**, 225303 (Nov. 2018). DOI: 10.1103/PhysRevLett.121.225303.

[39] S. Kolkowitz, S. Bromley, T. Bothwell, M. Wall, G. Marti, A. Koller, X. Zhang, A. Rey, and J. Ye. *Spin–orbit-coupled fermions in an optical lattice clock*, Nature **542**, 66–70 (Dec. 2016). DOI: 10.1038/nature20811.

[40] A. González-Tudela and J. I. Cirac. *Quantum Emitters in Two-Dimensional Structured Reservoirs in the Nonperturbative Regime*, Phys. Rev. Lett. **119**, 143602 (Oct. 2017). DOI: 10.1103/PhysRevLett.119.143602.

[41] A. González-Tudela and J. I. Cirac. *Markovian and non-Markovian dynamics of quantum emitters coupled to two-dimensional structured reservoirs*, Phys. Rev. A **96**, 043811 (Oct. 2017). DOI: 10.1103/PhysRevA.96.043811.

[42] A. González-Tudela and J. I. Cirac. *Non-Markovian Quantum Optics with Three-Dimensional State-Dependent Optical Lattices*, Quantum **2**, 97 (Oct. 2018). DOI: 10.22331/q-2018-10-01-97.

[43] A. González-Tudela and J. I. Cirac. *Exotic quantum dynamics and purely long-range coherent interactions in Dirac conelike baths*, Phys. Rev. A **97**, 043831 (Apr. 2018). DOI: 10.1103/PhysRevA.97.043831.

[44] L. Krinner, M. Stewart, A. Pazmiño, J. Kwon, and D. Schneble. *Spontaneous emission of matter waves from a tunable open quantum system*, Nature **559**, 589–592 (July 2018). DOI: 10.1103/PhysRevLett.101.260404.

[45] A. Acín *et al. The quantum technologies roadmap: a European community view*, New Journal of Physics **20**., 080201 (Aug. 2018). DOI: 10.1088/1367-2630/aad1ea.

[46] D. Greif, M. F. Parsons, A. Mazurenko, C. S. Chiu, S. Blatt, F. Huber, G. Ji, and M. Greiner. *Site-resolved imaging of a fermionic Mott insulator*, Science **351**., 953–957 (Feb. 2016). DOI: 10.1126/science.aad9041.

[47] R. Islam, R. Ma, P. M. Preiss, M. E. Tai, A. Lukin, M. Rispoli, and M. Greiner. *Measuring entanglement entropy in a quantum many-body system*, Nature **528**., 77–83 (Dec. 2015). DOI: 10.1038/nature15750.

[48] T. Nicholson *et al. Systematic evaluation of an atomic clock at* 2×10^{-18} *total uncertainty*, Nature Communications **6**, 6896 (Apr. 2015). DOI: 10.1038/ncomms7896.

[49] X. Xu, T. H. Loftus, J. L. Hall, A. Gallagher, and J. Ye. *Cooling and trapping of atomic strontium*, J. Opt. Soc. Am. B **20**., 968–976 (May 2003). DOI: 10.1364/JOSAB.20.000968.

[50] I. Nosske, L. Couturier, F. Hu, C. Tan, C. Qiao, J. Blume, Y. H. Jiang, P. Chen, and M. Weidemüller. *Two-dimensional magneto-optical trap as a source for cold strontium atoms*, Phys. Rev. A **96**, 053415 (Nov. 2017). DOI: 10.1103/PhysRevA.96.053415.

[51] M. M. Boyd. "High Precision Spectroscopy of Strontium in an Optical Lattice: Towards a New Standard for Frequency and Time". PhD thesis. University of Colorado, 2007. URL: https://jila.colorado.edu/yelabs/sites/default/files/uploads/theses_2007_08_martyboyd.pdf.

[52] A. D. Ludlow, M. M. Boyd, J. Ye, E. Peik, and P. O. Schmidt. *Optical atomic clocks*, Rev. Mod. Phys. **87**, 637–701 (June 2015). DOI: 10.1103/RevModPhys.87.637.

[53] M. M. Boyd, T. Zelevinsky, A. D. Ludlow, S. Blatt, T. Zanon-Willette, S. M. Foreman, and J. Ye. *Nuclear spin effects in optical lattice clocks*, Phys. Rev. A **76**, 022510 (Aug. 2007). DOI: 10.1103/PhysRevA.76.022510.

[54] M. A. Cazalilla and A. M. Rey. *Ultracold Fermi gases with emergent SU(N) symmetry*, Reports on Progress in Physics **77**., 124401 (Nov. 2014). DOI: 10.1088/0034-4885/77/12/124401.

[55] S. G. Porsev and A. Derevianko. *Hyperfine quenching of the metastable $^3P_{0,2}$ states in divalent atoms*, Phys. Rev. A **69**, 042506 (Apr. 2004). DOI: 10.1103/PhysRevA.69.042506.

[56] A. Derevianko. *Feasibility of Cooling and Trapping Metastable Alkaline-Earth Atoms*, Phys. Rev. Lett. **87**, 023002 (June 2001). DOI: 10.1103/PhysRevLett.87.023002.

[57] M. Yasuda and H. Katori. *Lifetime Measurement of the $^3P_2$ Metastable State of Strontium Atoms*, Phys. Rev. Lett. **92**, 153004 (Apr. 2004). DOI: 10.1103/PhysRevLett.92.153004.

[58] H. Metcalf and P. van der Straten. *Laser Cooling and Trapping*. Graduate Texts in Contemporary Physics. Springer New York, 2001. ISBN: 9780387987286.

[59] I. Courtillot, A. Quessada, R. P. Kovacich, J.-J. Zondy, A. Landragin, A. Clairon, and P. Lemonde. *Efficient cooling and trapping of strontium atoms*, Opt. Lett. **28**., 468–470 (Mar. 2003). DOI: 10.1364/OL.28.000468.

[60] R. Grimm, M. Weidemüller, and Y. B. Ovchinnikov. *Optical dipole traps for neutral atoms*, Advances in Atomic, Molecular, and Optical Physics **42**, 95 (2000). DOI: 10.1016/S1049-250X(08)60186-X.

[61] M. Takamoto, H. Katori, S. I. Marmo, V. D. Ovsiannikov, and V. G. Pal'chikov. *Prospects for Optical Clocks with a Blue-Detuned Lattice*, Phys. Rev. Lett. **102**, 063002 (Feb. 2009). DOI: 10.1103/PhysRevLett.102.063002.

[62] A. J. Daley, M. M. Boyd, J. Ye, and P. Zoller. *Quantum Computing with Alkaline-Earth-Metal Atoms*, Phys. Rev. Lett. **101**, 170504 (Oct. 2008). DOI: 10.1103/PhysRevLett.101.170504.

[63] C. K. Hong, Z. Y. Ou, and L. Mandel. *Measurement of subpicosecond time intervals between two photons by interference*, Phys. Rev. Lett. **59**, 2044–2046 (Nov. 1987). DOI: 10.1103/PhysRevLett.59.2044.

[64] M. Greiner. "Ultracold quantum gases in three-dimensional optical lattice potentials". PhD thesis. Ludwig-Maximilians-Universität München, 2003. URL: https://edoc.ub.uni-muenchen.de/968/1/Greiner_Markus.pdf.

[65] S. Will. "Interacting bosons and fermions in three-dimensional optical lattice potentials : from atom optics to quantum simulation". PhD thesis. Johannes Gutenberg-Universität Mainz, 2011. URL: https://pdfs.semanticscholar.org/e081/b3dad5eb6cb849aa9eb38dc358d09ec198c4.pdf.

[66] N. Ashcroft and N. Mermin. *Solid State Physics*. Fort Worth: Saunders College Publishing, 1976. ISBN: 9780030839931.

[67] R. Jördens, N. Strohmaier, K. Günter, H. Moritz, and T. Esslinger. *A Mott insulator of fermionic atoms in an optical lattice*, Nature **455**., 204–207 (Sept. 2008). DOI: 10.1038/nature07244.

[68] C. Weitenberg. "Single-atom resolved imaging and manipulation in an atomic Mott insulator". PhD thesis. Ludwig Maximilians Universität München, 2011. URL: https://edoc.ub.uni-muenchen.de/13425/1/Weitenberg_Christof.pdf.

[69] T. A. Hilker. "Spin-resolved microscopy of strongly correlated fermionic many-body states". PhD thesis. Ludwig Maximilians Universität München, 2017. URL: https://edoc.ub.uni-muenchen.de/21633/1/Hilker_Timon.pdf.

[70] E. Hecht. *Optik*. 2009. ISBN: 9783486588613.

[71] J. Greivenkamp. *Field Guide to Geometrical Optics*. 2004. ISBN: 9780819452948.

[72] A. Mosk, S. Jochim, H. Moritz, T. Elsässer, M. Weidemüller, and R. Grimm. *Resonator-enhanced optical dipole trap for fermionic lithium atoms*, Opt. Lett. **26**., 1837–1839 (Dec. 2001). DOI: 10.1364/OL.26.001837.

[73] J. Léonard. "A supersolid of matter and light". PhD thesis. ETH Zurich, 2017. URL: https://www.research-collection.ethz.ch/handle/20.500.11850/262194.

[74] D. Jaksch, H.-J. Briegel, J. I. Cirac, C. W. Gardiner, and P. Zoller. *Entanglement of Atoms via Cold Controlled Collisions*, Phys. Rev. Lett. **82**, 1975–1978 (Mar. 1999). DOI: 10.1103/PhysRevLett.82.1975.

[75] T. Calarco, E. A. Hinds, D. Jaksch, J. Schmiedmayer, J. I. Cirac, and P. Zoller. *Quantum gates with neutral atoms: Controlling collisional interactions in time-dependent traps*, Phys. Rev. A **61**, 022304 (Jan. 2000). DOI: 10.1103/PhysRevA.61.022304.

[76] J. D. Hood, A. Goban, A. Asenjo-Garcia, M. Lu, S.-P. Yu, D. E. Chang, and H. J. Kimble. *Atom–atom interactions around the band edge of a photonic crystal waveguide*, Proceedings of the National Academy of Sciences **113**., 10507–10512 (Aug. 2016). DOI: 10.1073/pnas.1603788113.

[77] S. Snigirev, A. J. Park, A. Heinz, I. Bloch, and S. Blatt. *Fast and dense magneto-optical traps for strontium*, Phys. Rev. A **99**, 063421 (June 2019). DOI: 10.1103/PhysRevA.99.063421.

[78]   W. Haynes. *CRC Handbook of Chemistry and Physics*. CRC Press, 2016. ɪsʙɴ:
       9781498754293.

[79]   E. Staub. "Developing a High-Flux Atomic Beam Source for Experiments with
       Ultracold Strontium Quantum Gases". MA thesis.
       Ludwig-Maximilians-Universität München, 2019. ᴜʀʟ:
       http://ultracold.sr/publications/thesis_etienne_staub.pdf.

[80]   N. Janša. "A frequency-stable diode laser system for spectroscopy and trapping
       of Sr atoms". MA thesis. Ludwig-Maximilians-Universität München, 2016. ᴜʀʟ:
       http://ultracold.sr/publications/thesis_nejc_jansa.pdf.

[81]   R. Uberna, A. Bratcher, and B. G. Tiemann. *Coherent Polarization Beam
       Combination*, IEEE Journal of Quantum Electronics **46**., 1191–1196 (Aug.
       2010). ᴅᴏɪ: 10.1109/JQE.2010.2044976.

[82]   E. Donley, T. Heavner, F. Levi, M. Tataw, and S. Jefferts. *Double-pass
       acousto-optic modulator system*, Review of Scientific Instruments **76**, 063112
       (June 2005). ᴅᴏɪ: 10.1063/1.1930095.

[83]   S. Stellmer. "Degenerate quantum gases of strontium". PhD thesis. Universität
       Innsbruck, 2013. ᴜʀʟ: http://www.ultracold.at/theses/2013-stellmer.pdf.

[84]   H. L. Stover and W. H. Steier. *Locking of Laser Oscillators by Light Injection*,
       Applied Physics Letters **8**., 91–93 (Apr. 1966). ᴅᴏɪ: 10.1063/1.1754502.

[85]   C. J. Buczek, R. J. Freiberg, and M. L. Skolnick. *Laser injection locking*,
       Proceedings of the IEEE **61**., 1411–1431 (Oct. 1973).
       ᴅᴏɪ: 10.1109/PROC.1973.9294.

[86]   T. Aoki, K. Umezawa, Y. Yamanaka, N. Takemura, Y. Sakemi, and Y. Torii. *A 461
       nm Laser System and Hollow-Cathode Lamp Spectroscopy for Magneto-Optical
       Trapping of Sr Atoms*, Journal of the Physical Society of Japan **81**., 034401 (Feb.
       2012). ᴅᴏɪ: 10.1143/JPSJ.81.034401.

[87]   Y. Shimada, Y. Chida, N. Ohtsubo, T. Aoki, M. Takeuchi, T. Kuga, and Y. Torii. *A
       simplified 461-nm laser system using blue laser diodes and a hollow cathode lamp
       for laser cooling of Sr*, Review of Scientific Instruments **84**., 063101 (June
       2013). ᴅᴏɪ: 10.1063/1.4808246.

[88]   R. K. Raj, D. Bloch, J. J. Snyder, G. Camy, and M. Ducloy. *High-Frequency
       Optically Heterodyned Saturation Spectroscopy Via Resonant Degenerate
       Four-Wave Mixing*, Phys. Rev. Lett. **44**, 1251–1254 (May 1980).
       ᴅᴏɪ: 10.1103/PhysRevLett.44.1251.

[89]   Ducloy, M. and Bloch, D. *Theory of degenerate four-wave mixing in resonant
       Doppler-broadened systems - I. Angular dependence of intensity and lineshape of
       phase-conjugate emission*, J. Phys. France **42**., 711–721 (Jan. 1981).
       ᴅᴏɪ: 10.1051/jphys:01981004205071100.

[90] D. O. Sabulsky, C. V. Parker, N. D. Gemelke, and C. Chin. *Efficient continuous-duty Bitter-type electromagnets for cold atom experiments*, Review of Scientific Instruments **84**., 104706 (Oct. 2013). DOI: 10.1063/1.4826498.

[91] E. L. Raab, M. Prentiss, A. Cable, S. Chu, and D. E. Pritchard. *Trapping of Neutral Sodium Atoms with Radiation Pressure*, Phys. Rev. Lett. **59**, 2631–2634 (Dec. 1987). DOI: 10.1103/PhysRevLett.59.2631.

[92] R. González Escudero. "Magnetic Field Control and Laser Frequency Stabilization for Strontium Magneto-Optical Traps". MA thesis. Ludwig-Maximilians-Universität München, 2016. URL: http://ultracold.sr/publications/thesis_rodrigo_gonzalez_escudero.pdf.

[93] D. S. Barker, B. J. Reschovsky, N. C. Pisenti, and G. K. Campbell. *Enhanced magnetic trap loading for atomic strontium*, Phys. Rev. A **92**, 043418 (Oct. 2015). DOI: 10.1103/PhysRevA.92.043418.

[94] *The National Institute of Standards and Technology (NIST) database*. https://www.nist.gov/pml/atomic-weights-and-isotopic-compositions-relative-atomic-masses. Accessed: 2019-12-20.

[95] S. B. Nagel, C. E. Simien, S. Laha, P. Gupta, V. S. Ashoka, and T. C. Killian. *Magnetic trapping of metastable $^3P_2$ atomic strontium*, Phys. Rev. A **67**, 011401 (Jan. 2003). DOI: 10.1103/PhysRevA.67.011401.

[96] T. H. Loftus, T. Ido, M. M. Boyd, A. D. Ludlow, and J. Ye. *Narrow line cooling and momentum-space crystals*, Phys. Rev. A **70**, 063413 (Dec. 2004). DOI: 10.1103/PhysRevA.70.063413.

[97] S. L. Campbell. "A Fermi-degenerate three-dimensional optical lattice clock". PhD thesis. University of Colorado, 2010. URL: https://jila.colorado.edu/yelabs/sites/default/files/uploads/slc_thesis_0.pdf.

[98] S. Bali, K. M. O'Hara, M. E. Gehm, S. R. Granade, and J. E. Thomas. *Quantum-diffractive background gas collisions in atom-trap heating and loss*, Phys. Rev. A **60**, R29–R32 (July 1999). DOI: 10.1103/PhysRevA.60.R29.

[99] N. Teranishi and Y. Ishihara. *Smear reduction in the interline CCD image sensor*, IEEE Transactions on Electron Devices **34**., 1052–1056 (May 1987). DOI: 10.1109/T-ED.1987.23043.

[100] A. D. Ludlow. "The strontium optical lattice clock: optical spectroscopy with sub-Hertz accuracy". PhD thesis. University of Colorado, 2008. URL: https://jila.colorado.edu/yelabs/sites/default/files/uploads/theses_2008_AndrewLudlow.pdf.

[101] S. H. Wissenberg. "Stabilizing diode lasers to an ultrastable reference cavity". MA thesis. Ludwig-Maximilians-Universität München, 2017. URL: http://ultracold.sr/publications/thesis_stephan_wissenberg.pdf.

[102]   R. U. Haindl. "A clock laser system for quantum simulations with ultracold strontium atoms". MA thesis. Ludwig-Maximilians-Universität München, 2019. URL: http://ultracold.sr/publications/thesis_rudolf_haindl.pdf.

[103]   F. Finger. "A transport laser with shape and amplitude control for ultracold strontium atoms". MA thesis. Technische Universität München, 2018. URL: http://ultracold.sr/publications/thesis_fabian_finger.pdf.

[104]   A. Heinz, A. J. Park, N. Šantić, J. Trautmann, S. G. Porsev, M. S. Safronova, I. Bloch, and S. Blatt. *State-dependent optical lattices for the strontium optical qubit*, arXiv: 1912.10350 (Dec. 2019).

[105]   B. M. Henson, R. I. Khakimov, R. G. Dall, K. G. H. Baldwin, L.-Y. Tang, and A. G. Truscott. *Precision Measurement for Metastable Helium Atoms of the 413 nm Tune-Out Wavelength at Which the Atomic Polarizability Vanishes*, Phys. Rev. Lett. **115**, 043004 (July 2015). DOI: 10.1103/PhysRevLett.115.043004.

[106]   F. Schmidt, D. Mayer, M. Hohmann, T. Lausch, F. Kindermann, and A. Widera. *Precision measurement of the ^{87}Rb tune-out wavelength in the hyperfine ground state $F = 1$ at 790 nm*, Phys. Rev. A **93**, 022507 (Feb. 2016). DOI: 10.1103/PhysRevA.93.022507.

[107]   R. H. Leonard, A. J. Fallon, C. A. Sackett, and M. S. Safronova. *High-precision measurements of the $^{87}Rb D$-line tune-out wavelength*, Phys. Rev. A **92**, 052501 (Nov. 2015). DOI: 10.1103/PhysRevA.92.052501.

[108]   T. Mazzoni, X. Zhang, R. Del Aguila, L. Salvi, N. Poli, and G. M. Tino. *Large-momentum-transfer Bragg interferometer with strontium atoms*, Phys. Rev. A **92**, 053619 (Nov. 2015). DOI: 10.1103/PhysRevA.92.053619.

[109]   M. Bishof, M. Martin, M. Swallows, C. Benko, Y. Lin, G. Quéméner, A. Rey, and J. Ye. *Inelastic collisions and density-dependent excitation suppression in a ^{87}Sr optical lattice clock*, Phys. Rev. A **84**, 052716 (Aug. 2011). DOI: 10.1103/PhysRevA.84.052716.

[110]   A. J. Daley, J. Ye, and P. Zoller. *State-dependent lattices for quantum computing with alkaline-earth-metal atoms*, The European Physical Journal D **65**., 207–217 (Feb. 2011). DOI: 10.1140/epjd/e2011-20095-2.

[111]   T. A. Savard, K. M. O'Hara, and J. E. Thomas. *Laser-noise-induced heating in far-off resonance optical traps*, Phys. Rev. A **56**, R1095–R1098 (Aug. 1997). DOI: 10.1103/PhysRevA.56.R1095.

[112]   M. Gehm, K. O'Hara, T. Savard, and J. Thomas. *Dynamics of noise-induced heating in atom traps*, Phys. Rev. A **58**, 3914 (Nov. 1998). DOI: 10.1103/PhysRevA.58.3914.

[113]   M. Gehm, K. O'Hara, T. Savard, and J. Thomas. *Erratum: Dynamics of noise-induced heating in atom traps [Phys. Rev. A 58, 3914 (1998)]*, Phys. Rev. A **61**, 029902 (Jan. 2000). DOI: 10.1103/PhysRevA.61.029902.

[114] L. Riegger. "Interorbital spin exchange in a state-dependent optical lattice". PhD thesis. Ludwig-Maximilians-Universtität München, 2019. URL: https://edoc.ub.uni-muenchen.de/23994/1/Riegger_Luis.pdf.

[115] I. Courtillot, A. Quessada-Vial, A. Brusch, D. Kolker, G. D. Rovera, and P. Lemonde. *Accurate spectroscopy of Sr atoms*, Euro. Phys. J. D **33**, 161 (May 2005). DOI: 10.1140/epjd/e2005-00058-0.

[116] H. Miyake, N. C. Pisenti, P. K. Elgee, A. Sitaram, and G. K. Campbell. *Isotope-shift spectroscopy of the $^1S_0 \to{}^3P_1$ and $^1S_0 \to{}^3P_0$ transitions in strontium*, Phys. Rev. Research **1**, 033113 (Nov. 2019). DOI: 10.1103/PhysRevResearch.1.033113.

[117] W. F. Holmgren, R. Trubko, I. Hromada, and A. D. Cronin. *Measurement of a Wavelength of Light for Which the Energy Shift for an Atom Vanishes*, Phys. Rev. Lett. **109**, 243004 (Dec. 2012). DOI: 10.1103/PhysRevLett.109.243004.

[118] C. D. Herold, V. D. Vaidya, X. Li, S. L. Rolston, J. V. Porto, and M. S. Safronova. *Precision Measurement of Transition Matrix Elements via Light Shift Cancellation*, Phys. Rev. Lett. **109**, 243003 (Dec. 2012). DOI: 10.1103/PhysRevLett.109.243003.

[119] E. Copenhaver, K. Cassella, R. Berghaus, and H. Müller. *Measurement of a ^{7}Li tune-out wavelength by phase-patterned atom interferometry*, Phys. Rev. A **100**, 063603 (Dec. 2019). DOI: 10.1103/PhysRevA.100.063603.

[120] R. Loudon. *The Quantum Theory of Light*. 3rd. Oxford University Press, 2000. ISBN: 0198501765.

[121] M. S. Safronova, S. G. Porsev, U. I. Safronova, M. G. Kozlov, and C. W. Clark. *Blackbody-radiation shift in the Sr optical atomic clock*, Phys. Rev. A **87**, 012509 (Jan. 2013). DOI: 10.1103/PhysRevA.87.012509.

[122] S. Nagel, P. Mickelson, A. Saenz, Y. Martinez, Y. Chen, T. Killian, P. Pellegrini, and R. Côté. *Photoassociative Spectroscopy at Long Range in Ultracold Strontium*, Phys. Rev. Lett. **94**, 083004 (Mar. 2005). DOI: 10.1103/PhysRevLett.94.083004.

[123] M. Yasuda, T. Kishimoto, M. Takamoto, and H. Katori. *Photoassociation spectroscopy of ^{88}Sr: Reconstruction of the wave function near the last node*, Phys. Rev. A **73**, 011403(R) (Jan. 2006). DOI: 10.1103/PhysRevA.73.011403.

[124] U. Brinkmann. *Lebensdauern und Oszillatorstärken im Sr I- und Ca I-Spektrum*, Zeitschrift für Physik **228**., 440–453 (Aug. 1969). DOI: 10.1007/BF01558342.

[125] M. D. Havey, L. C. Balling, and J. J. Wright. *Direct measurements of excited-state lifetimes in Mg, Ca, and Sr*, J. Opt. Soc. Am. **67**., 488–491 (Apr. 1977). DOI: 10.1364/JOSA.67.000488.

[126] G. Jönsson, C. Levinson, A. Persson, and C.-G. Wahlström. *Natural radiative lifetimes in the $^1P_1$ and $^1F_3$ sequences of Sr I*, Z. Phys. A **316**, 255 (Oct. 1984).

[127] R. Bause, M. Li, A. Schindewolf, X.-Y. Chen, M. Duda, S. Kotochigova, I. Bloch, and X.-Y. Luo. *Tune-out and magic wavelengths for ground-state* $^{23}Na^{40}K$ *molecules*, arXiv: 1912.10452 (2019).

[128] S. Blatt, A. Mazurenko, M. F. Parsons, C. S. Chiu, F. Huber, and M. Greiner. *Low-noise optical lattices for ultracold* ^{6}Li, Phys. Rev. A **92**, 021402 (Aug. 2015). DOI: 10.1103/PhysRevA.92.021402.

[129] I. de Vega, D. Porras, and J. Ignacio Cirac. *Matter-Wave Emission in Optical Lattices: Single Particle and Collective Effects*, Phys. Rev. Lett. **101**, 260404 (Dec. 2008). DOI: 10.1103/PhysRevLett.101.260404.

[130] J. Argüello-Luengo, A. González-Tudela, T. Shi, P. Zoller, and J. I. Cirac. *Analog quantum chemistry simulation*, Nature **574**, 215–218 (Oct. 2019). DOI: 10.1103/PhysRevLett.101.260404.

[131] B. E. A. Saleh and M. C. Teich. *Fundamentals of photonics; 2nd ed.* Wiley series in pure and applied optics. New York, NY: Wiley, 2007. ISBN: 9780471358329.

[132] N. Hodgson and H. Weber. *Laser Resonators and Beam Propagation*. Vol. 108. 2005. ISBN: 9780387400785.

[133] G. Berden and R. Engeln. *Cavity Ring-Down Spectroscopy: Techniques and Applications*. 2009. ISBN: 9781405176880.

[134] A. Siegman. *Lasers*. University Science Books, 1986. ISBN: 9780935702118.

[135] J. Goodman. *Introduction to Fourier Optics*. McGraw-Hill physical and quantum electronics series. W. H. Freeman, 2005. ISBN: 9780974707723.

[136] Q.-Y. Tong and U. Gösele. *Semiconductor Wafer Bonding: Science and Technology*. Wiley, 1998. ISBN: 9780471574811.

[137] E. Black. *An introduction to Pound-Drever-Hall laser frequency stabilization*, American Journal of Physics **69**, 79–87 (Jan. 2001). DOI: 10.1119/1.1286663.

[138] M. J. Martin. "Quantum Metrology and Many-Body Physics: Pushing the Frontier of the Optical Lattice Clock". PhD thesis. University of Colorado, 2006. URL: https://jila.colorado.edu/yelabs/sites/default/files/uploads/MJMartinThesisFinal_April%202013.pdf.

[139] B. Bernhardt. "Dual Comb Spectroscopy". PhD thesis. Ludwig-Maximilians-Universität München, 2011. URL: https://edoc.ub.uni-muenchen.de/13435/1/Bernhardt_Birgitta.pdf.

[140] K. Boller, R.-P. Haelbich, H. Hogrefe, W. Jark, and C. Kunz. *Investigation of carbon contamination of mirror surfaces exposed to synchrotron radiation*, Nuclear Instruments and Methods in Physics Research **208**, 273–279 (Apr. 1983). DOI: 10.1016/0167-5087(83)91134-1.

[141] K. Yamada *et al. Saturation of cavity-mirror degradation in the UV FEL*, Nuclear Instruments and Methods in Physics Research Section A: Accelerators, Spectrometers, Detectors and Associated Equipment **393**, 44–49 (July 1997). DOI: 10.1016/S0168-9002(97)00425-7.

[142] V. B. Braginsky and F. Y. Khalili. *Quantum measurement*. Ed. by K. S. Thorne. Cambridge University Press, Cambridge, 1992. ISBN: 052141928X.

[143] S. Origlia *et al. Towards an optical clock for space: Compact, high-performance optical lattice clock based on bosonic atoms*, Phys. Rev. A **98**, 053443 (Nov. 2018). DOI: 10.1103/PhysRevA.98.053443.

[144] S. B. Koller, J. Grotti, S. Vogt, A. Al-Masoudi, S. Dörscher, S. Häfner, U. Sterr, and C. Lisdat. *Transportable Optical Lattice Clock with 7×10^{-17} Uncertainty*, Phys. Rev. Lett. **118**, 073601 (Feb. 2017). DOI: 10.1103/PhysRevLett.118.073601.

[145] J. Grotti *et al. Geodesy and metrology with a transportable optical clock*, Nature Physics **14**, 437 (Feb. 2018). DOI: 10.1038/s41567-017-0042-3.

[146] T. E. Mehlstäubler, G. Grosche, C. Lisdat, P. O. Schmidt, and H. Denker. *Atomic clocks for geodesy*, Reports on Progress in Physics **81**., 064401 (Apr. 2018). DOI: 10.1088/1361-6633/aab409.

[147] G. D. Domenico, S. Schilt, and P. Thomann. *Simple approach to the relation between laser frequency noise and laser line shape*, Appl. Opt. **49**., 4801–4807 (Sept. 2010). DOI: 10.1364/AO.49.004801.

Acknowledgements

After more than four years as a PhD student, the number of people who supported me to accomplish this work is fairly high and I want to thank all of them here in no particular order.

First and foremost, I want to thank my supervisor Prof. Immanuel Bloch for granting me the opportunity to work in his group. I would like to thank you in particular for sharing such strong enthusiasm for physics with me. This is especially visible during physics discussions and your talks, which are always a good example for anyone. In addition, thank you for being absolutely reliable although being constantly busy.

Equally, I want to acknowledge my group leader, Sebastian Blatt. We worked almost every day with each other, since I was the first PhD student in this lab. In hours of discussions, for instance when we designed and improved things in the lab, you shared an unseen wide range of knowledge with me. From physics over computer science to barbecuing, you showed me how to do things right. You definitely influenced my way of thinking and I have developed a much more efficient working style, which I will benefit from for the rest of my life. Also, you always had an open door to listen to my concerns and you calmed me down, when things did not work out as planned. It always helped to talk to you.

Special thanks go to the PhD students Annie Jihyun Park and Jan Trautmann. You guys are great colleagues and friends to me and are always trying to help whenever someone needs it. You guys are awesome. Equal thanks go to Nejc Janša and Fabian Finger. You guys are good friends and competent colleagues to me during your year of your masters' thesis. Thanks for your company beyond work hours, even after you have left the group. Thanks go also to our two Postdocs and good colleagues of mine to Stepan Snigirev and Neven Šantić. Thanks for enlightening discussions about physics and interesting topics far beyond that. I also like to thank many of the other lab members I worked with: Rodrigo González Escudero, Stephan Wissenberg, Rudolf Haindl, Etienne Staub, Lukas Homeier, Eva Casotti, and Florian Wallner. I learned a lot from you guys. Might it be about physics, lifestyle or sports.

A person who played a very important role during my PhD was Anton Meyer. You always fed me with lots of high-precision construction ideas, created heroic CAD drawings and did your best to get things done in time by negotiating with the machine shop. Sometimes, you even machined things for me right away, so I could continue to work on other projects in the meantime. The crossed cavity, as it is now, would have never been possible without your contribution. Thanks for other interesting discussions we had. You deserve a part of my PhD hat.

Thanks to Boris Braverman, who was my previous adviser in the lab back in the time when I was a master student at MIT. Your pragmatism in combination with inventive